IN-VENTO 2024 PISA

Università di Pisa

ANV

DICI Dipartimento di Ingegneria Civile e Industriale

XVIII International Conference of the Italian Association for Wind Engineering

Pisa, Italy | 9-11 September 2024

Centro Congressi Le Benedettine

Piazza S. Paolo a Ripa D'Arno, 16

BOOK OF ABSTRACTS

With the support of

GERB Controllo delle Vibrazioni

pininfarina

Organizing Committee

- **Maria Vittoria Salvetti** (Chairperson) – *University of Pisa, Italy*
- **Alessandro Mariotti** (Chairperson) – *University of Pisa, Italy*
- **Guido Buresti** (Honorary Chairperson) – *University of Pisa, Italy*
- **Giovanni Lombardi** – *University of Pisa, Italy*
- **Simone Camarri** – *University of Pisa, Italy*
- **Alessio Innocanti** – *University of Pisa, Italy*

Scientific Committee

- **Thomas Andrianne** – *Université de Liège, Belgium*
- **Tommaso Argentini** – *Politecnico di Milano, Italy*
- **Alberto Maria Avossa** – *Università della Campania, Italy*
- **Gianni Bartoli** – *Università di Firenze, Italy*
- **Luca Bruno** – *Politecnico di Torino, Italy*
- **Massimiliano Burlando** – *Università di Genova, Italy*
- **Stefano Cammelli** – *WSP, United Kingdom*
- **Luca Caracoglia** – *Northeastern University, USA*
- **Luigi Carassale** – *Università di Genova, Italy*
- **Andrea Cimarelli** – *Università di Modena e Reggio Emilia, Italy*
- **Vincent Denoel** – *Université de Liège, Belgium*
- **Cristoforo Demartino** – *Università Roma Tre, Italy*
- **Davide Fransos** – *Sauber Motorsport, Swiss*
- **Massimiliano Gioffré** – *Università di Perugia, Italy*

- **Kenny Kwok** – *University of Sydney, Australia*
- **Greg Kopp** – *Western University, Canada*
- **Giacomo Valerio Iungo** – *UT Dallas, USA*
- **Guy Larose** – *RWDI*
- **Giampiero Manara** – *Permasteelisa Group, Italy*
- **Claudio Mannini** – *Università di Firenze, Italy*
- **Antonino Maria Marra** – *Università di Firenze, Italy*
- **Sara Muggiasca** – *Politecnico di Milano, Italy*
- **Felix Nieto** – *Universidade da Coruña, Spain*
- **Luisa Carlotta Pagnini** – *Università di Genova, Italy*
- **Luca Patruno** – *Università di Bologna, Italy*
- **Francesco Petrini** – *Sapienza Università di Roma, Italy*
- **Giuseppe Piccardo** – *Università di Genova, Italy*
- **Maurizio Quadrio** – *Politecnico di Milano, Italy*
- **Lorenzo Raffaele** – *Politecnico di Torino, von Karman Institute, Italy, Belgium*
- **Maria Pia Repetto** – *Università di Genova, Italy*
- **Alessio Ricci** – *Scuola Universitaria Superiore IUSS Pavia, Italy*
- **Fabio Rizzo** – *Politecnico di Bari, Italy*
- **Daniele Rocchi** – *Politecnico di Milano, Italy*
- **Paolo Schito** – *Politecnico di Milano, Italy*
- **Vincenzo Sepe** – *Università "G. d'Annunzio" di Chieti-Pescara, Italy*
- **Federica Tubino** – *Università di Genova, Italy*
- **Ilaria Venanzi** – *Università di Perugia, Italy*

Index

15. *Dehareng, S., Gemine, T., Lumay, G., Andrianne, T.*:
Characterization of the full turbulent spectrum of the flow in a small-scale wind tunnel using a multi-hole probe

16. *Doerffer, K., Doerffer, P., Grzelak, J., Kotus, J., Eltayesh, A., Pagnini, L., Piccardo, G., Repetto, M.P.*:
Wind tunnel testing on the high rotational urban Savonius turbine

17. *Dorigatti, F., Browne, M.T.L., Taylor, Z.J.*:
Wind loading on ground-mounted solar PV structures: Comparison with Eurocode

18. *Eissa, M., Metwally, O., Canepa, F., Mengistu, M.T., Elawady, A., Burlando, M., Repetto, M.P., Piccardo, G.*:
Uniting the Realms of Physical Simulations and Field Measurements of Downburst Events Through an International Collaboration

19. *Francioli, M., Petrini, F.*:
A simplified procedure for assessing nonlinear behavior of steel plane frames under wind

20. *Frontini, G., Muggiasca, S., Argentini, T.*:
Overview of current methodologies for photovoltaic tracker parks analysis

21. *Giaccu, G.F., Caracoglia, L.*:
Improving long-span bridge flutter performance by gyroscopic stabilizers: recent wind tunnel experiments

22. *Hii, E., Cammelli, S.*:
Stack Effects in High-rise Buildings: Challenges, Design Constraints and Mitigation Measures

23. *Kolli, S. Bind, A., Hemida, H., Dammala, P.K.*:
Influence of dune-dune interaction on sand dune migration and evolution: Wind tunnel experiment

24. *Leone, T., Calamelli, F., Schito, P., Zasso, A.*:
Wind tunnel numerical modeling for wind farm control strategies

25. *Li, H., Cotteleer, L., Gambale, A., Parente, A.*:
Reduced-Order modeling for Atmospheric Boundary Layer Flows integrating Dimensionality Reduction and Non-linear Regression

26. *Lunghi, G., Morello, M., Mariotti, A., Salvetti, M.V., Corsini, R., Cimarelli, A., Stalio, E.*:
Flow characteristics around a 5:1 rectangular cylinder at moderate Reynolds number: DNS, LES, and experiments

27. *Luzzati, E., Mariotti, A., Salvetti, M.V.*:
Development of an actuator line model for pitching airfoils with aerodynamic moment corrections

28. *Malasomma, A., Picozzi, V., Avossa, A.M., Caracoglia, L., Ricciardelli, F.*:
Design of full-scale monitoring system for a mid-rise building under wind action

29. *Mannini, C., Massai, T., Barni, N.*:
A refined surface roughness approach to trigger the transcritical flow regime past a circular cylinder

30. *Meinhhardt, C., Lauzi, M., Bottoni, F.*:
Tuned Mass Inerter Dampers to reduce Vortex Induced Vibrations during the construction stage of Onshore Wind Turbines

31. *Mengistu, M.T., Repetto, M.P.*:
Estimation of aerodynamic properties of a polygonal cylinder from full-scale monitoring

32. *Modé, P., Demartino, C., Lagaros, N.D., Georgakis, C.T.*:
Correlation between predictability of extreme wind speeds and wind directionality

33. *Morello, M., Lunghi, G., Brusco, S., Mariotti, A., Salvetti, M.V.*:
Effect of accelerating flows around elongated rectangular cylinders

34. *Nieto, F., Álvarez, A.J., Laws, P., Patruno, L., Kwok, K.*:
Turbulent flow on a 3:2 rectangular cylinder: small-scale rod-induced turbulence and synthetic turbulence methods

35. *Orlando, A., Pagnini, L., Repetto, M.P.*:
Drag crisis nonlinear effect on aerodynamic damping of vertical slender structures

36. *Orlando, A., Pagnini, L., Repetto, M.P.*:
Experimental investigation of monotubular steel poles: case studies and dynamic identification

37. *Pace, M.A., Calamelli, F., Argentini, T., Rocchi, D.*:
Numerical simulation of the aeroelastic response of a long-span bridge subjected to different non-synoptic wind scenarios

38. *Pavan, A., Cimarelli, A., Costa, P., Stalio, E.*:
Towards a general approach for the study of urban heat island

39. *Piazza, A., Repetto, M.P., Bitsuamlak, G.T.*:
Aerodynamic and dynamic behavior of an aeroelastic tree model

40. *Picozzi, V., Sørensen, J.D., Avossa, A.M., Ricciardelli, F.*:
Calibration of Wind Action Partial Factor for the Italian Climate

41. *Polucci, M., Francioli, M., De Angelis, M., Petrini, F.*:
Integrated optimal design of TMDI and structure for slender elements under wind

42. *Raffaele, L., Bruno, L., Colucci, E.*:
The Italian wind map – part I: a critical analysis of measurements at land anemometric stations

43. *Raffaele, L., Bruno, L., Colucci, E.*:
The Italian wind map – part II: an approach based on mesoscale wind modelling

44. *Raghunathan Srikumar, S.K., Mosca, G., Gambale, A.*:
A combined CFD and ML based approach to perform a feasibility study of wind energy harvesting in the vicinity of the built environment using medium-sized wind turbines

45. *Ricciardelli, F., Akbaba, A., Picozzi, V., Avossa, A.M.*:
A proposal for updating the extreme wind map of Italy

46. *Rizzo, F., Caracoglia, L., Mansour, S., Sabba', M.F., Maddaloni, G., Foti, D.*:
Multi-hazard analysis of structural and nonstructural building elements under simultaneous seismic and wind loads

47. *Rizzo, F., Caracoglia, L., Piccardo, G.*:
Improving post-critical galloping analysis of square-shaped cylinders through Artificial Neural Networks

48. *Roncallo, L., Mengistu, M.T., Tubino, F., Repetto, M.P.*:
Thunderstorm gust response factor: application to a full-scale monitored slender vertical structure

49. *Salvatori, L., Marra, A.M., De Stefano, M., Spinelli, P.*:
Wind load simulations on bridge decks during a downburst

50. *Sánchez, C.A., Torre, S., Ruffini, E., Bagnara, A., Piccardo, G., Tubino, F.*:
Thunderstorm-induced actions on CAARC building wind tunnel studies

51. *Sarkar, P.P., Alipour, A., Caracoglia, L., Kaye, N.B., Prevatt, D.O., Sharma, A., Selvam, R.P., Yan, G., Zuo, D.*:
Some considerations on the design of a novel, large-scale testing facility (NEWRITE) for non-stationary wind loads

52. *Sciarretta, L., Manes, L., Xu, M., Patruno, L., de Miranda, S.*:
Fluid-structure interaction simulations using open-source software couplers

53. *Sorge, E., Riascos, C., Caterino, N.*:
Structural load mitigation against operational and extreme wind speeds for HAWTs equipped with a friction-based control system.

54. *Xhelaj, A., Burlando, M., Romanic, D., Hangan, H.*:
Advanced insights into stationary downburst phenomena: a POD analysis of LES CFD data

55. *Yuan, Y., Yan, B., Ran, Q., Li, X.*:
An active-controlled multi-blade system for simulation of downburst outflows in boundary layer wind tunnel

56. *Žužul, J., Ricci, A., Burlando, M.*:
Advancing towards the creation of a digital twin for Genoa, Italy: Facilitating CFD simulations to produce the wind hazard map

IN-VENTO 2024
International Conference of the Italian Association for Wind Engineering
Pisa, September 8th – 11th, 2024

Enhancing Resilience in Wind-Prone Regions: A Unified Framework for Assessing Integrated Tree-Induced and Wind-Induced Building Damage

M. Bakhshandeh[a], J.-P. Pinelli[b], A. Elawady[c], H. A. Ibrahim[c], F. Ahmed[c]

[a]*Florida Institute of Technology, Melbourne, FL 32901, USA, mbakhshandeh2023@my.fit.edu*
[b]*Florida Institute of Technology, Melbourne, FL 32901, USA, pinelli@fit.edu u*
[c]*Florida international University, Miami, FL 33174, USA, aelawady@fiiu.edu*

SUMMARY:
This study presents a comprehensive approach that combines vulnerability models for trees and tree-induced building damage with wind-induced building damage, within the framework of the Florida Public Hurricane Loss Model (FPHLM). The paper compares existing methodologies implemented in MH-HAZUS to the proposed new framework in the FPHLM and discusses the pros and cons of each approach. In each case, the outcomes from independent tree-building damage and wind-induced building damage models are combined through empirical relationships. The development of sophisticated wind-induced building damage models that consider regional tree cover damage represents an advance in predictive capabilities. Improved models enable more accurate predictions of hurricane impacts, which is vital for effective emergency preparedness, resource allocation, and rapid post-storm recovery. These models support resilience by ensuring that communities are better equipped to handle and bounce back from natural disasters.

Keywords: vulnerability models, wind-induced building damage, tree-induced damage, empirical relationships, risk assessment, resilience

IN-VENTO 2024
International Conference of the Italian Association for Wind Engineering
Pisa, September 8th – 11th, 2024

Gust buffeting response of a wind turbine tower in mild and severe wind conditions at Østerild Test Center

T. Ballantini[a], A. Giusti[b], A. Torrielli[c,d], C. Mannini[e]

[a]*Department of Civil and Environmental Engineering, University of Florence, Florence, Italy, ballantini.tommaso@gmail.com*
[b]*Siemens Gamesa Renewable Energy A/S, Brande, Denmark, alessandro.giusti@siemensgamesa.com*
[c]*Siemens Gamesa Renewable Energy A/S, Brande, Denmark, alessio.torrielli.ext@siemensgamesa.com*
[d]*R&D Test Systems A/S, Hinnerup, Denmark, alt@rdas.dk*
[e]*CRIACIV/Department of Civil and Environmental Engineering, University of Florence, Florence, Italy, claudio.mannini@unifi.it*

SUMMARY:
This work focuses on the gust buffeting response of an isolated wind turbine tower (without rotor-nacelle assembly) about 116 m tall placed at Østerild Test Center (Denmark). The tower was instrumented with strain gauges mounted close to the base, which indirectly measure the bending moment (net of the mean component), and an accelerometer at about the top. The wind environment is characterized in terms of mean velocity profile and turbulence intensity, power spectral density and integral length scale by the post-process of the wind data recorded by the meteorological masts nearby. Mild wind conditions, differently from more severe winds, result not well described by the formulations provided by design standards. The measured along-wind and across-wind response (bending moment) is compared with the values got from the direct integration of gust buffeting theory for line-like structures, by using the actual wind characteristics. Moreover, a comparison with common design standards is developed for the along-wind response, which results significantly underestimated in mild wind conditions.

Keywords: gust buffeting, along-wind response, across-wind response, full-scale measurements, mild/severe wind

1. INTRODUCTION

In the offshore wind industry, towers are usually manufactured in different sections and assembled at the quayside of a selected harbor, before being loaded onto the installation vessel. Towers, erected at harbor quayside without rotor-nacelle assembly on freestanding foundations, are usually arranged in clusters at small center to center distance, to facilitate crane operations. These activities typically last 6-12 months. Because of the magnitude (mass even larger than 1000 t and height above 100 m) of the towers and the relatively long exposure, the wind-structure interaction of such a system has a strong engineering interest. The response of slender towers to turbulent wind has recently been studied by wind tunnel tests, with focus on the aerodynamic coefficients of clusters of towers in different group arrangements (Mannini et al., 2023, 2024) and by a probabilistic approach highlighting the effect of different sources of uncertainty (Torrielli and Giusti, 2023). A multidisciplinary approach to gust buffeting calculations has also been proposed as a completion of design standards where they lack of information (Giusti and Torrielli, 2024). However, none of the aforementioned works develops a comparison with the system full-scale response. This work focuses on the gust buffeting response of an isolated wind turbine tower (without rotor-nacelle assembly) in mild and severe wind conditions with the main purpose to assess the accuracy of analytical models and design standards in the prediction of the response of the system determined through full-scale measurements.

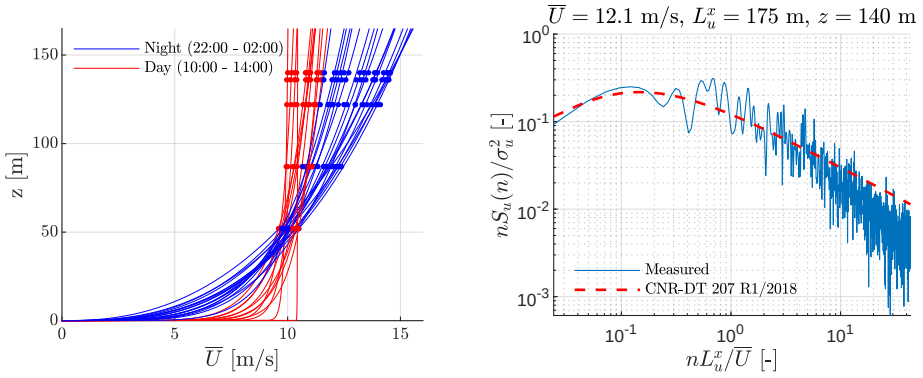

(a) mean wind velocity (b) PSDF of the longitudinal turbulence

Figure 1. Mean wind velocity profiles and PSDF of the longitudinal turbulence u in mild wind conditions. Measurements taken (a) from July 16th 2021 (00:00) to July 22nd 2021 (00:00); (b) on July 18th 2021 (8:20-8:30).

2. CASE STUDY

The gust buffeting response is studied with reference to a tower (a prototype of an offshore wind turbine) about 116 m tall with equivalent diameter of about 5.4 m installed at Østerild Test Center (Denmark). The tower was instrumented with strain gauges, mounted at 18 m height from the bottom, which indirectly measure the bending moment net of the mean component, and an accelerometer at about the top. In the same area, nearby the tower, there are also two meteorological masts, equipped with anemometers (or weather stations) at different heights and recording wind velocity and direction with a sampling frequency of 25 Hz. The same dataset has been analyzed by Kurniawati et al. (2024) from the perspective of across-wind vibrations and main focus on vortex-induced vibrations (VIV). This work can be seen as a complementary study. Further details on the measurement setup can be found in Kurniawati et al. (2024).

3. RESULTS

Design standards, which are generally focused on neutral conditions of the atmosphere, typical of wind storms, do not account for mild wind conditions. Indeed, for mean wind velocities at 104 m height in the range of about 5-20 m/s, the exponent (in case of power law) of mean wind profiles significantly changes from day to night (see Fig. 1(a)), as an indication that neutral conditions are not met and thermal effects are dominant. Similarly, the turbulence power spectral density does not have the classical slope of -5/3 in the bi-logarithmic plot (see Fig. 1(b)). By contrast, in case of severe wind conditions, i.e., mean wind velocity at 104 m height larger than about 25 m/s, the mean wind profile and the turbulence intensity and spectra comply much better with the models proposed by design standards (see Fig. 2 and Fig. 3(a)), even though the integral length scale L_u^x shows a significant spread (see Fig. 3(b)).

Looking at the along-wind dynamic response of the tower, the gust buffeting load calculated in accordance with design standards (with reference to the aerodynamic coefficients from wind tunnel tests) tends to overestimate the peak bending moment (net of the mean) at high mean wind velocities (see Fig. 4(a)), and this is particularly true for mean wind velocities at 104 m height larger than 25 m/s. In this sense, the use of design standards for ultimate limit state (ULS) verifications seems to be conservative, i.e., safe. By contrast, the bending moment corresponding to mild wind conditions is significantly underestimated, and, although it is not driving ULS load cases, may affect fatigue verifications. Such a tendency is also found with

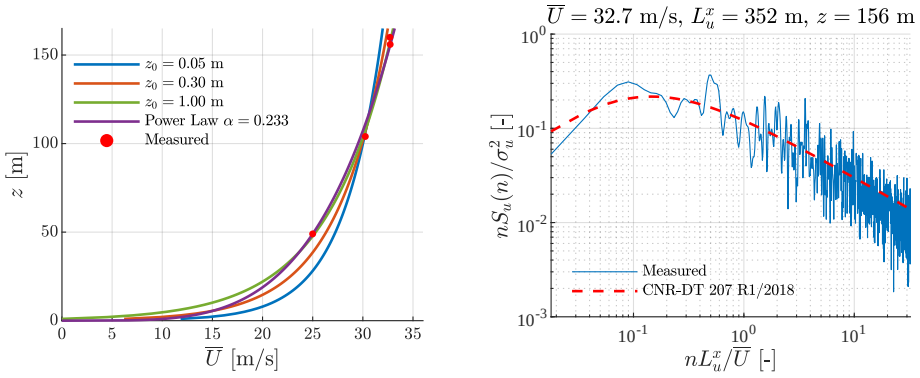

(a) mean wind velocity (b) PSDF of the longitudinal turbulence

Figure 2. Mean wind velocity profiles and PSDF of the longitudinal turbulence u in severe wind conditions. Measurements taken on Jan. 29th 2022 (21:50-22:00)

a dynamic gust buffeting calculation, based on the combination of the analytical formulation (e.g., Piccardo and Solari, 2002) with the actual mean wind profile and turbulence spectra, and a linear distribution of the force coefficient equivalent to the aerodynamic (force and moment at the base of the tower) coefficients measured in the wind tunnel.

On the other hand, looking at the across-wind response, the dynamic gust buffeting calculation revealed that the response is also affected by other phenomena, such as VIV (see Fig. 4(b)). Despite the assumptions that the buffeting force has the same correlation of the turbulent wind field and the sectional aerodynamic admittance function is unitary, the overly extension of what seems a lock-in range does not seem to be explained by lateral gust buffeting, not even significantly reducing the damping force in the calculations. Further investigations are needed.

4. CONCLUSIONS AND REMARKS

This work focuses on the gust buffeting response of towers in mild and severe wind conditions, by means of a comparison of experimental full-scale data (wind and tower bending moment) against the models given by design standards and literature. Those models can well describe the

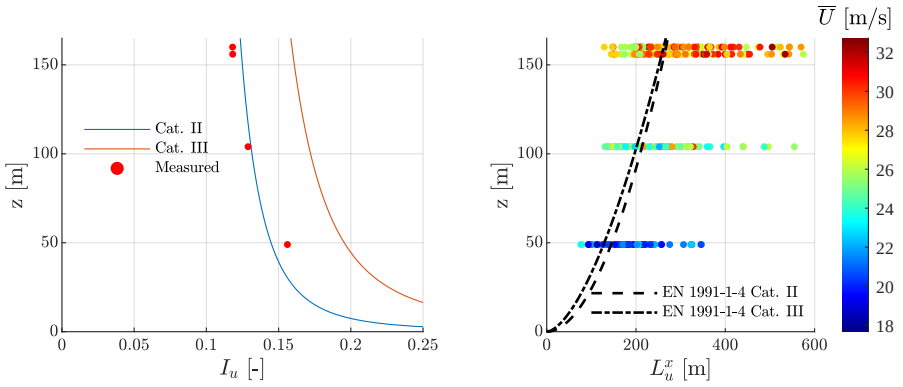

(a) intensity of turbulence (b) integral length scale

Figure 3. Turbulence intensity I_u and integral length scale L_u^x (longitudinal direction x), evaluated for the 10-minutes time intervals having a mean wind velocity at 160 m height larger than 25 m/s. Measurements taken (a) on Jan. 29th 2022 (21:50-22:00); (b) from Jan. 27th 2022 (12:00) to Jan. 31st 2022 (23:00).

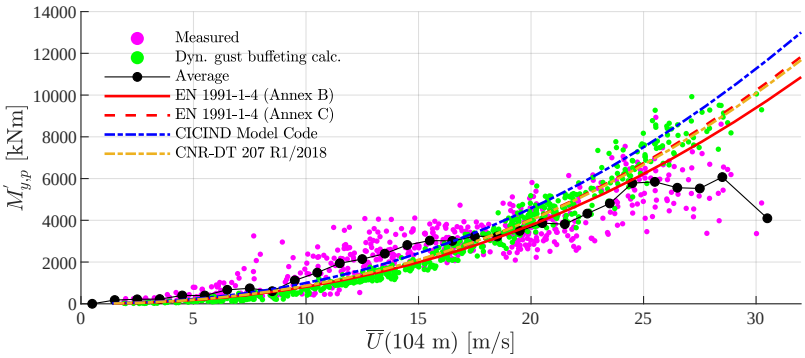

(a) peak along-wind bending moment

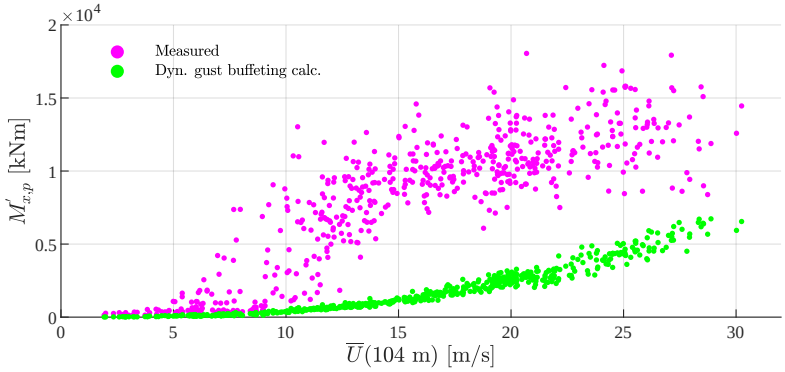

(b) peak across-wind bending moment

Figure 4. Peak along-wind bending moment $M'_{y,p}$ and across-wind bending moment $M'_{x,p}$ over 10-minutes time intervals (net of the mean) at 18 m height. Dynamic gust buffeting calculations are based on a structural damping ratio of 0.5%. Measurements taken from Jan. 27$^{\text{th}}$ 2022 (12:00) to Jan. 31$^{\text{st}}$ 2022 (23:00).

wind flow in severe wind conditions and generally overestimate the peak along-wind response. By contrast the peak across-wind response, evaluated by a dynamic gust buffeting calculation based on the actual wind conditions, tends to be significantly underestimated, and a kind of extended VIV lock-in range does not seem to be explained by lateral gust buffeting. This needs further investigations. Finally, mild wind conditions show significant deviations both in the characterization of the wind flow and in the tower gust buffeting response.

REFERENCES

Giusti, A. and A. Torrielli (2024). A multidisciplinary approach to optimize the gust loading on groups of wind turbine towers at the quayside. Proceedings of Proceedings of the XVII Conference of the Italian Association for Wind Engineering – IN-VENTO 2022. Milan, Italy, 175–186.

Kurniawati, I., F. Lupi, M. Seidel, R. Höffer, and H.-J. Niemann (2024). Across-wind vibration of wind turbine tower based on field measurements. Journal of Wind Engineering and Industrial Aerodynamics (*under review*).

Mannini, C., T. Massai, A. Giachetti, and A. Giusti (2023). Aerodynamic loads on groups of offshore wind turbine towers stored on quaysides during the pre-assembly phase. Journal of Wind Engineering and Industrial Aerodynamics 242, 105569.

— (2024). Aerodynamic loads on wind turbine towers arranged in groups with and without helical strakes. Proceedings of Proceedings of the XVII Conference of the Italian Association for Wind Engineering – IN-VENTO 2022. Milan, Italy, 260–269.

Piccardo, G. and G. Solari (2002). 3-D gust effect factor for slender vertical structures. Probabilistic Engineering Mechanics 17, 143–155.

Torrielli, A. and A. Giusti (2023). Uncertainties in the response of tower-like structures to wind gust buffeting. Journal of Wind Engineering and Industrial Aerodynamics 236, 105404.

IN-VENTO 2024
International Conference of the Italian Association for Wind Engineering
Pisa, September 8th – 11th, 2024

Bridge random flutter in turbulent flow

Niccolò Barni[a], Gianni Bartoli[a], Claudio Mannini[a]

[a]*CRIACIV/Department of Civil and Environmental Engineering, University of Florence, Via S. Marta 3, 50139 Florence, Italy, niccolo.barni@unifi.it, gianni.bartoli@unifi.it, claudio.mannini@unifi.it*

SUMMARY:
This investigation delves into the random flutter stability of bridges, taking into account the variations in aerodynamic derivatives due to turbulence-induced angle of attack. This parametric variation in self-excited forces renders the dynamic system time-varying, necessitating the use of specialized analytical tools for stability assessment, such as Lyapunov exponents and stability index derived from moment Lyapunov exponents. This study utilizes the 2D Rational Function Approximation model developed by the authors to incorporate time-variant self-excited forces, and applies it to a simplified two-dimensional, three-degree-of-freedom model of a suspension bridge. The results indicate that, while the analysis of sample stability generally provides a clear indication of the onset of flutter stability, there are specific conditions where the evaluation of moment stability is imperative.

Keywords: Random flutter, angle of attack, sample stability, moment Lyapunov exponents, stability index

1. INTRODUCTION

Atmospheric turbulence can markedly affect the self-excited forces of bridges. Indeed, large-scale turbulence leads to dynamic systems that change over time, potentially rendering bridges prone to nonlinear instability mechanisms like random flutter. The literature has started to tackle this issue with the foundational study by Lin and Ariaratnam (1980), which delved into the parametric effects due to longitudinal turbulence on torsional random flutter instability. Then, further research, such as the works by Bucher and Lin (1988) and Bartoli et al. (1995), included also the aerodynamic coupling with the vertical bridge mode and shed some light on the dual role of turbulence in both stabilizing and destabilizing the structures depending on the aerodynamic properties. The more recent analyses by Diana et al. (2013) and Barni et al. (2022) emphasized the critical role of variations in the angle of attack, induced by turbulence, in determining bridge flutter stability. Barni and Mannini (2024) also demonstrated that the impact of time-variant angle of attack generally surpasses that of velocity-magnitude modulations. Despite the interest of researchers, a calculation of the random flutter stability threshold considering the fluctuations in the angle of attack has not been carried out yet.

This study addresses this issue, relying on the 2D Rational Function Approximation (2D RFA) model introduced by Barni et al. (2021). This model handles self-excited forces in turbulent flow, accommodating changes in aerodynamic damping and stiffness resulting from wind angle-of-attack fluctuations. Given that the dynamic system properties vary in time, traditional methods of stability assessment, such as eigenvalue analysis in the frequency or time domain, cannot be applied. Instead, this work employs Lyapunov exponents and moment Lyapunov exponents, derived through Monte Carlo methods. A simplified three-degrees-of-freedom (3-dof) 2D model of the Hardanger Bridge, in Norway, is considered as a case study.

2. METHODOLOGY

Building on a nonlinear approach to buffeting response in turbulent flow (Barni et al., 2022), the autonomous part of the bridge motion equation can be expressed in matrix form as:

$$\ddot{\mathbf{r}} = -\mathbf{M}^{-1}\left\{[\mathbf{C}+\mathbf{C}_{ae}(\alpha)]\,\dot{\mathbf{r}}+[\mathbf{K}+\mathbf{K}_{ae}(\alpha)]\,\mathbf{r}-\frac{1}{2}\rho V_m^2\sum_{l=1}^{N-2}\mathbf{A}_{l+2}(\alpha)\boldsymbol{\psi}_l\right\} \tag{1}$$

where,

$$\mathbf{C}_{ae}(\alpha) = -\frac{1}{2}\rho V_m^2\mathbf{A}_2(\alpha)\ ;\ \mathbf{K}_{ae}(\alpha) = -\frac{1}{2}\rho V_m^2\mathbf{A}_1(\alpha)$$

The mass, damping and stiffness matrices, denoted as $\mathbf{M},\mathbf{C}$, and $\mathbf{K}\in\mathbb{R}^{3\times3}$, respectively, define the structural properties. The quasi-steady component of the aerodynamic damping and stiffness are represented by $\mathbf{C}_{ae}$ and $\mathbf{K}_{ae}$. $\mathbf{r}=[y\ z\ \theta]^T$ is the bridge girder motion vector (refer to Fig. 1), where $\boldsymbol{\psi}_l$ indicates the $N-2$ additional aeroelastic states. The 2D RFA model requires the knowledge of aerodynamic derivatives at various angles of attack to define $\mathbf{C}_{ae},\mathbf{K}_{ae},A_{l+2}$, and $\boldsymbol{\psi}_l$, addressing changes in aerodynamics due to the angle of attack (see, e.g., A_2^* in Fig. 1). The latter, defined as $\alpha(t)=\arctan[w(t)/(V_m+u(t))]$, depends on the longitudinal and, above all, the vertical turbulent wind velocity, $u(t)$ and $w(t)$, respectively. These are modeled by fitting the wind turbulence spectra through the calibration of the drift and diffusion terms of an Ornstein-Uhlenbeck process, aligning with the approach by Bartoli et al. (1995). Transforming Eq. (1) to state-space form yields a linear homogeneous stochastic differential equation:

$$\dot{\boldsymbol{\gamma}}(t) = \boldsymbol{\Omega}(\alpha)\boldsymbol{\gamma}(t) \tag{2}$$

Here, $\Omega(\alpha)\in\mathbb{R}^{3[2+(N-2)]\times3[2+(N-2)]}$ denotes the time-variant state matrix of the system, which depends on time through the angle of attack, α.

Flutter stability of a time-invariant system is determined by the sign of the real parts of the eigenvalues of its state matrix. However, in the present case, these eigenvalues fluctuate over time, requiring the introduction of different concepts of stability, such as sample or p-th moment stability. The main tool for assessing the sample stability of a stochastic system is the largest Lyapunov exponent (LE), which quantifies the system asymptotic sensitivity to a perturbation of the initial state. The LE indicates the exponential rate at which the system expands or contracts over the observation time T. The largest LE is defined as follows:

$$\lambda_{\boldsymbol{\gamma}} = \lim_{T\to\infty}\frac{1}{T}\log\|\boldsymbol{\gamma}\| \tag{3}$$

where, $\|\cdot\|$ denotes the Euclidean norm. A system is deemed stable over time if the largest LE is negative, while a positive exponent signals inevitable instability.

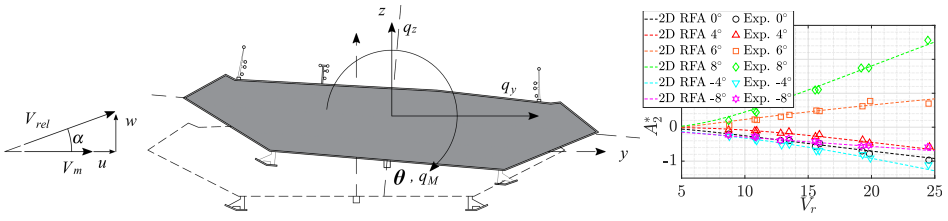

Figure 1. Sketch of the Hardanger Bridge section with the reference system for displacements, forces, and wind velocities (left); aerodynamic derivative A_2^* measured in the wind tunnel for various angles of attack (right).

However, in certain scenarios, the LE does not fully capture all the aspects of random flutter stability. Specifically, in cases where a system is almost surely stable, the bridge response may still exhibit rare, yet significantly large and unacceptable oscillations. These events can increase the asymptotic expected value of the response, particularly affecting higher-order statistics, and lead to an unstable p-th order moment of the response. This issue is quantified by the moment Lyapunov exponents (MLE), defined as:

$$\Lambda_{\boldsymbol{\gamma}}(p) = \lim_{T\to\infty} \frac{1}{T} \log\left\{\mathrm{E}\left[\|\boldsymbol{\gamma}(t)\|^p\right]\right\} \tag{4}$$

where $\mathrm{E}[\cdot]$ represents the ensemble average operator. The system p-th statistical moment is asymptotically stable if $\Lambda_{\boldsymbol{\gamma}}(p) < 0$. Arnold (1984) further demonstrated that the slope at the origin, $\Lambda'_{\boldsymbol{\gamma}}(p=0)$, of the moment Lyapunov exponent curve is the LE, $\lambda_{\boldsymbol{\gamma}}$. MLE are employed to define the stability index (identified by the non-trivial zero of the MLE) associated with a given mean wind velocity. The stability index, hereafter indicated with $\delta_{\boldsymbol{\gamma}}$, serves as an indicator of the transition of stability across the statistical moments.

3. NUMERICAL ANALYSIS

In this study, LE and MLE are calculated using Monte Carlo simulations, following the methodologies outlined by Xie (2006) for LE and Xie and Huang (2009) for MLE. It is worth remarking that estimating MLE in the context of stochastic differential equations with physical noise is challenging, especially for unstable systems, for which the potential for exponential growth in $\|\boldsymbol{\gamma}\|^p$ increases the variance of MLE numerical estimators, reducing the efficacy of conventional Monte Carlo techniques. The selected algorithm addresses these challenges by examining the statistics of $\log\|\gamma\|$, after demonstrating its normal distribution.

The analyses utilize 1000 samples for LE and 5000 for MLE, based on the response decay from unit sphere initial conditions. Sample observation time $T = 10800$ s for LE and 7200 s for MLE, with a sampling rate of 12 Hz, are adopted. Longitudinal turbulence intensities between (I_u) 10% and 25%, and integral length scales (L_u) of 100, 200 and 300 m are considered. The parameters for the vertical velocity fluctuations are set to half and 10% of the I_u and L_u metrics, respectively. For the details of the 2D model of the bridge, see Barni et al. (2024).

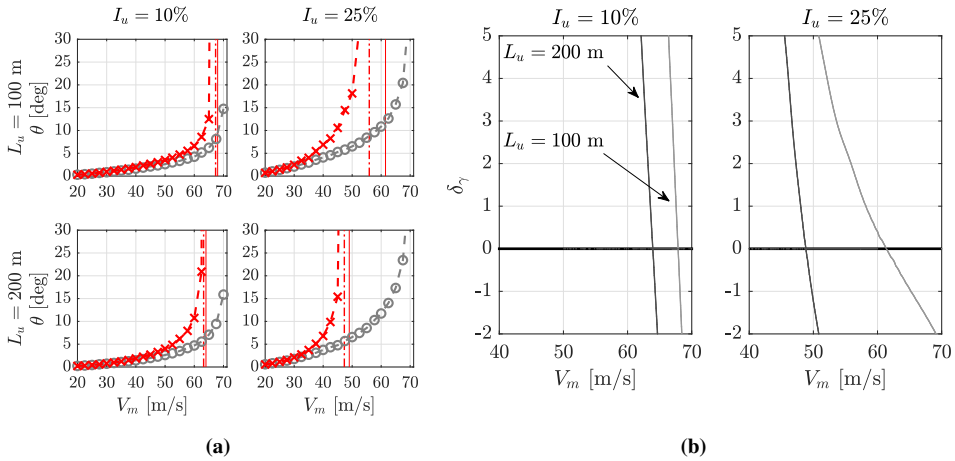

Figure 2. (a) RMS of the torsional buffeting response of the 2D bridge model, based on time-invariant (grey circles) and time-variant (red crosses) self-excited forces, alongside LE and 2nd-order MLE stability thresholds (solid and dash-dotted lines, respectively). (b) Stability index based on MLE for the time-variant model.

4. RESULTS AND CONCLUSION

Fig. 2a presents the root-mean-square (RMS) of the nonlinear buffeting torsional response for selected turbulence cases of the Hardanger Bridge, analyzed using both the classical time-invariant and the 2D RFA models for self-excited forces (Barni et al., 2024). Although the response is significantly amplified by the current assumption of perfectly-correlated external buffeting forces (refer to Barni et al. (2022) for results in case of a realistic partially-correlated random wind field), such amplification does not affect the system stability. The results indicate that turbulence generally reduces the flutter stability threshold. This destabilizing effect increases with greater turbulence intensity, especially for larger integral length scales, which redistribute the energy to lower-frequency wind fluctuations. The destabilization arises from the average parametric effect and coupled parametric resonances: some insight into these phenomena are reported in Barni and Mannini (2024). For a integral length scales of 200 m and for all the reported turbulence intensities, the flutter stability threshold associated with the LE matches the vertical asymptote of the bridge response, akin to cases with $L_u = 100$ m and $I_u = 10\%$. In these cases, the stability index shown in Fig. 2b presents a nearly vertical pattern with the mean wind velocity, signifying that rare and intense unstable transient responses only appear very close to the bridge sample stability limit. Therefore, sample stability emerges as a viable metric for defining the bridge random flutter critical wind velocity (e.g., the $p = 2$ moment stability threshold is depicted in Fig. 2(a) by a vertical dash-dotted line; also refer to Fig. 2(b)). However, for high turbulence intensity and low integral length scale, as shown in the top-right frame of Fig. 2a, the flutter problem becomes more complex, making the interpretation of bridge stability not univocal and the threshold provided by LE (sample stability) non-conservative. Indeed, the stability index flattens, invoking for the analysis of MLE to fully grasp random flutter stability. In this case, the chance of experiencing a rare but severe bridge response increases, even in systems considered sample or almost-surely stable.

REFERENCES

Arnold, L. (1984). A formula connecting sample and moment stability of linear stochastic systems. SIAM Journal on Applied Mathematics 44, 793–802.

Barni, N., M. Gioffrè, and C. Mannini (2024). Bridge flutter stability in turbulent flow. Proceedings of the XVII Conference of the Italian Association for Wind Engineering. Springer, 248–259.

Barni, N. and C. Mannini (2024). Parametric effects of turbulence on the flutter stability of suspension bridges. Journal of Wind Engineering and Industrial Aerodynamics 245, 105615.

Barni, N., O. A. Øiseth, and C. Mannini (2021). Time-variant self-excited force model based on 2D rational function approximation. Journal of Wind Engineering and Industrial Aerodynamics 211, 104523.

— (2022). Buffeting response of a suspension bridge based on the 2D rational function approximation model for self-excited forces. Engineering Structures 261, 114267.

Bartoli, G., C. Borri, and V. Gusella (1995). Aeroelastic behaviour of bridge decks: a sensitivity analysis of the turbulent nonlinear response. Proceedings of 9th International Conference on Wind Engineering. Wiley Eastern Ltd., New Delhi, 851–862.

Bucher, C. G. and Y. K. Lin (1988). Stochastic stability of bridges considering coupled modes. Journal of Engineering Mechanics 114, 2055–2071.

Diana, G., G. Fiammenghi, M. Belloli, and D. Rocchi (2013). Wind tunnel tests and numerical approach for long span bridges: The Messina bridge. Journal of Wind Engineering and Industrial Aerodynamics 122, 38–49.

Lin, Y. K. and S. T. Ariaratnam (1980). Stability of bridge motion in turbulent winds. Journal of Structural Mechanics 8, 1–15.

Xie, W. C. (2006). Dynamic Stability of Structures. Dynamic Stability of Structures. Cambridge University Press.

Xie, W. C. and Q. Huang (2009). Simulation of moment Lyapunov exponents for linear homogeneous stochastic systems. Journal of Applied Mechanics 76, 031001.

IN-VENTO 2024
International Conference of the Italian Association for Wind Engineering
Pisa, September 8th – 11th, 2024

Long-term analysis of the Halsafjorden Bridge accounting for parametric effects of turbulence

Niccolò Barni[a], Ole A. Øiseth[b], Øyvind W. Petersen[b], Claudio Mannini[a]

[a]*CRIACIV/Department of Civil and Environmental Engineering, University of Florence, Via S. Marta 3, 50139 Florence, Italy, niccolo.barni@unifi.it, claudio.mannini@unifi.it*
[b]*Norwegian University of Science and Technology, Trondheim, Norway. ole.oiseth@ntnu.no, oyvind.w.petersen@ntnu.no*

SUMMARY:
This work incorporates for the first time the nonlinear effects related to turbulence-induced angle of attack variations in a long-term buffeting response analysis. The selected case study is the Halsafjorden Bridge, Norway, which features a twin-deck box girder and consequently a different behaviour with respect to the angle of attack compared to the more studied single-box girder geometries. Multimodal frequency-domain calculations are performed for the buffeting response, employing aerodynamic derivatives modified according to the equivalent linear time-invariant approach, recently proposed by the authors. The full long-term analysis is able to consistently account for the potentially strong influence of turbulence on self-excited forces. The deviations from the results of short-term approaches will be highlighted in the paper.

Keywords: Long-term analysis, buffeting response, suspension bridge, angle of attack, nonlinear effects

1. INTRODUCTION

Over the last three decades, it has extensively been documented that atmospheric turbulence significantly influences self-excited forces on bridges, thus emerging as one of the major sources of uncertainty in the estimation of the dynamic response. The impact of turbulence on bridge response and stability can primarily be attributed to the parametric effects related to variations in longitudinal wind velocity (e.g., Bucher and Lin, 1988; Lin and Ariaratnam, 1980) and angle of attack (e.g., Barni et al., 2022; Chen and Kareem, 2003; Diana et al., 2013), even if the latter has been found to be largely dominant (Barni and Mannini, 2024). Although much of research effort has concentrated on single-box girders, twin-deck girders, widely used in long-span bridges, exhibit a markedly different behavior with respect to the angle of attack.

This work focuses on the Halsafjorden Bridge, in Norway, as a case study. This is a 2000 m-suspension bridge with a twin-deck section, whose aerodynamic derivatives have shown a strong sensitivity to the angle of attack. Initially, a short-term analysis is conducted to determine the buffeting response based on mean wind velocities associated with different return periods. Subsequently, to consider the variability of wind storm parameters and their effects over the design life of the structure, extreme load effects are calculated using a full long-term (FLM) analysis. The FLM offers a more accurate estimation of wind-induced effects compared to short-term methods (Lystad et al., 2021), albeit at the cost of computationally demanding calculations. The discrepancy between long- and short-term estimations is expected to increase when incorporating the nonlinear effects of turbulence, as turbulence affects not only the external buffeting loads but also the self-excited forces. Thanks to the equivalent linear time-invariant model proposed in Barni and Mannini (2024), the most significant turbulence parametric effects can efficiently be addressed using a frequency-domain approach and considered for the first time in long-term calculations.

2. SHORT-TERM ANALYSIS

The short-term buffeting analyses of the Halsafjorden Bridge (Fig. 1a) are conducted in the time domain, following linear time-invariant and linear time-variant formulations for self-excited forces, akin to the analyses presented in Barni et al. (2022) for the Hardanger Bridge, Norway. To determine the nonlinear buffeting response, the coefficients of the 2D Rational Function Approximation (2D RFA) model are identified based on the aerodynamic derivatives measured for different angles of attack, as in Barni et al. (2021). Notably, the derivative A_2^* associated with the aerodynamic damping in torsion is shown in Fig. 1b, along with the 2D RFA section traces for some angles of attack. This coefficient is part of the complete set of 18 aerodynamic derivatives (associated with horizontal, vertical and torsional motion) measured in the wind tunnel at the Fluid Mechanics Laboratory of NTNU, Trondheim (Norway), utilizing the same setup described in Barni et al. (2021). The bridge modal properties are derived from a finite element model of the Halsafjorden Bridge, generated with the ABAQUS software. The modal analysis, conducted after the application of the dead load, accounts for the geometrical stiffness provided by the cables. Buffeting calculations utilize 20 modes, with a structural damping ratio of $\xi = 0.5\%$ for all of them. Finally, the turbulence parameters used to artificially generate the random wind field are based on the Hardanger Bridge site and are identical to those reported in Barni et al. (2022). The nonlinear bridge buffeting response (linear time-variant model, LTV) is finally obtained by solving a time-varying state-space differential equation, compactly represented as:

$$\dot{\boldsymbol{\gamma}}(t) = \boldsymbol{\Omega}(\tilde{\alpha})\boldsymbol{\gamma}(t) + \mathbf{B}\mathbf{q}_b(t) \tag{1}$$

Here, $\boldsymbol{\gamma}(t) \in \mathbb{R}^{3[2+(N-2)]}$ is the state vector, $\mathbf{B} \in \mathbb{R}^{3[2+(N-2)]\times 3}$ is the input matrix, $\boldsymbol{\Omega}(\tilde{\alpha}) \in \mathbb{R}^{3[2+(N-2)]\times 3[2+(N-2)]}$ represents the time-variant state matrix of the system, which includes all structural information and the time-varying self-excited force coefficients, whereas $\mathbf{q}_b(t)$ denoting the external buffeting load vector. The expressions of both $\boldsymbol{\Omega}(\tilde{\alpha})$ and $\mathbf{q}_b(t)$ are reported in Barni et al. (2022). $\alpha(t) = \arctan\left[\frac{w(t)}{V_m+u(t)}\right]$ defines the angle of attack resulting from longitudinal (u) and vertical (w) turbulent velocity fluctuations, whereas $\tilde{\alpha}(t)$ specifies the angle of attack associated exclusively with large-scale, low-frequency turbulence, obtained using a low-pass filter (in this respect, a multi-cutoff frequency approach is proposed in Barni et al. (2022).

When the angle of attack is identically set to zero ($\tilde{\alpha} \equiv 0°$), the previous buffeting analysis becomes a linear time-invariant calculation (LTI). Barni and Mannini (2024) showed that the major nonlinear parametric contribution of turbulence can be ascribed to the so-called "average parametric effect". This effect arises from the difference between the aerodynamic derivatives

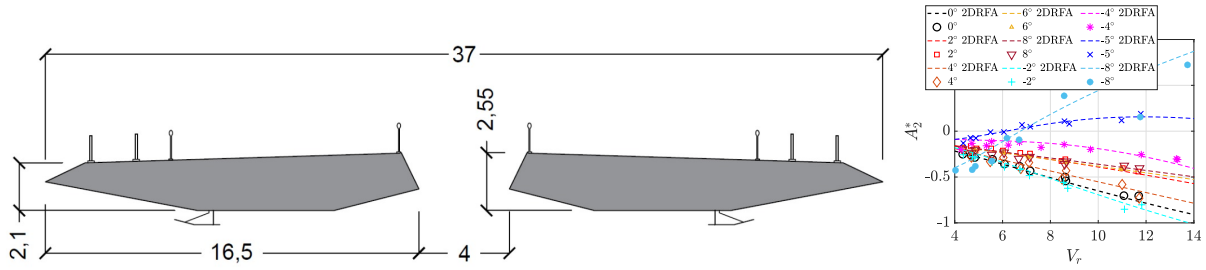

Figure 1. Sketch of the Halsafjorden Bridge deck section (left); aerodynamic derivative A_2^* measured in the wind tunnel for various angles of attack (right).

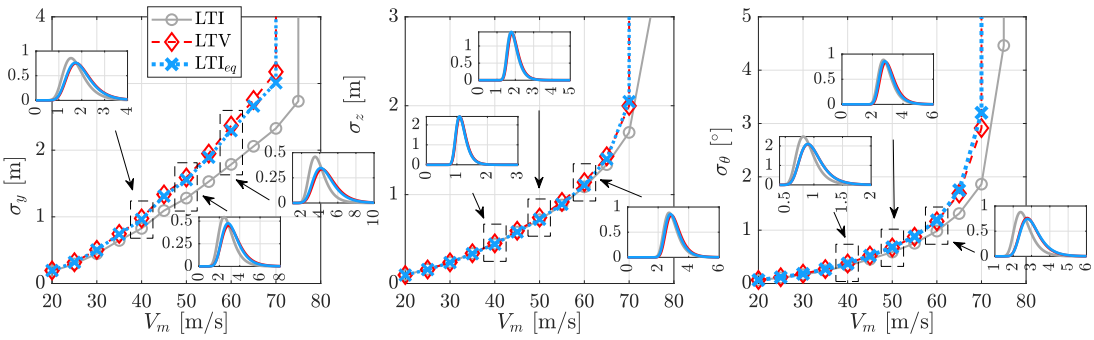

Figure 2. RMS of the nonlinear buffeting torsional response of the Halsafjorden Bridge, obtained using the LTI approach (grey circles), the LTV formulation of Eq. (1) (red diamonds), and the LTI$_{\text{eq}}$ model (blue crosses) for self-excited forces. The inset plots display the Gumbel PDF of response maxima.

averaged over the time history of $\tilde{\alpha}$ and those calculated for the mean wind angle of attack. This discrepancy can become pronounced for significantly nonlinear and non-antisymmetric variations in the aerodynamic derivatives around the mean wind angle of attack and increases with turbulence intensity (mainly the vertical component, I_w). Following the approach in Barni and Mannini (2024), the average aerodynamic derivatives can be incorporated into Eq. (1) by modifying the state matrix $\mathbf{\Omega}(\tilde{\alpha}) = \mathbf{\Omega}_{eq}$ (according to the so-called LTI$_{\text{eq}}$ approach).

Fig. 2 presents the root-mean-square (RMS) of the mid-span bridge buffeting response in the horizontal, vertical, and torsional directions for the LTV, LTI, and LTI$_{\text{eq}}$ approaches described above. Results are reported for a wide range of mean wind velocities V_m, encompassing that associated with the one hundred-year return period. In the LTV model, $\tilde{\alpha}$ leads to variations in the aerodynamic derivatives, altering the bridge modal frequencies and damping values (Barni and Mannini, 2024; Barni et al., 2022). This results in an increased horizontal and torsional response compared to the LTI model, primarily due to changes in the corresponding aerodynamic damping coefficients, namely P_1^* and A_2^*. These parametric effects also decrease the bridge flutter stability by approximately 7%. In addition, they broaden the Gumbel probability density function (PDF) of response maxima. Fig. 2 also shows that these nonlinear effects are effectively captured by the LTI$_{\text{eq}}$ approach in terms of both RMS and probability distribution of response maxima. This confirms the validity of the LTI$_{\text{eq}}$ approach for addressing parametric effects of turbulence.

3. LONG-TERM ANALYSIS

In contrast to the short-term method, the full long-term analysis takes into account variations in weather conditions and their impact on the buffeting response throughout the bridge lifespan. As a result, this methodology yields a more sensible estimation of the extreme buffeting response. Naess and Moan (2012) proposed three approaches to full long-term analysis: the first one based on the distribution of short-term peaks, another on all short-term extremes, and the third one on the response upcrossing rate. Specifically, the first, more general, method incorporates the average upcrossing rate ν_R^+ of the threshold r for the short-term buffeting response R and the joint probability density function of the wind variables, $f_{\boldsymbol{W}}(\boldsymbol{w})$, allowing the calculation of the cumulative distribution function of the long-term response $R(T_{LT})$:

$$\text{Prob}\{R(T_{LT}) \leq r\} = F_{R(T_{LT})}(r) \tag{2}$$

$$F_{R(T_{LT})}(r) = \exp\left\{-T_{LT}\int_{\boldsymbol{W}} \nu_R^+(r|\boldsymbol{w}) f_{\boldsymbol{W}(\boldsymbol{w})} d\boldsymbol{w}\right\}$$

where $\boldsymbol{W}$ represents the vector of stochastic turbulent wind parameters, including the mean wind velocity V_m, and the turbulence intensities I_u and I_w. T_{LT} denotes the long-term period, defined as a sequence of stationary short-term conditions ($T_{LT} = N_{ST} T_{ST}$, where N_{ST} is the number of short-term periods T_{ST} considered). $\nu_R^+(r|\boldsymbol{w})$ is the short-term average upcrossing rate of the response level r, given the wind conditions $\boldsymbol{w}$. The determination of the probability distribution $F_{R(T_{LT})}(r)$ is computationally demanding, as it requires the calculation of a large number of short-term responses (with the complexity of the problem quickly increasing with the number of turbulent parameters considered as random variables). For this reason, computationally efficient short-term analyses are performed by applying the LTI_{eq} model within a multimodal frequency-domain approach.

The probabilistic model for the turbulent wind characteristics of the Norwegian Sulafjorden Bridge site (Castellon et al., 2022) is used in the current work to determine $f_{\boldsymbol{W}}(\boldsymbol{w})$. Indeed, the Sulafjord crossing is close to the Halsafjord and shares a similar terrain morphology, making reasonable the work assumption that this data can effectively represent the Halsafjord wind conditions. The short-term analyses presented in Section 2 will be updated with the Sulafjorden turbulent wind conditions to serve as a baseline for comparing results between short- and long-term bridge responses.

Unlike existing literature on long-term calculations of bridge buffeting response (e.g., Castellon et al., 2023; Lystad et al., 2023; Lystad et al., 2021), this work extends the traditional full long-term approach to include the long-term impact of nonlinear self-excited force modulation due to turbulence-induced time-variations in the angle of attack.

REFERENCES

Barni, N. and C. Mannini (2024). Parametric effects of turbulence on the flutter stability of suspension bridges. Journal of Wind Engineering and Industrial Aerodynamics 245, 105615.

Barni, N., O. A. Øiseth, and C. Mannini (2021). Time-variant self-excited force model based on 2D rational function approximation. Journal of Wind Engineering and Industrial Aerodynamics 211, 104523.

— (2022). Buffeting response of a suspension bridge based on the 2D rational function approximation model for self-excited forces. Engineering Structures 261, 114267.

Bucher, C. G. and Y. K. Lin (1988). Stochastic stability of bridges considering coupled modes. Journal of Engineering Mechanics 114, 2055–2071.

Castellon, D. F., A. Fenerci, and O. Øiseth (2022). Environmental contours for wind-resistant bridge design in complex terrain. Journal of Wind Engineering and Industrial Aerodynamics 224, 104943.

Castellon, D. F., A. Fenerci, Ø. W. Petersen, and O. Øiseth (2023). Full long-term buffeting analysis of suspension bridges using Gaussian process surrogate modelling and importance sampling Monte Carlo simulations. Reliability Engineering & System Safety 235, 109211.

Chen, X. and A. Kareem (2003). Aeroelastic analysis of bridges: effects of turbulence and aerodynamic nonlinearities. Journal of Engineering Mechanics 129, 885–895.

Diana, G., G. Fiammenghi, M. Belloli, and D. Rocchi (2013). Wind tunnel tests and numerical approach for long span bridges: The Messina bridge. Journal of Wind Engineering and Industrial Aerodynamics 122, 38–49.

Lin, Y. K. and S. T. Ariaratnam (1980). Stability of bridge motion in turbulent winds. Journal of Structural Mechanics 8, 1–15.

Lystad, T. M., A. Fenerci, and O. Øiseth (2023). Full long-term extreme buffeting response calculations using sequential Gaussian process surrogate modeling. Engineering Structures 292, 116495.

Lystad, T. M., A. Fenerci, and O. Øiseth (2021). Long-term extreme buffeting response of cable-supported bridges with uncertain turbulence parameters. Engineering Structures 236, 112126.

Naess, A. and T. Moan (2012). Stochastic Dynamics of Marine Structures. Cambridge University Press, New York.

IN-VENTO 2024
International Conference of the Italian Association for Wind Engineering
Pisa, September 8th – 11th, 2024

Transient linear galloping analysis of square cylinder under time-varying mean wind angles of attack

Hao-Yu Bin [1], Stefano Brusco [2], Giuseppe Piccardo [3]

[1]*DICCA, University of Genoa, Genoa, Italy, hao-yu.bin@edu.unige.it*
[2]*Faculty of Engineering, Western University, London, Canada, sbrusco@uwo.ca*
[3]*DICCA, University of Genoa, Genoa, Italy, giuseppe.piccardo@unige.it*

SUMMARY
Full-scale measurements of thunderstorm outflows, as those collected from the anemometric network in the High Tyrrhenian Sea coordinated by the Giovanni Solari (GS) WinDyn research group, reveal that abrupt changes in the mean wind direction constitute a distinctive feature of non-synoptic phenomena. Experimental simulations of the effects of such rotation on the transient aerodynamics of a two-dimensional sharp-edged square cylinder are conducted in the GS Wind Tunnel at the University of Genoa. Through appropriate time-frequency analyses based on the continuous wavelet transform, time-varying aerodynamic coefficients in the alongwind and crosswind directions are obtained. These coefficients show influences from both the initial wind-body incidence and the temporal duration of the angle of attack change. Employing a quasi-steady modelling of wind loading, a preliminary assessment of the two degree-of-freedom galloping sensitivity for a square cross-section is then carried out.

Keywords: Time-varying angle of attack, Transient galloping, Thunderstorm outflows, Quasi-steady approach.

1. INTRODUCTION

With the surge in extreme weather events, potentially linked to ongoing climate change, the frequency of disasters caused by non-synoptic winds is on the rise. Recognizing the significant impact of these winds on community safety, the Wind Engineering community has prioritized the enhancement of current wind-load design codes. Technological advancements have provided access to high-sensitivity and precision instruments, such as LiDAR profilers or scanners, facilitating the collection of comprehensive data related to wind events.

Since 2012, the Giovanni Solari Wind Engineering and Structural Dynamics Research Group (GS-WinDyn) at the University of Genoa has recorded over 250 wind events with non-stationary characteristics in the High Tyrrhenian Sea through an extensive monitoring network. This dataset has become the foundation for a research line on thunderstorms, covering site detection, physical and numerical simulations, as well as analytical modelling of aerodynamic loading. Concurrently, innovative wind simulators, such as the WindEEE Dome at Western University in Canada, capable of replicating downbursts through an impinging jet, have been designed and constructed. In parallel, there has been a modification of the traditional wind tunnel concept to reproduce partial aspects of the phenomenon. Multiple-fan wind tunnels, originating in Asia at the close of the last century, can generate accelerating flows in a straight channel by using small fans before the inlet section. This design enables studies on bluff-body aerodynamics in transient conditions (e.g., Brusco et al., 2024).

On the other hand, abrupt wind direction shifts are known to constitute another peculiar characteristic of full-scale thunderstorms (e.g., De Gaetano et al., 2014). This remark has inspired a wind tunnel test campaign conducted at the University of Genoa aimed at reproducing the effects of such rotation on the transient aerodynamics of a sectional model of a sharp-edged square cylinder. Starting from the outcomes of such experimental campaign, the current paper proposes an initial exploration into the potential transient aeroelasticity of 2D sharp-edged square cylinders. Operating under the assumption of a quasi-steady characterization of motion-induced forces during transient thunderstorms (Brusco and Solari, 2021), the analysis delves into assessing transient galloping across various scenarios.

2. EXPERIMENTAL RESULTS

The experimental campaign was conducted in the GS Wind Tunnel at the University of Genoa, a closed-loop facility characterized for its low turbulence levels (Fig. 1a). It is equipped with actively controlled motors capable of replicating instantaneous changes in the wind's angle of attack (AoA, α). This control is achieved by manipulating three parameters: the initial angle, the target angle, and the rotation speed, as illustrated in Fig. 1b. The investigation draws on the full-scale thunderstorm registration database of the GS-WinDyn group (e.g., De Gaetano et al., 2014; Xhelaj et al., 2020), specifically focusing on the ten events selected by Brusco and Solari (2021).

From these events, data on wind velocity (U), wind direction (α), and rotational speed (α', i.e., the temporal derivative of the wind direction) are extracted. Time-histories for one of the selected events are depicted in Fig. 1c and Fig. 1d. The quantities presented in Fig. 1d serve as the basis for calibrating the actions of the controlled motors, responsible for rotating a sectional wind tunnel model. Given that the simulated variations of the angle of attack are scaled 1:1 from full-scale events, the anticipated effects are expected to be applicable to structures with geometric dimensions equivalent to the wind tunnel model.

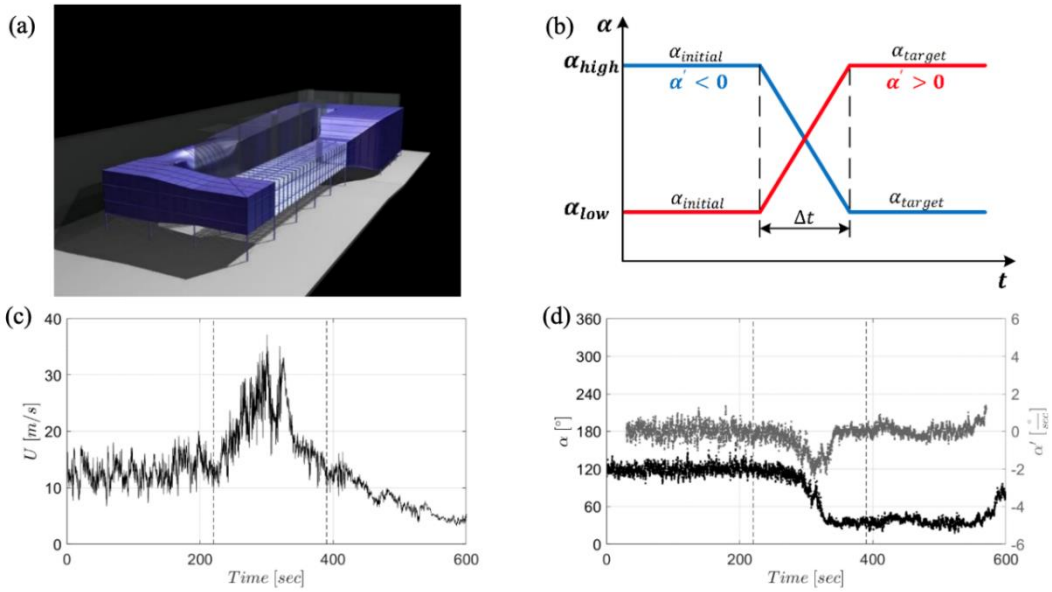

Figure 1. (a) The Giovanni Solari (GS) Wind Tunnel; (b) Schematic representation of a single cycle of time-varying angle conditions; (c) Time history of wind speed U and of (d) wind direction α (black) and rotational speed α' (grey) from a thunderstorm event in Brusco and Solari (2021).

This study employs a square cylinder with sharp corners to investigate the transient aerodynamics resulting from an abrupt change in the Angle of Attack (AoA). The model is outfitted with 44 pressure taps located in its central ring. 12 different nominal time-varying cases with time-varying AoA cases are reproduced; each of them has been repeated at least 15 times. The maximum rotational wind variation from full-scale measurements has been considered as a similarity parameter for the experimental tests, which have been conducted in correspondence with the critical region (for galloping) of the square cylinder (i.e., -15 to + 15 degrees). Due to the intrinsic non-stationary nature of these experiments, time-frequency analyses, specifically based on the continuous Wavelet transform, are used to analyze the experimental data. In Figure 2, the ensemble mean of the transient drag and lift coefficients is presented against the angle of attack across various rotation speeds (indicated through the colorbar), and compared with their stationary counterparts (in black). Noticeable disparities emerge, particularly at the highest negative rotation speeds; however, variations are evident even for lower rotation speeds, and they seem significant enough to potentially influence the derivatives of the aerodynamic coefficients with respect to the stationary case.

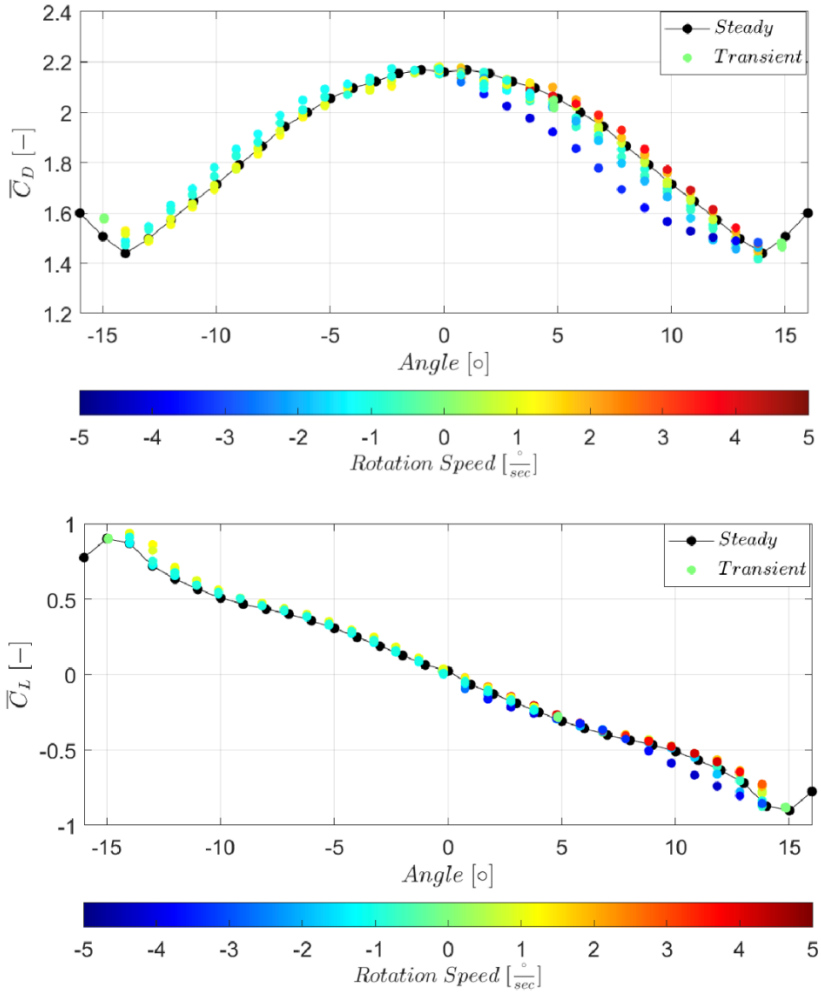

Figure 2. Ensemble mean of (a) drag and (b) lift coefficients against the angle of attack for stationary (black lines) and transient conditions (colorbar).

3. TWO DEGREE-OF-FREEDOM QUASI-STEADY MODEL

Building on the methodology proposed in Brusco and Solari (2021) regarding motion-induced forces, the aerodynamic damping matrix $\mathbf{C}_a$ may be extended to account for the influence of a slowly-varying mean wind speed $U(t)$ and a slowly-varying angle of attack $\alpha(t)$. By considering the effects of transient aerodynamics, the hypothesis that the passage of the gust front is moderately slow is adopted, as proposed in prior studies (e.g., Solari et al., 2015; Yang and Mason, 2019). As a result, the aerodynamic coefficients constituting the $\mathbf{C}_a$ matrix become functions of the Reynolds number, dependent on $U(t)$, and of the slowly-varying angle of attack $\alpha(t)$:

$$\begin{aligned}
C_{a11}(t) &= +c_d(t)[\sin^2\alpha(t) + 2\cos^2\alpha(t)] - [c_l(t) + c'_d(t)]sin\alpha(t)cos\alpha(t) + c'_l(t)\sin^2\alpha(t) \\
C_{a12}(t) &= -c_l(t)[2\sin^2\alpha(t) + \cos^2\alpha(t)] + [c_d(t) - c'_l(t)]sin\alpha(t)cos\alpha(t) + c'_d(t)\cos^2\alpha(t) \\
C_{a21}(t) &= +c_l(t)[\sin^2\alpha(t) + 2\cos^2\alpha(t)] + [c_d(t) - c'_l(t)]sin\alpha(t)cos\alpha(t) - c'_d(t)\sin^2\alpha(t) \\
C_{a22}(t) &= +c_d(t)[2\sin^2\alpha(t) + \cos^2\alpha(t)] + [c'_d(t) + c_l(t)]sin\alpha(t)cos\alpha(t) + c'_l(t)\cos^2\alpha(t)
\end{aligned} \tag{1}$$

This approach leads to the formulation of a two-degree-of-freedom motion equation, wherein the influence of aeroelasticity is accounted for by adjusting the damping matrix. This matrix is composed of both structural and aerodynamic components. Due to the typically non-diagonal nature of the aerodynamic damping matrix, the equations of motion become coupled, eliminating the possibility of evaluating modal displacements in isolation. The state space technique emerges as a viable numerical solution for such coupled systems.

4. ON-GOING ACTIVITIES

The aerodynamic coefficients obtained from experimental data in transient conditions (Sect 2) can be numerically approximated, for instance using smoothing splines. This permits to determine their values and derivatives with respect to the instantaneous angle of attack. Subsequently, employing Eq. (1), the time-varying aerodynamic damping matrix $\mathbf{C}_a$ may be evaluated during non-stationary events. Assuming a Scruton number sufficiently high to ensure a clear separation between vortex-induced vibrations and galloping oscillations (e.g., greater than 20), time-domain integrations of the equations of motion are performed to assess the resulting dynamic responses in both the alongwind and crosswind directions. Various scenarios are considered, including cases where the angle of attack variability is examined in isolation or concurrently with a variation in mean wind speed.

REFERENCES

Brusco, S., H.-Y. Bin, Y.-L. Lo, and G. Piccardo (2024). Transient aerodynamics of a square cylinder under downburst-like accelerating flows reproduced in a multiple-fan wind tunnel. Journal of Fluids and Structure 124, 104038.

Brusco, S. and G. Solari (2021). Transient aeroelasticity of structures subjected to thunderstorm outflows. Engineering Structures 245, 112801.

De Gaetano, P., M. P. Repetto, T. Repetto, and G. Solari (2014). Separation and classification of extreme wind events from anemometric records. Journal of Wind Engineering and Industrial Aerodynamics 126, 132-143.

Solari, G., M. Burlando, P. De Gaetano, and M. P. Repetto (2015). Characteristics of thunderstorms relevant to the wind loading of structures. Wind and Structures 20, 763–91.

Xhelaj, A., M. Burlando, and G. Solari (2020). A general-purpose analytical model for reconstructing the thunderstorm outflows of travelling downbursts immersed in ABL flows. Journal of Wind Engineering and Industrial Aerodynamics 207, 104373.

Yang, T. and M. S. Mason (2019). Aerodynamic characteristics of rectangular cylinders in steady and accelerating wind flow. Journal of Fluids and Structures 90, 246–62.

IN-VENTO 2024
International Conference of the Italian Association for Wind Engineering
Pisa, September 8th – 11th, 2024

Enhanced Reduced-Order Modeling of Atmospheric Boundary Layer Flows: Integrating Advanced Dimensionality Reduction and Regression Techniques

Emanuele Bombardi[1,2], Leo Cotteleer[1,2], Alessandro Gambale[3], Alessandro Parente[1,2]

[1] *ATM Laboratory, Universite Libre de Bruxelles, Brussels, Belgium, emanuele.bombardi@ulb.be*
[2] *Brussels Institute for Thermal-fluid systems and clean Energy, ULB and VUB, Brussels, Belgium*
[3] *BuildWind SRL, Brussels, Belgium, gambale@buildwind.net*

SUMMARY
This study delves into the development and application of reduced-order models (ROM) for predicting pollutant concentration within the atmospheric boundary layer of urban environments. The focus lies on predicting pollutant levels under unexplored operating conditions, characterized by constant flow dynamics amid varying urban geometries. Three-dimensional simulations of pollution dispersion are conducted across a range of urban geometries to encompass various urban features. Two distinct cases are investigated to assess the efficiency of different ROM architectures. Initially, a simplified urban geometry, featuring a single building configuration, serves as a testbed for evaluating the most suitable ROM architecture. Subsequently, a more intricate urban configuration, reflective of real-world scenarios, is analyzed using the identified optimal architecture from the initial case study. These simulations inform the development of a ROM capable of predicting pollutant fields for geometry features not explicitly considered during the model's development phase.

Keywords: atmospheric boundary layer flows, CFD, reduced-order model

1. INTRODUCTION

The Atmospheric Boundary Layer (ABL) represents the lowest portion of Earth's atmosphere. Within this layer, interactions between the Earth's surface and the overlying atmosphere play a crucial role in various environmental processes, including air quality and pollutant dispersion. Understanding and accurately modelling the dynamics of the ABL, particularly in urban environments, is essential for safeguarding public health, urban design and tackling broader climate change-related challenges.
To overcome the computational challenges associated with CFD simulations in urban atmospheric boundary layer flows, reduced-order modelling (ROM) approaches offer a promising alternative. ROM techniques aim to capture the essential physics of complex systems while significantly reducing computational costs compared to full-scale simulations. They can provide efficient approximations of flow behavior while maintaining acceptable levels of accuracy. A ROM consists of two primary stages: an offline stage and an online stage. The offline stage of the ROM presented in this study involves constructing a dataset through CFD simulations of pollutant dispersion across multiple urban geometry configurations. Following this, a dimensionality reduction step is applied, followed by regression, which maps from the latent space to the parameter space. Subsequently, an online stage allows for obtaining full-field solutions through projection, bypassing the need for costly CFD simulations.

The CFD simulations are conducted ensuring a consistent and appropriate representation of the ABL flows. To achieve this, the ABL *comprehensive* SST k-Omega turbulence model (Kumar et al., 2024;

Bellegoni et al., 2022) and the pollutant transport model (Longo et al., 2019) are employed.

2. METHODS

The Reduced Order Model (ROM) developed in this study emerges from a comparative analysis of two distinct methodologies encompassing dimensionality reduction and regression. The primary approach integrates Principal Component Analysis (PCA) for dimensionality reduction coupled with Neural Network (NN) regression. Conversely, the secondary method incorporates an autoencoder framework augmented with an additional term within the loss function to refine the regression process.

2.1. DIMENSIONALITY REDUCTION

2.1.1.Principal Component Analysis (PCA)

Principal Component Analysis (PCA) is a dimensionality reduction technique commonly used in data analysis. In the context of our study, PCA is applied to a dataset represented as an $(m\ x\ n)$ matrix, where m denotes the number of spatial points in the simulation domain, and n represents the number of parameters. Each column in the matrix corresponds to the pollutant concentration at a given condition. PCA works by identifying the principal components, which are linear combinations of the original variables that capture the maximum variance in the data. By reducing the dimensionality of the dataset while retaining as much variance as possible, PCA allows for a more concise representation of the data, facilitating subsequent analysis and modelling tasks.

2.1.2. Autoencoder with augmented loss function

An autoencoder is a neural network architecture commonly used in unsupervised learning tasks to learn efficient representations of input data. It consists of an encoder network that compresses the input data into a latent space representation, followed by a decoder network that attempts to reconstruct the original input from this compressed representation. The structure of an autoencoder can be customized according to specific needs and tasks. Incorporating a regression method into the structure of an autoencoder can enhance its predictive capabilities. Inspired by Fresca et al., 2021, our approach integrates a regression method into the autoencoder. However, unlike Fresca et al., 2021, where the regression method interacts with the latent space of the autoencoder, our method performs regression on the weights of the last layer of the decoder. Fig. 1 summarizes the architecture of the proposed ROM. The initial part of the autoencoder comprises a conventional encoder-decoder architecture. The input matrix $u(\mu)$ resides in the space $\mathbb{R}^{\mathrm{Npoints} \times \mu}$, where Npoints is the number of spatial points of our simulations and μ the parameters. Preceding the output layer, a deep feedforward neural network (DFNN) is integrated to predict the weights and biases of the final layer based on the data labels μ. At each training iteration a prediction on the coefficients of the last layer is performed. The error between the prediction and θ_{D_3} is then incorporated into the loss function:

$$\mathcal{L}(\mu;\theta) = \frac{\omega}{2}\|\hat{u}(\mu,\theta_{DF},\theta_D) - u(\mu)\| + \frac{1-\omega}{2}\left\|\theta_{D_{3_{PRED}}} - \theta_{D_3}\right\| \quad (2)$$

In Eq. (2), $\omega \in [0,1]$ weighs the contribution of the two terms. The additional term in the loss function enables simultaneous training of both the regression method and the autoencoder. By leveraging the prediction of the regression method, our model adjusts the parameters of the decoder to converge towards the regression prediction, and vice versa.

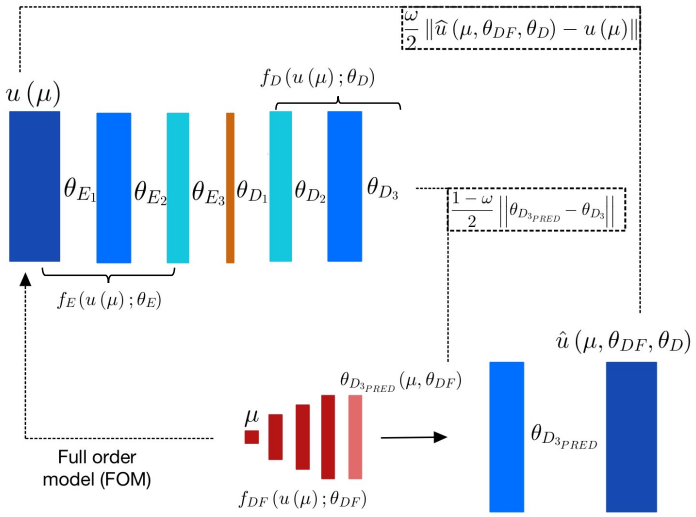

Figure 1. ROM architecture (offline stage, training and validation)

A deep feedforward neural network is utilized for regression tasks and integrated in the training process of the autoencoder. The integration of the regression method enhances the effectiveness of regression and optimizes the overall performance of the autoencoder. The parameters of the DFNN are influenced not only by the gradients of the error between the prediction and the parameters of the last layer but also by the gradients of the reconstruction error. This comprehensive consideration enhances the model's robustness, ensuring stability of the neural network against potential perturbations impacting the output $\theta_{D_{3_{PRED}}}$.

2.2. REGRESSION

Regression is a statistical method used to model the relationship between one or more independent variables and a dependent variable.

2.2.1. Neural Network

Using Neural Networks for regression tasks, the model learns the relationship between input variables and a continuous output variable by iteratively adjusting the weights and biases of interconnected neurons based on the available data. The neural network regression process of this study involves mapping the input geometry, described by a signed distance function, to the output model coefficients. The signed distance function $\phi(x)$ computes the distance from a given point x to the nearest building surface:

$$\phi(x) = d(x, \partial\Omega) \qquad if \;\; x \in \Omega, \tag{2}$$

where, in this context, Ω is the CFD domain, $\partial\Omega$ is the assigned urban features and d is the chosen metric. Each cell within the domain is assigned a value indicative of its distance from $\partial\Omega$, allowing for a comprehensive representation of spatial relationships within the domain. The neural network comprises multiple layers of neurons, each layer performing a series of linear and nonlinear transformations on the input data. The output of the final layer of the network is then used in the reduced-order model for pollutant concentration prediction. The network is trained using a dataset containing paired examples of input signed distance function values and corresponding model coefficients, using optimization techniques to minimize the difference between the predicted and

actual coefficients.

3. RESULTS

While our research is ongoing and concrete results are pending, the strength of our approach lies in the integration of a regression method within the training architecture of an Autoencoder. Drawing inspiration from the methodology outlined by Fresca et al. (2021), our method distinguishes itself by integrating regression directly into the final layer of the decoder. This distinctive approach allows for simultaneous optimization of both regression tasks and the reconstruction capabilities of the autoencoder. Leveraging predictions from a DFNN, our technique facilitates more efficient convergence of the decoder's parameters toward the regression prediction and vice versa. While we cannot guarantee the outcomes at this stage, we anticipate promising results from our approach in both regression analysis and data reconstruction tasks. The results will be evaluated by comparison with the benchmark technique with PCA dimensionality reduction, providing insights into the potential advancements in robust regression modeling and efficient data compression techniques.

4. CONCLUSION

This study aims to develop a Reduced-Order Model (ROM) capable of predicting pollutant concentrations as a function of urban geometry within the atmospheric boundary layer (ABL). The Autoencoder with an augmented loss function architecture is expected to outperform the combination of Principal Component Analysis (PCA) and Neural Network for dimensionality reduction and regression tasks.

ACKNOWLEDGEMENTS

The study has received funding from the European Union's Horizon Europe research and innovation programme under grant agreement No 101072559.

REFERENCES

Bellegoni, M., Cotteleer, L., Kumar S., Mosca, G., Gambale, A., Tognotti, L., Galletti, C., Parente, A. (2022). An extended SST k − ω framework for the RANS simulation of the neutral Atmospheric Boundary Layer. Environmental Modelling & Software. 160. 105583.

Fresca, S., Dede', L. & Manzoni, A. (2021). A Comprehensive Deep Learning-Based Approach to Reduced Order Modeling of Nonlinear Time-Dependent Parametrized PDEs. *J Sci Comput* 87, 61.

Kumar, S., Cotteleer, L., Mosca, G., Gambale, A., Parente, A. (2024). Application of a comprehensive atmospheric boundary layer model to a realistic urban-scale wind simulation. Building and Environment.

Longo, R., Fürst, M., Bellemans, A., Ferrarotti, M., Derudi, M., & Parente, A. (2019). CFD dispersion study based on a variable Schmidt formulation for flows around different configurations of ground-mounted buildings. Building and Environment, 154, 336–347.

IN-VENTO 2024
International Conference of the Italian Association for Wind Engineering
Pisa, September 8th – 11th, 2024

A benchmark of the aerodynamics of a gable-roofed structure for load case development of ASCE7-28

Stefano Brusco [1], Timothy J. Acosta [1], Yitian Guo [1], Jin Wang [1], Gregory A. Kopp [1]

[1]*Faculty of Engineering, London, Ontario, Canada, sbrusco@uwo.ca*

SUMMARY
This abstract describes the benchmark of the aerodynamics of a gable-roofed structure commonly tested by RWDI, CPP and Western University by means of wind tunnel test. The wind tunnel models are 1:100 replicas of the target building, and they are equipped with pressure sensors. Overall, 5 different exposures were tested to simulate the action of turbulent atmospheric boundary layer flows on the aerodynamics of the building. When comparing cases characterized by similar characteristics in terms of wind fields, the results offer a satisfactory match in terms of mean and fluctuating overall wind loading. Moreover, the turbulent properties of the wind are found to play a role in governing the building aerodynamics. This role seems to vary with the orientation of the building with respect to the incoming wind, perhaps because of the different flow fields and the possible flow reattachment phenomena.

Keywords: wind tunnel test, aerodynamics benchmark, wind loading code

1. INTRODUCTION

To support the ASCE 7 (American Society of Civil Engineering) Main Wind-Force Resisting System (MWFRS) Consolidation Project, the project team at Western University (Western, hereinafter) performed a series of wind tunnel tests to investigate the wind effects on buildings with sloped roofs. Specifically, the aerodynamic database that was developed in such study consists of 156 different configurations (74 gable and 82 hip roof-shaped building cases, all with a roof slope of 6/12). The turbulent Atmospheric Boundary Layer flows that were generated were calibrated to simulate both “Open” and “Suburban” terrain categories.

As a benchmark study, one of the geometries of the gable roof-shaped building cases (for a ~3:1 rectangular cross-section) was also tested by Rowan Williams Davies and Irwin (RWDI), Inc., and Cermak Peterka Petersen (CPP), Inc., for comparable wind field exposures. This abstract examines the results gathered from the different databases. Firstly, the different vertical profiles of mean wind velocity and turbulent properties of the wind field are discerned. Based on them, meaningful comparison in terms of mean, fluctuating and peak loads are conducted, verifying the consistency of the results taking the measurement uncertainties into account. Secondly, the effects played by the different turbulent properties of the tested exposures on the aerodynamics of the wind tunnel model are assessed.

2. DESCRIPTION OF THE BENCHMARK

The geometry of the commonly tested structure is indicated in Figure 1. It is characterized by a plan width, *w*, equal to 12.19 m, and by the other plan dimension, *d*, equal to 38.10 m. The eave height of the gable roof, h_e, is 48 m, and the total heigh, *h*, is 51.05 m.

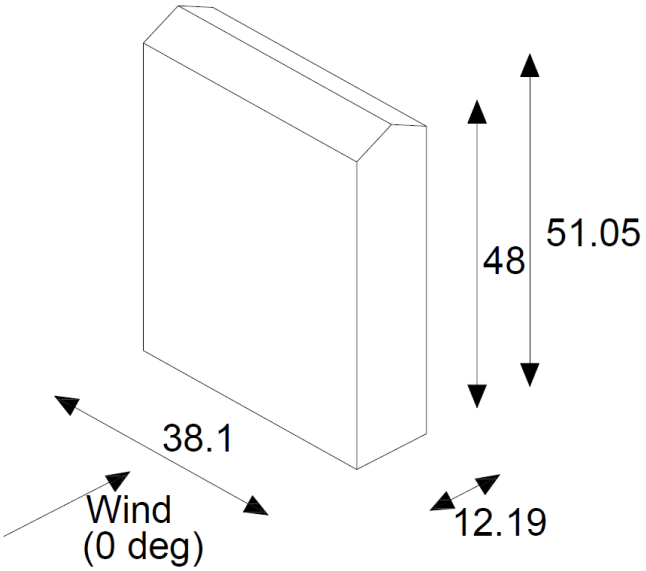

Figure 1. Geometry of the benchmark gable-roofed building (full-scale dimensions, in meters).

The wind tunnel models tested by the three laboratories are all 1:100 scaled replica of that geometry. They were instrumented with pressure taps nearly uniformly distributed all around the surfaces. The models were tested in isolation for wind orientations spanning from 0 (i.e., wind perpendicular to the long side of the cross-section) to 90 degrees (i.e., wind perpendicular to the short side of the cross-section) with 10 degrees increments step. Table 1 includes general information about the wind tunnel testing campaigns conducted by the three different laboratories. The third column expresses in percentage terms the level of turbulence intensity, I_u, defined as the standard deviation of the wind velocity fluctuation divided by its mean value.

Table 1. General overview of the wind tunnel test campaigns performed by RWDI, CPP and Western

Label	Number of tested wind exposures	I_u (%) at *h*	Number of pressure taps	Sampling frequency (Hz)
RWDI	1 (Open)	15	632	512
CPP	2 (Open, Suburban)	15, 22	796	250
Western	2 (Open, Suburban)	12, 20	800	625

The comparison in terms of wind loading first concerns overall quantities, such as base shear force and base overturning and torsional moments. As a note of caution, it is mentioned that the difference between the total number of taps that transpires from Table 1 is mainly associated with the tapping scheme of the roof. On the other hand, the walls are characterized by pressure taps that are located in a consistent way, hence comparison of pressure distributions along specific lines represent a meaningful operation to verify the consistency between the datasets.

3. PRELIMINARY RESULTS AND CONCLUSIONS

The comparisons are conducted in two steps. Firstly, tests characterized by similar wind fields are considered (i.e., "Open" or "Suburban" exposures only, Table 1). The results in terms of mean load coefficients are excellent, as well as the ones concerning fluctuating loads. Besides, the comparison in terms of peak coefficients lets transpire a satisfactory agreement. When comparing the results coming from the 5 different datasets (second step), the role played by the different exposures stands out. In particular, the different mean wind field seems to influence the mean aerodynamic loading, while the different turbulent properties are reflected on the fluctuating load coefficients. Moreover, the effects played by the turbulence appear to be different with the considered wind direction. For the purpose of this abstract, focus will be given to 0 and 90 degrees of incidence. These conditions constitute two significantly different situations for the building from an aerodynamic perspective (e.g., Yu et al., 2012). In fact, for 0 degrees (Figure 1), the shear layers separated from the leading edge of the structure do not reattach on its lateral sides. Conversely, the flow reattachment occurs for 90 degrees and for the considered levels of turbulence intensity. These facts may have a repercussion on the applicability of the quasi-steady theory (e.g., Holmes, 2015) to predict the peak loading.

To facilitate the comparison between the different datasets, a ring of pressure taps of the cross-section of the building is analyzed. This is located at 32.6 cm ($\sim 0.7\ h_e$) from the ground, and it is composed of 32 pressure sensors. The nominal position of each of them is the same for all the datasets. The mean and fluctuating pressure distributions are employed to estimate the time-varying drag and the lift coefficients of the cross-section with the wind direction. These values may be compared to data from various literature, although mostly related to two-dimensional configurations. For the wind oriented at 0 degrees, the aerodynamic of the cross-section is compared to the data provided by Bearman and Trueman (1972), Norberg (1993) and Yang and Mason (2019) for 1/3 side ratio (large side perpendicular to the wind direction). On the other hand, for 90 degrees of wind orientation, the data are compared with Norberg (2003), Noda and Nakayama (2003) and Yang and Mason (2019) for 3/1 side ratio.

Concerning that ring of pressure taps and the 90 degrees wind orientation, Figure 2 shows the variation of the mean (Figure 2a), $\bar{C}_p$, and the standard deviation (Figure 2b), σ_{Cp}, of the relevant pressure coefficients, C_p, which is defined as:

$$C_{p_{ref}} = \frac{P - P_o}{\frac{1}{2}\rho \bar{u}_h^2}, \tag{1}$$

where P is the measured pressure, P_o is the static pressure, ρ is the air density, $\bar{u}_h$ is the mean wind velocity at the mean roof height. The abscissa indicates the non-dimensional perimeter of the cross-section, which is made non-dimensional by dividing it with the side dimension d. The dashed vertical lines indicate the separation between windward (on the right side), leeward (the second one from the left) and lateral sides.

Observing the data in Figure 2, the role played by the different properties of the considered wind fields is already qualitatively graspable.

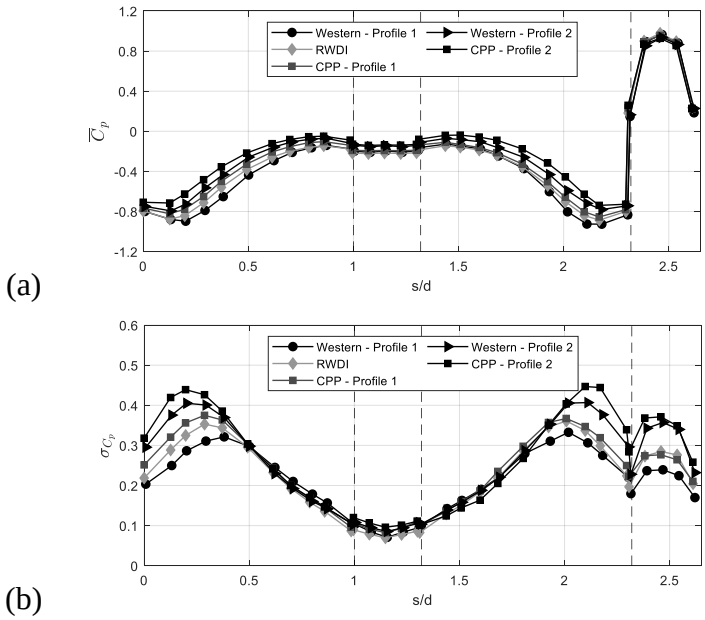

Figure 2. Mean (a) and standard deviation (b) of the pressure coefficients for wind oriented at 90 degrees on the analyzed ring extracted from the five different datasets.

In particular, the mean distribution appears to be characterized by a stronger suction in the afterbody for "Open" exposures, while an increase in turbulence is reflected into an increase of the corresponding mean pressure coefficient. On the other hand, the standard deviation of the coefficients shows an increase when moving from "Open" to "Suburban" exposures. Nonetheless, the role played by the turbulence intensity appears to be reflected also on the location where the maximum of the standard deviation occurs, suggesting the presence of different vorticity patterns.

The full paper will quantify these differences, as well as considering the measurement uncertainty in the discussion of the results.

ACKNOWLEDGEMENTS

The Authors thankfully acknowledge the technical support of RWDI's and CPP's staff in providing wind field and pressure raw data, as well as in assisting them to properly interpreting them.

REFERENCES

Bearman, P. W. and D. M. Trueman (1972). An investigation of the flow around rectangular cylinders. Aeronautical Quarterly 23, 229-237.

Holmes, J. D. (2015). Wind Loading of Structures, CRC Press, Boca Raton, FL, USA.

Noda, H. and A. Nakayama (2003). Free-stream turbulence effects on the instantaneous pressure and forces on cylinders of rectangular cross-section. Experiments in Fluids 34, 332 – 344.

Norberg, C. (1993). Flow around rectangular cylinders: pressure forces and wake frequencies. Journal of Wind Engineering and Industrial Aerodynamics 49, 187–196.

Yang, T. and Mason, M. S. (2019). Aerodynamic characteristics of rectangular cylinders in steady and accelerating wind flow. Journal of Fluids and Structures 90, 246–262.

Yu, D., K. Butler, A. Kareem, J. Glimm, and J. Sun (2013). Simulation of the Influence of Aspect Ratio on the Aerodynamics of Rectangular Prisms. Journal of Engineering Mechanics 139 (4), 429 - 438.

IN-VENTO 2024
International Conference of the Italian Association for Wind Engineering
Pisa, September 8th – 11th, 2024

Project -WIND RISK: Measurement and simulation of thunderstorm winds

Massimiliano Burlando [1], Mario Marcello Miglietta [2,3], Elenio Avolio [3]

[1] *University of Genoa, Genoa, Italy, massimiliano.burlando@unige.it*
[2] *University of Bari, Bari, Italy, mario.miglietta@uniba.it*
[3] *Institute of Atmospheric Sciences and Climate, National Research Council, Lamezia Terme, Italy, e.avolio@isac.cnr.it*

SUMMARY
The Project –WIND RISK is a research project dealing with measurement and modelling of wind fields within thunderstorm cumulonimbus clouds and outflows at the ground (i.e., downbursts and gust fronts). The general objective of the project is to advance the knowledge about the processes occurring inside thunderstorm clouds that can bring about particularly strong outflows, and the identification of the environmental (synoptic and mesoscale) conditions favourable to their development. The area under investigation is the North-western Italy and the Ligurian Sea, which are among the regions most prone to strong thunderstorms in Europe. Two measurement campaigns using remote-sensing and ground-based anemometry, and ad-hoc simulations using the WRF model will be carried out to build a database of thunderstorm wind fields with special focus on downdrafts and downburst formation. The database will be shared within the scientific community after the end of the project through an open access platform.

Keywords: thunderstorm outflows, radar and lidar measurements, WRF simulations

1. INTRODUCTION

Despite wind is the most destructive natural phenomenon in Europe, accounting for more than 70% of damages and casualties yearly (Ulbrich et al., 2013), a thorough knowledge of thunderstorm outflows and their impact on the natural and built environment does not exist yet. Since the last decades, the wind engineering community has focused on thunderstorm outflows mainly regarding the characterization of the surface wind fields produced during downbursts in terms of signal analysis of thunderstorm records (e.g., Zhang et al., 2018) and vertical profiles (e.g., Canepa et al., 2020) by means of experimental campaigns (e.g., Solari et al., 2012) and numerical simulations (e.g., Zuzul et al., 2023), in an attempt to find a suitable downburst model for codification (e.g., Xhelaj et al., 2020). However, a comprehensive and reliable database of real thunderstorm outflows, which is of paramount relevance to validate downburst models, is still missing. This is the main goal of the research project described hereafter.

In 2022, the Giovanni Solari Wind Engineering and Structural Dynamics (GS-Windyn) Research Group of the University of Genoa and the University of Bari/the Institute of Atmospheric Sciences and Climate of the National Research Council (ISAC-CNR) have been awarded by the Italian Ministry of the University and Research a grant for research projects of relevant national interest (PRIN-2022) for the Project "Thunderstorm outflows measurement and modeling for strong–WIND nowcast and RISK mitigation" (–WIND RISK). This project is intended to provide the wind engineering community with relevant wind field reconstructions inside thunderstorm clouds

at least from the middle troposphere (around 5.5 km above sea level) to the ground, which is the region where downdrafts are expected to accelerate due to negative buoyancy and eventually produce strong outflows at the ground. The area under investigation is the North-western Italy and the Ligurian Sea, since these regions are among the most prone to strong thunderstorms in Europe (Mateusz et al., 2020).

The database of wind field retrievals and reconstructions within real thunderstorm clouds will be made up of observations as well as numerical simulations. During the project, two field campaigns using coupled radar/lidar remote-sensing techniques will be carried out in Piedmont and Liguria region, and proper algorithms will be applied to reconstruct the high-resolution 4D (i.e., in space and time) wind fields within cumulonimbus clouds. In addition, ad-hoc numerical simulations will be performed to analyze a set of case studies that will be investigated to find common meteorological precursors and environmental conditions favourable to the development of gust fronts/downbursts.

In Section 2, the project structure is briefly described. Section 3 and 4 are devoted to observations and numerical simulations, respectively. Conclusions are drawn in Section 5.

2. PROJECT STRUCTURE

The project consortium is made up of two research units: the University of Genoa, which is in charge of organizing the field campaigns, collect and post-process all measurements, and that of the University of Bari/National Research Council, in charge of performing the numerical simulations.

According to this subdivision of competencies and activities, the project is structured into 3 main Work Packages (WP) as shown in Fig. 1. WP1 is devoted to thunderstorm measurement and analysis and, in its turn, organized in 4 Tasks (T). T1.1 concerns the definition of the overall measurement setup, instrument deployment and data management during the field campaigns, while T1.2 includes all the activities needed to carry out the two 3-month long field campaigns during their executive phase. T1.3 deals with the analysis of wind measurements and post-processing to reconstruct the 3D wind fields. T1.4 is a demonstration activity of the algorithms developed in T1.3 applied in real-time in an operational environment for nowcasting purposes.

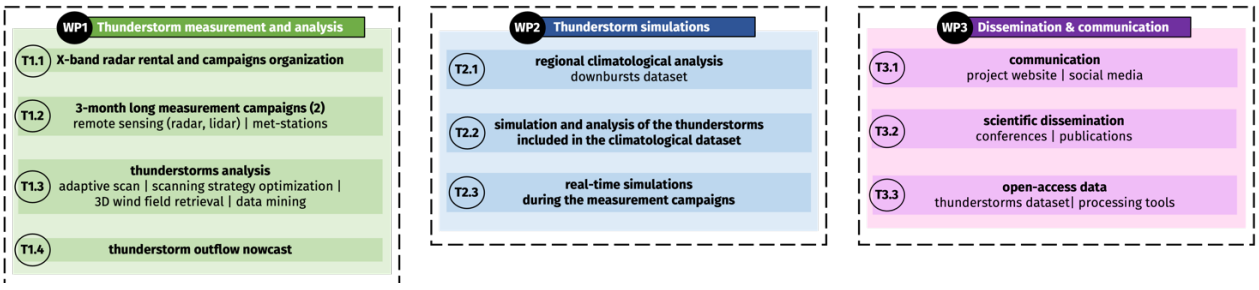

Figure 1. Structure of Project –WIND RISK

WP2 is devoted to thunderstorm simulation by means of a state-of-the-art numerical weather prediction (NWP) model, and it is subdivided in 3 Tasks. T2.1 and T2.2 aim at simulating in hindcast mode some relevant thunderstorms that occurred in the past in order to investigate the

development mechanisms of these events over the area under study. In T2.3, the same NWP model will be used in forecast mode during the field campaigns and compared to measurements.

Finally, WP3 is entirely focused on dissemination and communication activities through the internet, including social media, publication of the relevant results in journal papers, and presentation in conferences. In addition, the project is expected to publish in open access the database of the thunderstorm-related 3D wind fields from measurements as well as numerical simulations.

3. MEASUREMENT CAMPAIGNS

Two measurement campaigns are expected to be carried out during the project's lifetime. The first campaign (tentatively May-Jul 2024) is based in Piedmont, over the urban area of Turin and its surroundings (yellow box in Fig. 2a), whereas the second one (tentatively Oct-Dec 2024) is in Liguria (red box in Fig. 2a).

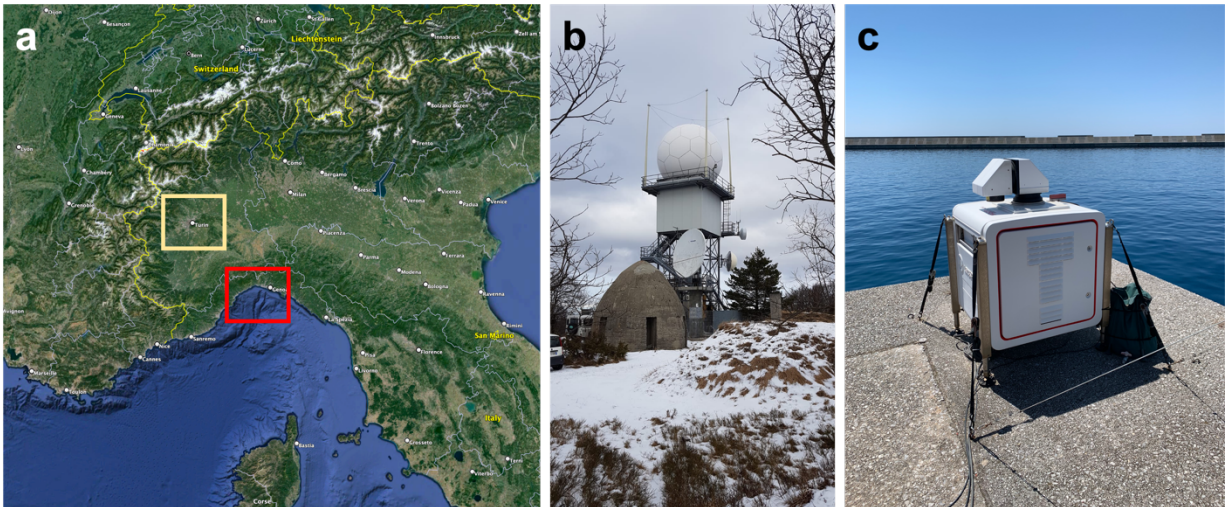

Figure 2. Areas of the 2 measurement campaigns in the north-western Italy (a); the Doppler radar (b) and scanning lidar (c) installed in Liguria

In both campaigns, remote-sensing measurements based on Doppler radars (Fig. 2b) will be used to scan the within-cloud wind fields, complemented by Doppler lidars (Fig. 2c, in Genoa) to measure the thunderstorm outflows at the ground. In addition, ground-based met-stations belonging to the regional meteorological networks of Piedmont and Liguria will be used for rain and cold pool detection.

4. NUMERICAL SIMULATIONS

Numerical simulations of relevant thunderstorm events will be performed using the Weather Research and Forecast (WRF, Skamarock et al., 2019) meteorological model. This is a state-of-the-art numerical weather prediction model widely used both for research and operational purposes.

WRF will be implemented over 3 nested grids with 9, 3, and 1 km of horizontal resolution, respectively centered over the area of investigation: the largest domain will cover all the north-

western Italy, while at the finest grid level (1 km) two sub-domains will be used in order to simulate both Piedmont and Liguria during the respective campaigns. Since the development and the triggering mechanisms of thunderstorms are expected to be influenced by the Alps as well as by the difference of local meteorological conditions (e.g., temperature, wind direction, etc.) between the Po Valley and the Ligurian Sea, this strategy is expected to capture, for instance, the mesoscale topographic forcing that might increase the wind shear along the vertical as well as the presence of fronts or low level jets close to the ground.

5. CONCLUSIONS

This paper gives a general overview of a new research project that is being implemented at the University of Genoa (as leading partner) and is expected to contribute to the advancement in the knowledge of thunderstorm winds through systematic full-scale measurements and simulations in the area of north-western Italy. During the conference presentation the project will be presented in detail and the results from the first measurement campaign will be reported.

ACKNOWLEDGEMENTS

This research is funded by the European Union – Next Generation EU for the Project –WIND RISK "Thunderstorm outflows measurement and modeling for strong–WIND nowcast and RISK mitigation" (Grant no. 2022NPKCLX, CUP D53D23004790006).

REFERENCES

Canepa F., M. Burlando, and G. Solari (2020). Vertical profile characteristics of thunderstorm outflows. J. Wind Eng. Ind. Aerodyn. 206, 104332.

Solari G., M. P. Repetto, M. Burlando, P. De Gaetano, M. Parodi, M. Pizzo, and M. Tizzi (2012). The wind forecast for safety management of port areas. J. Wind Eng. Ind. Aerodyn. 104-106, 266–277.

Mateusz T., J. T. Allen, P. Groenemeijer, R. Edwards, H. E. Brooks, V. Chmielewski, and S.-E. Enno (2020). Severe Convective Storms across Europe and the United States. Part I: Climatology of Lightning, Large Hail, Severe Wind, and Tornadoes. J. of Climate 33, 10239-10261.

Skamarock W. C., J. B. Klemp, J. Dudhia, D. O. Gill, Z. Liu, J. Berner, W. Wang, J. G. Powers, M. G. Duda, D. M. Barker, and X.-Y. Huang (2019). A Description of the Advanced Research WRF Version 4. Tech. Note NCAR/TN-556+STR, NCAR, 145 pp.

Ulbrich, U., G. C. Leckebusch, and M. G. Donat (2013). Windstorms, the most costly natural hazard in Europe. In: Boulter, S., J. Palutikof, D. Karoly, and D. Guitart (Eds.), Natural Disasters and Adaptation to Climate Change. Cambridge University Press, 109-120.

Xhelaj A., M. Burlando, and G. Solari (2020). A general-purpose analytical model for reconstructing the thunderstorm outflows of travelling downbursts immersed in ABL flows. J. Wind Eng. Ind. Aerodyn. 207, 104373.

Zhang S., G. Solari, P. De Gaetano, M. Burlando, and M.P. Repetto (2018). A refined analysis of thunderstorm outflow characteristics relevant to the wind loading of structures. Probabilistic Engineering Mechanics 54, 9-24.

Zuzul J., A. Ricci, M. Burlando, B. Blocken, and G. Solari (2023). CFD analysis of the WindEEE dome produced downburst-like winds. J. Wind Eng. Ind. Aerodyn. 232, 105268.

IN-VENTO 2024
International Conference of the Italian Association for Wind Engineering
Pisa, September 8th – 11th, 2024

An overview of the Julsundet Bridge aerodynamic design

Filippo Calamelli[a], Giulia Pomaranzi[b], Tommaso Argentini[c], Alberto Zasso[d], Jungao Wang[e]

[a]*Politecnico di Milano, Milan, Italy, filippo.calamelli@polimi.it*
[b]*Politecnico di Milano, Milan, Italy, giulia.pomaranzi@polimi.it*
[c]*Politecnico di Milano, Milan, Italy, tommaso.argentini@polimi.it*
[d]*Politecnico di Milano, Milan, Italy, alberto.zasso@polimi.it*
[e]*Norwegian Public Roads Administration, Stavanger, Norway, jungao.wang@vegvesen*

SUMMARY:
The design of the Julsundet Bridge, included in the E39 fjord crossing project in Norway, is affected by both the complex wind scenario induced by the local terrain and the aerodynamic properties of the deck. Specifically, the relevant fjords that characterize the Norwegian coastline could induce strong modification in the incoming wind impacting the bridge's dynamic response. Additionally, the 1625m span covered with a single-box deck section makes the critical flutter speed close to the design value. In this context, an experimental campaign was carried out in the Politecnico di Milano wind tunnel to properly address both issues. A 1:1000 scale terrain model is used to investigate the expected wind field at the bridge site while a deck sectional model suspended on springs is employed to check the aeroelastic stability. In this abstract, the experimental tests are described and a preliminary set of results is presented.

Keywords: wind tunnel tests, topographic effects, flutter instability, super long-span bridges, bridge aeroelasticity

1. INTRODUCTION

Wind-induced effects play a key role in the design of long-span bridges (Argentini et al., 2022). Investigating those effects implies accounting for both the aerodynamic properties of the deck itself and the wind conditions expected at the bridge site. The latter may become particularly critical in case the site is characterized by hilly regions that make the prediction of the topography-induced effects not straightforward.

The Julsundent Bridge project is a typical example where both aspects are important. Specifically, the wind scenario is strongly influenced by the complex fjords that distinguish the country's coastline, while the significant span combined with the single-box deck section makes the aeroelastic design of the bridge particularly challenging. This deck solution has already been used effectively for shorter suspension bridges, e.g. the Hardanger Bridge or the Humber Bridge. Nevertheless, increasing the length of the main span, the flutter speed decreases and, for the Julsundet Bridge, we are close to the value that allows the applicability of this solution ($V_{crit} = 65.6 m/s$, computed as reported by Vegnormal N400 Bruprosjektering, clause 5.6.8-1, 2023). This aspect may be further worsened by the complex wind conditions induced by the fjords. This is the main reason why, in recent years, information about terrain-induced effects has been incorporated into bridge design through large measurement campaigns (Castellon et al., 2022). However, if such information is somehow incomplete due to the installation of the sensors (usually on land and far from the bridge) (Fenerci et al., 2023), they can be supplemented by topographic tests performed through wind tunnel tests or numerical simulations (Lystad et al., 2018).

Hence, to properly cover the aerodynamic design of the Julsundet Bridge, an experimental campaign was conducted in the Politecnico di Milano Wind Tunnel, addressing both the terrain effects and the investigation of the aerodynamic properties of the deck section. In the present abstract, after briefly presenting the experimental setup for both test types, some relevant results are reported and commented on.

2. METHODOLOGY

2.1. Topographic Study

To have an accurate description of the wind field, a dedicated topographic study has been performed in the boundary layer test section of the Politecnico di Milano Wind Tunnel, as depicted in Figure 1; a 10 km diameter surround area is reproduced, assuming a length scale of 1:1000, allowing a proper representation of the elevations closest to the site of the Julsundet bridge. During the experimental tests, 16 different incoming wind directions are considered. The wind directions include those perpendicular and parallel to the bridge axis and 10, 20, 30 and 45 degrees yawed to the normal axis in northwest, southwest and southeast sectors. Among others, the most interesting outputs for design purposes are the mean angle of attack over the deck axis (at 76.52m from water level) for stability issues and the lateral scales of the wind. For the towers (271m high), the flow field over the tower development can be measured, allowing the investigation of the buffeting response of such structures.

Figure 1. The terrain model in the wind tunnel test section

2.2. Evaluation of deck aeroelastic stability

Different deck configurations have been tested in the high-speed test section of Politecnico di Milano wind tunnel using a suspended sectional model, as shown in Figure 2. The main purpose is to investigate the aerodynamic stability of the bridge changing small details while keeping constant the deck shape. Therefore, different sets of barriers, railings and gantry rails were tested. For the sake of brevity, a limited set of configurations is here presented. Specifically, the baseline configuration ("JUL-R0", see Figure 3 without modelled snow) and the bare deck ("JUL-B", see Figure 3 without any fitting) will be considered. Moreover, the impact of the snow on the deck aerodynamics is investigated ("JUL-S", see Figure 3).

3. RESULTS AND DISCUSSION

3.1. Topographic study

As an example of the results, Figure 4 shows flow measures along the deck axis, for two different incoming wind directions. Specifically, the first subplot shows the magnitude of the velocity vector normalized to the reference velocity measured by a Pitot tube placed at the beginning of the turning table at tower height. The second and third subplots report yaw and pitch angles

Figure 2. Julsundet Bridge deck sectional model suspended on springs

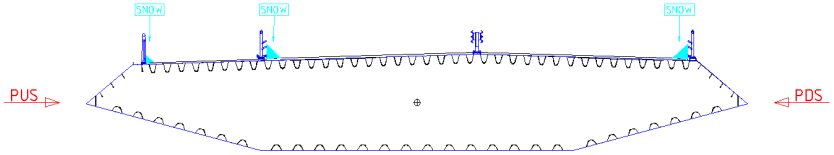

Figure 3. Sketch of the Julsundet Bridge deck sectional model. The fittings representing the snow accumulation at the roadside are also reported. Both wind directions were investigated (PUS=Pedestrian UpStream, PDS=Pedestrian DownStream)

defined with respect to the inlet wind. Yaw angle is in the horizontal plane and it is positive when we have a counterclockwise rotation; pitch angle is in the vertical plane and it is positive if upward. For wind direction normal to the deck axis (blue markers), the flow is subjected to a slight acceleration resulting in normalized velocities over 1 along the deck axis. The mean angle of attack (pitch angle) is null, except for the closest location to the Nautneset tower, where it reaches -5°. Considering instead the wind direction 302° (red markers in Figure 4), the effects due to the fjords result in a drop of the mean wind speed, due to the sheltering effects on the Nautenest side, and in a flow deviation, as highlighted by a -25° yaw angle.

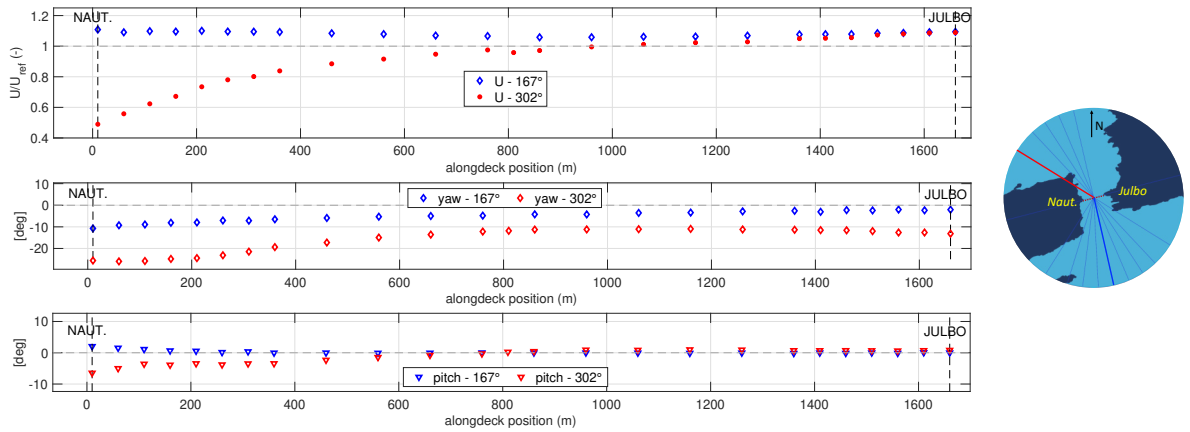

Figure 4. Results from velocity measurements along the deck axis. Incoming wind directions are depicted in the right figure.

3.2. Stability Investigation

In this section, a selection of results related to the investigation of the deck stability is presented. Figure 5(a) illustrates the damping ratio as a function of the full-scale mean wind speed, considering the "PUS" wind direction (refer to Figure 3). A deck static angle of rotation equal to 0° is selected since, as shown in Figure 4, when the wind direction is perpendicular to the bridge,

the angle of attack approaches 0° across almost the entire span. For all the selected configurations, the flutter speed is greater than $70m/s$. On the other hand, considering the "PDS" wind direction, the stability of the deck is strongly affected by the presence of the snow positioned at the roadside (see Figure 5(b)). The presence of the snow could induce the detachment of eddies from the section, strongly modifying its aeroelastic behavior. This hypothesis is also confirmed by Figure 6, showing the a_2^* coefficients expressed according to Zasso, 1996. Specifically, the negative values related to the "JUL-S" configuration represent a negative torsional aerodynamic damping and thus, an eventual 1-dof torsional instability. As for the other configurations, the adopted deck solution can be considered aerodynamically robust. In the extended version of the paper, a more complete set of results will be presented.

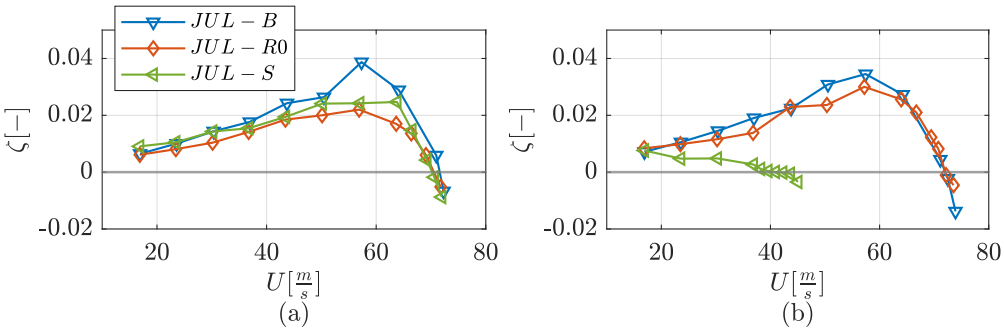

Figure 5. Damping ratio as a function of the full-scale mean wind speed. Figure (a) shows the results related to the "PUS" wind direction while, Figure (b), those related to the "PDS" wind direction. In both cases, the deck angle of rotation is set equal to 0°

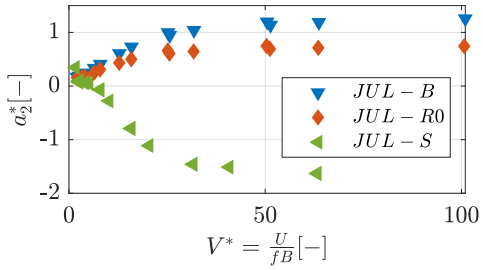

Figure 6. a_2^* coefficient as a function of the reduced velocity V^* (defined as the ratio between the mead wind speed U and fB, where f is the frequency of oscillation of the imposed torsional motion and B=27.5m is the deck chord) for the different configurations, related to the "PDS" wind direction and a deck angle of rotation equal to 0°.

REFERENCES

Argentini, T., D. Rocchi, C. Somaschini, U. Spinelli, F. Zanelli, and A. Larsen (Jan. 2022). Aeroelastic stability of a twin-box deck: Comparison of different procedures to assess the effect of geometric details. Journal of Wind Engineering and Industrial Aerodynamics 220, 104878.

Castellon, D. F., A. Fenerci, and O. Øiseth (2022). Environmental contours for wind-resistant bridge design in complex terrain. Journal of Wind Engineering and Industrial Aerodynamics 224, 104943.

Fenerci, A., T. M. Lystad, and O. Øiseth (2023). Full-scale monitored wind and response characteristics of a suspension bridge compared with wind tunnel investigations at the design stage. Journal of Wind Engineering and Industrial Aerodynamics 242, 105583.

Lystad, T. M., A. Fenerci, and O. Øiseth (2018). Evaluation of mast measurements and wind tunnel terrain models to describe spatially variable wind field characteristics for long-span bridge design. Journal of Wind Engineering and Industrial Aerodynamics 179, 558–573.

Zasso, A (1996). Flutter derivatives: Advantages of a new representation convention. Journal of Wind Engineering and Industrial Aerodynamics 60, 35–47.

A hazard map of extreme winds in the Municipality of Genoa, Italy

Federico Canepa [1] and Massimiliano Burlando [1]

[1]*Department of Civil, Chemical and Environmental Engineering, University of Genoa, Italy.*
federico.canepa@unige.it – massimiliano.burlando@unige.it

SUMMARY (10 pt)
In the context of the European Project ADAPTNOW, which is funded by the Interreg Alpine Space Program, a comprehensive map of extreme wind speeds across the municipality of Genoa, Italy, is being developed. To achieve this objective, extensive statistical analysis was conducted on medium- to long-term datasets comprising 10-minute mean wind speeds and directions obtained from eight meteorological stations within the network operated by the Ligurian Regional Agency for Environmental Protection (ARPAL). Starting from Parent Population Analysis (PPA) and Extreme Value Analysis (EVA), we aim to build a map of extreme wind occurrences for various return periods and direction sectors. This study is anticipated to offer significant contributions on multiple fronts, including informing the decision-making processes of municipal authorities aimed at citizen safety and mitigating risk exposure. Additionally, it aids in conducting preliminary windiness assessments during the design phase of emerging structures, infrastructures, and urban green spaces.

Keywords: Extreme wind map, Extreme value distribution, Genoa Municipality

1. INTRODUCTION

Genoa is a municipality of about 243 km^2 located in the north-western part of Italy between the Ligurian Sea and the Apennine Mountains. The city stretches along the coast for about 30 km. The particular geographical position and the complex orography make the municipality very susceptible to high-intensity winds coming from a range of direction sectors.
Within the municipality area, several meteorological stations belonging to the Ligurian Regional Agency for Environmental Protection (ARPAL) were examined with the aim to perform a comprehensive statistical investigation of wind speeds and directions and build a map of extreme winds. Eight met-stations presenting medium to long term records were selected among those available. The minimum length of available records in a database is 4 years. All the databases present data up to October 30, 2023.

2. INSTRUMENT SPECIFICATIONS

A List of met-stations utilized in the present study is reported in Table 1 along with their code, geographical coordinates, and starting date of the databases. Figure 1 shows their locations.

Table 1. List and specifications of the ARPAL met-stations involved in this study

No.	Name	Code	Lat (°N)	Lon (°E)	Height (m ASL)	Initial date (mm/yyyy)
1	Castellaccio	RIGHI	44.42797	8.93433	360	12/2014
2	Certosa	GECER	44.42439	8.88997	30	06/2019

3	Fontana Fresca	FFRES	44.40290	9.09318	791	01/2006
4	Monte Pennello	MOPEN	44.48017	8.79867	980	05/2014
5	Passo Turchino	PTURC	44.48613	8.73602	590	03/2010
6	Porto Antico	GEPOA	44.40816	8.92317	25	03/2016
7	Punta Vagno	GEPVA	44.39278	8.95222	10	01/2013
8	S. Ilario	STILA	44.38400	9.06066	174	03/2010

Figure 1. Map of ARPAL met-stations in the Municipality of Genoa

3. METHODOLOGY

The selected eight databases of 10-min mean wind speed and direction records underwent a meticulous inspection. A database shall be representative, reliable, and homogeneous to be correctly submitted to a probabilistic analysis. A database is representative if it is acquired over a sufficiently long period of time by an adequately located anemometric station. While the first point is strictly dependent on the type of probabilistic analysis to be conducted—refined probabilistic techniques enables to analyze shorter databases—the second provides that the met-station is located in an open terrain with no obstacles shielding the incoming wind and at least at 10 m height above ground level (AGL). The reliability of the database is assured by a proper maintenance of the measuring instrument and correction procedures to account and replace erroneous or missing measurements. The homogeneity of the database requires the application of ad-hoc criteria to separate and classify different wind events into homogenous sub-datasets that shall be analyzed independently. These three requirements have been cross-checked and verified before submitting the eight long-term wind speed and direction records to a probabilistic analysis.

Furthermore, the wind data shall be homogenized when combined together to produce the final maps of extreme winds. The wind recorded by an individual station strictly depends on the roughness and topography characteristics of the recording site where the anemometer is installed. Wind measurements shall be transformed to reference conditions before extrapolating their values to geographical points outside the location of measurement. The original recorded values are transformed into simulated values at a reference site that is defined as 10 m AGL on a flat open country terrain with roughness length z_0 = 0.05 m.

4. PROBABILISTIC ANALYSIS

Each met-station was first analyzed in terms of probabilistic distribution of the parent population

of current values. The analysis was performed both on the overall wind speed timeseries (population) (non-directional analysis) and separating them according to the incoming wind direction (directional analysis), considering 12 sectors 30° wide— from 0° to 360° with step 30°. 0° (and 360°) corresponds to a wind approaching from the north. A Weibull model was used to describe the distribution of the parent population of data (Weibull, 1951). The shape parameter k and the scale parameter c were evaluated by means of the resistant method (Hoaglin et al., 1983). Figure 2 shows the non-directional and directional PPA applied on a selected database.

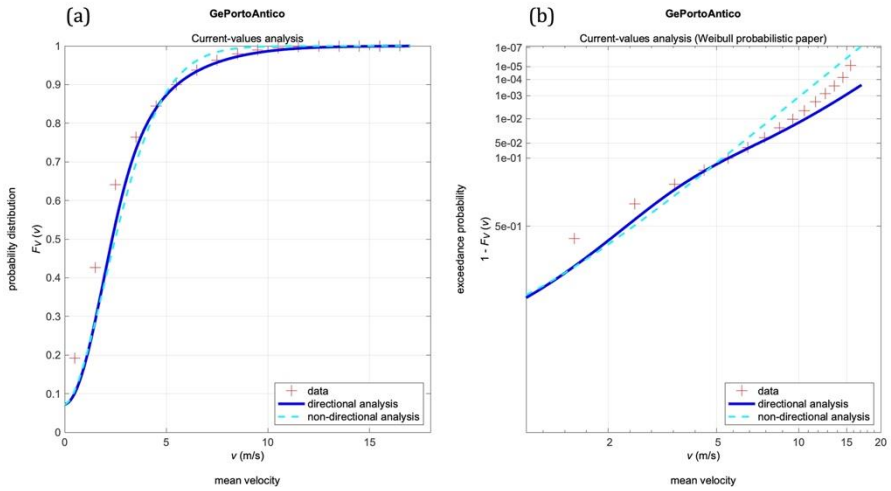

Figure 2. Cumulative distribution (a) and exceeding probability (b) of 10-min mean wind speed for the GEPOA dataset

Figure 3 shows the joint density function of 10-min mean wind speed (on radial axis) and direction (30° wide sectors) values in polar form. The innermost diagram corresponds to the most common and weak wind (1% exceeding probability), while the outermost diagram refers to the rarest and most intense winds (10^{-6} % exceeding probability).

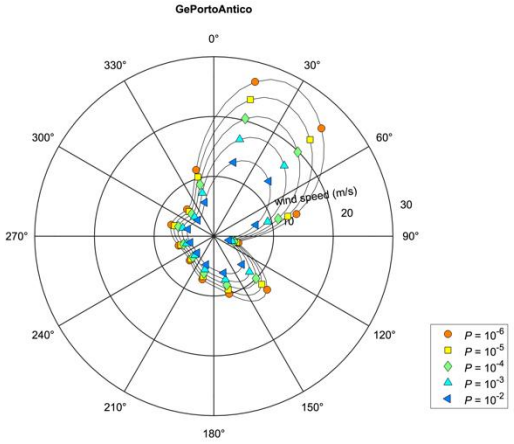

Figure 3. Polar diagram of probability distribution of directional 10-min mean wind speed for the GEPOA dataset

Extreme Value Analysis (EVA) is applied on the database of measurements to define the distribution of the yearly maxima and derive the maxima associated with different return periods.

The three main asymptotic distributions (Gumbel, 1958) were applied. Wind engineers usually adopt the type I distribution (shown in Figure 4) for its ease to use in the technical and codification sectors. However, Torrielli et al. (2013) developed an iterative Monte Carlo algorithm for simulating long-term (> 10.000 years) 10-min mean wind speed values and found that the Process Analysis (Rice, 1944) best represents the distribution of yearly maxima.

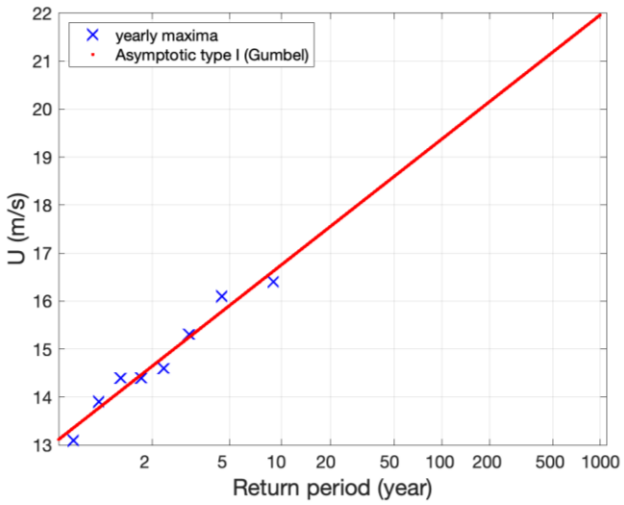

Figure 4. Type I distribution of yearly maxima of the 10-min mean wind speed for the GEPOA dataset

5. CONCLUSIONS AND PROSPECTS

The application of the Extreme Value Analysis (EVA) to the series of yearly maxima of the eight met-stations analyzed, the value transformation to reference conditions as outlined in Section 3, their subsequent extrapolation and interpolation according to specific weighting functions that account for the distance between stations, leads to the formulation of hazard maps of extreme wind speeds for different return periods and level of analysis. The complete statistical procedure and the output probabilistic maps will be shown during the congress.

ACKNOWLEDGEMENTS

The work done by F. Canepa was carried out within the RETURN Extended Partnership and received funding from the European Union Next-Generation EU (National Recovery and Resilience Plan – NRRP, Mission 4, Component 2, Investment 1.3 – D.D. 1243 2/8/2022, PE0000005). This study was partially funded by ADAPTNOW Project – "ADAPTation Capacity Strengthening for Highly Affected and Exposed Territories in the Alps NOW" (Grant No. ASP0100048). ADAPTNOW is co-financed by the European Regional Development Fund through the Interreg Alpine Space Programme.

REFERENCES

Gumbel, E.J., 1958. Statistics of Extremes. Columbia University Press, New York.

Hoaglin, D.C., Mostaller, F., Tukey, J.W., 1983. Understanding robust and exploratory data analysis. Wiley, New York.

Rice, S.O., 1944. Mathematical analysis of random noise. The Bell System Technical Journal 23, 282–332. https://doi.org/10.1002/j.1538-7305.1944.tb00874.x

Torrielli, A., Repetto, M.P., Solari, G., 2013. Extreme wind speeds from long-term synthetic records. Journal of Wind Engineering and Industrial Aerodynamics 115, 22–38. https://doi.org/10.1016/j.jweia.2012.12.008

Weibull, W., 1951. A Statistical Distribution Function of Wide Applicability. Journal of Applied Mechanics 18, 293–297. https://doi.org/10.1115/1.4010337

IN-VENTO 2024
International Conference of the Italian Association for Wind Engineering
Pisa, September 8th – 11th, 2024

Efficacy of a torsional flutter harvester by moment-arm augmentation

Luca Caracoglia[a]

[a]*Visiting Professor, Department of Civil, Envir. & Mechanical Engr. (DICAM), University of Trento, Italy (permanent address: Northeastern Univ., Boston, MA, USA), lucac@coe.neu.edu*

SUMMARY:
Wind energy harvesters are usually designed to operate in the low wind speed range. Continued investigation on a torsional-flutter-based apparatus is documented herein. A nonlinear hybrid restoring toque mechanism, installed at equally spaced supports, and eddy currents are used to extract wind energy through limit-cycle vibration. The flow model can simulate both stationary and non-stationary turbulence conditions, and time-varying mean wind speed, if necessary (e.g., a gust front). This work evolves from recent studies to examine stochastic stability and post-critical, random output power in turbulent flows. Variable configurations are considered. More specifically, the increment of moment arm is examined to enhance output power and energy efficiency. The post-critical model is based on stochastic differential equations.

Keywords: Energy harvesting, torsional flutter, gust fonts, output power, stochastic differential equations

1. INTRODUCTION

The recent increasing demand for electricity and renewable energy sources has promoted the use of innovative wind-based methods for power extraction. Apart from macro-scale systems, i.e., large wind turbines, and micro-scale energy harvesters for miniature sensors, "meso-scale" devices at the scales of a few meters are still partially uncharted technology solutions. To bridge this gap, a meso-scale system that exploits torsional flutter to extract wind energy, has been proposed (Caracoglia, 2018, 2023, 2024). The idea is to favorably exploit the "flutter-mill" phenomenon (Matsumoto, 2013) and to convert airflow kinetic energy. The torsional flutter concept originates from pioneering studies by Ahmadi (e.g., Roohi et al., 2023), who studied power production of an H-section with curved flanges undergoing flutter instability.

The apparatus (Fig. 1) is composed of a rigid blade-airfoil of chord-wise length $2b$ (with half-chord $0.5 \leq b \leq 1.0$ m) and span-wise length ℓ. The blade-airfoil is a NACA0012 streamlined profile of aspect ratio $\mathrm{AR} = \ell/b$ with $4 \leq \mathrm{AR} \leq 10$. The blade-airfoil is attached to a support mast using a flexible plate-like interface component, shown as "torsional-rotational" mechanism in Fig. 1. This interface is flexible and allows for a nonlinear, elastic torsional restoring moment about pivot "O", with the distance from the airfoil's mid-chord point "C" being designated as ab in Fig. 1 (right). Energy conversion is achieved by eddy currents (Kwon et al., 2013), as explained by Caracoglia (2018).

Contrary to previous studies, in which the pivot-axis position was varied between $a = -1$ (windward edge) and $a \approx -0.75$ (quarter chord point), this study explores the increase of moment-arm by considering an external pivot point, i.e., the restoring-torque mechanism and support mast are located at a distance $a < -1.0$. The dimensionless distance $a < 0$ corresponds to an upwind axis of rotation with respect to the mid-chord point C in Fig. 1; designations follow the classical flutter theory (Theodorsen, 1935).

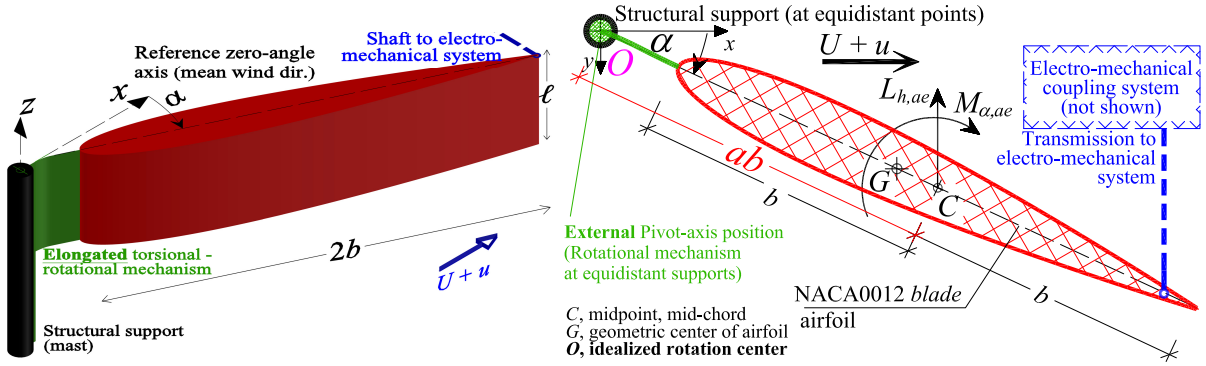

Figure 1. Torsional flutter harvester: (left) 3D schematics, (right) 2D plan-view on XY axis

2. MODELING BACKGROUND

2.1. Incipient flutter instability

The linear, incipient flutter solution under uniform, constant wind speed U without turbulence ($u = 0$), and for an apparatus without structural damping and electrical coupling, is controlled by two dimensionless equations (Caracoglia, 2018):

$$\gamma^2 = 1 + \varepsilon\eta_{3D}\left[(0.125 + a^2) + k^{-2}(2a+1)F(k) + k^{-1}(2a^2 - 0.5)G(k)\right] \tag{1a}$$

$$-G(k)(2a+1) + k(0.5-a) + kF(k)(2a^2 - 0.5) = 0 \tag{1b}$$

In Eq. (1a), $\gamma = \omega_\alpha/\omega$ is the frequency ratio between the angular frequency of the system (ω_α) and the frequency of the torsional flutter harmonic motion (ω); $\varepsilon = \pi\rho b^4\ell(I_{0,\alpha})^{-1}$ is a dimensionless inertia parameter; $I_{0\alpha}$ is the total polar mass moment of inertia with respect to pivot O; $F(k)$ and $G(k)$ are the real and imaginary parts of the Theodorsen (1935) function with $k = \omega b/U > 0$; $\eta_{3D} = \mathrm{AR}/(2+\mathrm{AR})$ accounts for three-dimensional aeroelastic load effects (Argentina and Mahadevan, 2005). The dimensionless or reduced frequency at incipient flutter k^*, independent of ε and η_{3D}, is found by solving numerically Eq. (1b) first; then k^* is substituted into Eq. (1a) to find the frequency ratio at flutter, γ^*. Thus, critical flutter wind speed is $U^* = \omega_\alpha b/(k^*\gamma^*)$ [m/s], or $U_r^* = (k^*\gamma^*)^{-1}$ in dimensionless form.

2.2. Post-critical output power in gusty wind environments

The post-critical flutter behavior depends on torsional rotation α and derivative $\mathrm{d}\alpha/\mathrm{d}\tau$ with respect to dimensionless time $\tau = \omega_\alpha t$. The dynamic equilibrium equation of the flapping is:

$$\frac{\mathrm{d}^2\alpha}{\mathrm{d}\tau^2} + 2\zeta_\alpha\frac{\mathrm{d}\alpha}{\mathrm{d}\tau} + \alpha + \mathrm{H}_{\mathrm{NL}}\left(\alpha, \frac{\mathrm{d}\alpha}{\mathrm{d}\tau}\right) = \frac{M_{0z} + M_{(\mathrm{e.m.})}}{\omega_\alpha^2 I_{0\alpha}} \tag{2}$$

Linear structural damping is simulated through damping ratio $0 < \zeta_\alpha < 1$ in Eq. (2). Nonlinear restoring torque is simulated by function $\mathrm{H}_{\mathrm{NL}} = \left(\kappa\alpha^3 - 2\zeta_\alpha\gamma\alpha^2\right)$ with $\kappa > 0$ and $\gamma > 0$ (Caracoglia, 2023). Noting the moment arm $(1-a)b$ from the pivot O to the leeward edge in Fig. 1, the electro-motive torque, with $I(\tau)$ being the output current of the power system, is:

$$M_{(\mathrm{e.m.})} = -(1-a)b\Phi_{(\mathrm{e.m.c.})}I(\tau), \tag{3}$$

$\Phi_{(\mathrm{e.m.c.})}$ is the electro-mechanical coupling coefficient [newton/ampère]. The moving coil introduces magnetic induction and interacts with a moving shaft, translating inside a coil.

The aeroelastic torque M_{0z} is about pivot O. Along-wind turbulence $\hat{u} = u/U$ is Gaussian and included in M_{0z} as a Wiener process (Itô, 1951). Eq. (2) is transformed to Itô-type equation:

$$\mathrm{d}\mathbf{W}_{\mathrm{em}} = \mathbf{q}_{\mathrm{em,NL}}(\mathbf{W}_{\mathrm{em}})\,\mathrm{d}\tau + \sqrt{2\pi}\left[\mathbf{t}_{\mathrm{NL},\hat{u}}(\mathbf{W}_{\mathrm{em}})\,\mathrm{d}B_{\hat{u}}(\tau) + \mathbf{Q}_{\mathrm{L},\Delta 2}\mathbf{W}_{\mathrm{em}}\mathrm{d}B_{\Delta 2}(\tau)\right] \tag{4}$$

In Eq. (4), $\mathbf{W}_{\mathtt{em}} = [\alpha, \mathrm{d}\alpha/\mathrm{d}\tau, \nu_{ae,1}, \nu_{ae,2}, \mu_{ae,1}, \mu_{ae,2}, \imath]^T$ is the state vector; $\mathbf{W}_{\mathtt{em}}$ includes both physical, aeroelastic states $\nu_{ae,1}, \nu_{ae,2}, \mu_{ae,1}, \mu_{ae,2}$ and dimensionless output current $\imath$. In Eq. (4), the scalar, Wiener noise $B_{\hat{u}}(\tau)$ separately addresses turbulence perturbation from the noise $B_{\Delta 2}(\tau)$, used for torque and load perturbation. Quantity $\mathbf{q}_{\mathtt{em,NL}}$ is a nonlinear vector-function; $\mathbf{t}_{\mathtt{NL},\hat{u}}$ is a nonlinear turbulence diffusion vector-function. $\mathbf{Q}_{\mathtt{L},\Delta 2}$ is a constant, diffusion matrix that controls load perturbation and depends on the standard deviation of torque load error, σ_{d2}.

Eq. (4) is resolved in weak form by numerical integration (Kloeden et al., 1994) and by collecting samples of $\mathbf{W}_{\mathtt{em}}(\tau)$ over time with appropriate initial conditions, imposed on the probability distribution of $\mathbf{W}_{\mathtt{em}}$ at $\tau = 0$. Monte Carlo sampling and Euler method are used to approximate the second moment Lyapunov exponents (Xie, 2005) of a suitable sub-vector of $\mathbf{W}_{\mathtt{em}}$. Moment Lyapunov exponents can detect unstable and post-critical conditions, i.e., limit-cycle flapping (Caracoglia, 2024). Because of Eq. (5), the post-critical, output power is a random process. The output power expectation at sustained flapping is (Caracoglia, 2024):

$$\mathbb{E}\left[\mathrm{P}_{\mathtt{out}}(\tau)\right] = \omega_\alpha^3 \Psi I_{0\alpha} \mathbb{E}\left[\imath^2(\tau)\right], \tag{5}$$

with $\Psi = 4b^2(\Phi_{(\mathtt{e.m.c.})})^2/(\omega_\alpha I_{0\alpha} R_C)$; R_C is the resistance of the power circuit and $\mathbb{E}\left[\imath^2(\tau)\right]$ is the variance of $\imath$.

3. INCIPIENT FLUTTER AND POST-CRITICAL FLAPPING RESULTS

Fig. 2 illustrates the incipient flutter solution for the linear system without structural damping. The panels emphasize the role of the augmented moment arm.

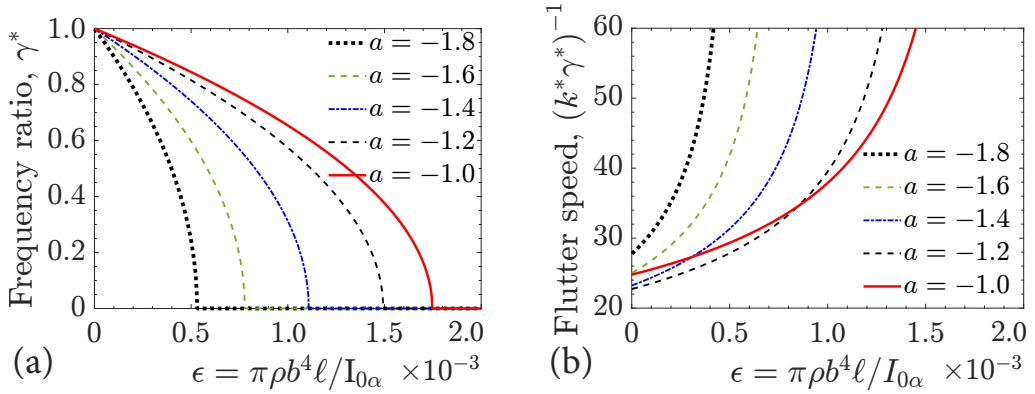

Figure 2. Incipient flutter: (a) critical reduced freq. k^* and (b) dimensionless flutter speed $U_r^* = (k^*\gamma^*)^{-1}$ *vs.* ε

In Fig. 2a, Eq. (1a) is solved as a function of parameter a; in Fig. 2b the dimensionless flutter speed $U_r^* = (k^*\gamma^*)^{-1}$ is presented. This figure extends previous results by Caracoglia (2018) to the range $-1.8 \leq a \leq -1.0$. The operational range of the harvester is indicated in Fig. 2a for $\gamma^* > 0$ only, where the solution exists because Eq. (1a) is strictly positive; the range of ε corresponding to $\gamma^* > 0$ reduces as the moment arms increases.

This remark suggests that the tuning of the harvester at $a < -1.0$ is more difficult. In Fig. 2b, if the graph found for $a = -1$ is used as reference (thick continuous line), the critical flutter speed $U_r^* = (k^*\gamma^*)^{-1}$ is 13% lower for a pivot with $a = -1.2$ for $\varepsilon < 10^{-3}$, and 9% lower for a pivot with $a = -1.2$ and $\varepsilon < 2 \times 10^{-4}$. Since operational conditions at lower wind speeds are possible, post-critical flutter should be more carefully examined, for $a = -1.2$ and $a = -1.4$, in this range of ε. By contrast, the moment arm positions with $a = -1.8$ and $a = -1.6$ yield larger values of U_r^* and should be avoided.

Fig. 3 depicts an example of output power analysis vs. time. Simulations examine the standard apparatus with pivot axis at the apex ($a = -1$), AR $= 4$ and $\Psi = 0.01$. Three "Types" ["Ty."=Type] are selected from Caracoglia (2018).

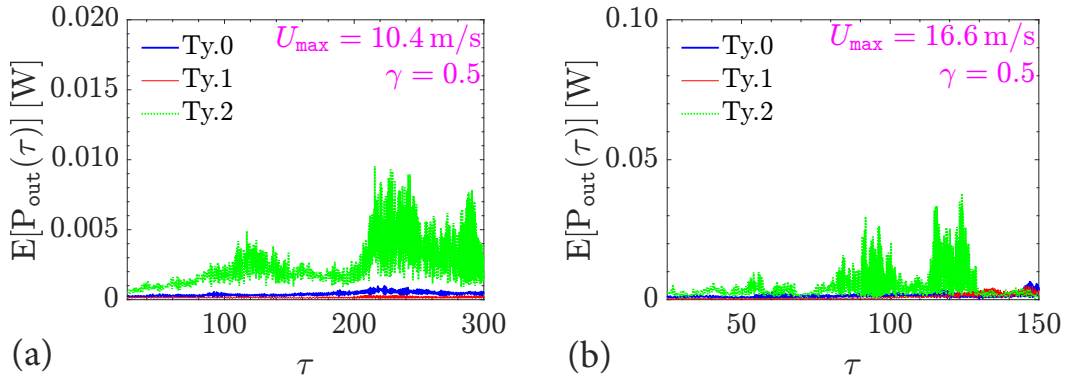

Figure 3. Output power $\{\mathbb{E}[P_{out}(\tau)]\}$ of a Duffing – van-der-Pol hybrid model harvester with $\gamma = 0.5$, $\kappa = 100$, subject to stationary gusty wind (turbulence intensity 10%) and mean speed $U = 10.4$ m/s (a), $U = 16.6$ m/s (b).

Eq. (2) is considered along with Duffing – van-der-Pol nonlinear model and H_{NL} with restoring torque $\kappa = 100$ and damping parameter $\gamma = 0.5$. Eq. (5) is examined during pre-critical (Fig. 3a) and post-critical (Fig. 3b) vibrations in gusty winds.

4. CONCLUSIONS

The conference presentation will introduce the most recent research results, examine additional post-critical flutter cases, quantify the output power by Eq. (5) as a function of pivot position and for augmented moment arm with $a = -1.2$ and $a = -1.4$.

ACKNOWLEDGEMENTS

This work was supported in part by the National Science Foundation (NSF) of the USA, Award CMMI-2020063. Any conclusions and recommendations are those of the author and do not necessarily reflect the views of the NSF.

REFERENCES

Argentina, M. and L. Mahadevan (2005). Fluid-flow-induced flutter of a flag. PNAS - Proc. Natl. Acad. Sci. USA 102, 1829–1834.

Caracoglia, L. (2018). Modeling the coupled electro-mechanical response of a torsional-flutter-based wind harvester with a focus on energy efficiency examination. J. Wind Eng. Ind. Aerodyn. 174, 437–450.

— (2023). Stochastic stability of a torsional-flutter energy harvester in thunderstorm-like winds: Duffing vs. Hybrid Duffing – van der Pol restoring force mechanisms. Proceedings of 2023 International Mechanical Engineering Conference & Exposition. [ASME Paper IMECE2023-116381].

— (2024). Stochastic performance of a torsional-flutter harvester in non-stationary, turbulent thunderstorm outflows. J. Fluids Struct. 124, 104050.

Itô, K. (1951). On stochastic differential equations. Vol. 4. Memoirs of the American Mathematical Society. ISBN 978-0-8218-1204-4. American Mathematical Society, Providence, Rhode Island, USA.

Kloeden, P. E., E. Platen, and H. Schurz (1994). Numerical solution of stochastic differential equations through computer experiments. Springer-Verlag, Berlin-Heidelberg, Germany.

Kwon, S.-D., J. Park, and K. Law (2013). Electromagnetic energy harvester with repulsively stacked multilayer magnets for low frequency vibrations. Smart Mater. Struct. 22, 055007.

Matsumoto, M. (2013). Flutter and its application - flutter mode and ship navigation. J. Wind Eng. Ind. Aerodyn. 122, 10–20.

Roohi, R., R. Hosseini, and G. Ahmadi (2023). Parametric study of an H-section oscillatory wind energy converter. J. Ocean Eng., 113652.

Theodorsen, T. (1935). *General theory of aerodynamic instability and the mechanism of flutter*. Tech. rep. National Advisory Committee for Aeronautics, Washington, D.C., USA.

Xie, W.-C. (2005). Monte Carlo simulation of moment Lyapunov exponents. J. Appl. Mech. 72, 269–275.

IN-VENTO 2024
International Conference of the Italian Association for Wind Engineering
Pisa, September 8th – 11th, 2024

Understanding the role of porosity in vortex-shedding behaviour through URANS approaches

Marcello Catania[a], Stefano Negri[b], Giulia Pomaranzi[c], Alberto Zasso[d]

[a]*Politecnico di Milano, Milan, Lombardia, Italy, marcello.catania@polimi.it*
[b]*Politecnico di Milano, Milan, Lombardia, Italy, stefano.negri@polimi.it*
[c]*Politecnico di Milano, Milan, Lombardia, Italy, giulia.pomaranzi@polimi.it*
[d]*Politecnico di Milano, Milan, Lombardia, Italy, alberto.zasso@polimi.it*

SUMMARY:

Modelling porous elements in the Computational Fluid Dynamics (CFD) environment usually requires relying on a porous media model to address the multi-scale nature of the problem, due to the scale separation between openings' size and the overall dimension of the structure they are applied to. This study investigates the capability of the Darcy-Forchheimer porosity model in predicting the aerodynamics of a rectangular cylinder covered by a perforated metal, representative of a rectangular building with a Permeable Double Skin Façade (PDSF). Specifically, we focus on the vortex-shedding mechanism and how it is affected by the porous layer. Using Unsteady Reynolds Averaged Navier Stokes Equations (URANS), results are validated against experimental results from wind tunnel tests. Results show strong agreement in mean and oscillating pressure distributions, affirming the model's accuracy in capturing porosity effects. The study underscores CFD's potential for efficient wind load estimation and wind-induced oscillation analysis in porous-element environments.

Keywords: Porosity, Darcy-Forchheimer, Vortex Shedding, CFD, URANS, Wind Tunnel Testing, Double Skin Porous Façade

1. INTRODUCTION

Porous elements such as screens, shrouds, barriers, and louvers have become popular solutions in contemporary civil infrastructure. These passive wind mitigation devices find applications spanning from bridges to towers and buildings. They can be adopted as standalone windshields or, in case of a building, being integrated into façade systems, realizing the so-called Porous Double Skin Façade (PDSF). When considering the wind interaction with a building with a PDSF, it is expected that the air can bleed through the porous elements, affecting the aerodynamic profile of the underlying structure. This influences the pressure distribution over the building façade and may have an impact on the onset of dynamic phenomena like Vortex Shedding (VS) (Teimourian and Teimourian, 2021). A precise evaluation of the porosity's impact is then crucial for accurately estimating static and dynamic wind forces. This kind of problem is typically addressed through experimental approaches involving wind tunnel tests (WTTs) on scale models, where porous elements are not geometrically scaled, but reproduced with a permeable layer realizing the same pressure drop as the one expected for the full-scale elements.

Within the Computational Fluid Dynamics (CFD) environment, modelling porous elements by reproducing their geometry in the computational domain would incur a prohibitively high computational cost. This is due to the necessity of resolving turbulence scales ranging from a few millimetres to several meters, leading to a multi-scale problem. To overcome this, we can rely on implicit modelling of the porous medium characteristics, by introducing an equivalent sink term into the momentum balance equations within the porous region. Models such as the

Darcy-Forchheimer one characterize porosity using a set of three scalar numbers representing the medium's resistance in three spatial directions.

The application of porous media models to wind engineering applications offers few examples in existing literature (Pomaranzi et al., 2021; Xu et al., 2023, 2020). The present study investigates the capability of the Darcy-Forchheimer model to reproduce the unsteady aerodynamics, with a special focus on vortex shedding phenomenon, of a rectangular cylinder covered by a perforated metal. Once validated through a comparison with experimental data from wind tunnel tests, a deeper understanding of the extent the porous layer can affect the vortex-shedding mechanism is enabled.

2. METHODS

This study investigates the aerodynamic behaviour of a rectangular cylinder covered by a perforated metal through a set of unsteady CFD simulations. The latter are then compared to the experimental results from wind tunnel tests for validation. Specifically, the aerodynamic behaviour of the cylinder is first investigated without the presence of the porous layer, by looking at mean pressure coefficient distribution, lift force and the dimensionless vortex shedding frequency (Strouhal number). Subsequently, the analysis is repeated by introducing the presence of the perforated metal through a set of cells obeying the Darcy-Forchheimer model.

In the following, the experimental tests used for validation purposes are briefly described. Then, the numerical setup is introduced.

2.1. Experimental setup

The model is a $2\,m$ high rectangular cylinder with an aspect ratio of $B/D = 3.33$, representative of a high-rise building. The rigid prism is mounted on an elastic base designed to allow low-frequency mono-harmonic oscillations at $2\,Hz$ in the cross-wind direction with adjustable damping. The model is equipped with 4 accelerometers and 254 pressure taps distributed on the surface at 8 different levels to capture the temporal and spatial variations of the displacement and pressure field. For the validation of the CFD model, the configuration with the highest damping ratio is considered, being comparable to the rigid configuration with no motion of the structure. In addition, the pressure field in the middle floors is considered to limit the influence of end effects.

Figure 1. Comparison between the front view of the model without (naked) and with the mesh (PDSF).

Two distinct façade configurations have been implemented in the same model: the *naked* configuration, simulating single-glazed cladding, and the *PDSF* configuration, replicating a permeable double skin façade (Figure 1). The latter is achieved by integrating a perforated mesh with an open-to-total surface ratio of $\beta = 55\%$, positioned $20\,mm$ away from the solid façade. The

mesh utilized in this setup has a pressure loss coefficient, defined as the ratio of the pressure drop and the dynamic reference pressure, of $k = 1.8$. All tests were conducted in the atmospheric boundary layer section of Politecnico di Milano wind tunnel (GVPM) in smooth-flow conditions (turbulence intensity $Iu \approx 2\%$).

2.2. Numerical setup

The numerical simulations employed a 2D, unsteady Reynolds-averaged Navier-Stokes (URANS) approach with the two-equation $k-\Omega$ *SST* turbulence model. Second-order numerical schemes were utilized for result accuracy. Due to the relatively low air speed in the domain ($4.5\,m/s$), an assumption of flow incompressibility was made. The computational domain was discretized using the finite volume method in OpenFOAM, representing the prism as an extruded rectangle.

2.2.1. Porosity modeling

The porous mesh is simulated including a special region of cells around the structure (marked in red in Figure 2), matching the geometry of the WT model. An equivalent momentum loss is introduced with the Darcy-Forchheimer tensor, whose coefficients have been estimated from a set of simulations on the fully resolved geometry and from experimental data.

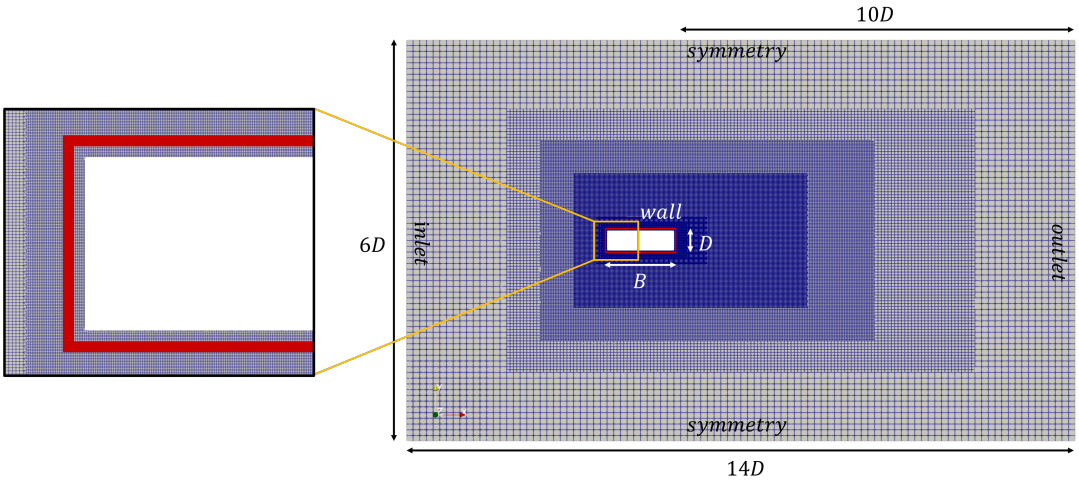

Figure 2. Sketch of the domain. The porous zone is marked in red.

3. RESULTS AND DISCUSSION

In vortex-shedding conditions, the model in the naked configuration experiences coherent vortex wake (Von-Karman wake), as depicted in Figure 3a. Figure 4a shows the power spectral density (PSD) of the lift force (F_y), showing a mono-harmonic signal with a peak at the Strouhal frequency. Compared to the experimental case, the CFD case captures this phenomenon with a slightly lower non-dimensional frequency.

With the application of the porous medium, the wake shape becomes more open, leading to a more homogeneous pressure distribution that impacts Vortex Shedding (VS) mechanism (Figure 3b). Figure 4b displays the correspondence between measured and simulated lift forces on the façade. Comparing the naked and PDSF configurations, the VS frequency decreases, and the forcing amplitude reduces by two orders of magnitude.

The full paper will provide a detailed analysis of pressure distribution on the façades, offering deeper insights into VS mechanics. Overall, strong agreement between experimental and

numerical results is observed for both configurations, with any discrepancies to be addressed.

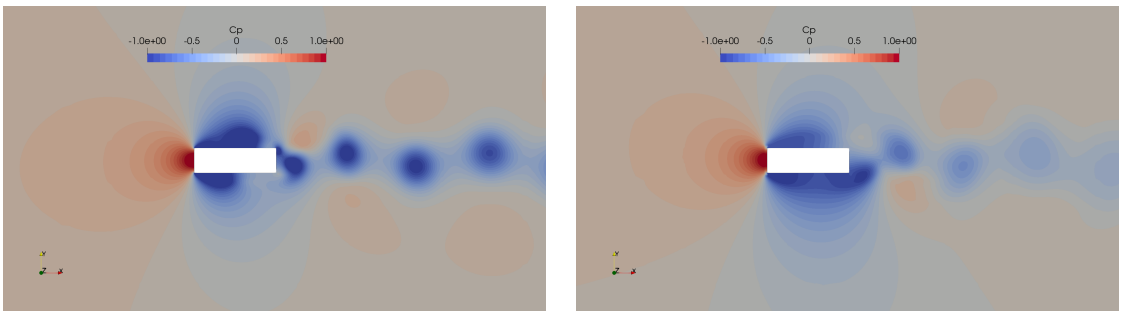

(a) Naked **(b)** PDSF

Figure 3. C_p distribution in steady-state vortex shedding condition in the naked and PDSF configurations.

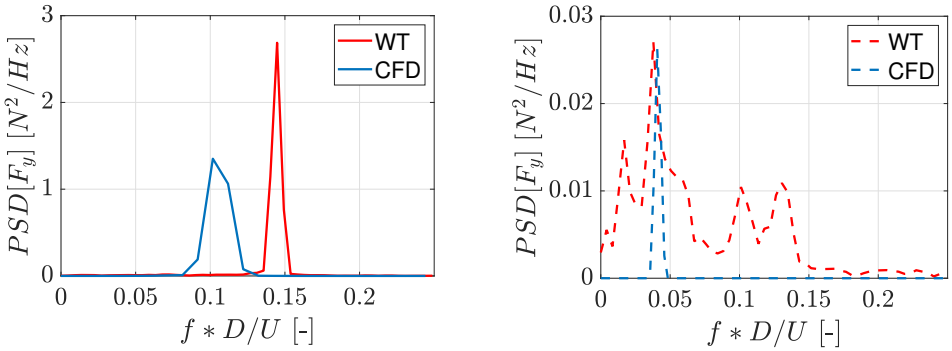

(a) Naked **(b)** PDSF

Figure 4. Comparison between WT (red curve) and CFD (blue curve) Power Spectral Density plot of the lift force (F_y) for the naked configuration (continuos curve) and the PDSF one (dashed curves).

4. CONCLUSIONS

This abstract presents the methodology adopted for the validation of the numerical representation of porosity employing the Darcy-Forchheimer model. A rectangular cylinder enveloped with a perforated mesh, resembling a high-rise building with a double-skin porous façade, serves as the benchmark. The results, comparing mean and oscillating pressure distribution and forcing components with wind tunnel measurements, highlight the potential of the porous media model in CFD in representing dynamic phenomena like vortex shedding. The validated numerical model offers insights into cladding estimation and wind-induced oscillation mitigation strategies for complex civil infrastructure.

REFERENCES

Pomaranzi, G., O. Bistoni, P. Schito, and A. Zasso (Nov. 2021). Numerical modelling of three-dimensional screens, treated as porous media. Wind and Structures 33, 409–422.

Teimourian, A. and H. Teimourian (2021). Vortex Shedding Suppression: A Review on Modified Bluff Bodies. Eng 2, 325–339.

Xu, M., L. Patruno, and S. de Miranda (2023). A pressure–velocity jump approach for the CFD modelling of permeable surfaces. Journal of Wind Engineering and Industrial Aerodynamics 233, 105317.

Xu, M., L. Patruno, Y.-L. Lo, and S. de Miranda (2020). On the use of the pressure jump approach for the simulation of separated external flows around porous structures:A forward facing step. Journal of Wind Engineering and Industrial Aerodynamics 207, 104377.

Towards Multi-Hazard approaches for structural design: extension of the "ADRS" method to wind engineering

Micol Ciabattoni [1], Francesco Petrini [1], Stefano Pampanin [1]

[1]*Sapienza University of Rome, Rome, Italy, francesco.petrini@uniroma1.it*

SUMMARY

This work focuses on the design trade-off aspects related to the structural behavior of mid-rise buildings subjected to the actions of wind and earthquake. A multi-hazard approach is developed and proposed, through the use of an efficient equivalent baseline reference to compare the structural performance under two independent whilst competing hazards. Following a capacity-vs-demand approach an Acceleration Displacement Response Spectrum (ADRS) domain, well established in the earthquake engineering environment, is suggested to be extended and adapted to wind design. The innovative procedure is developed and implemented with reference to two case study tall buildings, 18 storey and 36 storey high, respectively. Peak interstorey drifts are selected as seismic performance indicator, while peak floor accelerations are selected as wind performance indicator with the intent to focus on the building occupants' comfort serviceability limit state. The structural responses under the two actions are compared within the proposed innovative common baseline ADRS domain, allowing to establish the governing design hazard depending on the intensity levels and adopted return periods. Based on these developments, a true multi-hazard approach is proposed for the preliminary design phase of a building subjected to wind and earthquake loading.

Keywords: Multi-Hazard, Earthquake, Tall buildings

1. INTRODUCTION

Assessing the effects of the wind in the design of tall structures is crucial because, as the height of the building increases, the relevance of the effects induced by the wind increases as well (Boggs et al 2006). Usually, the main design issue for slender tall buildings under wind is related with the excessive wind-induced floor accelerations, that can cause discomfort to the building occupants. As a result, the Serviceability Limit State (SLS) performance criteria tend to govern the design when compared to those related to the Ultimate Limit State (ULS). The design guidelines "CNR-DT 207 R1/2018" (CNR 2018), published by the Italian National Research Council, provides a procedure to estimate the peak floor accelerations and their associated limit values not to be exceeded in order to ensure the comfort of the occupants of tall buildings. Moreover, when the fundamental frequency of the building falls in a range where the spectral magnitudes of wind and earthquake are comparable, a trade-off between design configurations as independently driven by the two hazards is necessary.

As specified in Petrini et al. 2020, when dealing with these type of structural design scenarios, there are a number of issues to be addressed in order to reach a true multi-hazard design. One of these issues concerns the so called "unified framework problem": different hazards should be treated by a common language and common frameworks to efficiently compare their effects in the analysis of the performances panorama. In this view, the performances of the different case-study structures under the two hazards are compared within the so-called ADRS (Acceleration Displacement Response Spectrum) domain, commonly used in earthquake engineering studies.

This allows to understand what hazard is dominant for the building performances on a case-by-case basis. The extension of the ADRS method to wind engineering problems is the second original contribution provided by this paper. The procedure is applied to two case study steel tall buildings, 18 storey and 36 storey high, respectively (Figure 1)

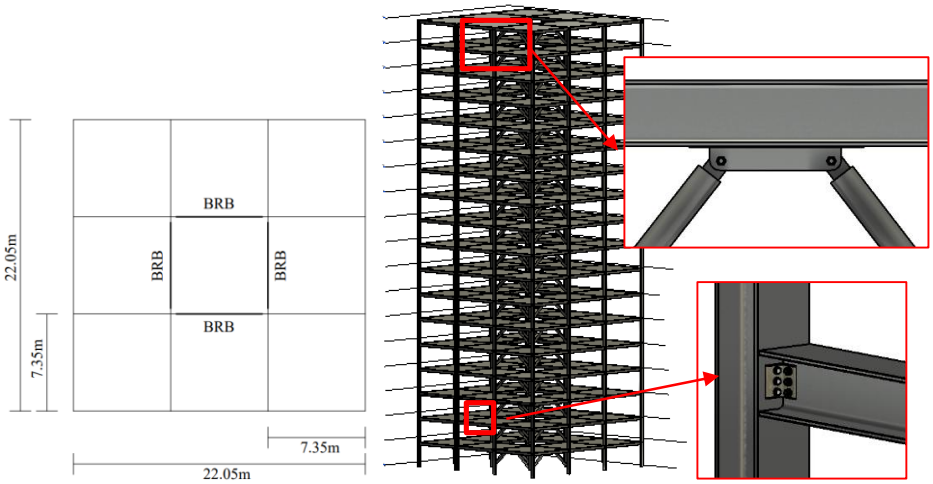

Figure 1. 18-storey case-study building with traditional bolted connection (the connections shown refer to the X and Y directions)

2. ADRS DOMAIN FOR WIND PERFORMANCE-BASED DESIGN

The ADRS domain, originally proposed as part of the Capacity Spectrum Method in the mid-1970s, has been widely adopted in literature to study the response of a structure under earthquakes Fajifar 1998). The ADRS curves are determined starting from the pseudo-acceleration elastic spectra according on the site, the nominal life and the class of the use of the building and the characteristics of the terrain. Starting from these spectra that provide the values of the pseudo-accelerations (Sa), as a function of the building period (T), the pseudo-displacements (Sd), are obtained using Equation (1):

$$S_d = \frac{S_a}{\frac{4\pi^2}{T^2}} g \tag{1}$$

in this paper the ADRS format is shown to be an effective way to compare the two actions under a common language/nomenclature, something that is crucial to obtain true MH design procedures. In case of wind ADRS, along-wind and across-wind accelerations are first obtained, with the simplified CNR procedure (CNR-DT 207 R1/2018) and are then divided by the gravity to obtain pseudo accelerations. Such accelerations are determined for several cases: buildings with the same geometry and the same structural scheme but having different values of the bulk density ρ_m (varying between 20 e 400 kg/m^3) are considered. The fundamental natural frequency n_i of the building in the direction "i" (with i=D or L) dependents from ρ_m according to the Equation (2)

$$n_i = \frac{1}{2\pi}\sqrt{\frac{K}{\rho_m \cdot V_{tot}}} \tag{2}$$

Where K is the stiffness of the case study building (evaluated as $K = (2 \cdot \pi)^2 \cdot \frac{m}{T}$), being "$m$" and "$T$" the modal mass and period of the considered mode, and V_{tot} is the total volume of the structure. Being the equation (1) valid for the base excitation case, cannot be applied in case of wind, then

the displacements have been determined by applying the equivalent static forces to the FE structural model of the building. The variation of the bulk density for the evaluation of the wind ADRS has been imposed by assigning a multiplication factor to the masses deriving from the non-structural loads. Depending on the bulk density value, the acceleration trend is determined by the CNR procedure as a function of the oscillation frequency of the structure obtained by Equation (2). High frequencies, low periods, high accelerations and high displacements correspond to low values of ρ_m. For the case-study building (double inertial symmetry in plan, then the first oscillation frequency is the same in the two orthogonal directions corresponding with the principal inertial axes of the floor, which also coincides with the along- and across- wind directions), it is assumed that the wind comes orthogonally to one of the building external vertical faces (most severe load conditions for across-wind building accelerations due to the occurring of the vortex shedding). The trend of the peak top floor pseudo accelerations and pseudo displacements with the building vibration period T are shown in Figure 2 and Figure 3 for the along and across wind directions respectively, and with reference to the 36-storey case, and by considering wind speed intensity corresponding to the specified return periods TR taken equal to 1, 10 or 100 years.

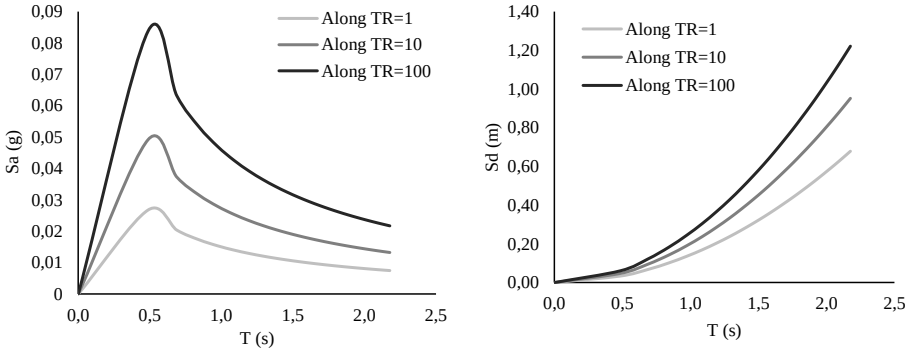

Figure 1. Along-wind direction: (left) trend of the peak top floor accelerations with the building vibration period; (right) trend of the peak top floor displacements with the building vibration period.

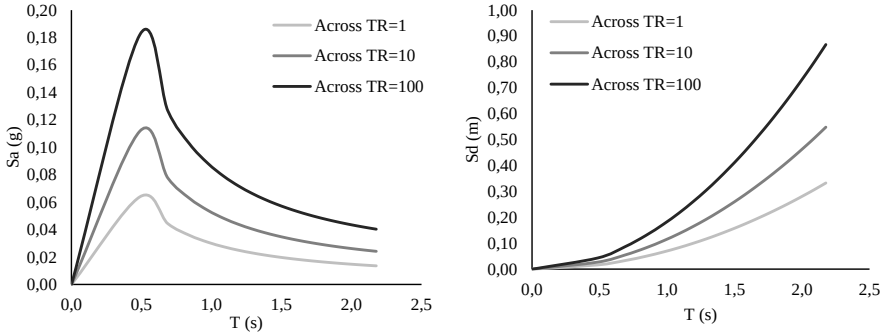

Figure 2. Across-wind direction: (left) trend of the peak top floor accelerations with the building vibration period; (right) trend of the peak top floor displacements with the building vibration period

3. MULTI-HAZARD PRELIMINARY DESIGN METHODOLOGY

The preliminary design of the buildings has been conducted by taking into account the two hazards individually. In a true multi-hazard view, the preliminary design phase should be conducted by considering simultaneously earthquake and wind. With this in mind, a methodology is proposed in this section to allow the multi-hazard preliminary design by using the ADRS method introduced in previous parts. Two limit values have been superimposed on the ADRS plane: the first is referred to the wind induced SLSs by checking the peak accelerations of the top floor, with a return period TR= 10 years; the second limit value is given by a drift limit linked to the ULS under

earthquake. The first value provides the initial stiffness that the structure should have so that the verification of habitability is respected, the second, instead, defines the target demand for ductility of the system. Thus, an ideal capacity curve has been obtained.
The case of the building of 36 floors made of steel is shown in Figure 4. Only the transverse component of the wind is represented because it is the most significant. By having this ideal capacity curve in the preliminary design phase, the target elastic stiffness and ductility are then defined by taking into account both wind and earthquake hazards.

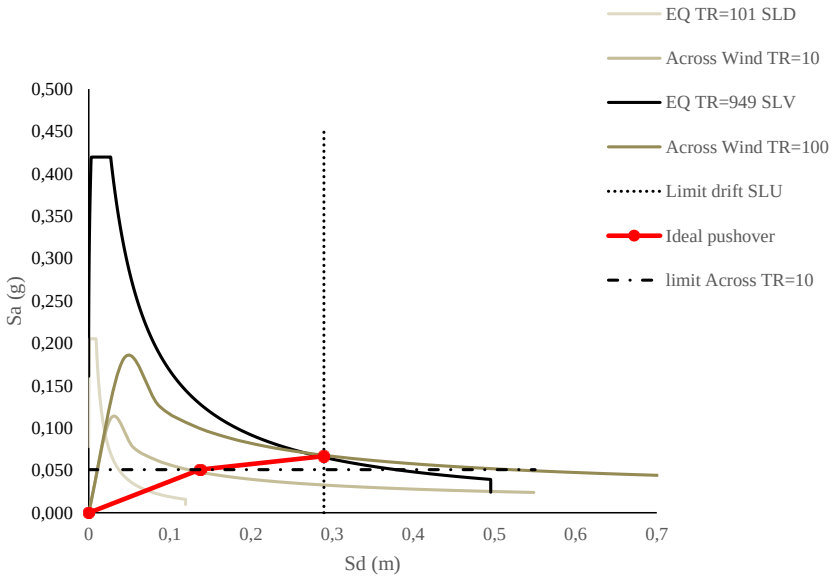

Figure 4. Ideal curve for building of 36 floors.

4. CONCLUSIONS

Iin a MH view, the actions of wind and earthquake have been compared in terms of structural masses and in terms of ADRS curves. The results showed that, as expected, the action of the wind becomes more and more important as the number of floors increases while, for the structures with hybrid connections, the preponderance of the wind on the earthquake attenuates. The comparison in terms of ADRS curves allowed to identify capacity an ideal curve for the building by introducing 2 limit values for the response parameters, each corresponding to a limit state. Specifically, the first is related to accelerations induced by wind and provides the initial stiffness that the structure must have in order to ensure comfort for the occupants, while the second is a drift limit associated to the ultimate limit state and affects the ductility demand and, in turns, the actual energy dissipation. The ideal capacity curve can be used to preliminary design the building in a true MH approach by considering both wind and earthquake.

REFERENCES

Boggs D, Dragovich J (2006). The Nature of Wind Loads and Dynamic Response. CPP online report SP-240—2. Available at https://www.cppwind.com/wp-content/uploads/2020/12/WindLoadsDynamicResponses-Boggs2006.pdf (accessed April, 9, 2021)

CNR- National Research Council of Italy, Guide for the assessment of wind actions and effects on structures CNR-DT 207 2008, Rome, June 2010. Available at: ww.cnr.it/en/node/2642 (accessed Sept , 9, 2023).

Fajfar, P. (1998). Capacity Spectrum Method Based on Inelastic Demand Spectra, Report EE-3/98, IKPIR, Ljubljana, Slovenia

Petrini, F., Gkoumas, K., Rossi, C. Bontempi, F. (2020). Multi-Hazard Assessment of Bridges in Case of Hazard Chain: State of Play and Application to Vehicle-Pier Collision Followed by Fire. Frontiers in Built Environment - Bridge Engineering, 15 September 2020.

IN-VENTO 2024
International Conference of the Italian Association for Wind Engineering
Pisa, September 8th – 11th, 2024

A comparative analysis of extreme wind speed statistics in Italy based on anemometer data, GWA and ERA5

Gonzalo Crespi[1], Giulia Pomaranzi[2], Gisella Tomasini[3], Stefano Giappino[4]

[1]*Politecnico di Milano, Milan, Department of mechanical engineering, Italy, gonzalo.crespi@polimi.it*
[2]*Politecnico di Milano, Milan, Department of mechanical engineering, Italy, giulia.pomaranzi@polimi.it*
[3]*Politecnico di Milano, Milan, Department of mechanical engineering, Italy, gisella.tomasini@polimi.it*
[4]*Politecnico di Milano, Milan Department of mechanical engineering, Italy, stefano.giappino@polimi.it*

SUMMARY
Accurate measurement of extreme wind speeds is crucial for various applications, including assessing aerodynamic loads in civil structures such as bridges, slender buildings, and stadiums. Additionally, it plays a significant role in the transport industry for the evaluation of the risk of overturning due to crosswinds. To conduct statistical analysis of wind data, long-term wind records are required. Anemometer data can be utilized for this purpose, if available; alternatively, reanalysis data such as the Global Wind Atlas (GWA) and ERA5 can provide long-term time series data. This study aims to compare wind speed statistics based on GWA and ERA5, with a specific focus on low-probability occurrence winds in Italy. The comparison is conducted across three different locations in Italy, by comparing Weibull distributions. It has been found that the agreement between the databases, especially at low probability occurrences, is significantly poor.

Keywords: ERA5 Land, GWA, validation, wind speed, extreme wind analysis

1. Introduction

Due to the stochastic nature of wind, an accurate assessment of wind, preferably relying on sufficiently long wind speed time series, is a fundamental prerequisite for the design of civil structures such as slender buildings, bridges, or stadiums, as well as for assessing the risk of overturning due to crosswind in the transport industry, such as along railway lines. Reanalysis data, which assimilate a large amount of historical observations into a numerical weather prediction model to accurately represent the state of the atmosphere, are increasingly being used as a source of long-term time series for wind energy assessment studies (Gualtieri, 2021). They provide an appealing alternative when measured observations are sparse or have limited temporal coverage.

ERA5 is the fifth generation and the most updated (2019) global reanalysis product developed by the European Centre for Medium-Range Weather Forecasts (ECMWF) within the Copernicus Climate Change Service (CDS). ERA5 has a 1 h time resolution, with a ~31 km horizontal grid spacing.

The present study aims to investigate the extent to which reanalysis databases can be trusted in driving a reliable assessment for civil and crosswind applications in the transport industry. We consider the database from Raffa et al. (2021), obtained by dynamically downscaling ERA5 reanalysis, from the original ~31 km grid to ~2.2 km resolution, and the Global Wind Atlas (GWA), developed by DTU (Davis et al., 2023). ERA5 reanalyses have been validated for wind

energy assessment by Murcia et al. (2022). However, these applications are more related to mean wind speed statistics rather than the low probability of occurrence wind events.
The analysis is carried out comparing these databases with data measured by three reference anemometers placed at the airports of Milan Malpensa, Florence, and Naples. Hourly time series of reanalysis data and anemometer measurements are processed based on a time period longer than 30 years.

2. METHODOLOGY

To properly compare the data, the databases should exhibit as much consistency as possible, including the same roughness length, altitude, and time interval. ERA5 downscaled data over Italy provides temporal coverage from 1989 to 2020, aligning with the period of anemometer measurements. The latter are downloaded from HadISD (Dunn, 2019), a global sub-daily dataset based on NOAA database (National Oceanic and Atmospheric Administration). Regarding the Global Wind Atlas (GWA), it does not directly offer wind measurement populations; instead, it outputs synthetic values based on a Weibull distribution, with a time coverage significantly lower with respect to ERA5, spanning from 2008 to 2017. Such distributions are available for different roughness conditions (z_0 = [0; 0,03; 0,10; 0,40; 1,50]m). For the experimental data, to ensure robust analysis, we opt for a 31-year period, increasing the likelihood of capturing rare wind events. We consider three different airports' anemometers across Italy: Milan Malpensa, Florence Peretola, and Naples Capodichino.
The characteristics of each database are summarized in Table 1.

Table 1. Characteristics of each database

Database	HadISD	ERA5 downscaled over Italy	GWA
Output	Population of wind measurements	Population of wind simulation	Weibull Parameters: scale and shape
Temporal Coverage	1989 - 2020	1989 - 2020	2008 - 2017
Roughness length	Local roughness	0,03 m	various
Resolution	N.A.	2,2 km	250 m

The applied methodology to compare the databases at the same reference conditions, namely z_0 = 0.03m and z = 10m, is summarized in the block diagram of Figure 1 and consists of the following steps:

1) The output from HadISD is a population of wind velocity measurements, defined in magnitude and direction. Starting from the NOAA data, HadISD includes a quality check on wind records, according to the procedure explained by Dunn (2019).
2) In order to ensure data consistency, we need to standardize the data to a roughness of 0.03m. This correction is carried out by evaluating the roughness around the anemometer within a radius of 10km, according to the method proposed by ESDU (ESDU, 2003). The roughness of the area is estimated using the Corine Land Cover database and the conversion table proposed by Silva et al. (2007). These correction factors are applied at a directional level, divided into 12 sectors of 30 degrees each, centered in the north direction.
3) All the data are standardized at the same reference conditions, (z_0 = 0.03m and z = 10m).
4) From the standardized population of both databases, a Weibull fitting is performed, enabling the comparison with GWA data with z_0 = 0.03m.
5) A comparison of the maximum wind speeds per year is conducted to assess the simulations'

ability to replicate annual occurrences. This analysis is relevant for further analysis to determine the 50- and 100-year return period winds, which are typically considered for the design of civil structures.

6) The low probability events are compared with a synthetic analysis of the Weibull parameters, considering exceedance probabilities of $10^{-6}, 10^{-7}, 10^{-8}$, which are pertinent to the assessment of crosswinds in rail vehicles and comfort in civil structures.

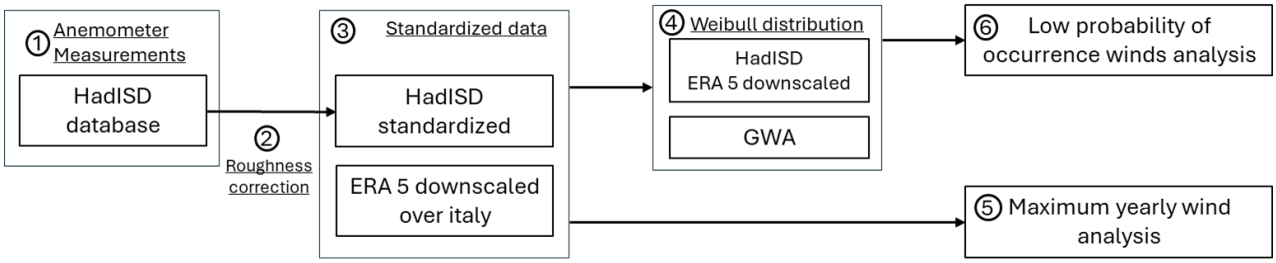

Figure 1. Block diagram of the methodology for the analysis

3. RESULTS

Transfer coefficients applied to experimental data to refer them to the same reference site are presented in Table 3.

Table 3. Transfer coefficients for the anemometric stations.

Anemometer	0°	30°	60°	90°	120°	150°	180°	210°	240°	270°	300°	330°
Milano Malpensa	0.94	1.10	1.16	1.09	1.04	1.09	1.21	1.10	1.08	1.08	1.02	1.00
Firenze Peretola	1.33	1.17	1.11	1.25	1.31	1.23	1.28	1.26	1.26	1.10	1.01	1.21
Napoli Capodichino	1.45	1.22	1.11	1.29	1.36	1.35	1.06	1.25	1.15	1.14	1.45	1.57

To estimate low probabilities values, data must be extrapolated from the left tail of the probability curves, as shown in Figure 3. It results that ERA5 provides, for all the locations here considered, smaller wind speeds at a given probability exceedance than the ones obtained from anemometers' data. Although the GWA database tends to align more closely with experimental measures, discrepancies exist also for this database, as presented in Table 4.

Table 4. Results of the Weibull analysis

Airport	Database	10^{-6}	10^{-7}	10^{-8}
Milano Malpensa	HadISD	28.5	34.3	40.4
	ERA5	14.7	16.3	17.8
	GWA	33.7	39.4	44.9
Florence	HadISD	23.6	26.4	29.2
	ERA5	15.8	17.5	19.0
	GWA	34.1	39.8	45.5
Naples	HadISD	25.8	28.9	32.0
	ERA5	12.1	13.2	14.3
	GWA	22.3	26.0	29.7

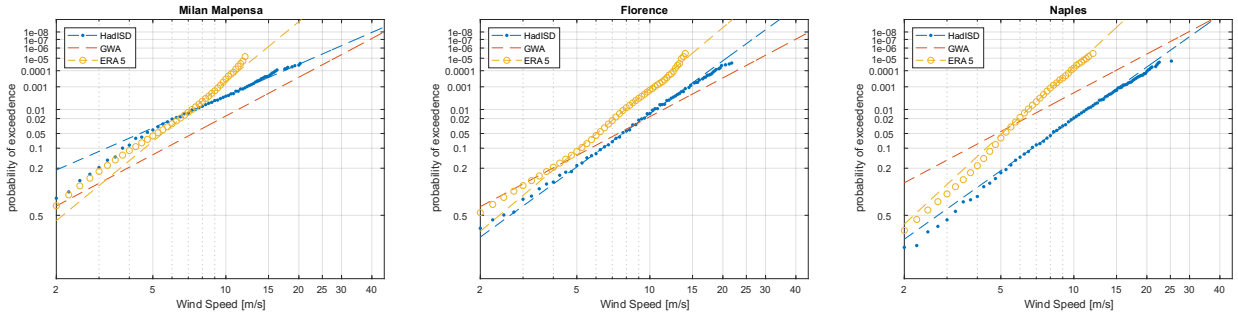

Figure 3. 10-minute wind speed at 10 m and $z_0 = 0{,}03m$

Finally, the comparison of the maximum wind speeds per year evaluated starting from ERA5 population and anemometers measurements is presented in Figure 4. If consistent, the points should align along the dashed line at 45 degrees. At all the locations, ERA5 maximum speeds are in the range of 14 m/s ± 2 m/s, smaller than the records obtained from experimental data.

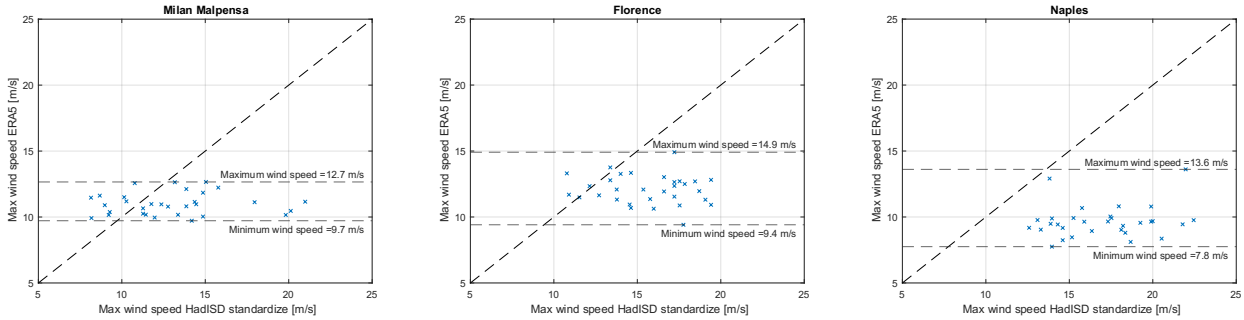

Figure 4. Maximum wind speed per year

4. CONCLUSIONS

This study provides a comparative analysis of extreme wind speed statistics in Italy, utilizing anemometer data, GWA, and ERA5 reanalysis. Discrepancies appear more important for ERA5 than GWA, that aligns more closely with experimental data. These results highlight that reanalysis database appear to be not suitable for applications related to extreme winds estimation.

REFERENCES

Davis, N. N., Badger, J., Hahmann, A. N., Hansen, B. O., Mortensen, N. G., Kelly, M., ... & Drummond, R. (2023). The Global Wind Atlas: A high-resolution dataset of climatologies and associated web-based application. Bulletin of the American Meteorological Society, 104(8), E1507-E1525. https://doi.org/10.1175/BAMS-D-21-0075.1

Dunn, R. J. H., (2019), HadISD version 3: monthly updates, Hadley Centre Technical Note

ESDU 82026 Strong winds in the atmospheric boundary layer. Part 1: hourly-mean wind speeds. (2003)

Gualtieri, G. (2021). "Reliability of ERA5 Reanalysis Data for Wind Resource Assessment: A Comparison against Tall Towers" Energies 14, no. 14: 4169. https://doi.org/10.3390/en14144169

Murcia, J. P., Koivisto, M. J., Luzia, G., Olsen, B. T., Hahmann, A. N., Sørensen, P. E., & Als, M. (2022). Validation of European-scale simulated wind speed and wind generation time series. Applied Energy, 305, 117794.

Silva, J., Ribeiro, C., & Guedes, R. (2007, May). Roughness length classification of Corine Land Cover classes. In Proceedings of the European wind energy conference, Milan, Italy (Vol. 710, p. 110).

Raffa, M.; Reder, A.; Marras, G.F.; Mancini, M.; Scipione, G.; Santini, M.; Mercogliano, (2021) Very High Resolution Dynamical Downscaling of ERA5 Reanalysis over Italy by COSMO-CLM. https://doi.org/10.3390/data6080088

IN-VENTO 2024
International Conference of the Italian Association for Wind Engineering
Pisa, September 8th – 11th, 2024

Characterization of the full turbulent spectrum of the flow in a small-scale wind tunnel using a multi-hole probe

Simon Dehareng[a], Thomas Gemine[b], Geoffroy Lumay[b], Thomas Andrianne[a]

[a]*Wind Tunnel Lab, University of Liège, Belgium*
[b]*GRASP Laboratory, University of Liège, Belgium*

SUMMARY:
The turbulence characteristics of the flow within a small-scale wind tunnel, specifically designed for studying the interaction between air flow and particles at low Reynolds numbers, were assessed using a multi-hole probe. The limited frequency range of the probe does not give direct access to the dissipative turbulence scales. For that purpose, Kolmogorov's (1941) theory was employed to extrapolate the inertial subrange. Preliminary results suggest a good applicability of Kolmogorov's theory in fitting turbulent spectra, allowing the estimation of dissipative scales. Further comparison with hot-wire anemometry is planned to validate the findings.

Keywords: wind tunnel, static grid, turbulence characteristics, cobra probe, hot-wire

1. INTRODUCTION

A small-scale low speed wind tunnel was built and its flow was characterized. This versatile wind tunnel will be used to study the interaction between air flow and particles in low Reynolds configuration, with applications such as pneumatic powder conveying, fluidized bed, drug powder inhalers, and more. These experiments will then be rescaled and reiterated at higher Reynolds, in the large-scale wind tunnel of the University of Liège. For that purpose, turbulence characteristics such as the integral length scale, L_u, Taylor length scale, λ_T, Kolmogorov scale, η, and dissipation rate, ε, were estimated using the multi-hole Cobra probe. One of the main objectives of this research is to determine whether the fitting of the Kolmogorov (1941a,b,c) phenomenology can be applied to a turbulence spectrum to determine its characteristics, even in cases where the frequency resolution is limited and does not cover the entire spectrum. As turbulence is an unsteady phenomenon, hot-wire and Cobra probes serve as instruments to study its characteristics with a certain accuracy. While hot-wire anemometry allows for high-frequency sampling, it entails complexity in setting up cross-wire probes to estimate turbulence anisotropy. On the other hand, Cobra probe enables measurement of all three velocity components, comes pre-calibrated, and ready for use but has a limited sampling frequency.

2. EXPERIMENTAL SETUP

The experimental setup consists in an open-loop small-scale 3D-printed wind tunnel. The test-section has dimensions of 0.068 m $\times$ 0.068 m $\times$ 0.4 m on height, width and length, respectively. This suction-type wind tunnel is powered by a DC axial compact fan, which can be throttled to achieve the desired velocity in the test-section. Figure 1a shows the experimental setup. For early experiments, the flow velocity U was adjusted to have a hydraulic diameter (D_h) based Reynolds number of $Re = UD_h/\nu \approx 44300$. The freestream turbulence (FST) in the clean section is around 0.4%. Turbulence spectra were measured with a Cobra probe from TFI at the centerline of the wind tunnel, at various sampling frequencies to determine the maximum frequency f_s for which the frequency response remained linear. The spectra remained acceptable

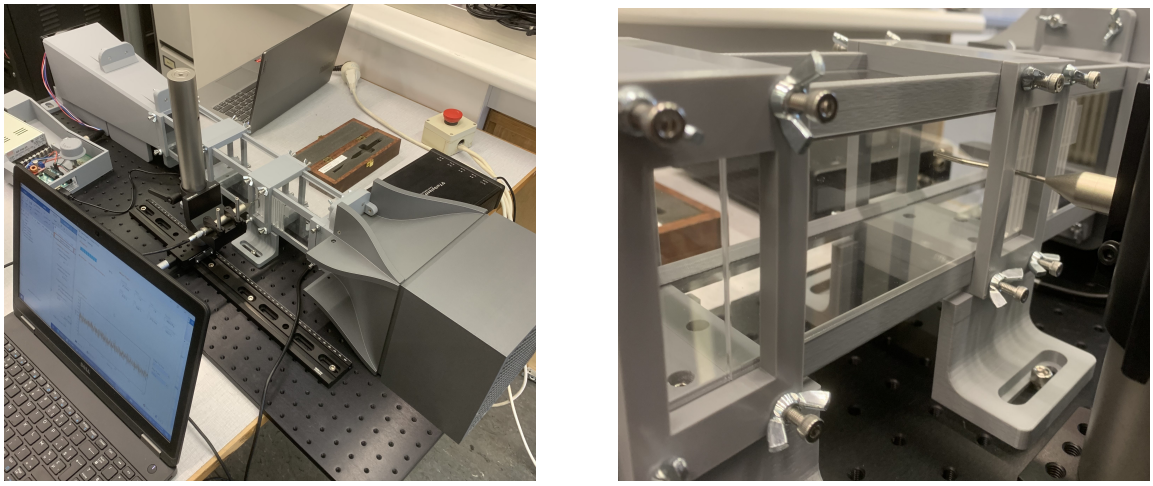

(a) (b)

Figure 1. (a) Full-view of the micro-WT. (b) Zoom on multi-hole Cobra probe inside the test-section.

up to a sampling frequency of 2800 Hz, which was chosen as the sampling frequency. The acquisition frequency f_a of the data acquisition system (DAQ) was set at 16 times the sampling frequency to reduce measurement noise, i.e., 44800 Hz. The probe was introduced into the test-section from the side to face the incoming wind on the centerline as shown in figure 1b. Data were collected for 60 seconds. Finally, FST was generated by setting different turbulence grids at the inlet of the test-section. Grids are denoted from A to E corresponding to an increase of the generated FST.

3. PRELIMINAR RESULTS

The resulting turbulence spectra obtained for the different grids are shown in figure 2a. Turbulence characteristics were computed from several estimation methods. For the integral length scale, autocorrelation-based methods were initially employed: integration up to the first zero crossing of the autocorrelation function $B_{uu} = \overline{u'(t)u'(t+\tau)}$ (O'Neill et al., 2004), and integration up to the first $1/e$ crossing of B_{uu} (Tritton, 1977). Then, L_u was computed via Roach (1987) estimation, which involves computing the range of frequency used to linearly extrapolate the value of the energy spectrum at 0 Hz. The exponential fitting of B_{uu} introduced by Hinze (1975) and Tritton (1977) was also used. Additionally, Voronoï tessellation-based zero-crossing method by Mora and Obligado (2020) was implemented. The last method involved a simple visual fitting of the von Karman spectrum with the obtained spectra.

The Taylor length scale is more sensitive to estimate because of the limited information at high frequency. Roach (1987), Pope (2000), and Mora and Obligado (2020) methods were initially implemented. But the resulting dissipative scales seemed too high. As shown in figure 2a, despite a well marked energy-containing range, there is a lack of information regarding the dissipation range. In addition, the inertial subrange does not fit correctly with $(\kappa\eta)^{-5/3}$, indicating some flow anisotropy due to the static grid, and/or that the frequency range may be too small to capture the entire transition from large-scale to small-scale turbulence. To overcome the frequency range limitation and to get an estimation of the dissipative scales, the spectra were fitted with the prediction of Kolmogorov's 1941 theory (K41) for isotropic and homogeneous turbulence (HIT) (Kolmogorov, 1941a,b,c)

$$E(\kappa) = C_\kappa \varepsilon^{2/3} (\kappa - \kappa_0)^{-5/3}, \tag{1}$$

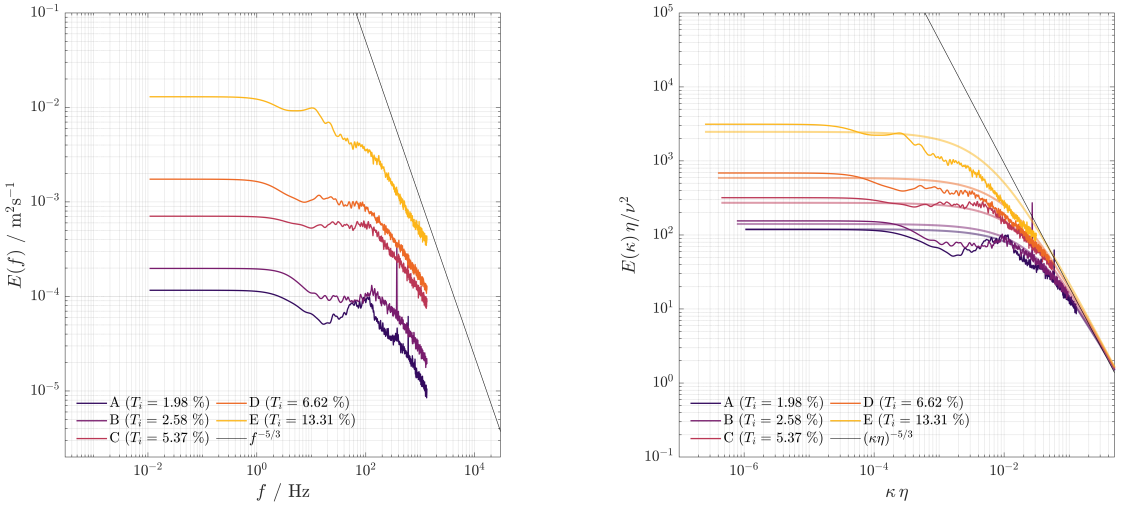

(a) **(b)**

Figure 2. Velocity spectra for all grid cases plotted in (a) dimensional frequency-space and (b) wavenumber-space normalized by dissipative scales (estimated through K41 estimation process). Plain lines represent the K41 fitting spectra.

where $\kappa = 2\pi f/\overline{u}$ is the wavenumber, κ_0 is an arbitrary constant, and C_κ is the Kolmogorov constant for local isotropic turbulence (Sreenivasan, 1995). The corresponding spectra are represented by plain lines in figure 2b. These fitted spectra give access to estimates of λ_T and η. It is planned to compare these Cobra measurements with hot-wire anemometry, which can capture higher-frequency eddies, to validate the extrapolation.

4. CONCLUSION

A small-scale wind tunnel was designed to study the interaction between air flow and particles in low Reynolds configuration, where the influence of freestream turbulence holds significant importance. It is essential to have a comprehensive understanding of the flow within the test-section itself. Therefore, the characterization of the section is conducted based on various methods for estimating fundamental turbulence parameters. The multi-hole Cobra probe is suitable for a specific range of velocities and limited to a certain sampling frequency. For this reason, it is unable to capture the smallest eddies characterized by high frequencies in the flow. For that purpose, Kolmogorov's phenomenology (K41) is employed due to its apparent robustness. To verify the validity of this method within the scope of this small wind tunnel, the results obtained with the Cobra probe will be compared with hot-wire anemometry. Finally, the homogeneity of the flow will be assessed for different velocities, incoming FST, and streamwise sections.

REFERENCES

Hinze, J. (1975). Turbulence. McGraw-Hill classic textbook reissue. McGraw-Hill.

Kolmogorov, A. N. (1941a). Dissipation of Energy in the Locally Isotropic Turbulence. Dokl. Akad. Nauk SSSR 32.

— (1941b). On degeneration of isotropic turbulence in an incompressible viscous liquid. Dokl. Akad. Nauk SSSR 31.

— (1941c). The Local Structure of Turbulence in Incompressible Viscous Fluid for Very Large Reynolds Numbers. Dokl. Akad. Nauk SSSR 30.

Mora, D. O. and M. Obligado (2020). Estimating the integral length scale on turbulent flows from the zero crossings of the longitudinal velocity fluctuation. Experiments in Fluids 61, 82–92.

O'Neill, P., D. Nicolaides, D. Honnery, and J. Soria (2004). Autocorrelation Functions and the Determination of Integral Length with Reference to Experimental and Numerical Data. 15th Australasian fluid mechanics conference 1, 1–4.

Pope, S. B. (2000). Turbulent Flows. Cambridge University Press.

Roach, P. (1987). The generation of nearly isotropic turbulence by means of grids. International Journal of Heat and Fluid Flow 8, 82–92.

Sreenivasan, K. R. (1995). On the universality of the Kolmogorov constant. Physics of Fluids 7, 2778–2784.

Tritton, D. J. (1977). Physical Fluid Dynamics. 1st ed. Springer Dordrecht.

Wind tunnel testing on the high rotational urban Savonius turbine

Krzysztof Doerffer[1], Piotr Doerffer [1], Joanna Grzelak[1], Józef Kotus[1], Abdelgalil Eltayesh[2], Luisa Pagnini [2], Giuseppe Piccardo [2], Maria Pia Repetto [2]

[1]*Gdansk University of Technology, Gdansk, Poland, Email: krzysztof.doerffer@pg.edu.pl, piotr.doerffer@pg.edu.pl, joanna.grzelak@pg.edu.pl, joseph@sound.eti.pg.gda.pl*
[2]*DICCA, University of Genoa, Genoa, Italy, Email: abdelgalil.eltayesh@edu.unige.it, luisa.pagnini@unige.it, giuseppe.piccardo@unige.it, maria.pia.repetto@unige.it*

SUMMARY
This study presents the outcomes of an experimental activity conducted as part of the European Project ERIES (Engineering Research Infrastructures for European Synergies) at the Giovanni Solari Wind Tunnel of the University of Genoa. The investigation is a pivotal component of the THRUST project, led by researchers from the Gdansk University of Technology, focusing on the performance assessment of a Savonius rotor engineered to operate efficiently across a wide range of wind speeds. Specifically designed to withstand high rotational speeds and turbulent conditions, this rotor undergoes thorough evaluation within the project. The research effectively demonstrates the rotor's resilience to intense rotations, making it suitable for deployment in high-wind areas without the need for a braking system. Of particular interest is the investigation into noise generation at high rotational speeds, an aspect that remains poorly understood in the current literature.

Keywords: Savonius rotor, wind tunnel tests, small size wind turbines

1. INTRODUCTION

Small size wind turbines are becoming a very popular topic when dealing with renewable energy and smart cities (Pagnini et al., 2015). Unfortunately, during the operating conditions, they may undergo to severe vibrations induced by gusty wind, turbulence and by sudden stops of the machine. These phenomena, besides having a detrimental effect on the energy production, can lead to damages and even collapses that have the effect of undermining the distributed wind production market. In this context, the simplified maintenance requirements of Savonius rotors offer a great advantage that sustains their appeal in the market for small size installations and makes them ideal for meeting the wind power needs of prosumers.

One of the key advantages of Savonius rotors is their self-restraining ability, which allows for operation without the need for braking systems. This is due to a unique feature: as rotational speed increases, the power produced decreases. This phenomenon occurs naturally, with power output reaching zero at a certain rotational speed (for a tip speed ratio, TSR, of approximately 2).

The proposed research considers a small diameter Savonius rotor wind turbine that is specifically engineered to withstand high rotational wind speed without being provided by any braking system. During very high wind speeds, while other types of wind turbines must be stopped, this Savonius rotor is still operating. In this condition, it supplies limited power, but allows producing energy

without excessive concern for very high rotational speed. Given the distinctive behavior in extremely high winds and high TSR power generation, which have not been thoroughly investigated to date, there is a pressing need for detailed measurements at high wind speeds and under various turbulence conditions, including the essential measurement of rotor noise at high rotor speed of rotation (RPM).

The Giovanni Solari Wind Tunnel at the University of Genoa is equipped to address the specific research questions at hand. Its state-of-the-art design, precise instrumentation, and adaptable configuration offer an ideal environment for conducting in-depth investigations into various aerodynamic phenomena. On the other hand, experimental investigation of the rotor in a wind tunnel, particularly within a closed test section such as in Genoa, necessitates consideration of the blockage effect. Typically, blockage correction for Savonius rotors involves accounting for solid object blockage and wake blockage effects (blockage factor). Assessing these factors can be challenging, as Savonius rotors are influenced by the unsteady nature of the model rotation.

2. CASE STUDY AND WIND TUNNEL SETUP

The experimental tests were carried out at the “Giovanni Solari” atmospheric boundary layer wind tunnel of the University of Genoa. It is a closed-circuit type operating at atmospheric pressure; the working section is 8.8 m long, with a cross-section of 1.70 (width) ×1.35 (height) m. The model under investigation consists of a steel Savonius rotor, with a diameter of 0.25 m and a height of 1.0 m, serving as a representative segment of an actual prototype wind turbine. The model is equipped with a torque meter, and incorporates essential components such as a 3-phase PMG generator (inner rotor type), a Hall sensor, and a AC/DC current transducer that can be connected to NI PXI wind tunnel system to measure current parameters and RPM. A dedicated terminal block facilitates the acquisition of current and amperage data. Furthermore, the current transducer communicates with a resistor module capable of applying appropriate loads to the wind turbine.

Tests were conducted under both smooth and turbulence flow conditions. Flow velocities were varied within a range of 3 m/s to 21 m/s, while the rotor’s RPM was explored up to 2500. This comprehensive approach allowed for a thorough examination of the rotor's performance across a wide spectrum of operational scenarios. Turbulent flow conditions with intensities of about 4% and 8% in the longitudinal direction were achieved by employing wooden static grids positioned upstream of the model. For each test, the load on the rotor was varied, measuring wind velocity, temperature, torque, voltage, current, rotational speed, upstream and downstream flow velocity using hot-wire anemometers. Moreover, to establish the baseline noise levels within the wind tunnel, measurements were conducted by microphones in different positions and under various conditions. These included the wind tunnel with the rotor halted, with the rotor removed but the mounting supports in place, and with the tunnel completely empty.

Fig. 1a illustrates the steel rotor, a pivotal component of the experiment; Fig. 1b provides a glimpse into the wind tunnel, showcasing the model's placement and the utilization of hot-wire anemometers to capture airflow dynamics; Fig. 1c highlights the wooden grid positioned upstream, strategically employed to induce turbulent flows essential for the study.

a) b) c)

Figure 1. Savonius rotor (a), model in the wind tunnel with the generator and hot-wire anemometers (b); the wooden grid for turbulence generation (c)

3. PRELIMINARY RESULTS

An example of measurements for the wind tunnel inlet velocity v= 12.3 m/s under smooth flow conditions is illustrated in Fig. 2. The Reynolds number is calculated as Re = 3.9×10^4 based on these conditions. The measured data points establish the relationship between extracted power, in [W], and the corresponding RPM indicated by point markers labelled as 'measures'. Additionally, the reference Savonius power characteristic curve, as outlined by Blackwell et al. (1977) assuming a rotor effectiveness of 24%, is depicted in the figure as 'characteristic 12.3 m/s'.

Considering that the model frontal area is 0.25 m^2 and the wind tunnel cross section is 2.45 m^2, the ratio of these surfaces yields a blockage ratio of S/C= 10.2 %. By applying corrections, it becomes possible to determine the actual wind speed at which the rotor is tested. Following the approach of Pope and Harper (1966) as used by Blackwell et al. (1977), the power curve is corrected according to the curve labeled ‘Pope correction’ in Fig. 2. Following Maskell (1965), the corrected curve (as per Ross and Altman, 2011) is represented by the label ‘Maskell correction’ in the figure.

The corrected characteristic curve reveals a higher power output than what would be expected from the rotor at the wind tunnel's inlet velocity. The application of the Maskell correction results in significantly higher Savonius rotor characteristics. Specifically, it supplies power approximately 25% larger than obtained with the Pope’s correction, consistent with information documented in existing literature.

The characteristic curve adjusted using the Pope correction demonstrates a remarkable alignment with the measured data. In Fig. 2, the measurement points closely follow the rotor characteristics

at low RPM, until reaching the maximum power. However, as RPM values exceed the maximum power threshold, particularly at high rotational speeds (RPM > 1200), a decrease in power production is noticeable compared to free wind conditions. This discrepancy may signify a characteristic trait of Savonius wind turbine blockage within the close test section configuration. Utilizing CFD simulations can offer valuable insights into investigating this phenomenon further.

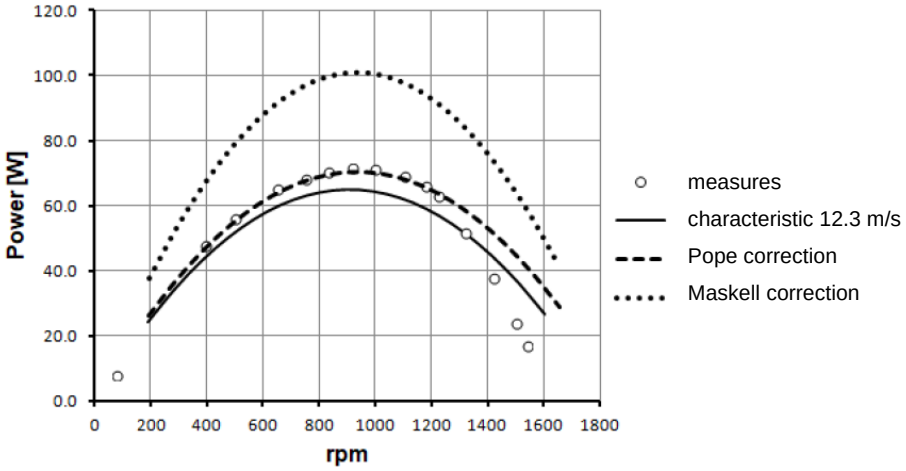

Figure 2. Power curve for the Savonius rotor at wind tunnel wind speed v=12.3 m/s in smooth flow conditions

4. FINAL REMARKS

Wind tunnel tests were carried out to investigate a Savonius rotor over a wide range of wind velocities and different turbulence conditions of the flow, supplying power curves for each wind velocity investigated. The experimental campaign effectively verified the rotor's capability to endure these intense rotations, thereby facilitating the deployment of the proposed Savonius rotor in high-wind locations without the need for excessive concern about extreme wind conditions and without requiring any braking system. This innovative design allows for continuous energy generation, even when other types of wind turbines would need to be stopped and secured.

ACKNOWLEDGEMENTS

This work is supported by the Engineering Research Infrastructures for European Synergies (ERIES) project (www.eries.eu), which has received funding from the European Union's Horizon Europe Framework Programme under Grant Agreement No. 101058684. This is ERIES publication number C18.

REFERENCES

Blackwell B.F., R.E. Sheldahl, and L.V. Feltz (1977). Wind tunnel performance data for two and three-bucket Savonius rotors. Sandia Lab Rep 1977. SAND 76-0131, 1–105.

Maskell E.C. (1965). A theory of the blockage effects on bluff bodies and stalled wings in a closed wind tunnel. ARCR and M3400.

Pagnini L.C., M. Burlando, and M.P. Repetto (2015). Experimental power curve of small-size wind turbines in turbulent urban environment. Applied Energy 154,112–21.

Pope A. and J.J. Harper (1966). Low speed wind tunnel testing. John Wiley & Sons, New York, USA.

Ross I., and A. Altman (2011). Wind tunnel blockage corrections: Review and application to Savonius vertical-axis wind turbines. Journal of Wind Engineering and Industrial Aerodynamics 99, 523–538

IN-VENTO 2024
International Conference of the Italian Association for Wind Engineering
Pisa, September 8th – 11th, 2024

Wind loading on ground-mounted solar PV structures: Comparison with Eurocode

Francesco Dorigatti [1], Matthew T.L. Browne [2], Zachary J. Taylor [3]

[1]*Rowan, Williams, Davies & Irwin (RWDI), Milan, Italy, francesco.dorigatti@rwdi.com*
[2]*Rowan, Willaims, Davies & Irwin (RWDI), Guelph, Canada, matthew.browne@rwdi.com*
[3]*Rowan, Willaims, Davies & Irwin (RWDI), Guelph, Canada, zachary.taylor@rwdi.com*

SUMMARY
The deployment of solar photovoltaics (PV) around the world continues to increase as it is an attractive source of renewable energy. The sheer size of the arrays of solar panels has led to them being properly referred to as utility scale plants. These large utility scale arrays represent significant financial investment implying the importance to stakeholders as well as to the general public that rely on the energy produced. Therefore, reliability of these structures is of obvious importance. The forces of the natural environment must be resisted by these structures with one of the most significant natural forces being the potential for high wind loads. The standard of practice in the industry continues to evolve and provisions are being incorporated into various codes and standards for the proper wind design of these solar PV structures. The current study compares wind tunnel data and provisions in ASCE 7 with the available provisions in the Eurocode. It is expected that this type of comparison will lead to increased reliability for the wind design of solar PV structures in Europe and elsewhere.

Keywords: wind tunnel testing, Eurocode, ASCE 7

1. INTRODUCTION

Both fixed-tilt systems and single-axis ground-mounted solar trackers are increasingly being deployed at utility scales for power production. These sites range in power production capacity from 1 MW to greater than 2 GW. There is a significant amount of financial investment in the power production of these arrays, which carries with it a strong desire for reliability. Therefore, the attention to the accurate determination of the wind loading on these solar PV structures continues to increase with their deployment around the world.

Building codes and standards were not developed to predict wind responses of small flexible structures near the ground, with the historical focus being on large low-rise and high-rise buildings. Therefore, design methodologies have had to be developed for solar PV structures (Browne et al., 2020). The methodology and dataset proposed by Browne et al. (2020) was adopted by the ASCE 7 standard in the 2022 edition (ASCE/SEI, 2022). There are also provisions for wind loading on ground-mounted solar PV structures in the Australian/New Zealand Standard (AS/NZS, 2021), which was informed by the work of Ginger et al. (2019). Both the American and Australian/New Zealand standards have recognized the need for specific design guidance for the wind loads on these solar PV structures. However, neither the National Building Code of Canada nor the Eurocode have adopted similar provisions for ground-mounted solar. The lack of specific provisions requires manufacturers to invest in system-specific wind tunnel

research. However, this approach may not be economically viable for small-sized projects and leaves designers to rely on the coefficients provided for '*monoslope free roofs*' and/or '*monopitch canopy roofs*'. The focus of the current study will be to present a comparison between a Eurocode approach to the design of ground-mounted solar PV structures with both wind tunnel data and the guidelines from ASCE 7.

2. BACKGROUND

When carrying out a wind tunnel test, the peak pressure is estimated from the time series and converted to a peak pressure coefficient normalized to the mean speed at nominal panel height as follows.

$$\widehat{C_{p}}_{WT} = \frac{\hat{p}_{WT}}{\frac{1}{2}\rho\overline{U}^2} = \frac{\hat{p}_{WT}}{\overline{q}_{WT}} \tag{1}$$

These results are then converted to a wind load through establishing the appropriate mean reference pressure, $\overline{q}$. This process is not always straightforward since each regional code or standard has different approaches to codifying extreme wind speeds, effects of wind directionality, and overall reliability. All codes and standards around the world employ the concept of quasi-steady theory to derive the design wind loads. In its simplest form, the quasi-steady theory for wind loading is given by:

$$\hat{p} = \hat{q}\overline{C}_p \tag{2}$$

which relates the peak pressure to the peak velocity pressure. The peak velocity pressure occurs due to fluctuations in the turbulent flow, which have been shown to be Gaussian in both wind tunnel and full-scale field data. This quasi-steady theory approach is well suited to code applications since the effects of different exposures can be directly accounted for in $\hat{q}$ without providing different aerodynamic coefficients. However, the validity of quasi-steady theory should not to be taken for granted and the potential shortfalls in ground-mounted solar PV structures is the focus of the current study. The quasi-steady implementation in Eurocode (EN, 2010) provisions relates the mean pressure coefficients c_p to the peak pressures, $\hat{p}_{EN}$, as follows:

$$\hat{p}_{EN} = \left(1 + 7 \cdot I_v(z)\right) \cdot \frac{1}{2} \cdot \rho \cdot v_m^2(z) \cdot c_p = c_e(z) \cdot q_b \cdot c_p \tag{3}$$

$$\overline{q}_{EN} = \frac{1}{2}\rho\left(\frac{v_m(z)}{1.065}\right)^2 \tag{4}$$

$$\widehat{C_{p}}_{EN} = \left(1 + 7 \cdot \left(\frac{1}{\ln\left(\frac{z}{z_0}\right)}\right)\right) \cdot 1.065^2 \cdot c_p \tag{5}$$

The relationship between a 10-minute mean wind speed v_m and the mean-hourly wind dynamic pressure $\overline{q}_{EN}$ in open terrain (i.e., terrain category II) is applied in Eq. (4) as estimated from Durst (1960) at 10 m elevation. The peak pressure coefficient normalized by the mean-hourly reference dynamic pressure $\widehat{C_{p}}_{EN}$ is then given by Eq.

(5). The ASCE 7 provisions (ASCE/SEI, 2022) summarized in Eq. (6) differ from the Eurocode provisions in the use of a 3-second gust wind speed V in contrast to the 10-minute mean speed. Furthermore, the relationship in Eq. (7) is directly given to convert a 3-second gust speed to a mean-hourly reference wind dynamic pressure $\overline{q}_{ASCE}$. This relationship allows for the peak pressure coefficient normalized by the mean-hourly reference $\widehat{C_p}_{ASCE}$ to be provided in Eq. (8).

$$\hat{p}_{ASCE} = \frac{1}{2}\rho K_z K_{zt} K_e V^2 \cdot GC_p \tag{6}$$

$$\overline{q}_{ASCE} = \frac{1}{2}\rho\left(\overline{b}\left(\frac{z}{10\text{ m}}\right)^{\overline{\alpha}} V\right)^2 \tag{7}$$

$$\widehat{C_p}_{ASCE} = \frac{K_z K_{zt} K_e}{\left(\overline{b}\left(\frac{z}{10\text{ m}}\right)^{\overline{\alpha}}\right)^2} GC_p \tag{8}$$

For open terrain (Exposure C), the following values are substituted in Eq. (9).

$$\widehat{C_p}_{ASCE} = \frac{2.41\left(\frac{z}{750\text{ m}}\right)^{\frac{2}{9.8}}}{\left(0.66\left(\frac{z}{10\text{ m}}\right)^{\frac{1}{6.4}}\right)^2} GC_p = 2.942 \cdot \left(\frac{z}{1\text{ m}}\right)^{-0.108} GC_p \tag{9}$$

Note that in both the Eurocode and ASCE 7 cases the minimum cutoffs on elevation (z) have not been applied at this point. These minimum elevations add an extra point of comparison that will be addressed in the full conference paper.

3. RESULTS

The data presented in this paper are enveloped over many different systems with broadly similar parameters. A similar dataset was used in Browne et al. (2020) which informed the ASCE 7 provisions for Ground-Mounted Fixed-Tilt Solar Panel Systems (GMFTSPS). Typical scales for the wind tunnel tests were approximately 1:30 with a photo of a typical model shown in Figure 1.

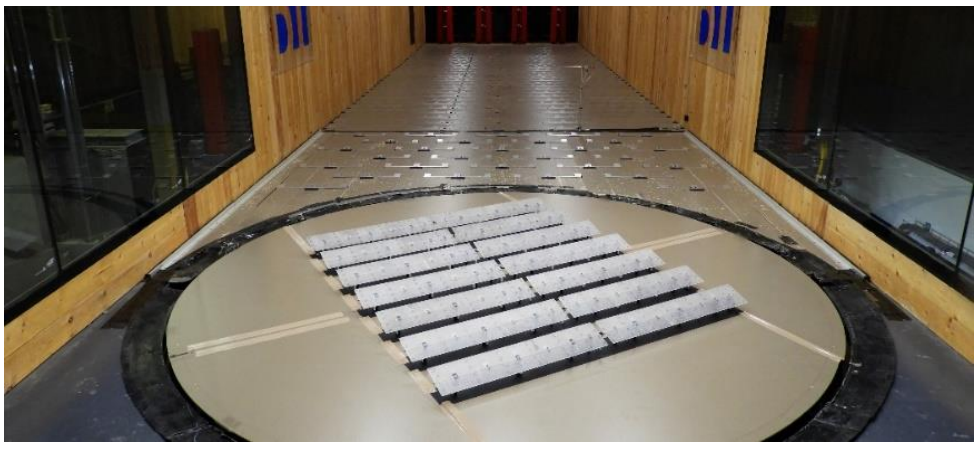

Figure 1. Example of a wind tunnel test of a solar PV structure array.

The canopy roof coefficients are typically used in Eurocode designs in the absence of specific provisions. Therefore, the enveloped coefficients from the wind tunnel studies are compared to overall force coefficients and net pressure coefficients provided in the Eurocode for canopy roofs with no blockage underneath, as a function of averaging area in Figure 2. ASCE 7 monoslope free roof coefficients for Main Wind Force Resisting System (MWFRS) and for Components and Cladding (C&C) are also included for comparison.

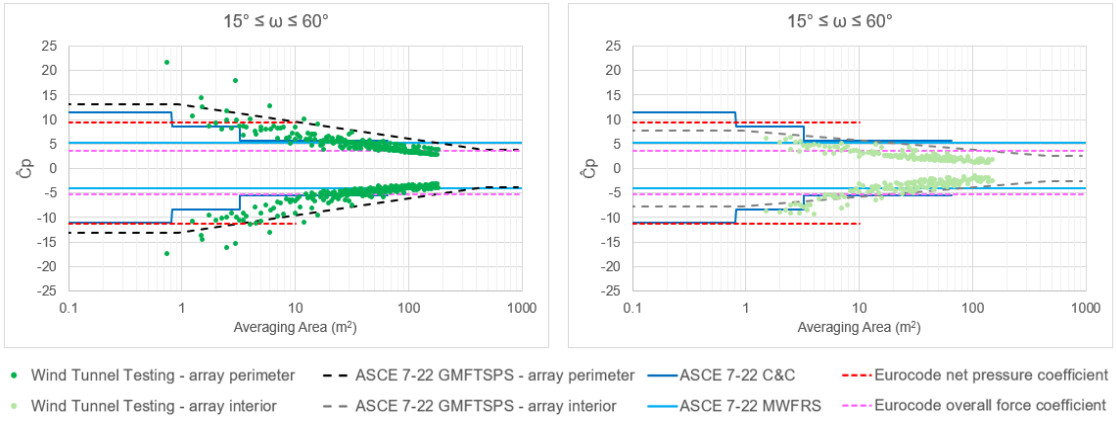

Figure 2. Normal peak pressure coefficients $\widehat{C_p}$ for uplift (negative) and downforce (positive), normalized by the mean hourly reference wind dynamic pressure (with no minimum cutoffs on elevation applied). Comparison of wind tunnel, Eurocode and ASCE 7-22 code provisions as a function of area for a nominal tracker. Left: array perimeter, right: array interior. ω: tilt angle from horizontal (WT and ASCE 7-22 GMFTSPS: 15°<ω≤60°; ASCE 7-22 MWFRS and C&C: 15°<ω≤45°; Eurocode 15°<ω≤30°)

4. DISCUSSION AND CONCLUSIONS

The wind engineering codes and standards were developed long before the advent of utility scale solar PV arrays. At present, some of these codes and standards are being updated to deal with important wind engineering aspects of these structures. The data provided in this abstract have demonstrated that the monoslope free roof / canopy roof coefficients reasonably envelope the data for larger averaging areas. However, greater differences are observed for smaller averaging areas especially in the perimeter of the array. The peak factors observed for these smaller averaging areas indicate the behaviour is not quasi-steady. The full conference paper will provide further discussion on these differences, the effect of considering a minimum cutoff on elevation, comparisons of the moment coefficients, and on inertial forces.

REFERENCES

ASCE/SEI (2022) Minimum Design Loads and Associated Criteria for Buildings and Other Structures. ASCE/SEI 7-22.

AS/NZS (2021) Australian/New Zealand Standard – Structural design actions – Part 2: Wind actions, AS/NZS 1170.2:2021.

Browne, M. T., Taylor, Z. J., Li, S. and Gamble, S. (2020), A wind load design method for ground-mounted multi-row solar arrays based on a compilation of wind tunnel experiments, J. Wind Eng. and Ind. Aerodyn. 205(July), 104294.

Durst, C. S. (1960), Wind Speeds over Short Periods of Time, *Meteorological Magazine* **89**(1056), 181-186.

EN (2010) Eurocode 1: Actions on structures – Part 1-4 : General actions – Wind actions, EN 1991-1-4:2005+A1:2010.

Ginger, J. D., Bodhinayake, G. G. and Ingham, S. (2019), Wind loads for designing ground-mounted solar-panel arrays, Aus. J. Struct. Eng. 20(3), 204-218.

IN-VENTO 2024
International Conference of the Italian Association for Wind Engineering
Pisa, September 8th – 11th, 2024

Uniting the Realms of Physical Simulations and Field Measurements of Downburst Events Through an International Collaboration

M. Eissa[a], O. Metwally[a], F. Canepa[b], M.T. Mengistu[b], A. Elawady[a,c], M. Burlando[b], M.P. Repetto[b], G. Piccardo[b]

[a]*Civil and Environmental Engineering, Florida International University, Miami, FL, USA, meiss002@fiu.edu*
[b]*Department of Civil, Chemical and Environmental Engineering, University of Genoa, Genoa, Italy*
[c]*Extreme Events Institute, Florida International University, Miami, FL, USA*

SUMMARY:
Downbursts, over the past few decades, have caused human fatalities and significant damage to the built environment globally. For instance, a 120-mph downburst struck Ontario, Canada in May 2022, resulting in 10 people being killed and widespread power outages that endangered the welfare of several communities in the affected province. With $875 million in losses, this is considered Canada's most destructive wind event in history (Raymond, 2022, June 15). Similar incidents occurred in Europe and around the globe (e.g., Calotescu et al., 2024). This drives an international collaboration between the research group at the Wall of Wind (WOW) Experimental Facility (EF) at Florida International University (FIU) and the Giovanni Solari WinDyn research group at the University of Genoa (UniGe) to unite their forces aiming at enhancing the resiliency of vulnerable communities against such a fierce wind event. The multi-institution international partnership offers unique international internship opportunities for graduate students at both institutions to exchange expertise. By empowering graduate students' learning experience through international collaboration, the project aims to advance the physical simulation at the WOW EF, allowing for a realistic assessment of the interplay between various structures and downburst winds. Starting with the field measurements collected by the team at UniGe, we are developing a novel algorithm for detecting downbursts and downburst-like events from long-term data by utilizing continuous wavelet transforms. This algorithm has demonstrated promising results. Additionally, we have conducted a comprehensive study of the lattice tower's structural response during three distinct wind events (one synoptic wind and two non-synoptic wind events). This analysis involved the simultaneous measurement of wind and structural response. Preliminary findings and thoughts are included in this study. The future work includes comparative studies between the field measurements and their experimental simulations replicas.

Keywords: Downburst, non-synoptic winds, event extraction algorithm, wind-induced vibrations, wavelet transform, physical simulations, field measurement, international collaboration

1. THE ESSENCE OF THE FIU-UNIGE COLLABORATION

Collaboration, per se, means "the act of working together with other people or organizations to create or achieve something". Thus, this collaboration unites two prestigious educational institutions in the wind engineering community to serve the goal of providing current and future engineers with an opportunity to delve into the nature of wind hazards and their effects on both the natural and built environment. The WOW at FIU is funded by the National Science Foundation (NSF) under the Natural Hazard Engineering Research Infrastructure (NHERI) program, which empowers the research community through its capabilities to better understand the wind effects on structural systems, building envelopes, and civil infrastructure systems (Gan Chowdhury et al., 2017). The facility was initially designed to simulate hurricane category 5 effects on large-scale and full-scale models. Most recently, a downburst simulator testbed was added

to complement the testing capabilities at the WOW (Mejia et al., 2022). The Giovanni Solari WinDyn research group at UniGe has a unique interdisciplinary composition, covering multiple sectors of wind science and engineering– namely atmospheric physics, meteorology, climatology and geophysics, aerodynamics and aeroelasticity, and structural and architectural engineering. To that end, the aim of joining the forces of the two institutions is to advance downburst-related knowledge by integrating physical simulations and field measurement domains into a series of collaborative research studies.

Exchange internships for graduate students is a pillar of this collaboration, through which their ability to establish educational connections despite national, cultural, disciplinary, and linguistic borders can evolve. These internships offer students a broader perspective on accepting and incorporating others' opinions in the process of defining and addressing engineering problems. In late 2023, two FIU Ph.D. students had a chance to intern at the UniGe where they participated in several field measurement projects to have a comprehensive understanding of integrating both realms (i.e., experimental and field measurements) in future research studies. This internship yielded an innovative extraction algorithm of potential downburst events from long-term registered data. These data were recorded through an extensive wind monitoring network that was made up of 40 ultra-sonic anemometers and 4 LiDARs (Solari et al., 2018). Additionally, simultaneous measurements of wind and structural response were provided for a lattice tower located in Romania (Calotescu et al., 2021) which was subjected to synoptic and non-synoptic winds. Wind-induced vibration analysis has been performed to assess the tower response using short-term data (4 hours in length). The next section discusses the aforementioned internship's preliminary outcomes.

2. PRELIMINARY RESULTS

2.1. A novel algorithm for detecting downburst events

Managing large sets of wind speed data to extract specific wind events is a crucial step in understanding the wind-induced response of structures under wind conditions. However, the mixed nature of wind records adds further complexity to this process. Customarily, the extraction and classification methods are categorized into meteorological-based and engineering-based methods. Meteorological-based methods concern scrutiny of meteorological conditions that are likely to occur during such wind events (Wakimoto, 1985). On the other hand, the second category relies on performing statistical analyses of large amounts of the recorded data, averting the idea of thoroughly investigating the meteorological conditions of wind events that occur (Choi and Hidayat, 2002; De Gaetano et al., 2014). Yet, the latter category has a primitive shortcoming that is inevitable due to disregarding the meteorological survey of the extracted data. De Gaetano et al., 2014 proposed an extraction algorithm that belongs to the second category of the aforementioned methods. This method employs three reference gust factors: G_{10}^{0} (a 10-min gust factor), G_{60}^{0} (a 1-h gust factor), and G_{1}^{0} (a 1-min gust factor). By comparing them with the measured gust factor, one can separate the events and proceed with the visual examination of the time histories. The reference gust factors may exhibit some deviation in the results due to subjectivity in their calculation process. Additionally, this method was developed using data collected in a flat port region and may not be suitable for separating downburst winds in mountainous regions, which limits its applicability (Huang et al., 2019). Furthermore, Zhang et al., 2018 showed that this method doesn't provide satisfactory performance when two or three different types of independent events occur in a small time window— mostly less than 4 hours. It also stated that this approach can result in extracting implausible types of events occurring in sequence within the same record , which contradicts the field observations. To

this end, a new method is currently under development, detecting the potential downburst or downburst-like events in the frequency domain by assessing the sudden changes in the signal energy content to extract either downburst events or like-downburst events. Through this, the setbacks of the preceded method can be evaded.

2.2. Wind-induced vibrations of telecommunication lattice tower

Telecommunication lattice towers play a crucial role in supporting the equipment necessary for signal transmission within the mobile networking industry. In today's world, effective communication during natural disasters heavily relies on telecommunication towers. If any of these towers get damaged, it can pose a significant risk to people in the affected areas, as they may not receive the proper aid during severe wind events. This draws the importance of enhancing their resiliency against the different types of wind events. To achieve this, the behavior investigation of a 50-m tall freestanding lattice tower (Calotescu et al., 2021) to wind loading is currently underway, utilizing three different wind events (synoptic and non-synoptic winds). The significance of this investigation is that it preserves the random nature of the wind field, which is often missing in physical simulations. This motivates conducting a thorough study of the lattice tower's structural response during three distinct wind events. As preliminary results, wind-induced vibration analysis has been conducted to identify the dominant vibration under certain wind conditions and assess the aeroelastic effect that may occur due to changes in the wind field. In a 50-sec segment from a synoptic wind recorded event, shown in Figure 1, the wind speed was nearly constant over the first 20s at 15.20 m/s then it decreased to almost around 10 m/s, and the same trend was found in the time history of wind direction. The like-along-wind acceleration increased in magnitude when the tower was exposed to relatively higher wind speed due to the along-wind buffeting effect. Around the 8th sec, the like-across-wind RMS acceleration started to exhibit a higher magnitude than in the like-along-wind direction. This also coincided with observing a concentrated high energy content at the natural frequency of the tower at the same period where the wind speed and direction were plateaued. This indicates that a significant amount of energy had been transmitted to the system causing a sudden change in the energy content. It can be concluded that the tower suffered the vortex-induced vibration during the first 20s. This interpretation aligns with the findings in the study by Zheng et al., 2019. Thus, the like-across-wind RMS acceleration increases drastically as the vortex-induced vibration occurs, accompanied by a significant deterioration in the total damping ratio as can be found in Table 1. These preliminary findings suggest that even though these vibration phenomena do not lead to catastrophic events, they adversely affect the fatigue life of such lightweight structures.

3. CONCLUSIONS

In this study, we emphasized the importance of the international collaboration between FIU and UniGe in advancing the current knowledge of non-synoptic winds. The interpretations of these entrained topics, in this document, will enhance the WOW capabilities to simulate such sophisticated wind events. The interpretations, results, and recommendations of this collaboration will be invested in a published series of collaborative research papers.

ACKNOWLEDGEMENTS

The first, second and fifth authors acknowledge the support from the National Science Foundation (NSF) under the award number CMMI 2146277. The opinions, findings, conclusions, or recommendations expressed in this article are solely those of the authors and do not represent the opinions of the funding agencies.

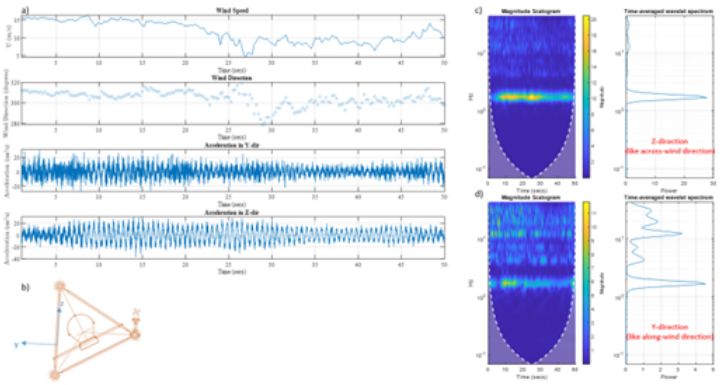

Figure 1. a) Wind speed and direction, acceleration in Y-direction (like along-wind direction), and acceleration in Z-direction (like across-wind direction), b) Plan view of the tower, c) Scalogram of the acceleration in the across-wind direction, and d) Scalogram of the acceleration in the along-wind direction.

Table 1. System properties within the studied segment

Mean Wind speed (m/s)	RMS ACC-Y (cm/s^2)	RMS ACC-Z (cm/s^2)	$\%\zeta_Y$	$\%\zeta_Z$
11.69	7.506	10.698	1.49%	0.3%

The third and last authors acknowledge the support of the RETURN Extended Partnership funded by the European Union Next-Generation EU (National Recovery and Resilience Plan – NRRP, Mission 4, Component 2, Investment 1.3 – D.D. 1243 2/8/2022, PE0000005).

REFERENCES

Calotescu, I., Bîtcă, D., and Repetto, M. P. (2021). Full-scale Behaviour of a Telecommunication Lattice Tower under Wind Loading. Lightweight Structures in Civil Engineering, XXVII LSCE Łódź, 2nd–3rd of December, 15–18.

Calotescu, I., Li, X., Mengistu, M. T., and Repetto, M. P. (2024). Thunderstorm impact on the built environment: A full-scale measurement and post-event damage survey case study. J. Wind Eng. Ind. Aerod. 245, 105634.

Choi, E. C. C. and Hidayat, F. A. (2002). Gust factors for thunderstorm and non-thunderstorm winds. J. Wind Eng. Ind. Aerod. 90, 1683–1696.

De Gaetano, P., Repetto, M. P., Repetto, T., and Solari, G. (2014). Separation and classification of extreme wind events from anemometric records. J. Wind Eng. Ind. Aerod. 126, 132–143.

Gan Chowdhury, A., Zisis, I., Irwin, P., Bitsuamlak, G., Pinelli, J.-P., Hajra, B., and Moravej, M. (2017). Large-scale experimentation using the 12-fan wall of wind to assess and mitigate hurricane wind and rain impacts on buildings and infrastructure systems. J. Struct. Eng. 143, 04017053.

Huang, G., Jiang, Y., Peng, L., Solari, G., Liao, H., and Li, M. (2019). Characteristics of intense winds in mountain area based on field measurement: Focusing on thunderstorm winds. J. Wind Eng. Ind. Aerod. 190, 166–182.

Mejia, A. D., Elawady, A., Vutukuru, K. S., Chen, D., and Chowdhury, A. G. (2022). Examination of different wall jet and impinging jet concepts to produce large-scale downburst outflow. Front. Built Environ. 8, 980617.

Raymond, T. (2022, June 15). May 21 storm ranked 6th most expensive natural disaster in Canadian history: IBC. Ottawa. https://ottawa.ctvnews.ca/may-21-storm-ranked-6th-most-expensive-natural-disaster-in-canadian-history-ibc-1.5948666.

Solari, G., Burlando, M., and Repetto, M. P. (2018). THUNDERR: an ERC Project for the "detection, simulation, modelling and loading of thunderstorm outflows to design wind-safer and cost-efficient structures". Proceedings of International workshop on wind-related disasters and mitigation, Sendai, Japan, 11–14.

Wakimoto, R. M. (1985). Forecasting dry microburst activity over the high plains. Mon. Weather Rev. 113, 1131–1143.

Zhang, S., Solari, G., Yang, Q., and Repetto, M. P. (2018). Extreme wind speed distribution in a mixed wind climate. J. Wind Eng. Ind. Aerod. 176, 239–253.

Zheng, C., Liu, Z., Wu, T., Wang, H., Wu, Y., and Shi, X. (2019). Experimental investigation of vortex-induced vibration of a thousand-meter-scale mega-tall building. J. Fluids Struct. 85, 94–109.

A simplified procedure for assessing nonlinear behavior of steel plane frames under wind

Mattia Francioli [1], Francesco Petrini [2]

[1]*Sapienza University of Rome, Rome, Italy, mattia.francioli@uniroma1.it*
[2]*Sapienza University of Rome, Rome, Italy, francesco.petrini@uniroma1.it*

SUMMARY
Recently, wind analyses have been increasingly directed towards the use of nonlinear analyses and models. These aim to achieve economically more favorable design solutions compared to those obtained through prescriptive code-based wind design, avoiding excessive safety margins. However, the significant computational burden associated with nonlinear analyses in wind cases can be a potential deterrent to their widespread adoption, except in particularly complex situations that are challenging to address through alternative methods. This work aims to propose an alternative method for assessing the progressive onset of plastic behavior in structural elements while preserving the cost-effectiveness of linear analysis methods through power spectral density.

Keywords: Wind analysis, Nonlinear analysis

1. INTRODUCTION

Nonlinear analysis in wind engineering is conducted to account for the complex and dynamic nature of wind loads on structures with a more accurate representation of their interactions, considering the dynamic and nonlinear aspects of both the wind and the structural response. Wind forces on structures are inherently nonlinear due to the turbulent and fluctuating nature of wind and typically nonlinear analysis allows for a more accurate representation of the varying wind loads over time, considering factors like gusts, turbulence, and directional changes. Complex aspects as material nonlinearities and large deformations can be taken into account when nonlinear analyses are developed, thus ensuring a more realistic representation of the structural behavior. Most recent codes and regulations (i.e., ASCE, 2023) in specific limit states allow some elements of the main structural system to enter the plastic field, albeit in limited conditions. However, the significant computational burden associated with nonlinear analyses in wind cases can represent a potential deterrent in some cases, especially in a preliminary phase of design, when different possible configurations must be taken into account and assessed. Here is proposed an analysis method which allows monitoring the progressive plasticization of structural members, exploiting the computational economy of linear analyses with Power Spectral Density (PSD).

2. METHODS

To avoid the high computational burden of NLTH analysis, an iterative PSD analysis enhanced by an element-by-element stiffness degradation procedure has been implemented to take into account plastic non-linear behaviors. The element-by-element stiffness degradation depends on the demand excursion in the plastic range and to the local buckling occurrence (i.e., Demand versus Capacity ratio, D / C). The procedure, which consists of several steps and is shown in the exemplary flowchart (figure 1), has been already introduced in literature for reinforced concrete

buildings (Franchin P. et al., 2018; Günay MS. Et al., 2010) and it has therefore been adapted here for plane steel frames with shear resisting connections, where excursion in the plastic range and buckling phenomena are expected to occur in bracing elements or in columns.

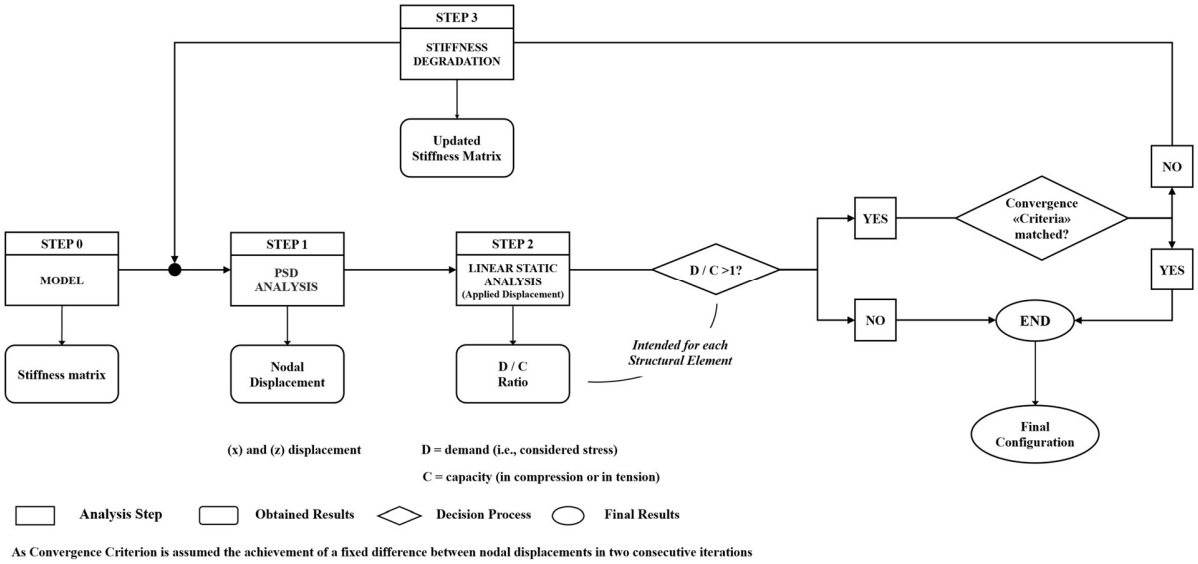

Figure 1. Iterative procedure for the element-by-element degradation of the stiffness matrix depending on the excursion in the plastic range and on the local buckling

3. RESULTS

In step 1 a linear spectral response analysis carried out. The absolute values of nodal displacements are then identified and stored. The capacity considered for columns, bracing elements and outriggers must be differentiated in the two cases of tension and compression due to the possible buckling of the compressed elements. To evaluate stresses, the displacements obtained in step 1 are applied to the structure by carrying out a linear static analysis (step 2); in this way it is possible to compare the tensile and compressive stresses in each structural element (which represents the actual "D") with their capacity "C", equal to the buckling strength (SB) in the case of compressed, slender elements, and the yielding strength (Sy) in the case of non-slender elements. In step 3 the deformation state of each element (axial deformation ε) is monitored, together with D/C ratio: if the element is slender ($|SB| < |Sy|$) and it is compressed ($\varepsilon < 0$), the value of the element elastic modulus E is reduced to the 7% of its original value (non-zero value needed for analysis convergence); if the element is slender ($|SB| < |Sy|$) and it is in tension ($\varepsilon > 0$), or if the element is not slender ($|SB| > |Sy|$) either the element is in compression ($\varepsilon < 0$) or in tension ($\varepsilon > 0$), the so-called equal displacement assumption is implemented to evaluate the secant elastic modulus E* to be assigned to the element given the elastic stress $\sigma^{\blacktriangle}$ evaluated by the linear static analysis carried out at step 2. The step 3 is iterated until convergence (the difference between the displacements of the previous and current iterations is lower than the fixed threshold).

4. DISCUSSION AND CONCLUSIONS

The case study is a steel shear-resisting frames, for which the initial configuration is identified following a pre-sizing for vertical loads only, considering a precautionary use of C/D utilization coefficients for the structural elements (for U.L.S. combination: bracing system and outriggers 30%, columns 60%, beams 30%), whose sections for the considered plane frame are reported in

Table 1. Note that out-of-plane deformations are disabled and that beam-column joints and beam-column-outrigger trusses (or bracing system trusses) are modelled as “hinges”. The software used for the analysis is ANSYS® APDL. The structural response of the building is evaluated only in the along wind direction and is obtained in the frequency domain by a Power Spectral Density (PSD) analysis by applying along wind force spectra at each floor of the building, following the formulation proposed by Solari et al., 2001, Carassale et al., 2006 also present in Chuang WC et al., 2022 and Zhou Y. et al, 2002 (only the alongwind force spectra are considered in this work).

Table 1. Configuration of the considered plane frame.

N Floors	17
H Interstory [m]	3.5
L Bays [m]	6
H_{TOT} [m]	59.5
Beams	IPE 360

Columns	Floors	Section	Bracing system	Floors	Section
	1 - 5	HEB 700		1 - 5	Steel tube 273x20
	6 – 10	HEB 600		6 – 10	Steel tube 244x20
	11 - 15	HEB 500		11 - 15	Steel tube 219.1x20
	16 - 17	HEB 400		16 - 17	Steel tube 219.1x16
			N° of outriggers		1
			At floor:		17

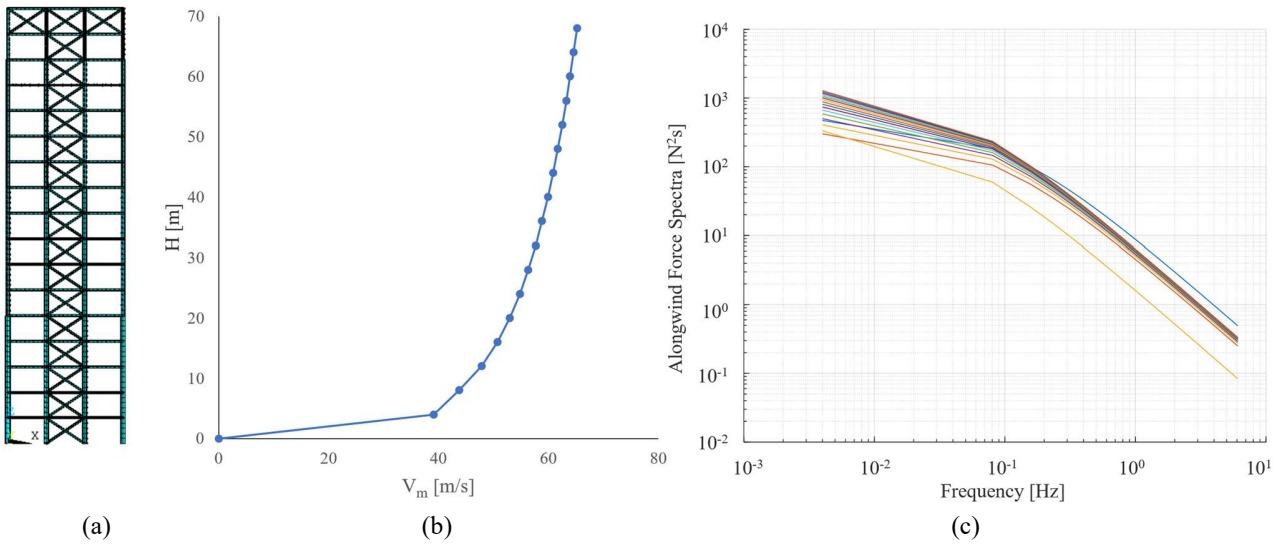

Figure 2. (a) FE model in Ansys APDL; (b) mean wind velocity profile; (c) alongwind force spectra.

The results are shown in figure 3, where the different iterations (in terms of Interstory Drift Ratio – IDR [%] and lateral displacements [m]) are reported.

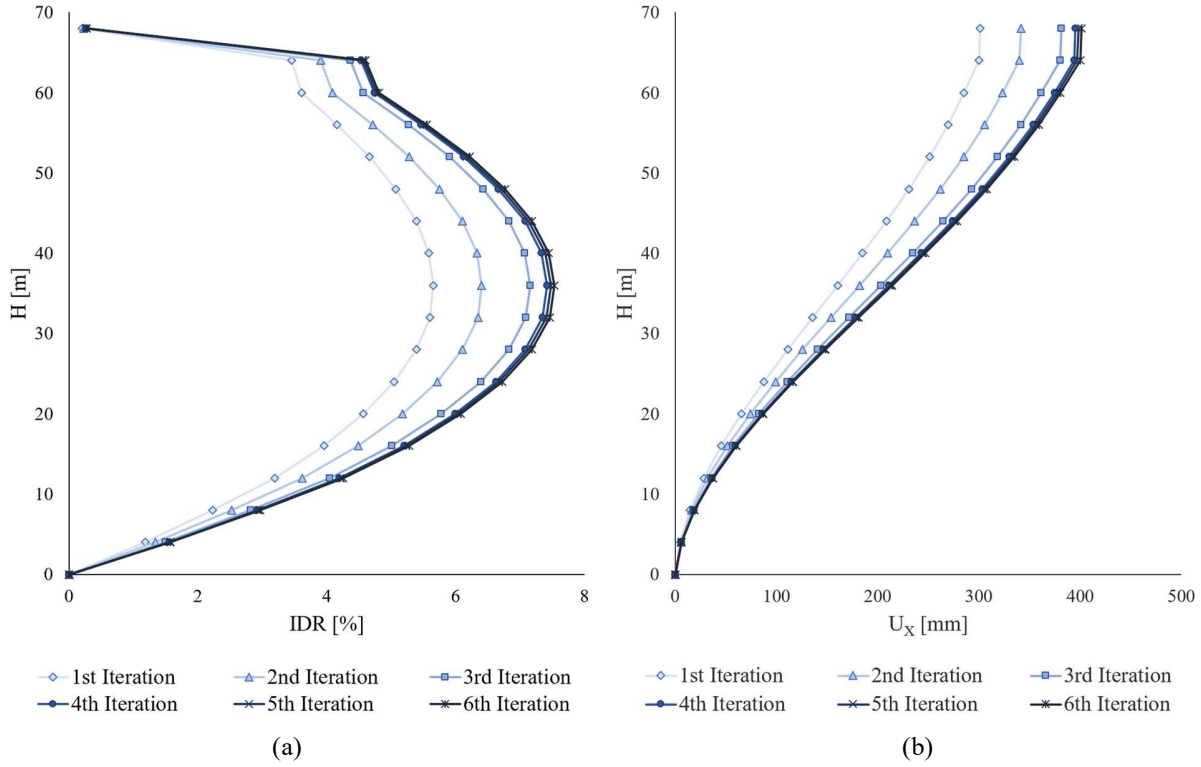

Figure 3. Results obtained during different iterations (6): (a) IDR profile; (b) U_X displacement profile.

In this way, it was possible to develop a method to evaluate the progressive plasticization of structural elements, while maintaining the cost-effectiveness of linear analyses; this simplified methodology allows you to quickly provide information on the state of the structural members without having to carry out NLTH analysis, a very useful aspect in the preliminary stages of design, when different configurations must be evaluated. This methodology is particularly useful in the event that the design of the structure must consider a multi-hazard environment, as it can also be applied to the case of seismic loads and it can be inserted into a design framework that effectively considers the performance for different hazards simultaneously.

REFERENCES

ASCE (2023). Pre-standard for Performance-based Wind Design, V1.1, American Society of Civil Engineers, Reston, Virginia. https://doi.org/10.1061/9780784484739.

Carassale, L., Solari, G., (2006). Monte Carlo simulation of wind velocity field on complex structures. Journal of Wind Engineering and Industrial Aerodynamics, 94 (1), 323–339. https://doi.org/10.1016/j.jweia.2006.01.004.

Chuang, Wei-Chu, Spence S.M.J., A framework for the efficient reliability assessment of inelastic wind excited structures at dynamic shakedown (2022), Journal of Wind Engineering and Industrial Aerodynamics, Volume 220, 2022, 104834, ISSN 0167-6105, https://doi.org/10.1016/j.jweia.2021.104834.

Franchin, P., Petrini, F., Mollaioli, F., (2018). Improved risk-targated performance-based seismic design of reinforced concrete frame structures, Earthquake Engng Struct Dyn. 2018;47:49–67. https://doi.org/10.1002/eqe.2936.

Günay MS, Sucuoglu H. An improvement to linear-elastic procedures for seismic performance assessment. Earthq Eng Struct Dyn. 2010;39(8):907-931. https://doi.org/10.1002/eqe.980.

Solari, G., Piccardo, G., (2001). Probabilistic 3-D turbulence modeling for gust buffeting of structures. Probabilistic Engineering Mechanics, 16, 73–86. https://doi.org/10.1016/S0266-8920(00)00010-2.

Zhou Y., Kijeswski T., Kareem A., Along-Wind Load Effects on Tall Buildings: Comparative Study of Major International Codes and Standards, Journal of Structural Engineering, Vol. 128, No. 6, June 1, 2002. https://doi.org/10.1061/(ASCE)0733-9445(2002)128:6(788).

IN-VENTO 2024
International Conference of the Italian Association for Wind Engineering
Pisa, September 8th – 11th, 2024

Overview of current methodologies for photovoltaic tracker parks analysis

G. Frontini [1*], S. Muggiasca [1], T. Argentini [1]

[1]*Politecnico di Milano, Department of Mechanical Engineering, Milano, Italy*
[*]*giorgio.frontini@polimi.it*

SUMMARY
In today's renewable energy landscape, solar tracker systems have emerged as vital tools for harnessing solar radiation efficiently. While traditional fixed-tilt systems have received considerable attention and have been extensively studied, the industry is increasingly adopting tracking systems. To provide cost-effective solutions, designers face the challenge of minimizing structural resources while ensuring resistance to wind loads. This abstract provides an overview of existing methodologies in photovoltaic tracker design. The state of the art for wind tunnel tests on both solar parks and standalone trackers, and their integration with finite element models, are presented. Different numerical analyses can be implemented, ranging from simplified evaluation of equivalent static wind loads, to more complex structural response time-domain analyses. The latter presents an ideal starting point to develop more in-depth assessments of the expected service life due to fatigue damage, or to perform structural optimization to improve the cost-efficiency of the tracker design.

Keywords: single-axis photovoltaic trackers, solar park, wind tunnel, experimental testing

1. INTRODUCTION

The current push towards renewable energy has brought attention to the development of efficient systems for harnessing energy from solar radiation. While traditional fixed-tilt systems are well-addressed in literature, new technologies implementing movable dynamic mechanism are increasingly used in the industry due to their potential to produce more energy given the same covered area. To improve return of investment and maintain competitiveness, designers strive to minimize structural resources while ensuring a sufficient level of structural resources to withstand the expected environmental loads. Since solar parks are usually installed in large open areas, and the individual systems are characterized by large surfaces and low degrees of constraint, wind loads are anticipated to be the predominant load conditions. Under this premise it is of uttermost importance for the designer to estimate as accurately as possible the wind loads acting on the structure and identify the more efficient and cost-effective solution. The present abstract provides in the next section a brief review of the currently existing and developed procedures used to aid engineers in the design task, while in Section 3 the development of numerical procedures is discussed.

2. PROBLEM CHARACTERIZATION

An overview of the current methodologies for photovoltaic trackers park analysis is summarized in Figure 1 and the main items are described in the following.

2.1.Structural properties

Typically, the first key information for characterizing the structural response is the identification of its mechanical properties, that is the structural stiffness, mass, and damping. While for the first two components the task is relatively easy due to ready availability of

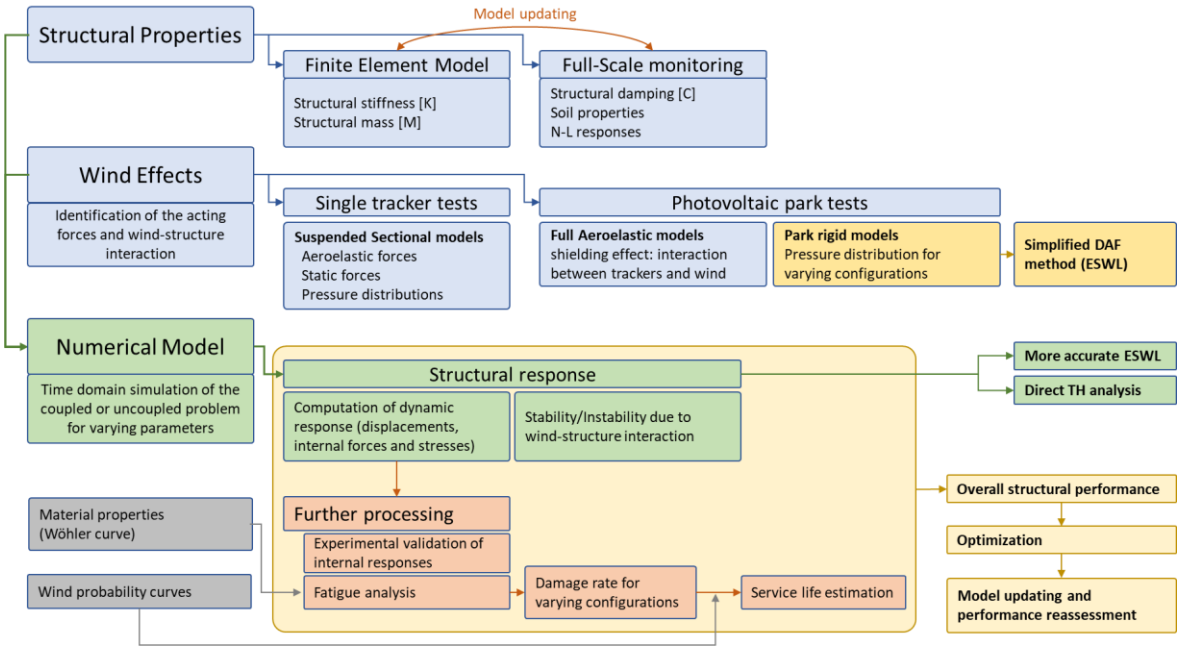

Figure 1. Schematic overview of the main activities concerning the design of PV systems against wind loads.

technical detailing and finite elements (FE) models, the evaluation of the damping ratio is more complicated. A conservative value of about 2%-5%, assuming no internal frictions and perfect connections between elements can be assumed; however, if a more accurate response is needed, it is possible to perform "Free Vibration Tests" (FVT) or monitoring in-situ.

2.2.Wind tunnel experimental tests

The second aspect analyzed concerns the structural response and interaction with the wind phenomena. For this purpose, wind tunnel experimental campaigns are a fundamental tool since they provide essential information for the structural design, optimization and verification of the mechanical systems. Moreover, wind tunnel tests allow for a cost-effective estimation of the response of PV system when interacting with the wind flow. Different typologies of experimental tests can be developed, and their results can be used jointly.

2.2.1. Rigid model of solar park

Rigid models of solar park were extensively adopted in literature and industry to investigate the response against wind actions of fixed-tilt PV panels for varying design parameters: for this reason, these models are well-established in current practice. A selection of the PV park, specifically the corner region which is the most affected by wind loads, is reproduced in model scale and instrumented with pressure taps fitted on the model surface, as shown in Figure 2a. The main results of this experiment are the buffeting loads acting on the tracker, that is the force due to the incoming mean wind and the associated fluctuations induced by turbulence. While in experimental campaigns the entire time histories of the phenomenon are acquired, in actual practice the design is carried out by means of simplified equivalent static wind loads (ESWL) derived from the application of a dynamic amplification factor approach (DAF) (Browne 2020). With this simplified methodology, the entirety of the pressure field is summarized in a distribution of normal force and torsional moment, and then further simplified in a coefficient representative of the extreme peak estimate and the associated dynamic amplification.

2.2.1. Aeroelastic model of solar park

A different type of experimental test that is possible to carry out in wind tunnel facilities involves the development of a fully-aeroelastic model reproduction of a portion of the PV park. This type of experimental investigation can provide more accurate reproduction of the shielding effect, the phenomenon that occurs when the leading perimetral trackers divert the incoming wind flow, reducing the wind speed observed in internal rows.

2.2.2. Aeroelastic sectional model of isolated tracker

A type of experimental tests that reproduce the response of an isolated tracker is given by the aeroelastic sectional model (Figure 2b). This type of test is well addressed in literature and is the approach adopted for the investigation of bridge aerodynamics to evaluate the coupled response between structural motion and wind flow. This test yields the trend of the aerodynamic derivatives, functions that allow the estimation of the self-excited response about a specific tracker's pitch angle (Taylor 2020, Frontini 2022, Cárdenas-Rondón 2023).

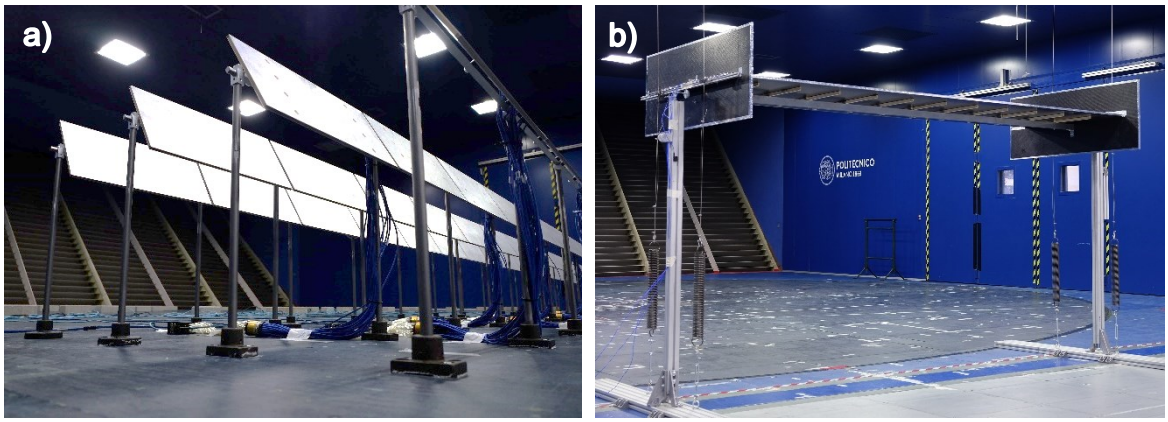

Figure 2. a) Rigid model of a PV park; b) Suspended sectional model of an isolated PV tracker.

3. STRUCTURAL PERFORMANCE EVALUATION

While the design and assessment of the full-scale structure is typically performed adopting ESWL deriving from the model experimentation of the rigid park, the same time histories can be used to develop an analysis in the time domain by means of a FEM approach. Following the schematics of Figure 1, the results of the structural properties identification are combined with the observed wind effects and, from this, the dynamic equilibrium of the single-axis tracker system can be defined. The solution of this governing equation provides the structural rotation and displacements, from which the internal actions and stresses can be derived (Figure 3a). By incorporating the coupled interaction between wind flow and structural motion (Taylor, 2020) into the problem formulation, a more precise structural response, which is also able to highlight potential unstable responses, is derived. This result is of uttermost importance for the tracker design, since for specific inclination ranges (10°-30°) experimental evidence shown that the aeroelastic response brings single axis tracker to be aerodynamically unstable (Taylor 2024), while at larger angles (50°-60°) the response tends to be more stable due to the same self-excited component.

3.1.1.Fatigue damage assessment

The knowledge of the structural response allows the designer to perform further analysis on the investigated system. The assessment of damage accumulation due to fatigue in structural elements typically subjected to large excursion in internal stress, such as the connections point (Frontini 2023), is particularly relevant. Processing the stress time histories with the

rainflow method (Figure 3b) and combining the stress excursion distribution with the component Wöhler curve, a damage accumulation rate (specific of a given set of parameters) can be estimated. The resulting damage rate, combined with the wind probability curves, can be used to estimate a possible service life for the tracker's structural components.

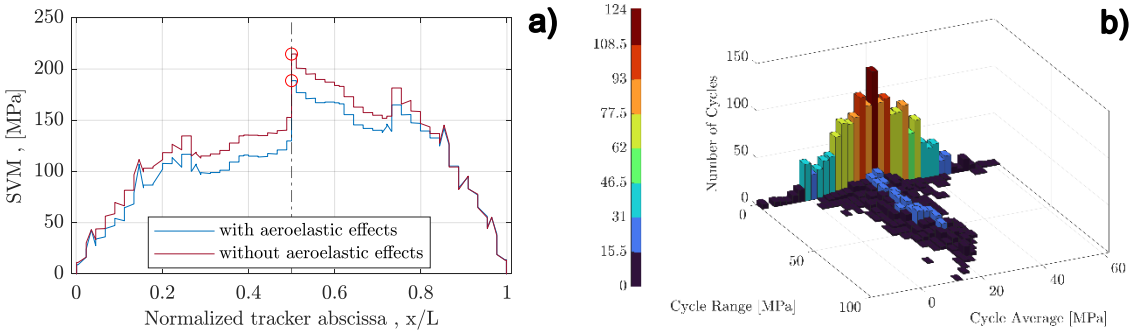

Figure 3. a) Envelope of an internal stress across all tracker's cross sections; b) Example of a rainflow distribution

4. FINAL REMARKS

In the present work an overview of the principal experimental and numerical procedures currently developed to analyze the PV trackers response has been presented. The methodologies are based on a hybrid approach that combines experimental measurements, numerical models, and eventually also full-scale monitoring (actual tracker installations, wind statistics). Several parameters concerning both the tracker's configuration (pitch angle, geometrical dimensions, structural damping and frequency), and the park layout (inter-row distance, position of individual trackers, effects of wind direction) have a relevant impact on the dynamic response and must be accurately analyzed. The presented time-domain procedures for the computation of the tracker response allow for a more accurate evaluation compared to what the simplified DAF approach can provide. It follows that the results can be used to develop more in-depth analyses, such as the estimation of the service life due to fatigue damage or the development of structural optimization procedures. The cost-effectiveness of the solution can be improved with an iterative procedure where the PV tracker (and the related park) is updated from time-to-time, consequently the solution is reassessed until a optimal level of performance (resistance, expected serviceability life) is reached.

REFERENCES

Browne M. T. L., Z. J. Taylor, S. Li, S. Gamble (2020). A wind load design method for ground-mounted multi-row solar arrays based on a compilation of wind tunnel experiments. Journal of Wind Engineering and Industrial Aerodynamics, 205. 10.1016/j.jweia.2020.104294

Cárdenas-Rondón J. A., M. Ogueta-Gutiérrez, S. Franchini, R. Manzanares-Bercial (2023). Stability analysis of two-dimensional flat solar trackers using aerodynamic derivatives at different heights above ground. Journal of Wind Engineering and Industrial Aerodynamics, 243. 10.1016/j.jweia.2023.105606

Frontini G., F. Calamelli, S. Muggiasca, T. Argentini, M. Belloli (2022). Solar trackers analysis: a parametric study to evaluate aeroelastic effects inside a photovoltaic park array. Proceedings of VIII European-African Conference on Wind Engineering (EACWE2022). Bucharest, Romania, 371-374.

Frontini G., T. Argentini, S. Muggiasca, M. Belloli (2023). A framework for fatigue damage estimate in single-axis solar trackers. Proceedings of Mini-symposium 24 on "Wind-induced vibration of slender structures", XII International Conference on Structural Dynamics (EuroDyn2023), European Association of Structural Dynamics (EASD). Delft, Netherlands.

Taylor Z. J., M. T. L. Browne (2020). Hybrid pressure integration and buffeting analysis for multi-row wind loading in an array of single-axis trackers. Journal of Wind Engineering and Industrial Aerodynamics, 197. 10.1016/j.jweia.2019.104056

Taylor Z. J., M. A. Feero, M. T. L. Browne (2024). Aeroelastic instability mechanisms of single-axis solar trackers. Journal of Wind Engineering and Industrial Aerodynamics, 244, 10.1016/j.jweia.2023.105626

IN-VENTO 2024
International Conference of the Italian Association for Wind Engineering
Pisa, September 8th – 11th, 2024

Improving long-span bridge flutter performance by gyroscopic stabilizers: recent wind tunnel experiments

Gian Felice Giaccu[a] and Luca Caracoglia[b,c,d]

[a]*Department of Architecture, Design and & Urban Planning, University of Sassari, Alghero, Italy, gf.giaccu@uniss.it*
[b]*Visiting Professor, Dept. of Civil, Envir. & Mechanical Engr. (DICAM), Univ. of Trento, Italy*
[c]*Visiting Professor (June 2024), Dept. of Civil & Envir. Engr. (DICA), Univ. of Perugia, Italy*
[d]*Northeastern University, Boston, MA, USA, lucac@coe.neu.edu*

SUMMARY:
Gyroscopic devices have been routinely employed by mechanical engineers; however, they are seldom considered in the civil engineering field. This study examines the use of a gyroscopic stabilizer to improve the performance of long-span bridges against flutter. Recent experimental evidence is presented. Results are preliminary; nevertheless they indicate that torsionally-dominated flutter of a section model of the Golden gate Bridge can be successfully suppressed by the gyroscope: torsional rotations at incipient flutter can be reduced by a factor of four.

Keywords: long-span bridges, flutter, gyroscopic stabilizer

1. INTRODUCTION

The last decades have witnessed significant steps in the evolution of long-span cable-supported bridges. Some recent examples are the Çanakkale 1915 Bridge over the Dardanelles straits with a main span $\ell = 2023$ m, the Stonecutters Cable-stayed Bridge in Hong Kong with $\ell = 1018$ m (Kite et al., 2005), the Yi Sun-Shin Bridge in Korea with $\ell = 1545$ m (Kim et al., 2015), and the Xihoumen Suspension Bridge in China with $\ell = 1650$ m (e.g., Ma et al., 2020). New design concepts include main spans that may reach lengths of 5 km (e.g., Ding et al., 2023) or beyond. Fig. 1 - panel (a) (Ding et al., 2023), illustrates the current technologies for the design of super long bridges, and various types of cross section (SBS: single-box section, LTS: lattice truss section, NSS: narrow slotted two-box section, WSS: wide slotted two-box section). Current designs cannot satisfy minimum wind speed requirements for main span length $\ell > 2000$ m. Therefore, longer bridge spans necessitate the study of new methodologies to increase performance and avoid catastrophic flutter failure.

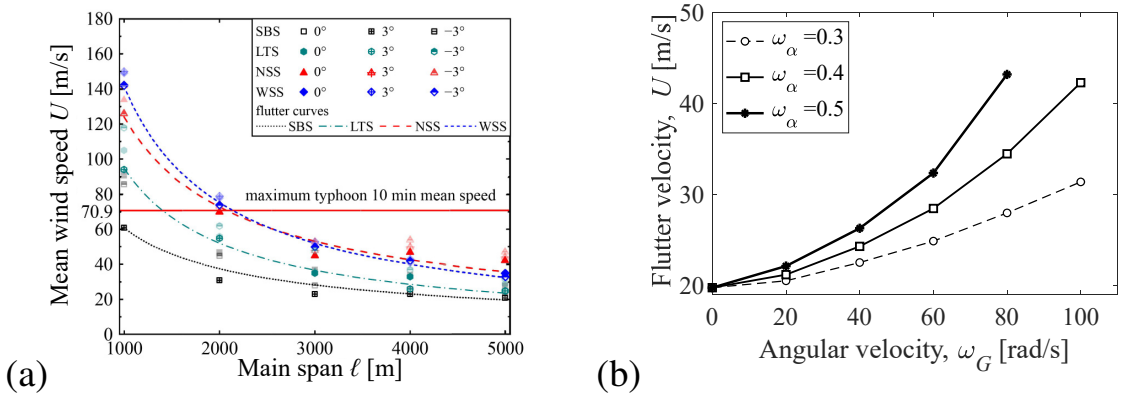

Figure 1. (a) Evolution of critical wind speed with bridge span length ℓ, reproduced from Ding et al. (2023). (b) G. Gate Bridge with proposed gyroscopic stabilizer: critical flutter speed vs. design-compatible ω_G values.

Existing solutions for improving long-span bridge performance against flutter, include aerody-

namic countermeasures, control surfaces and appendages, slotted girders, passive tuned-mass dampers and actively controlled devices. However, future long-span bridges can no longer rely on aerodynamic tailoring alone [Fig. 1 - panel (a)]. Dynamic control becomes the only viable option, especially for $\ell > 2000$ m. Gyroscopic devices have been employed by mechanical engineers (D'Eleuterio, 1986), and as a seismic protection system (Carta et al., 2017). This study demonstrates that a gyroscopic stabilizer can improve the performance of long-span bridges.

2. BACKGROUND

Two sets of gyroscopic devices are installed under the bridge deck at two deck cross sections, at sectional coordinates $x_{\Omega,1}$ and $x_{\Omega,2}$ (Giaccu and Caracoglia, 2024). Each gyroscopic unit is modeled as a system with a lumped mass moment of inertia and two three rotational DOFs (degrees of freedom), connected to the deck by a spring of stiffness k_α and a dashpot with damping coefficient c_α. The gyricity of the gyroscopic device can be expressed in general form as $\overrightarrow{\Omega} = J_{\Omega,p}\overrightarrow{\omega}_G$ where $\overrightarrow{\omega}_G$ is the angular velocity vector of the gyroscope, and $J_{\Omega,p}$ polar moment of inertia. Each $p = 1,2$ gyroscope has two main rotational DOFs: $\theta_1 = \theta(x_{\Omega,1},t)$, $\alpha_1(t)$ and $\theta_2 = \theta(x_{\Omega,2},t)$, $\alpha_2(t)$, respectively for device "1" at deck coordinate $x_{\Omega,1}$, and "2" at $x_{\Omega,2}$. The mean wind speed is U and direction is orthogonal to the deck axis. The aeroelastic lift and moment loads per unit deck span are $L_{ae}(x,t)$ and $M_{ae}(x,t)$; they are described by $H_i^*(K)$ and $A_i^*(K)$ Scanlan Derivatives (SDs) (Scanlan and Tomko, 1971) ($i = 1,...,4$); SDs depend on the mean wind speed U, i.e., reduced frequency $K = \omega B/U$ or velocity $U_r = 2\pi/K$. A schematic figure is presented below (Fig. 2) to demonstrate the proposed installation of the gyroscopic device under a bridge deck.

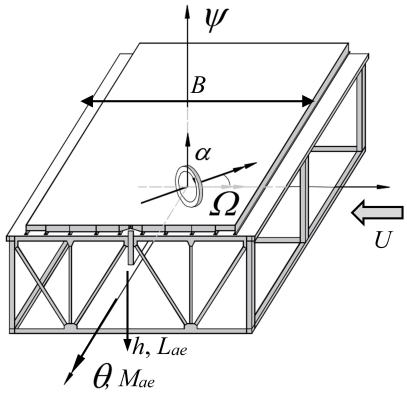

Figure 2. Schematics of bridge deck geometry and gyroscopic stabilizer

3. FULL-SCALE FLUTTER ANALYSIS RESULTS

The study evaluates a multi-unit gyroscopic stabilizer, installed on the Golden Gate bridge in San Francisco, California, USA. Aeroelastic instability is solved by multi-mode approach (Jain et al., 1996; Scanlan and Jones, 1990). The formulation is limited to two-mode coupled flutter of the deck, using modal expansion limited to vertical $g = v1$ and torsional $g = t1$ deck modes. The model is based on Giaccu and Caracoglia (2024).

The main bridge geometry quantities are: deck width $B = 27.43$ m, central span bridge length $\ell = 1263$ m. Structural properties of the bridge are derived from Jain et al. (1996). The first vertical deck mode (v1) has frequency 0.087 Hz and damping ratio 0.3%; the first torsional deck mode (t1) has frequency 0.192 Hz and damping ratio 0.3%; the mass of the deck is $m_h = 35,000$ kg/m; the mass moment of inertia of the deck is $J_\theta = 4,400,000$ kgm. The stabilizers are: two "twin devices" installed at $x_{\Omega,1} = 0.25\ell$, and two twin devices at $x_{\Omega,2} = 0.75\ell$. The

bridge's critical flutter speed without stabilizers can be as low as 22.0 m/s (Jain et al., 1996).

In Fig. 1 - panel (b), critical flutter speed is calculated by varying the gyricity of each single-unit gyroscope, Ω [kgm^2 rads^{-1}], i.e., the angular velocity ω_G. The angular frequency of the gyroscope's dynamics varies as $\omega_\alpha = \sqrt{k_\alpha / J_\alpha} = \{0.3, 0.4, 0.5\}$ [rad/s]. If the stabilizers are installed at deck sections $x_{\Omega,1} = 0.25\ell$ and $x_{\Omega,1} = 0.25\ell$, the t1 torsional modal rotations are opposite $\theta_{t1}(x_{\Omega,2}) = -\theta_{tv1}(x_{\Omega,1})$ (skew symmetric mode t1). Consequently, the sign of the gyricity, i.e., ω_G, imparted to twin devices at $x_{\Omega,2} = 0.75\ell$ and at $x_{\Omega,1} = 0.25\ell$ are opposite.

4. WIND TUNNEL TESTS

Wind tunnel section model tests have been conducted in Northeastern University's (NU's) wind tunnel in Fall 2023 to verify the technical feasibility, installation and device operations. Section model tests are carried out, using a 1:180 scale model of the Golden Gate Bridge, employed for verification purposes. The NU's aeroelastic setup for section model bridge deck tests is used. The two-DOF model setup replicates heave h and torsional rotation θ of the deck section; free-vibration tests at variable incoming U are employed.

The diameter of the rotating disk, which is part of the gyroscopic device, is about 25.4 mm and is made of brass to meet minimum requirements. The gyroscope is operated by two miniature, counter-rotating DC motors, model RF-370CH-10670-19.5, working at 0-12 V DC, 2400 RPM rated angular speed and with total power consumption equal to about 4 Watts.

The (a) panel in Fig. 3 shows the suspended model, connected to the balance and installed inside the test chamber; the air flows in the chamber from the bottom left corner. The horizontal motion of the model is restrained by piano wires. Vertical an rotational motions are enabled through appropriately calibrated, pre-stretched linear springs (visible in the panel's right corner). Vertical displacement and rotation of the deck are indirectly inferred from the measurements of forces transferred through the springs to the top/bottom fixed supports. Panel (c) of Fig. 3 illustrates fabrication and installation of the gyroscope. The gyroscopic device is embedded underneath the deck superstructure.

First, SDs are found by free-vibration (h, θ) coupled tests under uniform, low-turbulence flow conditions with mean flow speed U variable between 1.5 m/s and 13 m/s. The (b) panel of Fig. 3 presents, as an example, the measured A_2^* derivative vs. reduced velocity $U_r = U/(nB)$. The section model is equipped with the gyroscope. Measurements are carried out with inactive, turned-off gyroscope to separate the aerodynamics from the active stabilizer effects. Iterative Least-Squares are used to find SDs (Chowdhury and Sarkar, 2003). In panel (b) of Fig. 3, discrepancies are noticeable compared to experiments by Jain, visible at $U_r > 4$. Differences are plausibly associated with the simplified geometry used to replicate the bridge deck geometry at a small scale (1:180), the partial inability to reproduce the deck trusses composed of built-up steel members and the traffic/wind barriers that are not replicated in the NU's section model. In any case, the accuracy of A_2^* experimental values is still under investigation; more information will be provided in the near future.

Second, Fig. 4 documents another set of tests, conducted to verify the operations of the gyroscope by engaging post-critical flutter, unstable vibration at $U \approx 17$ m/s. The G. Gate Bridge deck model is initially clamped and suddenly released at time $t = 0$ in Fig. 4. The coupled vibration rapidly grows as the energy is absorbed from the flow. It must be noted that the unstable flutter stage is confined to a very short duration at the beginning of the time history in Fig. 4 to

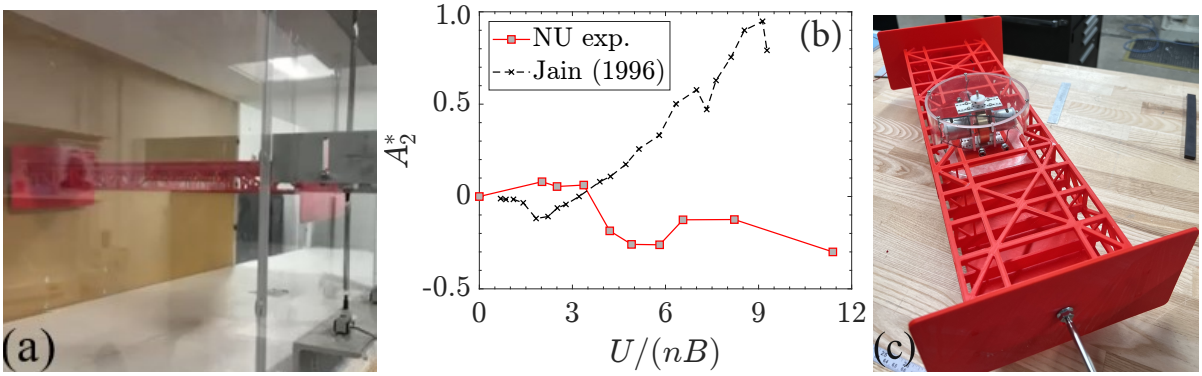

Figure 3. (a) G. Gate Bridge section model in NU's wind tunnel ; (b) A_2^* measured with inactive gyroscope vs. Jain et al. (1996); (c) fabrication of the gyroscope (bottom view).

avoid damaging the apparatus and the balance.

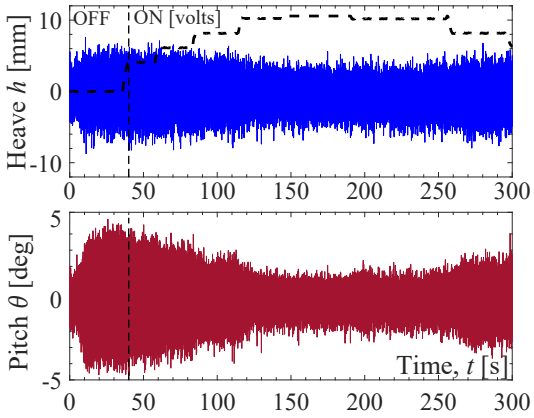

Figure 4. Wind tunnel: (top) heave h, (bottom) rotation θ of section model at incipient flutter - gyroscope off/on.

The gyroscope is subsequently activated at time $t = 40$ s. As the motor is turned on and the voltage is progressively varied at step-wise increments (4, 6 , 8, 10 V), as schematically indicated at the top of the h - heave panel) the angular rotation decreases and is reduced from large $\theta = \pm 5^\circ$ at $t = 30$ s to rotations $\theta = \pm 1^\circ$ at $t = 150$ s (bottom panel) that are four to five times smaller that the uncontrolled bridge case. It is anticipated that a much larger amplitude (amplitudes $\theta > 5^\circ$) would have been observed if no stabilization was applied. The bridge deck torsional vibration stops and post-critical flutter is basically avoided. At the same time, reduction of coupled heave motion (h) effect is noted, from 7mm amplitude ($h/B = \pm 0.04$ compatible with $\theta = 2.5^\circ$) by a factor of two (to about 3 mm or $h/B = \pm 0.01$).

5. CONCLUSIONS

The experimental results in Fig. 4 preliminarily demonstrate the efficacy of the apparatus, despite its simple operational mechanism. Additional, future examinations are still necessary.

ACKNOWLEDGEMENTS

Messrs. K. Braun and M. MacNeil (NU) are gratefully acknowledged for design and fabrication of the setup.

REFERENCES

Carta, G., I. Jones, N. Movchan, A. Movchan, and M. Nieves (2017). Gyro-elastic beams for the vibration reduction of long flexural systems. Proceedings of the Royal Society A: Mathematical, Physical and Engineering Sciences 473, 20170136.

Chowdhury, A. G. and P. P. Sarkar (2003). A new technique for identification of eighteen flutter derivatives using a three-degree-of-freedom section model. Engineering Structures 25, 1763–1772.

D'Eleuterio, G. (1986). *Dynamics of gyroelastic vehicles*. Tech. rep. UTIAS Report, No. 300. Univesity of Toronto Institute for Aerospace Studies.

Ding, Y., L. Zhao, R. Xian, G. Liu, H. Xiao, and Y. Ge (2023). Aerodynamic stability evolution tendency of suspension bridges with spans from 1000 to 5000 m. Frontiers of Structural and Civil Eng. 17, 1465–1476.

Giaccu, G. F. and L. Caracoglia (2024). Improving long-span bridge flutter reliability through gyroscopic stabilizer, considering random aeroelastic loads. Proceedings of XVII Conference of the Italian Association for Wind Engineering. Ed. by P. Schito and A. Zasso. Vol. 461. Lecture Notes in Civil Engineering (LNCE). Springer Nature Switzerland, 239–247.

Jain, A., N. P. Jones, and R. H. Scanlan (1996). Coupled aeroelastic and aerodynamic response analysis of long-span bridges. Journal of Wind Engineering and Industrial Aerodynamics 60, 69–80.

Kim, H., Y. Hwang, and S Kim (2015). Field monitoring and wind tunnel investigation of an unexpected wind-induced vibration of a suspension bridge. Proceedings of 7th International Conference on Structural Health Monitoring of Intelligent Infrastructure (SHMII 2015). Vol. 3. Intl. Society for Structural Health Monitoring of Intelligent Infrastructure.

Kite, S., K. Falbe-Hansen, T. Vejrum, N. Hussain, and J. Pappin (2005). Stonecutters Bridge — design for extreme events. Proceedings of IABSE Symposium: Structures and Extreme Events. Lisbon, Portugal, 14-17 September 2005, 27–34.

Ma, C., C. Pei, H. li Liao, M. Liu, and M. Li (2020). Field measurement and wind tunnel study of aerodynamic characteristics of twin-box girder. Journal of Wind Engineering and Industrial Aerodynamics 202, 104209.

Scanlan, R. H. and N. P. Jones (1990). Aeroelastic analysis of cable-stayed bridges. Journal of Structural Engineering, ASCE 116, 279–297.

Scanlan, R. H. and J. J. Tomko (1971). Airfoil and bridge deck flutter derivatives. Journal of Engineering Mechanics, ASCE 76, 1717–1737.

Stack Effects in High-rise Buildings: Challenges, Design Constraints and Mitigation Measures

E. Hii [1], S. Cammelli [2]

[1]*WSP, London, United Kingdom, elvin.hii@wsp.com*
[2]*WSP, London, United Kingdom, stefano.cammelli@wsp.com*

SUMMARY
Stack effect is a buoyancy-driven phenomenon that commonly occurs in high-rise buildings. It is primarily driven by temperature differences between the internal spaces of a building and the temperature of the outdoor environment. In winter, the warmer air inside the building typically rises through vertical airflow pathways (e.g. lift shafts, stairwells, risers, etc.), which creates a pressure difference that drives infiltration and exfiltration of air at the bottom and top of the building respectively. On the other hand, in summer, a 'reverse' stack effect process occurs – the colder air inside the building sinks to the lower levels and is pushed out close to street level. This paper is aimed at providing insights to the challenges, mitigation measures and design constraints that are typically encountered when considering the stack effect performance of high-rise buildings.

Keywords: Stack Effect, High-rise Buildings, Wind Pressures, Wind Tunnel Testing, Neutral Pressure Plane, HVAC, Wind-induced Noise, Airflow Network Model.

1. INTRODUCTION

Stack effect is a phenomenon that commonly occurs in high-rise buildings and that is primarily driven by temperature differences between the internal spaces of a building and the temperature of the outdoor environment (Jalayerian and Jensen, 2023). The authors of this technical paper have conducted stack effect studies on various high-rise building developments, particularly within the United Kingdom (UK). These studies were either aimed at informing the design process or to retrospectively diagnose and mitigate post-construction issues related to stack effect. Although the purview of this paper is inherently more relevant to the UK climate and building design practices and typologies, many of the underlying principles presented are applicable to a wider context. This paper is aimed at providing insights to the challenges, mitigation measures and design constraints that are typically encountered when considering the stack effect performance of high-rise buildings.

2. CHALLENGES

2.1.Modelling and Boundary Conditions

As part of a stack effect study, a multi-zone airflow network model is typically constructed for the purpose of conducting numerical simulations using programs such as CONTAM (Dols and Polidoro, 2020). A large amount of input data is inherently required for the construction of the detailed airflow network model – e.g., architectural layouts; airtightness data for various building elements; lift venting strategy; HVAC schedules/specifications; indoor and ambient design temperatures; door dimensions; door crack sizes, shaft/duct connections, etc. For the results to be relevant to the design of a building, the information used in the study needs to be accurate. During

the early stages of the design, detailed information is typically scarce. Additionally, changes to the design parameters as the design of a development progresses could have a significant impact on the results of the stack effect study. Discrepancies between the design specifications of various elements and the actual 'as-built' performance could result in further differences between the analytical results and the actual performance of the building from a stack effect perspective. External wind pressures acting on the façade of a building (positive pressures) tend to enhance infiltration and reduce exfiltration of air, whereas suctions (negative pressures) have the opposite effect. The wind pressure distribution on a high-rise building can have a significant impact on stack effect performance and should therefore always be considered within a stack effect study: this, inevitably, increases the complexity of the modelling process. The wind pressure distribution is either estimated using a code-based approach or derived from experimental data, with the latter being the preferred approach as it provides a more accurate representation of the actual wind pressure distribution at the project site.

2.2.Design Challenges

The following design challenges typically occur in relation to stack effect in a high-rise building (Mijorski and Cammelli, 2016):

- Excessive pressure differences across various doors, resulting in difficulties opening and closing them. Power-assisted doors could experience motor failure and breakage of the opening/closing device.
- Uncomfortable and/or excessive airflow movement within internal spaces.
- Flow-borne noise (whistling) caused by excessive airflow through narrow gaps or openings.
- Inefficient heating or cooling strategy due to excessive infiltration of cold/hot air – increased mechanical requirements and energy supply needed to heat/cool the internal spaces.
- Propagation of smoke, odours and other unwanted contaminants throughout the building.

3. MITIGATION MEASURES AND DESIGN CONSTRAINTS

Measures typically used to counter-act or mitigate the impact of stack effect include:

- Revolving doors.
- Vestibules.
- Strategic introduction of intermediate doors.
- Adjustments to the lift/stairwell shaft venting strategy.
- Mild net positive pressurization of the ground floor lobby areas, particularly during the winter months.
- Improvement of the air tightness of the building envelope.
- Introduction of vertical separations – e.g., sky lobbies to minimise continuous lift shafts, and intermediate landing areas (with vestibules) for stairwells.

Of the list above, the top two are particularly important and therefore further details on them are provided in the sub-sections below.

3.1.Revolving Doors

Revolving doors are often prescribed at key building entry points to prevent/mitigate stack effects. By design, a revolving door prevents an opening from being created in the building envelope when

pedestrian ingress/egress from a building occurs. As such, the pressure differences acting across the building envelope are not transferred to the internal spaces. However, building regulations in the UK typically stipulate the need for a pass door – which often comprises a swing door - to be provided in conjunction with the revolving door for accessibility reasons. The revolving doors are theoretically designated as the main access points, whilst the pass doors are meant to be used only when necessary (and therefore infrequently). However, in practice, the use of the revolving door is often neglected in favor of the pass door, as the latter tends to provide a more direct/convenient access. In doing so, the benefits provided by the revolving doors are negated. It is therefore advisable for the building management to restrict use of pass doors, for example by issuing customized access cards on a discretionary basis and/or appropriate signage to redirect pedestrian traffic through the main revolving doors (see Figure 1).

Figure 1. Example image of a revolving door and a pass door (left), and an enlarged image of the sign on the pass door (right).

3.2.Vestibules and Intermediate Doors

Vestibules and intermediate doors are commonly recommended as a means of preventing direct airflow pathways and transfer of pressures to the building cores (e.g., lift shafts, stairwells, and risers) from occurring when doors along the façade are open. The left image of Figure 2 shows the ground floor plan of a 50-storey residential building in London. As part of the design of the building, an intermediate door was introduced between the reception area and the lift lobby to pre-emptively mitigate stack effect. However, post-construction, the building management reported problems with lift doors getting stuck or not closing properly (middle image of Figure 2) and the occurrence of 'whistling' noises particularly on cold and/or windy days. A site inspection conducted by WSP revealed that even though the main entrance doors and the intermediate door were positioned approximately 6m apart, both sets of doors were often simultaneously open due to the volume of people moving in/out of the building – which would likely increase over time, given that the building was only at ~20% occupancy. Additionally, there were sizeable gaps between the intermediate door and its mounting frame (right image of Figure 2), through which significant wind-induced noise was generated. Therefore, the use of intermediate doors or vestibules to mitigate stack effect should be carefully considered and implemented. To prevent the

two sets of doors from being simultaneously open, an ‘airlock’ system (whereby one set of doors would not open until the other is closed) can be implemented. However, this creates ‘staging’ areas between the two sets of doors, which could cause interruptions/complications from a pedestrian flow perspective.

Figure 2. Illustration of ground floor plan (left), gap in lift doors resulting from inability to properly close (middle), and the gap between the intermediate door and its mounting frame (right).

REFERENCES

Jalayerian, M. and Jensen, T. (2023). Stack Effect in Tall Buildings. Council on Tall Buildings and Urban Habitat (CTBUH), Chicago, Illinois, USA.

Dols, W.S. and Polidoro, B.J. (2020). CONTAM User Guide and Program Documentation Version 3.4, National Institute of Standards and Technology (NIST) Technical Note 1887.

Mijorski, S. and Cammelli, S. (2016). Stack Effect in High-Rise Buildings: A Review. International Journal of High-Rise Buildings, Vol 5, No 4, 327-338.

IN-VENTO 2024
International Conference of the Italian Association for Wind Engineering
Pisa, September 8th – 11th, 2024

Influence of dune-dune interaction on sand dune migration and evolution: Wind tunnel experiment

Sumaja Kolli[1&2], Anuj Bind[2], Hassan Hemida[1], Pradeep Kumar Dammala[2]

[1]*Department of Civil Engineering, University of Birmingham, Birmingham, United Kingdom, sxk1375@student.bham.ac.uk*

[2]*Department of Civil and Infrastructure Engineering, Indian Institute of Technology Jodhpur, Rajasthan, India, kolli.1@iitj.ac.in*

SUMMARY (10 pt)

To comprehend a deeper understanding of wind-dune interaction in aeolian soil erosion, the effect of dune geometry in a single dune as well as a system of dunes settings is investigated. Associated dune dynamics are detailed through soil mass loss percentage (SML) at different stoss slopes of upwind dune and distance between them. From the experimental wind tunnel studies, it is realized that for same inlet speed, the dune shape of upwind dune (primary dune) hugely impacts the downward dune (secondary dune) evolution and erosion. With decrease in the stoss slope of primary dunes, secondary dunes experienced a considerably huge SML with almost complete erosion in contrast to single dune settings. The variation of zone of recirculation with stoss slope is realized as the crucial factor in secondary dune erosion at all slopes whereas the distance between the primary and secondary dunes played a huge role with increase in stoss slope.

Keywords: Aeolian erosion, Sand dune, Wind tunnel experiment

1. INTRODUCTION

Global warming and associated climate dynamics have accelerated aeolian soil erosion, a crucial process in shaping sand dunes and ripples (Baas & Delobel, 2022). Realizing the impact, many researchers since pioneering work of Bagnold (1941) studied dune morphology and related aspects. Since sand dunes evolve continuously with time, their interaction with wind and surroundings keeps modifying, hence extensive work was done on understanding on influence of windward and leeward slopes on sand transport dynamics (Walker and Nickling, 2002; Parson et al., 2004; Dong et al., 2007, Faria et al., 2011). However, most of these aeolian studies focus on understanding aeolian erosion in single dune settings or on stationary models with contrary settings of field where a system of mobile dunes or dunes in the wake of obstruction are found. While recent studies have been focusing on understanding the dune – dune interaction (Ferreira and Fino, 2012) and dune- obstacle interaction (Bacik et al., 2021), authors believe that the dune-dune interaction requires further advanced understanding in terms of impact of windward slope. In the present study, we aim to bridge this gap by investigating the impact of stoss slope in single dune setting and dune-dune interaction systems. By assuming an identical lee slope with same dune height, the effect of stoss slope is examined in wind tunnel setup simulating atmospheric boundary

layer conditions. The interference effect arising from dune-dune interaction is further investigated by varying the distance between primary and secondary dune system.

2. METHODOLOGY

2.1. Wind Tunnel

Experiments were carried out at the subsonic wind tunnel (WT) setup of 0.62m high, 0.6m wide and 4m long at Indian Institute of Technology Jodhpur, India. The schematic setup of WT is illustrated in Fig. 1(a) with details of position of dune models. The width of models is spanned across the width of WT as detailed in Fig. 1(b) representing a 2D transverse dune. Single channel electronic manometer connected to the pitot static tube was utilized to measure the wind velocities. The streamwise velocity profile at 0.5m from outlet of empty WT matches power law approximation with an exponent (α) of 0.13 similar to the arid settings of White (1996) study on sand dunes.

$$\frac{u_z}{u_0} = \frac{z}{z_0}^{\alpha} \quad (1)$$

Here u_z and u_0 are the streamwise velocities along wind tunnel height (z) and at the reference height ($z_0 \approx 0.22$m) beyond the boundary layer thickness of 0.18m. At an undisturbed wind velocity of 9.4m/s, all the test cases are investigated in WT for 5minute testing duration.

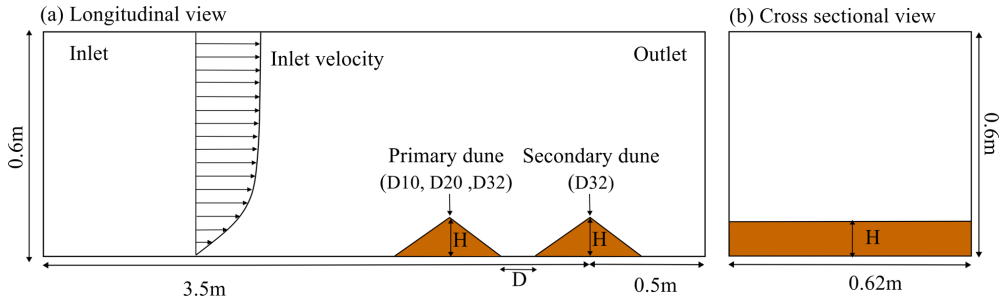

Figure 1. Schematic representation of WT at IITJ, India. (a) Longitudinal view (b) Cross sectional view

Table 1. Dune geometries and configurations for WT testing

S. No	Dune Configuration	Distance between dunes (D)	Dune geometry and placement	
			Primary Dune	Secondary Dune
1	Single Dune	-	D32	
2	Interaction studies	5H	D32, D20 and D10	D32
		10H		
		15H		

2.1. Model geometry and configuration

Desert sand sampled from Osian sand dunes of Thar Desert was used to develop the sand dune models of identical height (H-50mm) and lee slope (32°) matching the angle of repose of desert soils. Table 1 details all the test cases investigated in the current study. Dunes with different stoss slopes (10°, 20° and 32°) are denoted by D10, D20 and D32. The single dune setting focuses solely on D32, while the interaction studies examine the primary dune in the upwind direction and a fixed secondary dune (D32) in the downwind direction. The dune-dune distance (D) varied between 5H-15H. The reported soil mass loss (%) is the difference between initial weight and residue left after testing.

3. RESULTS & DISCUSSIONS

3.1. Single dune setting

Fig. 2 details the single dune setting of D32 eroded by 14.3% at an undisturbed wind speed of 9.4 m/s for 5minutes testing duration, placed at 0.5m from exit of WT. Visible crest disturbance is realized where sand migrated from stoss side is transported and eroded with partial soil deposition in the lee side. Given that steeper slope dunes like D32 with similar bluff body characteristics expect a zone of recirculation in lee side, shadow dunes or extended dune in lee side arises as shown in Fig. 2(b).

Figure 2. Temporal evolution of D32 at testing duration of (a) t=0' (b) t=5'. View from the top of testing section with arrow indicating inlet wind direction.

3.2. Dune-dune Interaction studies

Variation of SML (%) in dune-dune interaction settings is presented in Fig. 3. While the secondary dune is maintained constant as D32 in all cases, primary dune with different stoss slope and distance between the dunes is investigated.

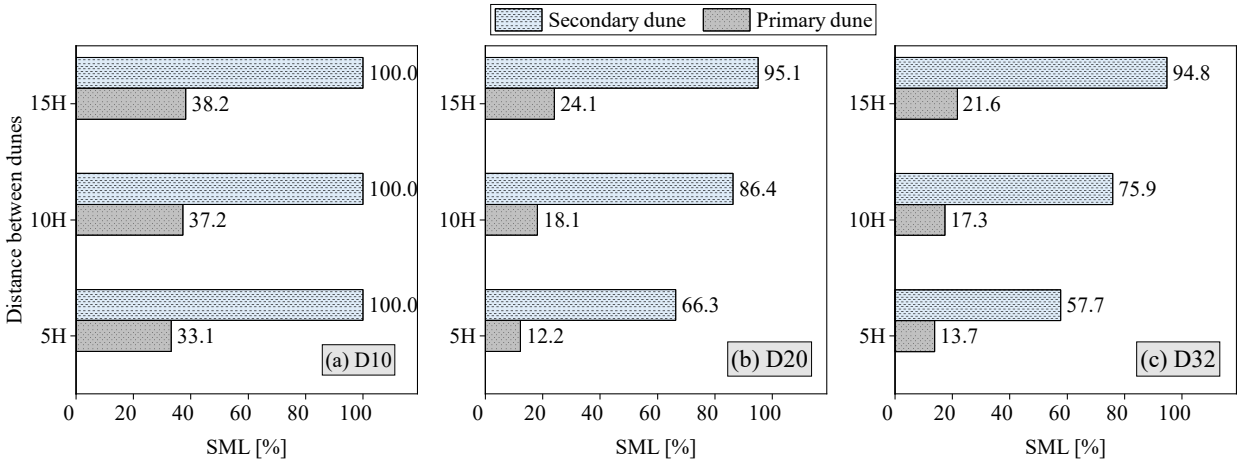

Figure 3. Variation of soil mass loss (SML) in the dune interaction studies

The maximum SML in primary dune is observed in the case of D10 followed by D20 and D32. SML findings of primary dune agree well with Faria et al., 2011 study on stoss slope effect on aeolian erosion. It is realized from current study and existing literatures that with increase in stoss slope, the resistance to wind flow increases reducing the erosion potential. A gentler slope offers better wind flow acceleration compared to steeper slopes and since aeolian erosion is driven by wind that explains the primary dune erosion phenomenon. Further, it is noted that secondary dune in downwind of D10 primary dune is completely eroded (100%) irrespective of distance between dunes. In case of D32 (see Fig. 3c) with both primary and secondary dunes as D32, the primary dune eroded similar to single dune settings. However, the secondary dune experiences considerably high erosion of 57.7% even at far distances of 15H, contrasting the single dune setting scenario where it was 14.3%. Walker et al., (2004) study on secondary flow highlights that flow separation at crest accompanied by adverse pressure gradient results in a zone of recirculation

characterized by reversal of flow in lee side of dune. This zone of recirculation largely depends on stoss angle and dune height rather than wind velocity (Parsons et al. 2004 and Dong et al., 2007). With the increase in stoss slope and dune height, the size of zone of recirculation increases. While the exact vortex and eddy definition for the current study requires further numerical investigation, it is expected that for the same wind velocity and dune height, D10 is expected to have the smallest flow reversal zone followed by D20 and D32. Ferreira et al., (2012) study concludes that the reattachment point after the zone of recirculation characterized by highly turbulent flow experiences enhanced erosion as seen in D10 and D20 (Fig. 3a and Fig. 3b). Furthermore, primary dunes experience streamline compression with flow acceleration upwind of dune whereas secondary dunes with modified streamline curvature and increased turbulence in lee of dune experience expedited erosion for the same inlet velocity.

4. CONCLUSIONS

Preliminary wind tunnel investigations were conducted on the single dune and dune-dune interaction studies to understand the influence of primary dune geometry on aeolian erosion. At an identical lee slope and model height, three stoss slopes of primary dune were varied at 5H, 10H and 15H distance from secondary dune. The soil mass loss (%) was used as quantitative estimate of aeolian erosion at an undisturbed wind speed of 9.4m/s. Contrary to the single dune settings, where D32 experienced 14.3% SML, secondary dunes in dune-dune interaction experienced huge SML at 15H. Further, gentler stoss slopes resulted in full sweep of secondary dune independent of distance between dunes. Influence of primary dune stoss slope on zone of recirculation ahead of secondary dune is also realized. However, it must be noted that the current investigation was limited to fixed secondary dune (D32) at unidirectional wind profile, whereas oblique wind and dune orientation could be expanded in future research.

ACKNOWLEDGEMENTS

We thank the Commonwealth Scholarship Commission in the UK (CSC) for funding the academic visiting period at University of Birmingham, UK.

REFERENCES

Baas, A. C., & Delobel, L. A. (2022). Desert dunes transformed by end-of-century changes in wind climate. Nature Climate Change, 12(11), 999-1006.

Bagnold, R. A. 1941. The physics of blown sand and desert dunes. Boca Raton, FL: Chapman & Hall.

Walker, I. J., & Nickling, W. G. (2002). Dynamics of secondary airflow and sediment transport over and in the lee of transverse dunes. Progress in Physical Geography, 26(1), 47-75.

Dong, Z., Qian, G., Luo, W., & Wang, H. (2007). A wind tunnel simulation of the effects of stoss slope on the lee airflow pattern over a two-dimensional transverse dune. Journal of Geophysical Research: Earth Surface, 112(F3).

Faria, R., Ferreira, A. D., Sismeiro, J. L., Mendes, J. C., & Sousa, A. C. (2011). Wind tunnel and computational study of the stoss slope effect on the aeolian erosion of transverse sand dunes. Aeolian Research, 3(3), 303-314.

Ferreira, A. D., & Fino, M. R. M. (2012). A wind tunnel study of wind erosion and profile reshaping of transverse sand piles in tandem. Geomorphology, 139, 230-241.

Bacik, K. A., Canizares, P., Caulfield, C. C. P., Williams, M. J., & Vriend, N. M. (2021). Dynamics of migrating sand dunes interacting with obstacles. Physical Review Fluids, 6(10), 104308.

Parsons, D. R., Walker, I. J., & Wiggs, G. F. (2004). Numerical modelling of flow structures over idealized transverse aeolian dunes of varying geometry. Geomorphology, 59(1-4), 149-164.

IN-VENTO 2024
International Conference of the Italian Association for Wind Engineering
Pisa, September 8th – 11th, 2024

Wind tunnel numerical modeling for wind farm control strategies

Tiziano Leone[a], Filippo Calamelli[a], Paolo Schito[a], Alberto Zasso[a]

[a]*Department of Mechanical Engineering, Politecnico di Milano, Milan, Italy,*
tiziano.leone@polimi.it, filippo.calamelli@polimi.it, paolo.schito@polimi.it,
alberto.zasso@polimi.it,

SUMMARY:
In wind energy and wind engineering research it is of fundamental importance to reproduce correctly the Atmospheric Boundary Layer (ABL). During wind tunnel testing various techniques are utilized, and the resulting ABL is borne out of the interaction of the peculiar chamber configuration with the incoming flow. Correctly reproducing this interaction in a numerical setting it is important to be able to validate the codes' performance through the experimental measurements performed in the wind tunnel. This study aims to reproduce numerically the Politecnico di Milano wind tunnel (GVPM) by comparing the performance of the numerical model with complete experimental mapping obtained through 3D hot-wire anemometer measurements. Subsequently, the results achieved by a numerical wind turbine model immersed in the wind tunnel simulation will be compared to the ones obtained with a standard precursor ABL simulation and to experimental data.

Keywords: Atmospheric boundary layer, Wind tunnel numerical modeling, Large eddy simulation, Actuator line model, Wake recovery

1. INTRODUCTION

To study the action of the wind on man-made structures in the lower part of the atmosphere (wind turbines, buildings, etc.) ad-hoc wind tunnels have been developed to reproduce the peculiar characteristics of the Atmospheric Boundary Layer (ABL). Engineering codes prescribe the characteristics of the ABL to be taken into account depending on the location of the structure. Correctly representing the wind characteristics during wind tunnel testing is a fundamental aspect of the craft (Blocken, 2018; Wu, 2017), both from an experimental and a numerical point of view. During wind tunnel testing it is thus necessary to reproduce a target boundary layer, through the use of turbulence-generating geometrical objects, such as spires and blocks, arranged in various configurations (Irwin, 1981). The resulting ABL is a product of the configuration chosen and the flow entering the test section, which depends on a lot of factors. It is often discounted, but the inlet flow at the beginning of the test section is affected by the objects inside the chamber, depending on their blockage ratio.

In the context of numerical simulations that have as objective the reproduction of the ABL with its unsteady characteristics, multiple approaches have been proposed (Yan and Li, 2015). Recycling methods and synthetic turbulence are very useful for reducing computational costs by replacing the physical modeling of the wind tunnel. Nevertheless, they are not usually able to fully capture the behavior of the flow that actually impinges on the object during the experiments. This is why, for validating numerical codes for wind energy applications, such as the Actuator Line Models (ALM) developed in-house (Cioffi et al., 2020; Muscari et al., 2023; Sanvito et al., 2023), with experiments performed in the wind tunnel, the correct representation of the behavior of the flow actually acting on the wind turbine cannot be discounted. This is especially true for wind farm control, due to the relevant impact of the length scales of the

flow (Hodgson et al., 2023).

It is thus important for a facility such as GVPM to be able to reproduce with fidelity, through the means of Large Eddy Simulations (LES), the behavior of the flow inside its test section under multiple ABL configurations. The GVPM facility is an interesting example, characterized by the presence of two test sections arranged in a vertical layout, as shown in Fig. 1. Moreover, the entrance of the ABL section comes after a pressure drop due to the presence of the heat exchanger, resulting in a background turbulence in the order of 2% throughout all the section. The numerical results will be validated against the experimental measurements performed during the CL-Windcon test campaigns, in which the mapping of the chamber through the use of 3D-hotwire anemometers has been carried out at 2 plane locations, in different roughness configurations.

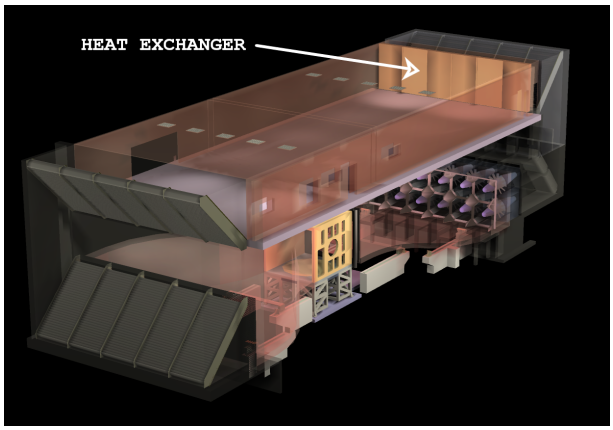

Figure 1. GVPM Wind tunnel rendering

In the context of wake control strategies, a complete numerical model of the GVPM wind tunnel will then allow us to compare the results obtained by the ALM codes with the experiments that will be performed in the GVPM wind tunnel. We will be able to quantify more accurately the impact of the length scales of the actual flow on the wake recovery behavior, by comparing the results with the ones obtained through more conventional practices, such as precursor-successor simulations or synthetic generation. Moreover, for what concerns synthetic turbulence generation for ABL, a numerical model of the GVPM wind tunnel will help us validate such methods by offering a complete insight into the wind to be matched at the test location. Lastly, such a model will also be able to inform the test engineers on the complete wind behavior varying the turbulence-generating objects configuration, to develop new ones more representative of the wind behavior at real scale.

2. METHODOLOGY

2.1. Part 1: GVPM numerical model

The first part of the work aims to accurately reproduce numerically the flow inside the test section of GVPM. Therefore, wall-modeled Large Eddy Simulations will be employed, describing as accurately as possible the wind tunnel geometry. The peculiar characteristics of the GVPM wind tunnel pose some challenges from the numerical point of view. It is incorrect to reproduce the flow impinging on the initial spires as a uniform zero-turbulence flow. The flow entering the chamber presents a background turbulence of 2%, and the presence of the spires close to the entrance generates a vertically non-uniform blockage, thus a non-uniform wind velocity profile. Initially, it is fundamental to reproduce the flow condition due to the si-

multaneous contribution of both spires and the porous media, representing the heat exchanger. To model the heat exchanger without resolving its geometry a Darcy-Forchaimer model will be employed. A first analysis will be carried out to evaluate the length of the upstream fetch, shown in Fig. 2, necessary to correctly reproduce the interaction of the flow with the spires and the porous media. The validation will be performed with the two configurations mapped during CL_Windcon, one off-shore low-turbulence, and the other on-shore high-turbulence. Since the high-turbulence configuration presents some brick elements, computationally expensive to mesh accurately, the results' dependency on grid refinement will be analyzed. To assess the predictive performances of the model, simulations of other different configurations will be carried out. For these, the model's performance will be evaluated on the wind profiles obtained at the test table location.

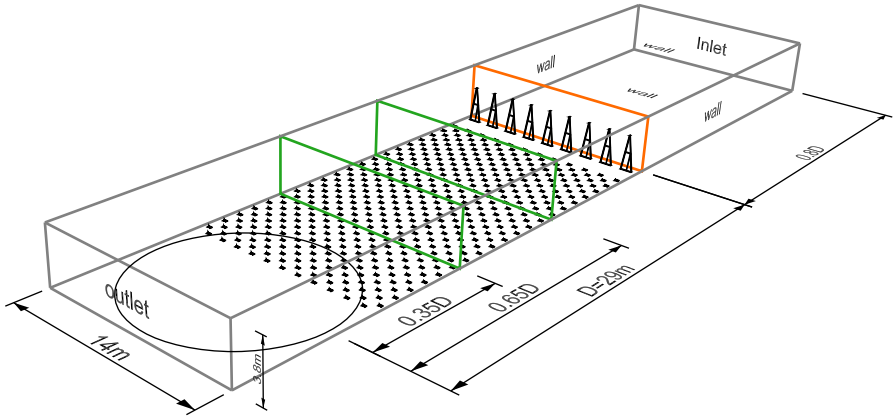

Figure 2. Scheme of the CFD model in the on-shore configuration. The orange plane indicates the heat exchanger, while the green planes represent the mapping made by 3D-hotwire anemometers. D indicates the distance between the center of the rotating test table and the heat exchanger.

2.2. PART 2: Validation of ALM codes in ABL flow

Once the GVPM numerical model has been validated, it will be possible to assess the results obtained with the in-house ALM codes. Extensive testing campaigns have already been carried out (Bayati et al., 2018), and others will be in the near future in which a Particle Image Velocimetry (PIV) mapping of the wind turbine wake will be produced in different tilt/yaw configurations. The ALM will be implemented in the simulations through the use of the SOWFA OpenFOAM open-source module. Comparing the results obtained through the use of precursor-successor simulations, the numerical wind tunnel simulations and experimental tests will offer insights into the wake recovery mechanisms for wind turbines immersed in the ABL, as well as a method to validate more accurately the ALM models.

3. PRELIMINARY RESULTS

The presentation of results will first focus on the performance of the GVPM model compared to the measurements performed during the CL_Windcon testing campaign. The impact of the most important modeling choices, i.e. the antecedent fetch, the modeling of the porous layer, and the mesh refinement, will be investigated. Some preliminary results in terms of velocity and turbulence intensity profiles are shown in Fig.3, at different distances from the entrance of the chamber. The simulated profiles show a good agreement with the experimental ones, specifically at the location near the rotating table. Moreover, the velocity profiles present a knee

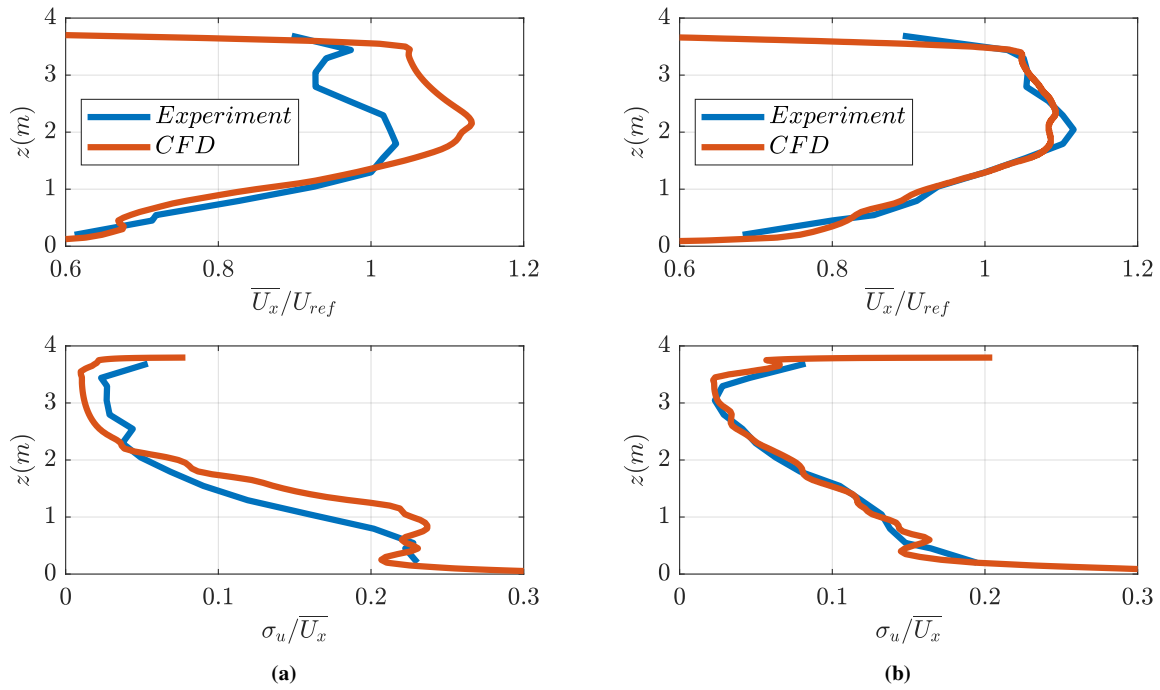

Figure 3. Normalized wind velocity (with respect to the velocity at z=1.3m) and longitudinal turbulence intensity profiles comparison for the on-shore configuration at **(a)** 0.65D and **(b)** 0.35D before the center of the test table, where D is defined in fig. 2.

at around 2m height, which could have a potential impact on the wake recovery mechanisms.

Subsequently, the results obtained by placing the modeled wind turbine in the numerical GVPM flow will be compared to the ones derived using a standard precursor-successor approach. Their performance with respect to experimental PIV data will be assessed in terms of wake recovery behavior.

REFERENCES

Bayati, I, M Belloli, L Bernini, D. Boldrin, K Boorsma, M Caboni, M Cormier, R Mikkelsen, T Lutz, and A Zasso (2018). UNAFLOW project: UNsteady aerodynamics of FLOating wind turbines. Proceedings of Journal of Physics: Conference Series. Vol. 1037. IOP Publishing, 072037.

Blocken, B. (2018). LES over RANS in building simulation for outdoor and indoor applications: A foregone conclusion? Proceedings of Building Simulation. Vol. 11. Springer, 821–870.

Cioffi, A., C. Muscari, P. Schito, and A. Zasso (2020). A steady-state wind farm wake model implemented in openfast. Energies 13, 6158.

Hodgson, E. L., M. H. A. Madsen, and S. J. Andersen (2023). Effects of turbulent inflow time scales on wind turbine wake behavior and recovery. Physics of Fluids 35.

Irwin, H. (1981). The design of spires for wind simulation. Journal of wind engineering and industrial aerodynamics 7, 361–366.

Muscari, C., P. Schito, A. Vire, A. Zasso, and J.-W. van Wingerden (2023). An advanced approach to velocity sampling in actuator line models. Authorea Preprints.

Sanvito, A. G., G. Persico, P. Schito, V. Dossena, and A. Zasso (2023). Comparative assessment of actuator-Line modeling of FOWT rotor aerodynamics to wind tunnel experiments. Proceedings of Journal of Physics: Conference Series. Vol. 2626. IOP Publishing, 012063.

Wu, X. (2017). Inflow turbulence generation methods. Annual Review of Fluid Mechanics 49, 23–49.

Yan, B. and Q. Li (2015). Inflow turbulence generation methods with large eddy simulation for wind effects on tall buildings. Computers & Fluids 116, 158–175.

IN-VENTO 2024
International Conference of the Italian Association for Wind Engineering
Pisa, September 8th – 11th, 2024

Reduced-Order modeling for Atmospheric Boundary Layer Flows integrating Dimensionality Reduction and Non-linear Regression

Haoyan Li [1,2], Leo Cotteleer[1,2], Alessandro Gambale [3],Alessandro Parente [1,2]

[1] *ATM Laboratory, Universite Libre de Bruxelles, Brussels, Belgium, haoyan.li@ulb.be*
[2] *Brussels Institute for Thermal-fluid systems and clean Energy, ULB and VUB, Brussels, Belgium*
[3] *BuildWind SRL, Brussels, Belgium, gambale@buildwind.net*

SUMMARY
The current work presents how to develop the reduced-order model (ROM) for atmospheric boundary layer flows in urban areas. A methodology combining dimensionality reduction, by means of Principal Component Analysis (PCA) and Local PCA, and non-linear regression, implementing Gaussian Process Regression (GPR), was developed to build the framework of ROMs for the prediction of pollutant concentrations at unexplored operating conditions. Three-dimensional simulations for flow over a single building were carried out, spanning a range of friction velocities, roughness lengths and pollutant sources velocities. Based on the conducted simulations, a ROM was developed to predict pollutant dispersion for operating conditions not included in the ROM development. Posterior tests demonstrated that ROM could reliably predict the pollutant concentration with mean absolute relative error below 10%.

Keywords: atmospheric boundary layer flows, CFD, reduced-order model

1. INTRODUCTION

Understanding the atmospheric boundary layer (ABL) flows in city regions is important in air pollution reduction. However, a range of uncertain parameters and large computational domain brings about challenges in the numerical studies of ABL flows in cities, the unaffordable computational costs for the exploration of the relevant boundary conditions and modelling parameters. Therefore, developing reduced-order models (ROMs) is an accessible route to investigate the physical processes taking place in ABL flows.

The objective of the current work is to build a physics-based ROM by using Principal Component Analysis (PCA) and Local PCA to extract the key flow features of the ABL flows, then the non-linear regression, utilizing Gaussian Process Regression (GPR) to map the input parameters of the operating conditions into coefficients of the extracted flow features. Once the mapping between inputs and outputs is embedded in a ROM, the system can predict flows under new operating conditions.

The ROM is demonstrated for the pollutant dispersion flow around a wall-mounted building and an array of buildings from the CEDVAL database. A set of training simulations is obtained by defining a realistic range of values for input parameters with respect to the benchmark ABL case. An ABL turbulence model based on k-omega (Bellegoni et al, 2019) and pollutant transport model (Longo et al., 2019) is employed for the numerical simulations.

2. METHODS

2.1. Principal Component Analysis

A matrix **Y** is the collection of the CFD simulations dataset with size $(m \times n)$, where the column is a vectorized 2D or 3D spatial field of variables such as velocity and turbulent kinetic energy fields, obtaining from one CFD simulation. Therefore, n is the total number of simulations and m is the number of grid-points times the number of chosen variables.

By computing the eigen-value decomposition for the covariance matrix of $\mathbf{Y}$, the principal components **A** (PCs) with size $(n \times n)$ are identified from:

$$\mathbf{C} = \frac{1}{\mathrm{n}-1}\mathbf{Y}^{\mathbf{T}}\mathbf{Y} = \mathbf{A}\mathbf{L}\mathbf{A}^{\mathbf{T}} \tag{1}$$

where **L** is the diagonal matrix of the eigen-values with size $(n \times n)$ and **A** is the orthogonal matrix. By projecting the original data **Y** to the principal components **A**, the PCA modes $\mathbf{Z} = \mathbf{Y}\mathbf{A}$ with size $(m \times n)$ are found as the spatial shapes. Then the original data can be reconstructed by only keeping important PCs as follows:

$$\mathbf{Y} = \mathbf{Z}\mathbf{A}^{\mathbf{T}} \approx \boldsymbol{Z_q A_q^T} \tag{2}$$

Different from the PCA, the Local PCA firstly classify the original data **Y** into different sets according by clustering methods (Zdybał et al, 2023) and then dimensionality of each set is reduced exploiting PCA.

2.2. Gaussian Process Regression

The column of **Y** represents various simulations so that one simulation can be expressed as a weighted sum of modes:

$$\boldsymbol{y}(\boldsymbol{x}) = \sum_{i=1}^{q} a_i(\boldsymbol{x})\boldsymbol{z}_i \tag{3}$$

where $\boldsymbol{x}$ is the set of input parameters relating to different operating conditions. The prediction of the coefficients in the unexplored operating conditions can be conducted using a GPR. In the framework of GPR, $\boldsymbol{a}(\boldsymbol{x})$ is expressed by multi-variate Gaussian distribution which is defined:

$$\boldsymbol{p}(\boldsymbol{a}|\boldsymbol{x}) \sim \boldsymbol{N}(\boldsymbol{a}|\boldsymbol{\mu}, \mathbf{K}) \tag{4}$$

This distribution is defined by mean functions $\boldsymbol{\mu}$ and covariance matrix **K**. By exploiting the Bayes' theorem, the posterior Gaussian distribution is given by:

$$\boldsymbol{p}(\boldsymbol{a}^*|\boldsymbol{x}^*, \boldsymbol{x}, \boldsymbol{a}) \sim \boldsymbol{N}(\boldsymbol{a}^*|\boldsymbol{\mu}^*, \mathbf{K}^*) \tag{5}$$

By means of the posterior Gaussian distribution, the coefficients $\boldsymbol{a}^*$ under new input parameters can be forecasted.

3. RESULTS

The flow over the single building with four pollutant sources at the leeward side is selected as the test case for developing the ROMs, see Fig 2. The logarithm function determined by input parameters – friction velocity $\mathbf{U}^*$, roughness length $\boldsymbol{Z}_0$ and Von-Karman constant k is implemented to fit the inlet velocity profile:

$$\mathbf{U_{inlet}} = \frac{\mathbf{U_*}}{k} \ln\left(\frac{\mathbf{Z+Z_0}}{\mathbf{Z_0}}\right) \tag{4}$$

where $\mathbf{Z}$ is the height of the computational domain. The flows fields differ via varying input parameters of the inlet velocity profile and giving different the source velocity $\mathbf{U}_s$. Through assigning various accessible values to the input parameters, 64 simulations were conducted. 53 from 64 simulations were used for the training and the rest of 11 were used for the testing.

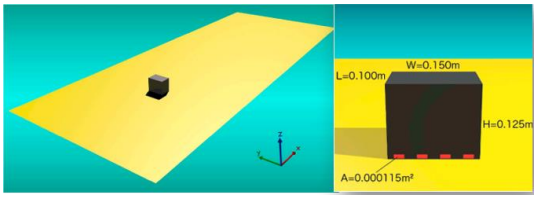

Figure 2. Cedval A1-1 (Leitl et al, 1998)

The modes, in Fig3, were extracted from the trained cases by PCA, the regression mapping input parameters and the coefficients of the modes were built based on the GPR. The result of one test case, in Fig4, demonstrates that ROM can give as accurate predictions as the CFD simulations but with much less computational costs.

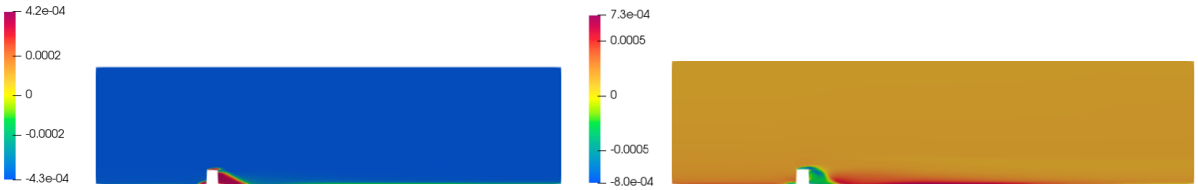

Figure 3. The 1st and 2nd modes of stream-wise velocity

Figure 4. The pollutant concentration predicted by CFD simulation (left) and ROM simulation (right)

4. DISCUSSION

Based on simulations of the parametric studies for input parameters: friction velocity $\mathbf{U}^*$, roughness length $\boldsymbol{Z_0}$ and source velocity $\mathbf{U}_s$, the physics-informed modes representing the processes of the ABL were extracted using PCA, the GPR built the regression between the input

parameters and the coefficients of the modes. For the dimensionality reduction, Dynamic Model Decomposition (DMD), Higher-Order Singular Value Decomposition (HOSVD) can be exploited in the future as the comparison to PCA. Regarding the non-linear regression approaches, Kriging and Artificial Neural Networks are considered as well. After selecting the most appropriate methods for ROM, ROM can be used in more practical applications, such as simulating pollutant dispersion flow in some cities.

5. CONCLUSION

In the present work, flow over a single building case with different realistic values of input parameters was used to generating the dataset. A methodology for the development of accurate and fast ROM using a combination of PCA approaches and non-linear regression was presented. The results showed that the combination of PCA with non-linear regression– GPR is a valid solution for the development of ROM for ABL flows.

6. REFERENCES

Bellegoni, M., Cotteleer, L., Raghunathan Srikumar, S. K., Mosca, G., Gambale, A., Tognotti, L., Galletti, C., Parente, A. (2023). An extended $k - \omega$ SST framework for the RANS simulation of the neutral Atmospheric Boundary Layer. Environ. Model. Softw. 160, 105583.

CEDVAL at Hamburg University Compilation of Experimental Data for Validation of Microscale Dispersion Models. WebSite provided by the Environmental Wind Tunnel Laboratory (EWTL) of the Meteorological Institute.

Longo, R., Fürst, M., Bellemans, A., Ferrarotti, M., Derudi, M., & Parente, A. (2019). CFD dispersion study based on a variable Schmidt formulation for flows around different configurations of ground-mounted buildings. Building and Environment, 154, 336–347.

Zdybał, K., D'Alessio, G., Attili, A., Coussement, A., Sutherland, J. C., & Parente, A. (2023). Local manifold learning and its link to domain-based physics knowledge. Applications in Energy and Combustion Science, 14, 100131.

ACKNOWLEDGEMENTS

The study has received funding from the European Union's Horizon Europe research and innovation programme under grant agreement No 101072559.

IN-VENTO 2024
International Conference of the Italian Association for Wind Engineering
Pisa, September 8th – 11th, 2024

Flow characteristics around a 5:1 rectangular cylinder at moderate Reynolds number: DNS, LES, and experiments

G. Lunghi[a], M. Morello[a], A. Mariotti[a], M.V. Salvetti[a], R. Corsini[b], A. Cimarelli[b], E. Stalio[b]

[a]*Dipartimento di Ingegneria Civile e Industriale, Università di Pisa, Pisa, Italy, gianmarco.lunghi@phd.unipi.it*
[b]*Dipartimento di Ingegneria Enzo Ferrari, Università di Modena e Reggio Emilia, Modena, Italy*

SUMMARY:
In this study, we investigate the dynamics of flows at moderate Reynolds numbers around a 5:1 rectangular cylinder, a structure commonly used to model tall buildings and bridge decks. Recent advancements in computational capabilities have enabled the performance of Direct Numerical Simulations (DNS) that closely resemble real-life scenarios, facilitating cross-validation with wind tunnel experiments. Therefore, experiments were conducted on the 5:1 rectangular cylinder at $Re = 14000$, and compared with DNS results from Corsini et al. (2024) for cross-validation. This comparison highlights the effects of differences in setup, such as the presence of freestream turbulence in the experiments. Furthermore, experimental and DNS data will be utilized to assess the accuracy and reliability of Large-Eddy Simulations (LES) under varying setups, including sensitivity analyses on grid refinement, upstream-edge treatments, and computational domain size.

Keywords: 5:1 rectangular cylinder, Direct Numerical Simulations, Large-Eddy Simulations, Experiment, Moderate Reynolds number

1. INTRODUCTION

Elongated rectangular cylinders of infinite span are simplified geometries relevant for real civil structures, e.g., tall buildings and bridge decks. In particular, the flow around the 5:1 rectangular cylinder is the object of the international Benchmark on the Aerodynamic of a Rectangular 5:1 Cylinder (BARC), which is a blind benchmark, i.e., with no *a priori* selected reference measurements. The flow is characterized by shear-layer separation at the upstream edges, followed by the roll up of these layers in which vortical structures form (Kelvin-Helmholtz instability), and their subsequent convection downstream and interaction with other vortical structures. A second separation occurs at the cylinder rear edges with the classical Von Karman vortex shedding in the near wake. The mean-flow topology is characterized by a closed separated region on the cylinder lateral side with flow reattachment occurring downstream (Fig. 1).

From the various contributions to the BARC benchmark, a significant dispersion emerged in the mean-flow topology aside the cylinder; that, in turn, translates in high discrepancies in some quantities of interest, as, for instance, the distribution of mean and fluctuating pressure on the cylinder side (Bruno et al., 2014). Experiments carried out in different facilities are available in the literature (Bruno et al., 2014; Mannini et al., 2017; Pasqualetto et al., 2022). These experiments are carried out at Reynolds numbers, based on the cylinder depth, D, and on the freestream velocity, ranging from 20000 to 110000. On the other hand, Direct Numerical Simulations (DNS) were carried out at $Re = 3000$ (Chiarini and Quadrio, 2021; Cimarelli et al., 2018) and more recently at $Re = 8000$ and 14000 (Corsini et al., 2024).

We compare herein DNS and experimental results at the same Reynolds number, i.e., $Re = 14000$. This provides cross-validation and can highlight the effects of differences in the setup, as, e.g., of the freestream turbulence present in the experiments. Furthermore, experimental and DNS data will be used to asses the accuracy and reliability of Large-Eddy Simulations (LES) with varying setup.

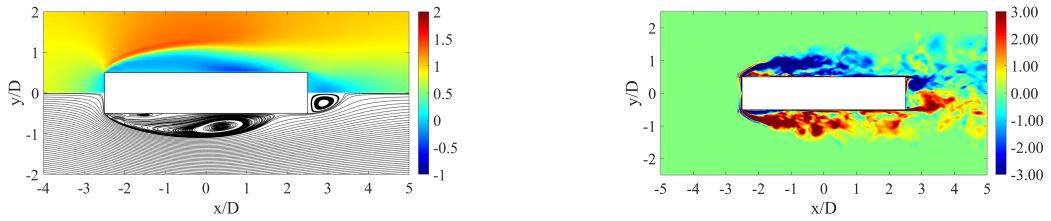

(a) (b)

Figure 1. Flow behavior around the 5:1 rectangular cylinder at $Re = 14000$: (a) time-average of the streamwise-velocity component (upper panel) and mean-flow streamlines (bottom panel); (b) instantaneous spanwise-average of the vorticity in the spanwise direction.

2. EXPERIMENTAL SET-UP AND METHODOLOGY

The experimental campaign is carried out in a closed-return subsonic wind tunnel, characterized by a circular open test section 1.1 m in diameter and 1.42 m in length, and 0.9% freestream turbulence level. The 5:1 aluminium-alloy hollow model is $200 \times 40 \times 800$ mm in the streamwise, crossflow and spanwise directions, respectively. Two end plates are located at the spanwise ends ($z/D = \pm 10$) to mitigate three-dimensional effects. The model is equipped with 495 pressure taps, 72 of which on the spanwise centreline, $z/D = 0$. Experiments are carried out at a Reynolds number, based on the freestream velocity and the cylinder depth, equal to 14000.

Differential pressures are measured through two Pressure Systems ESP-16HD miniature electronic pressure scanners, directly housed inside the model. Velocity measurements are obtained by using an IFA AN 1003 A.A. Lab System hot-wire anemometry module with Dantec 55P11 probes, which can be moved in all directions with an accuracy of 0.1 mm. For each realization, the sampling frequency is set to 16000 Hz and the acquisition time is 32.768 seconds. The manufacturing curvature radius of the upstream edges is evaluated by using the digital microscope RS PRO.

3. DIRECT NUMERICAL SIMULATION SET-UP

The numerical simulation of the turbulent flow around the 5:1 rectangular cylinder has been performed with the open-source code Nek5000. This solver is based on a high-order spectral element method where, within each element, the velocity components and the pressure are expanded in terms of tensor product of Legendre polynomials of order N and $N-2$, respectively. For the present DNS, the polynomial order is $N = 7$. Time integration is carried out by a second-order backward differentiation scheme combined with a second-order extrapolation scheme for the treatment of the nonlinear term. The non-dimensional time step is kept fixed at $\Delta t = 2.6 \cdot 10^{-4}$ during the simulation to fulfill CFL < 0.5 in each point of the domain.

Concerning the boundary conditions, a constant streamwise velocity profile is imposed at the inflow (no turbulence), traction-free boundary conditions are used at the outflow and in the cross-stream direction,, and no-slip condition is set at the surfaces of the cylinder. Spanwise

boundaries are periodic.

The Reynolds number is the same as in experiments. The dimensions of the computational domain are $80D \times 31D \times 5D$ in the streamwise, cross-stream and spanwise direction, respectively. The upstream face of the cylinder is located at $20D$ from the inflow and centred in the cross-stream direction. The number of elements is $N_e = 8988000$, which corresponds approximately to 3 billion of degrees of freedom per time step and per unknown. The element distribution is homogeneous in the spanwise direction, whereas it is refined in the wall-normal directions approaching the cylinder surfaces. The smallest grid spacing is obtained at the edges of the cylinder, $(\delta x_{\min}, \delta y_{\min}, \delta z) = (0.0021, 0.0021, 0.007)$. These grid spacings are computed as the distance between $N+1$ evenly spaced nodes within the spectral element. In the near-wall region the spatial resolution meets the following characteristics $(\delta x^+, \delta y_w^+, \delta z^+)_{\max} = (4.1, 0.66, 5.1)$, where the superscript $+$ denotes the normalization in viscous units and δy_w is the distance from the wall of the second computational node. In turbulent regions, the ratio between the grid spacings and the Kolmogorov scale η is at most $(\delta x/\eta, \delta y/\eta, \delta z/\eta)_{\max} = (4.2, 4.6, 6.3)$. Statistics are collected over a period of $250D/U_\infty$ while the flow is statistically stationary and then averaged in the spanwise direction and with respect to the xz symmetry plane.

4. LES SET-UP AND METHODOLOGY

LES simulations are carried out by adopting the open-source code Nek5000, as for DNS. The basic setup is the same as in Mariotti et al. (2017) and Rocchio et al. (2020). The order of basis functions inside the elements is $N = 6$ and a third-order backward finite-difference scheme based on the high-order splitting method is used for time advancing. The computational domain spans the following dimensions $-75 \leq x/D \leq 125$, $-75 \leq y/D \leq 75$ and $0 \leq z/D \leq 5$, the cylinder center being located at $x/D = y/D = 0$. The computational domain is thus larger than in DNS, as shown in Fig. 2.

A uniform velocity profile with no turbulence (smooth flow) is imposed at the inlet, traction-free boundary conditions are used for the outflow and for the upper and lower boundaries of the domain, and no-slip is imposed at the body surface; periodicity is applied in the spanwise direction. The spectral element size and distribution are the same used in Rocchio et al. (2020). In particular, the element size in the streamwise and crossflow directions is $\Delta x/D = \Delta y/D = 0.125$ near the cylinder, while in the spanwise direction the element size is uniform $\Delta z/D = 0.558$. A low-pass filter is applied to the velocity field in the modal space because the grid

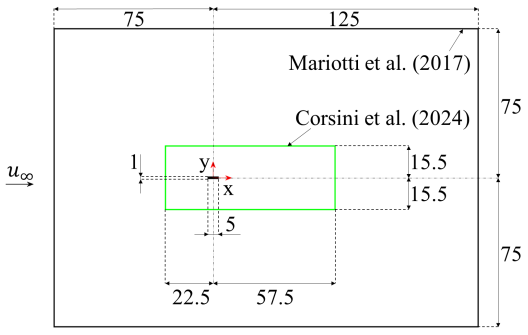

Figure 2. Sketch of the cross-flow section of the computational domains in the DNS in Corsini et al. (2024) with the green line, and the LES in Mariotti et al. (2017) with the black line.

resolution is not fine enough to resolve all turbulent scales at the considered Reynolds number. Since the filter introduces dissipation of the highest resolved modes only, this can be considered as a subgrid-scale dissipation. Two LES are performed at $Re = 14000$ on the flow around the rectangular cylinder having two different upstream-edge treatments.

5. RESULTS AND DISCUSSION

A first comparison between the experiment, the DNS and the LES is given in Fig. 3 showing the distribution on the cylinder lateral side of the time-averaged pressure coefficient and of its standard deviation. A good agreement is found for the mean pressure, while some differences are present in the standard deviation. As expected, the effect of the inflow turbulence is visible in the experiments on the front face. Moreover, the peak of the pressure fluctuations has the same location but a higher intensity in DNS than in experiments. The reasons of this discrepancy will be analyzed in the final presentation.

We plan to carry out sensitivity analyses to the grid refinement, the upstream-edge rounding, and the domain size.

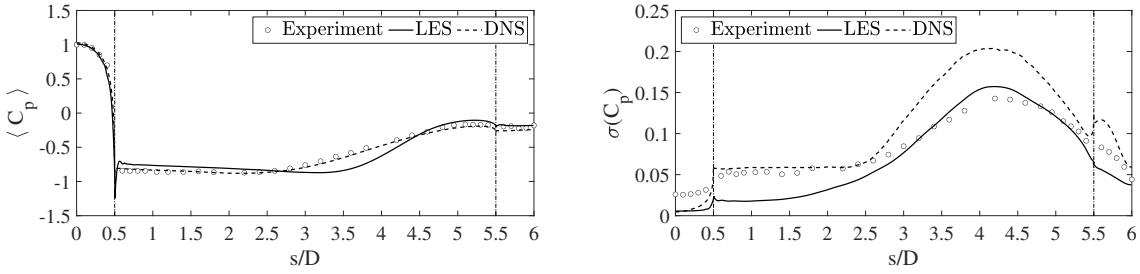

Figure 3. (a) Time-averaged pressure coefficient and (b) its standard deviation on the cylinder surface.

REFERENCES

Bruno, L., Salvetti, M. V., and Ricciardelli, F. (2014). Benchmark on the aerodynamics of a rectangular 5:1 cylinder: an overview after the first four years of activity. J. Wind Eng. Ind. Aerod. 126, 87–106.

Chiarini, A. and Quadrio, M. (2021). The turbulent flow over the BARC rectangular cylinder: a DNS study. Flow Turbulence Combust. 107, 875–899.

Cimarelli, A., Leonforte, A., and Angeli, D. (2018). Direct numerical simulation of the flow around a rectangular cylinder at a moderately high Reynolds number. J. Wind Eng. Ind. Aerod. 174, 39–49.

Corsini, R., Cimarelli, A., and Stalio, E. (2024). DNS of the Flow About a 5:1 Rectangular Body with Sharp Corners. Marchioli, C. et al. (eds) Direct and Large Eddy Simulation XIII. ERCOFTAC Series 31, 9–16.

Mannini, C., Marra, A. M., Pigolotti, L., and Bartoli, G. (2017). The effects of free-stream turbulence and angle of attack on the aerodynamics of a cylinder with rectangular 5:1 cross section. J. Wind Eng. Ind. Aerod. 161, 42–58.

Mariotti, A., Siconolfi, L., and Salvetti, M. V. (2017). Stochastic sensitivity analysis of Large-Eddy Simulation predictions of the flow around a 5:1 rectangular cylinder. Eur. J. Mech./B Fluids 62, 149–165.

Pasqualetto, E., Lunghi, G., Rocchio, B., Mariotti, A., and Salvetti, M. V. (2022). Experimental characterization of the lateral and near-wake flow for the BARC configuration. Wind Struct. 34, 101–113.

Rocchio, B., Mariotti, A., and Salvetti, M. V. (2020). Flow around a 5:1 rectangular cylinder: Effects of upstream-edge rounding. J. Wind Eng. Ind. Aerod. 204, 104237.

IN-VENTO 2024
International Conference of the Italian Association for Wind Engineering
Pisa, September 8th – 11th, 2024

Development of an actuator line model for pitching airfoils with aerodynamic moment corrections

E. Luzzati[a], A. Mariotti[a], M.V. Salvetti[a]

[a]*Dipartimento di Ingegneria Civile e Industriale, Università di Pisa, Pisa, Italy,*
emanuele.luzzati@phd.unipi.it

SUMMARY:
The present study aims to develop and implement a numerical tool in OpenFOAM to reduce the computational cost required for predicting the performance of vertical-axis wind turbines while accurately modelling the primary physical processes involved. We consider Reynolds-averaged Navier-Stokes simulations of pitching airfoils, in which the airfoil is modelled through the Actuator Line Model (ALM), as often done for turbine blades. The aerodynamic force coefficients are given by the Leishman-Beddoes model modified for low Mach numbers [1]. The present study implements a correction by introducing the aerodynamic moment. This becomes important for airfoils operating at high angles of attack and in deep stall conditions. Experimental data for steady airfoils are used to compute the value of the aerodynamic moment coefficient. The correction is implemented through a couple of equal and opposite body forces. The corrected version of the ALM with the integrated aerodynamic moment correction is used in RANS simulations of harmonic pitching scenarios for the NACA0021 airfoil. The results are compared with those of the classical ALM and with experimental data. We investigate how the implementation of the moment correction, i.e. the distance between the two opposite forces and the width of the kernel over which they are distributed, influences the dynamic stall. Continuous response surfaces in the parameter space are obtained using stochastic sensitivity analysis. Globally, the implemented moment correction has proven effective in reducing discrepancies between airfoil pitching experiments and predicted polars, notably during the downstroke motion.

Keywords: Actuator Line Model (ALM); dynamic stall model; aerodynamic-moment corrections; wind turbines; Computational Fluid Dynamics

1. INTRODUCTION

This research activity aims to study the effect of aerodynamic moment of relatively thick airfoils into a state-of-the-art Actuator Line Model developed in (Bachant et al., 2016). The aerodynamic moment coefficient is negligible in attached flow conditions, but it becomes relevant when the airfoil approaches stall, and even more important when studying its dynamic behaviour in deep dynamic stall conditions. Actuator line models are widely used in modelling rotating wind turbine blades and propellers, removing the complexity of simulating the real airfoil into the flow domain. Nevertheless, ALM application is constrained to light stall conditions, underestimating the airfoil effect on the flow and wake after the static stall angle is exceeded, as highlighted in (Rocchio et al., 2020). In the literature, various efforts have been made to better reproduce the effect of virtual airfoils on the surrounding flow, both in terms of spreading the distributed force kernel into a distributed set of points (Jha and Schmitz, 2018), both to find the optimal velocity sampling points capable of minimizing the error in wake prediction (Muscari et al., 2023). The main limitation of the former approach is that each distribution of points has to be thoroughly calibrated with higher fidelity data. The latter instead, is proven to be effective in correcting local induction effects while not affecting the wake characteristics in near stall conditions. Each variation of ALM should be tested for sensitivity to the spreading kernels of the force coefficient that are inserted into the momentum equation.

In this work a new aerodynamic moment correction term is implemented and tested under dynamic conditions, both in sinusoidal pitching experiments and in rotating airfoil motion. Moreover, a validation of the model against the available experimental data is carried out, together with a stochastic sensitivity analysis of the main model parameters.

2. ACTUATOR LINE MODEL SET-UP AND METHODOLOGY

A standard Actuator Line Model, initially developed by (Troldborg, 2009), was used as a baseline to construct the aerodynamic moment correction model. The distributed force inserted into the momentum equation is corrected using a dynamic stall model tailored for low Mach numbers, as outlined in (Sheng et al., 2007). Other sub-models such as flow curvature corrections and end-effect corrections were not used in the context of these simulations, since they are focused on the assessment of the effect of aerodynamic moment corrections.

A three-dimensional Gaussian spreading kernel was used to smooth the distributed aerodynamic forces and moments. The parameter determining the width of the spreading is denoted by the standard deviation of the Gaussian kernel, ε.

Several studies were carried out to investigate the influence of those two parameters on the ALM accuracy throughout airfoil dynamics. It was decided to follow the work of (Rocchio et al., 2020) and use $\varepsilon_L = \varepsilon_D = C_D/2$

Regarding the local flow velocity U_a, for a pitching profile in uniform free-stream condition, it was found that the free-stream velocity can be taken as the reference local flow velocity without impacting the ALM results. Nevertheless, it must still be investigated the most representative way of sampling the velocity magnitude and AoA when there is more then one distributed force inserted into the flow field and when the pitching profile is moving into the flow field. The initial choice for the local flow velocity was to take $U_a = U_{\text{inf}}$ and it is sampled upstream from the aerodynamic center at a distance spanning from 0 and $C/2$.

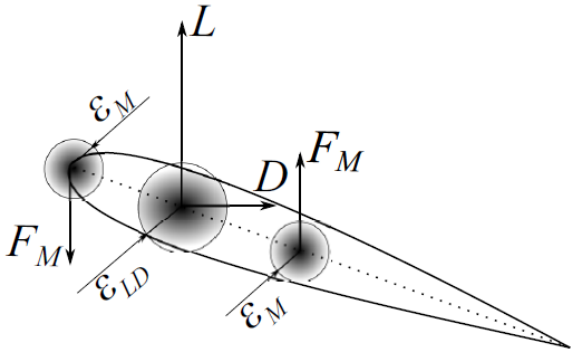

Figure 1. Sketch of the added aerodynamic moment Gaussian projection

Two equal and opposite forcing terms are added to the momentum equation to take into account the effects produced by the Cm on the flow, using a gaussian kernel ε_m. To be consistent with code implementation, the two forces are set as parallel to Lift and set at a distance δ from the aerodynamic centre at $C/4$ each. From simple geometric considerations, the equivalent $Cl*$ to be added to the distributed force can be calculated:

$$Cl^* = \frac{C_m(\alpha)c}{2\delta cos(\alpha)} \tag{1}$$

where $C_m(\alpha)$ is the tabulated static moment coefficient and α is the profile angle of attack. To have a coherent force input, however, the moment should be corrected for dynamic stall as well as it is done with lift and drag forces.

2.1. Simulation setup

A simplified case of a pitching NACA0021 airfoil was studied as a test bench for the dynamic stall model testing. A rectangular 2D grid of 12Cx10C with cylindrical refinement of 4C diameter. These values are taken from previous ALM simulation studies on domain sensitivity, (Mendoza et al., 2019). To reach grid convergence on the refined region, several grid densities were tested, keeping the same refinement ratio. Three grids were tested in an unsteady oscillating airfoil: C/10, C/20, and C/40 with no substantial difference in load estimation. The simulation was carried out in OpenFOAM using the TurbinesFOAM ALM library and RANS k-e turbulence model. The Steldhal-Klimas experimental airfoil polars were used. The distance δ between the dipole body forces inserting the moment coefficient into the flow was set between $C/8$ and $C/4$.

3. RESULTS AND DISCUSSION

As a validation case, the oscillating experiment from (McCroskey et al., 1976) was replicated for an oscillating naca0021 airfoil. The comparison between the experimental data, Sheng DS model and the in-house model with moment calculation is presented below. Regarding the DS model free parameters, standard values from (Sheng et al., 2007) were used as a reference.

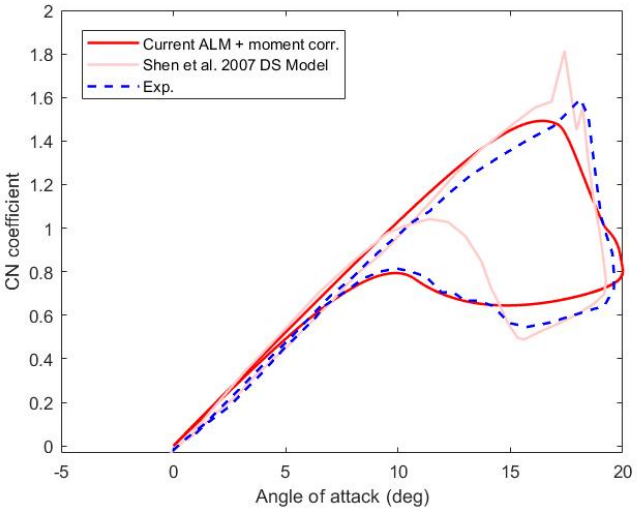

Figure 2. Static normal coefficient calculated with the proposed ALM with moment corrections (red), Sheng DS model (pink), experiment (dashed blue), k = 0.025, ReC = 2e6, 0-20 deg oscillation, experiments from (McCroskey et al., 1976)

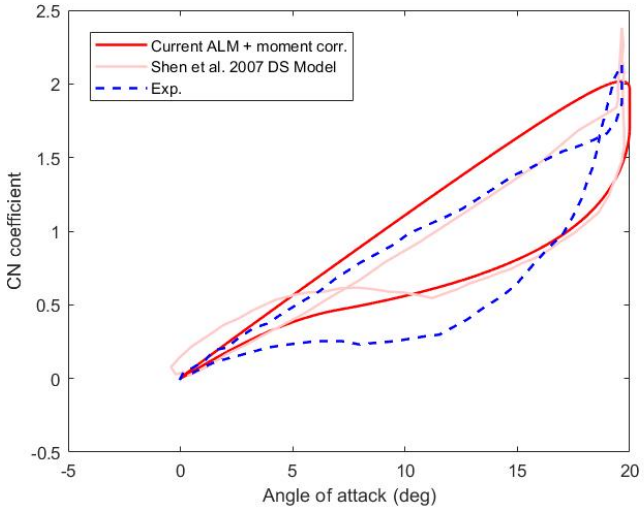

Figure 3. Static normal coefficient calculated with the proposed ALM with moment corrections (red), Sheng DS model (pink), experiment (dashed blue), k = 0.1, ReC = 2e6, 0-20 deg oscillation, experiments from (McCroskey et al., 1976)

The moment correction module was considered necessary as the downstream wake direction at a high angle of attack was not well captured by the standard model. This affects especially VAWT simulation with high solidity where the downwind rotation is not enough influenced by the upwind part. Moreover, the moment-related error near the actuator line, produces significant under-prediction in the AoA sampling, hence artificially reducing the hysteresis related to dynamic stall.

It can be seen that the present DS model with moment correction works reasonably well in predicting different deep stall pitching cases $(k > 0.01)$. Moreover, the current model is less constrained to follow the static polar in the reattachment phase as it happened with (Sheng et al., 2007) model evident in Figure 2 In some cases, the reattachment phase still has to be improved. However, in all the studied cases from light to deep stall, the peak normal coefficient was correctly estimated.

REFERENCES

Bachant, P., Goude, A., and Wosnik, M. (2016). Actuator line modeling of vertical-axis turbines. arXiv preprint arXiv:1605.01449.

Jha, P. K. and Schmitz, S. (2018). Actuator curve embedding–an advanced actuator line model. Journal of Fluid Mechanics 834, R2.

McCroskey, W. J., Carr, L. W., and McAlister, K. W. (1976). Dynamic stall experiments on oscillating airfoils. Aiaa Journal 14, 57–63.

Mendoza, V., Bachant, P., Ferreira, C., and Goude, A. (2019). Near-wake flow simulation of a vertical axis turbine using an actuator line model. Wind Energy 22, 171–188.

Muscari, C., Schito, P., Vire, A., Zasso, A., and Wingerden, J.-W. van (2023). An advanced approach to velocity sampling in actuator line models. Authorea Preprints.

Rocchio, B., Chicchiero, C., Salvetti, M. V., and Zanforlin, S. (2020). A simple model for deep dynamic stall conditions. Wind Energy 23, 915–938.

Sheng, W., Galbraith, R. A., and Coton, F. N. (2007). Improved dynamic-stall-onset criterion at low Mach numbers. Journal of aircraft 44, 1049–1052.

Troldborg, N. (2009). Actuator line modeling of wind turbine wakes.

IN-VENTO 2024
International Conference of the Italian Association for Wind Engineering
Pisa, September 8th – 11th, 2024

Design of full-scale monitoring system for a mid-rise building under wind action

A. Malasomma [1,*], V. Picozzi [1], A.M. Avossa [1], L. Caracoglia [2], F. Ricciardelli [1]

[1] *University of Campania "Luigi Vanvitelli", Aversa, IT*
[2] *Northeastern University, Boston, MA, USA*
[*] *antonio.malasomma@unicampania.it*

SUMMARY
The need for more accurate design criteria under wind action, in conjunction with the availability of cheaper and more efficient data acquisition hardware has led to several full-scale monitoring campaigns all over the world. Their objective is to verify and validate the predictions obtained from theoretical models, available in the literature, and from wind tunnel tests. In this paper, a comprehensive full-scale monitoring system of a mid-rise building is presented. The system is designed to measure the wind characteristics, wind loads and the building dynamic response.

Keywords: Mid-rise building, Full-scale monitoring, Wind action, Reliability.

1. INTRODUCTION

Full-scale monitoring of civil structures has become popular for ensuring a better structural safety level and comfort of users (or occupants). Examples are wind-sensitive structures, such as long-span suspension bridges and high-rise buildings. Moreover, the full-scale monitoring of an existing structure advances current knowledge in the assessment of wind loads (Davenport, 1961) to be used for the design of wind resisting structures. Although experiments on model-scale structures in wind tunnel and numerical simulations have achieved a mature stage, full-scale experiments are still necessary to investigate critical structural phenomena, induced by wind actions on buildings and structures, as well as for the validation of existing analytical models (Picozzi et al., 2024).

A full-scale monitoring campaign involves extended time and cost-intensive activities (Caracoglia and Jones, 2009). Among them, there are the choice and the supply of most appropriate measurement equipment, as well as any related installation issues. Indeed, selection of measurement devices must be based on the structural construction features including geometry, structural typology, and destination use. Furthermore, a large part of the experimental activity is devoted to establishing the appropriate contacts with the building owners, who must authorize installation of the equipment and its position so as not to interfere with daily activities. Finally, compatibility and communication between various devices are another critical aspect, since the measurement instruments are typically produced by different manufacturers that offer their own acquisition system and communication protocols. The main issue is the synchronization of the clock, making all the measurement sources aligned-in-time. This issue is sometimes complex, especially when the goal is a long-time data acquisition. All these aspects affect the fidelity of the measured data and the methodology for the data pre- and post-processing.

Some full-scale monitoring systems of tall buildings around the world are noteworthy. Within the Chicago full-scale monitoring program, three tall buildings of the city's downtown were instrumented with accelerometers, anemometers, and a GPS antenna (Kijewski-Correa et al., 2006). The buildings were chosen as they are landmark structures with lateral force resisting systems being that are widely employed in high-rise design. The monitoring system was defined as "wired hub-and-spoke", i.e., the sensors are physically wired to a main datalogger. Such a system has two specific vulnerabilities: (1) device cables are very costly and difficult to deploy and maintain, and (2) lengthy cables essentially serve as antennas, allowing interference and noise to infiltrate the system. The in-situ measurements of the dynamic response enabled the comparison with both analytical and wind tunnel model results, as well as an upgrading of the current state-of-the-art in tall-building design criteria.

Another noticeable full-scale monitoring program was designed for the world's tallest building, the Burj Khalifa, installed during the erection stage to evaluate its performance under seismic and wind loads (Kijewski-Correa et al., 2012). The structural health monitoring (SHM) system is slightly different from the one used for the Chicago Full-scale monitoring program. Advancements in communication technology and wireless connections, radio and wi-fi routers allowed to eliminate cabling in the specific application. Such technologies make installation, relocation, and maintenance easier. Nevertheless, transferring large amounts of data packets wirelessly increases the chances of data loss and interference from other radio frequencies. Moreover, the decentralized nature of the acquisition systems requires appropriate protocols of network synchronization. To minimize these vulnerabilities, the authors have developed specific high-tech systems along with the most recent informatic instruments.

The two previous monitoring projects did not measure the wind loads, but rather the dynamic building response. A more complete experimental campaign was recently conducted on a tall building on the left bank of the Dnieper River in Kiev, Ukraine (Kuznetsov and Pospisil, 2019). The research team measured the wind-induced pressure loads on the building using 12 pressure transducers with pneumatic connection tubing lines. The results obtained from the field measurements were compared with the BLWT (Boundary Layer Wind Tunnel) test results; a good agreement was found.

In this context, this paper introduces a new installation of a full-scale monitoring system, designed for a 19-story building located in Naples, Italy. The experimental campaign aims to (a) calibrate the building aerodynamic admittance function, (b) examine the uncertainty associated with the wind engineering models by comparison of the measured loads with the predicted ones. Wind tunnel testing is considered to provide a useful comparison of the results found by realistic, full-scale tests. Some preliminary results will be presented herein.

2. METHODOLOGY

The building under investigation is a medium-rise, composite concrete-steel structure. It is part of the University Hospital Campus located in the northern area of Naples, and it is denoted as *Torre Biologica*. The main lateral force resisting system of the building consists of three reinforced concrete vertical cores that are connected to every floor system through steel frames, i.e., a large central core of 10 m by 10 m plan dimension made by four different walls that intersect each other forming an hashtag-shape, and two L-shaped smaller cores placed at opposite building corners.

From a technical point of view, the construction is located in a hilly area and stands out compared to all the other buildings that surround it. It presents floorplan dimensions $B \times D = 25.10 \times 29.90$ m, which corresponds to a side ratio of approximately 1:1.2. The target building is close to the meteorological station of Naples Capodichino airport, as shown in Fig. 1. This proximity enables direct comparisons between real-time wind speed measurements and the historical database at the airport.

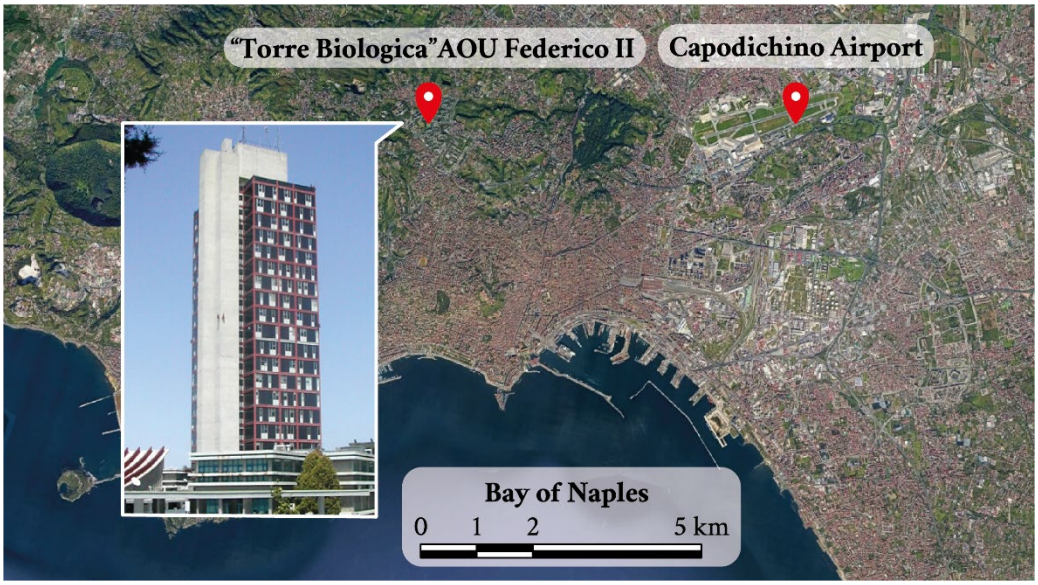

Figure 1. Target building location.

The designed monitoring system is summarized in Fig. 2, and consists of:

- 1 data logger: NI compact DAQ-9137;
- 2 sonic anemometers: Gill Wind Master 3D 20Hz;
- 16 differential pressure transducers: Setra 264;
- 1 static pressure probe: Quad static pressure probe;
- 22 accelerometers: PCB Piezotronics (393A03 and 393C).

The 2 sonic anemometers are placed above the rooftop of the structure, using two rigid antenna poles. A total of 16 pressure transducers are installed, eight of which are placed on the 14th floor and the remaining ones on the 18th floor. Pressure transducers measure the differential pressures, i.e., the difference with a static reference value through a pneumatic connection line. To establish the same static reference pressure for all the transducers, a static pressure probe is installed near one of the anemometers on the roof. This allows to account for fluctuations in the reference pressure over time due to meteorological variations. Several pairs of accelerometers are arranged to identify the structural dynamic behavior under wind and seismic loads.

The instruments are wired through cables to a central datalogger, placed in a control room located on the 18th floor; wireless communications were excluded as they would have caused interference with other communication systems and medical devices. An in-house custom software is used to control the operations of the instruments in real time and to save the acquired data. Except for the instruments positioned on the roof, all the others can be easily and safely inspected.

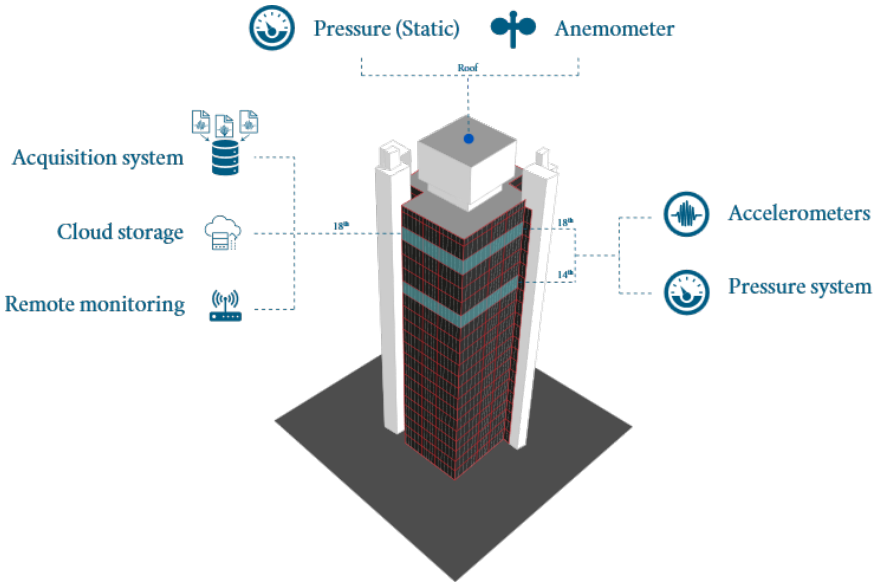

Figure 2. Monitoring system - schematics.

3. ANTICIPATED RESULTS

Some preliminary results will be described in the final presentation. First, the dynamic response of the real structure will be compared with the results of a finite-element model (FEM) to identify the building's structural dynamic properties (e.g., frequencies). Then, full-scale experimental wind load data, in terms of surface pressures, will be compared against the results of BLWT tests to be carried out on a rigid scale model at the Technical University of Cracov. In particular, the correspondence between the measured wind pressures at full-scale and BWLT equivalent pressures results will be evaluated.

ACKNOWLEDGEMENTS

Preliminary work was conducted while L. Caracoglia was a visiting professor at the University of Campania "L. Vanvitelli" in 2022. L. Caracoglia acknowledges the financial support of the University of Campania.

REFERENCES

Davenport, A, (1961). The application of statistical concepts to the wind loading of structures. Institution of Civil Engineers. Proceedings.,1961, Vol. 19, pp. 449–472.

Picozzi, V., V. Maietta, A.M. Avossa, and F. Ricciardelli (2024). Uncertainty in the dynamic properties of tall buildings and propagation to the wind-induced response. The Structural Design of Tall and Special Buildings, e2107.

Kijewski-Correa, T. et al. (2006). Validating Wind-Induced Response of Tall Buildings: Synopsis of the Chicago Full-Scale Monitoring Program. Journal of Structural Engineering 132(10):1509-1523.

Kijewski-Correa, T. et al. (2013). SmartSync: An Integrated Real-Time Structural Health Monitoring and Structural Identification System for Tall Buildings. Journal of Structural Engineering 139(10):1675-1687.

Kuznetsov, S., Pospisil, S. (2019). Full-Scale Measurements of Local Wind Loads on a High-Rise Building Using Wind Tunnel Based Predictions. 2019 IOP Conf. Ser.: Mater. Sci. Eng. 471 052053.

Caracoglia, L., Jones, N. P., (2009). Analysis of full-scale wind and pressure measurements on a low-rise building. Journal of Wind Engineering and Industrial Aerodynamics Volume 97, Issues 5–6, 2009: 157-173.

IN-VENTO 2024
International Conference of the Italian Association for Wind Engineering
Pisa, September 8th – 11th, 2024

A refined surface roughness approach to trigger the transcritical flow regime past a circular cylinder

Claudio Mannini[a], Tommaso Massai[a], Niccolò Barni[a]

[a]*CRIACIV/University of Florence, Florence, Italy, claudio.mannini@unifi.it, tommaso.massai@unifi.it, niccolo.barni@unifi.it*

SUMMARY:
The simulation in the wind tunnel of the high Reynolds number (transcritical) regime for a circular cylinder is of great interest for many civil engineering structures, but it is still a challenging task. The problem is further complicated by the free-stream turbulence investing the structures and by the need in some practical applications to adopt strategies that work independently of the wind direction. Having this in mind, a solution with staggered discontinuous roughness strips has previously been proposed by the authors and is refined and carefully studied in the present work with specific experiments. Two types of sandpaper strips are employed, and the less rough strips reveal to be very promising to trigger the transcritical regime at relatively low Reynolds number, in terms of mean drag coefficient, root-mean-square of the lift coefficient and Strouhal number. The experimental results also highlight the possibly misleading local behaviour of pressures in the sections of strip discontinuity.

Keywords: Circular cylinder, Reynolds number, transcritical regime, wind tunnel, roughness, turbulent flow

1. INTRODUCTION

Despite the long track of research, the simulation in the wind tunnel of the high Reynolds number behaviour of a circular cylinder, in particular the so-called transcritical (or postcritical) regime, is still an open issue, although it is crucial for load and vibration assessment of large structures such as chimneys and wind turbine towers. This task is made even more complicated by the uncertainty in the target statistics of force and pressure coefficients, demonstrated by the large spread of results collected from the literature (see, e.g., Mannini et al., 2023). Wind tunnel tests have shown that diffused surface roughness allows achieving a transcritical regime, but with earlier separation and significantly higher drag compared to a smooth cylinder due to the excessive subtraction of momentum to the attached turbulent boundary layers (Buresti, 1981; Dubois and Andrianne, 2022; Nakamura and Tomonari, 1982). In contrast, localized spanwise ribs or trip wires are more successful in just triggering the laminar-to-turbulent transition of the boundary layers and in simulating the behaviour of smooth cylinders at high Reynolds number (Duarte Ribeiro, 1991; Nakamura and Tomonari, 1982). An additional parameter that makes the problem even more intricate is the free-stream turbulence, which is always present in wind engineering problems and which is known to strongly affect the Reynolds number regimes. In particular, small-scale turbulent fluctuations contribute to anticipate laminar-to-turbulent transitions in free shear layers or in boundary layers.

Moreover, studies of groups of cylinders (e.g., offshore wind turbine towers without rotor and nacelle during the pre-assembly phase at the port quayside) highlight the need for an omnidirectional behaviour of surface roughness on wind tunnel models. To this end, a promising solution was proposed in Mannini et al. (2023) based on staggered discontinuous sandpaper strips. The goal of the current work is to explore in-depth that idea through a refined experimental setup.

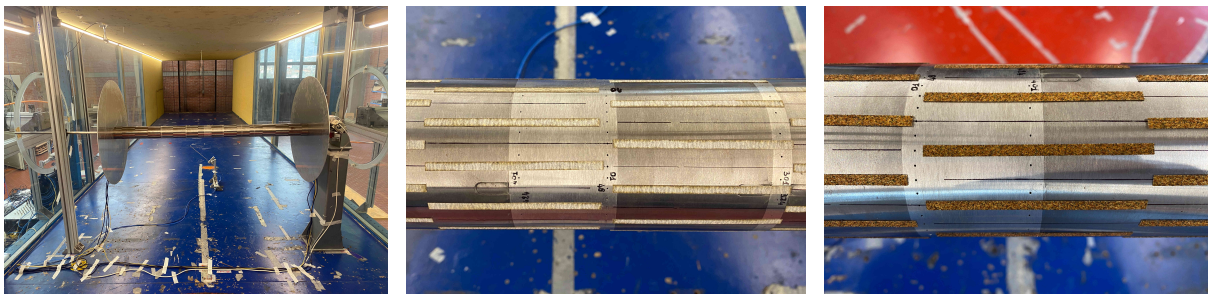

(a) (b) (c)

Figure 1. Cylinder model in the wind tunnel (a); sandpaper strips for roughness 1 (b) and roughness 2 (c).

2. WIND TUNNEL TESTS

The experimental tests are carried out in the CRIACIV wind tunnel, featuring a test section of 2.4 m $\times$ 1.6 m and a maximum flow speed of about 30 m/s. The cylinder model is made of stainless steel and is mounted horizontally in the wind tunnel (Fig. 1(a)). It is 1220 mm long and has a diameter D of 80 mm. Circular end-plates with a diameter of 660 mm are placed at both ends of the model to confine the flow. The blockage ratio is 5%, conservatively calculated as the ratio of the cylinder diameter to the wind tunnel height.

The model is equipped with 190 pressure taps, distributed between seven arrays (48 taps in the midspan array), and the measurements are carried with the PSI DTC Initium system at a sampling rate of 650 Hz. The sensor accuracy is ± 1.24 Pa. 500 mm-long Teflon tubes with an internal diameter of 0.8 mm are employed to connect the pressure taps with the miniaturized sensors. Measurement results are corrected to account for the transfer function of the tubes. Rough cylinder configurations are tested covering the model surface with sandpaper strips having a length of 80 mm (D) and a width of 4 mm ($0.05D$). The strips are spaced 30 deg apart and present a staggered arrangement, as shown in Fig. 1(b)-1(c). Sandpaper P220 with a total thickness k of 0.25 mm ($k/D = 3.1 \cdot 10^{-3}$) and P80 with a total thickness of 0.45 mm ($k/D = 5.6 \cdot 10^{-3}$) are employed for so-called "roughness 1" and "roughness 2", respectively.

Tests are performed in both smooth and turbulent flows. In the first case, the turbulence intensity is below 1%. In contrast, homogeneous isotropic turbulence is generated through a biplanar grid made of 140 mm-wide wooden slats assembled according to a 550 mm square mesh. For turbulent flow 1 the grid is placed 7.56 m upstream of the model, producing a longitudinal turbulence intensity I_u in the range 8.3-11% and a longitudinal integral length scale L_u^x between 220 mm and 280 mm, depending on the mean wind speed. Instead, the grid is located 5.65 m upstream of the model for turbulent flow 2, and I_u is between 11.5% and 13.2%, while 175 mm $\leq L_u^x \leq$ 240 mm. The grid also reduces the maximum wind tunnel flow speed.

3. DISCUSSION OF RESULTS

Fig. 2 shows the cylinder mean drag coefficient obtained by pressure integration as a function of the wind tunnel Reynolds number ($\mathrm{Re} = UD/\nu$, where U is the mean wind speed and ν the air kinematic viscosity). Without roughness, the cylinder is always in the subcritical regime in smooth flow, while the drag crisis is reached in turbulent flow. For the less rough cylinder (roughness 1), a nearly constant drag coefficient of about 0.6 is achieved for $\mathrm{Re} \gtrsim 1.3 \times 10^5$ in smooth flow and for $\mathrm{Re} \gtrsim 1.1 \times 10^5$ in turbulent flow. In fact, for higher turbulence intensity (turbulent flow 2) the saturation of the curve is not properly demonstrated due to the velocity

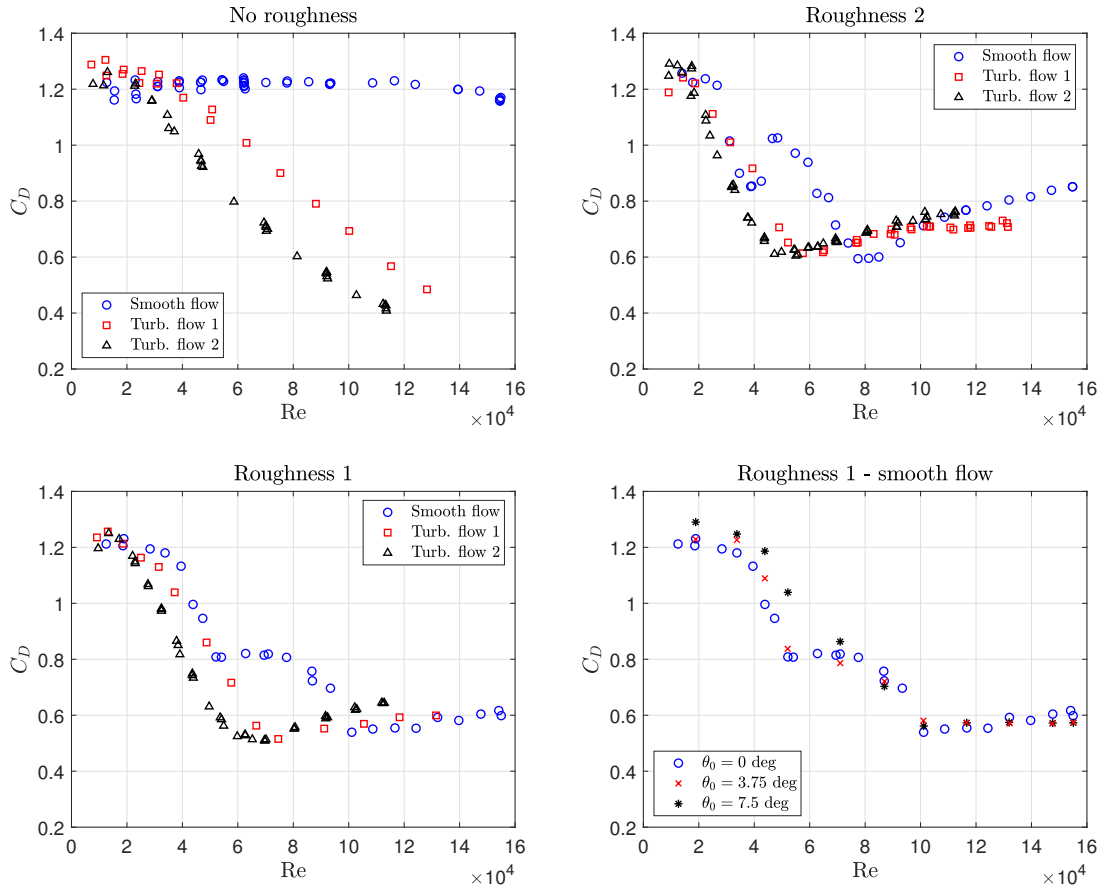

Figure 2. Drag coefficient vs. Reynolds number for various roughness solutions and turbulence intensities.

limitation in the wind tunnel. Such a drag value is only slightly higher than that measured by Schewe (1983) in a high pressure wind tunnel for a smooth cylinder at $\mathrm{Re} \gtrsim 6 \times 10^6$. In contrast, for the rougher cylinder (roughness 2), a higher drag coefficient is obtained, and no saturation of the C_D-curve with Re is attained. Moreover, though not shown here, the root-mean-square of the lift coefficient in smooth flow changes from about 0.55 in the subcritical regime to about 0.06 in the transcritical regime simulated with roughness 1, a result that well complies with those reported in Schewe (1983). A much higher value is got, instead, with roughness 2. The Strouhal number is equal to about 0.19 in the subcritical regime, and it increases to 0.26-0.27 in the transcritical regime with roughness 1, where it is apparent even in turbulent flow. In contrast, a value around 0.23 is measured with roughness 2. The bottom-right frame of Fig. 2 also demonstrates that the results are essentially independent of the wind direction, considering model rotations of 3.75 deg and 7.5 deg, while appreciable differences appear for roughness 2.

Finally, Fig. 3 compares the mean pressure coefficient C_p for roughness 1 solution in case of smooth flow and turbulent flow 1 (very similar results are obtained also for turbulent flow 2). The left frames in the figure refer to the finely instrumented central array #1, while the right frames correspond to the close array #2. The difference is that all roughness strips start or end in correspondence of array #1, while they cross array #2 (see Fig. 1(b)-1(c)). Though the experimental data in the literature are controversial and scattered (Mannini et al., 2023), the current C_p-results are close to the pattern proposed by Eurocode 1-4 for high Re. It is also apparent that the interruption of the roughness strips affects the local flow field, reflecting on the minimum value of the pressure coefficient, while the base pressure remains nearly unchanged.

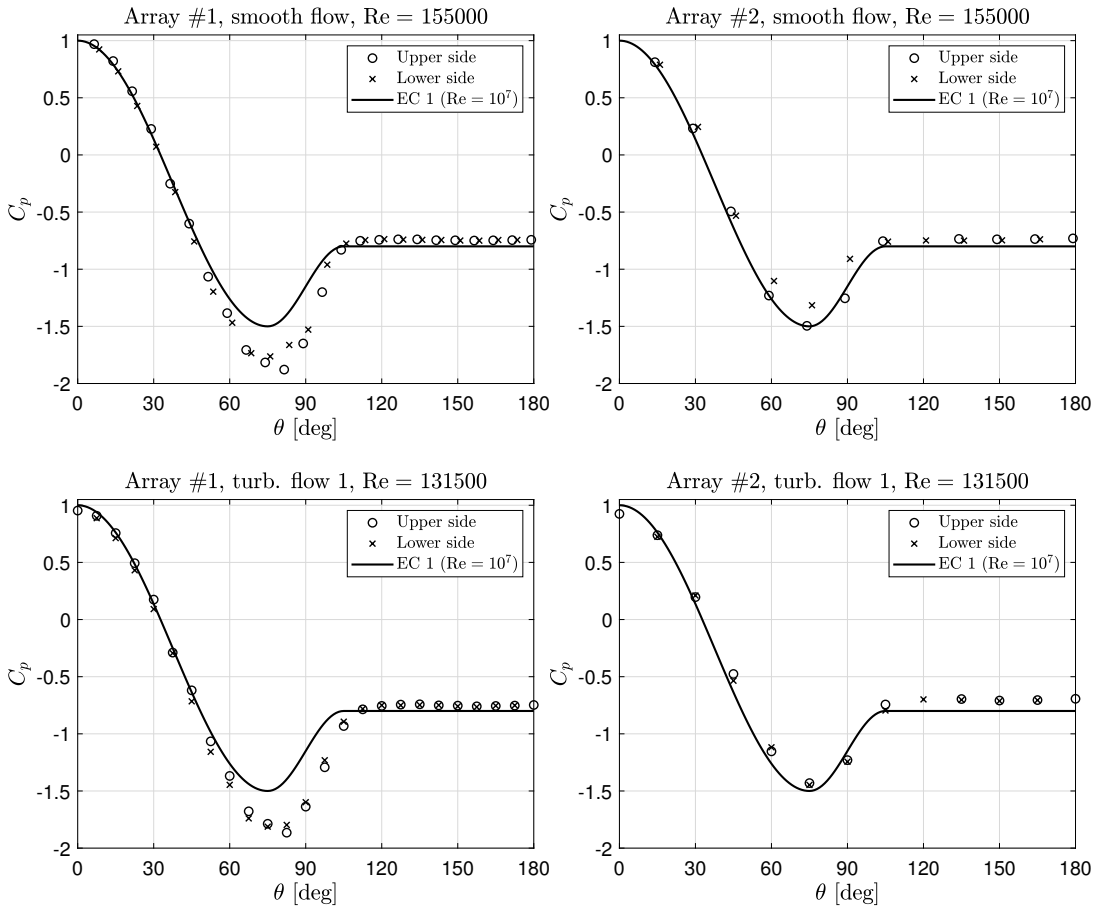

Figure 3. Pressure coefficient distribution as a function of the latitude θ for roughness 1 solution (array #1 corresponds to the cylinder midspan, whereas array #2 is a diameter D distance).

4. CONCLUDING REMARKS AND ONGOING WORK

Staggered discontinuous roughness strips revealed to be a promising strategy for reasonably simulating the transcritical flow regime past a circular cylinder under both smooth and turbulent wind, independently of the flow direction. The less rough solution (roughness 1) is clearly preferable, but additional tests with narrower roughness strips are underway. Incidentally, these strips could also cross the densely instrumented pressure tap array #1, fixing the problem underscored by Fig. 3.

REFERENCES

Buresti, G. (1981). The effect of surface roughness on the flow regime around circular cylinders. Journal of Wind Engineering and Industrial Aerodynamics 8, 105–114.

Duarte Ribeiro, J. L. (1991). Effects of surface roughness on the two-dimensional flow past circular cylinders I: mean forces and pressures. Journal of Wind Engineering and Industrial Aerodynamics 37, 299–309.

Dubois, R. and T. Andrianne (2022). Flow around tandem rough cylinders: Effects of spacing and flow regimes. Journal of Fluids and Structures 109, 103465.

Mannini, C., T. Massai, A. Giachetti, and A. Giusti (2023). Aerodynamic loads on groups of offshore wind turbine towers stored on quaysides during the pre-assembly phase. Journal of Wind Engineering and Industrial Aerodynamics 242, 105569.

Nakamura, Y. and Y. Tomonari (1982). The effects of surface roughness on the flow past circular cylinders at high Reynolds numbers. Journal of Fluid Mechanics 123, 363–378.

Schewe, G. (1983). On the force fluctuations acting on a circular cylinder in crossflow from subcritical up to transcritical Reynolds numbers. Journal of Fluid Mechanics 133, 265–285.

IN-VENTO 2024
International Conference of the Italian Association for Wind Engineering
Pisa, September 8th – 11th, 2024

Tuned Mass Inerter Dampers to reduce Vortex Induced Vibrations during the construction stage of Onshore Wind Turbines

C. Meinhardt[a], M. Lauzi[b], F. Bottoni[c]

[a]*GERB Vibration Control, Berlin, Germany, christian.meinhardt@gerb.de*
[b]*GERB Vibration Control, Berlin, Germany, matthias.lauzi@gerb.de*
[c]*GERB Italia, Milan, Italy, fulvio.bottoni@gerb.it*

SUMMARY:
Wind Turbine-Tower structures are susceptible to vortex induced vibrations (VIVs). This applies for different erection stages with a varying amount of segments. During a monitoring campaign the change of natural frequencies and the occurrence of resonant VIVs could have been monitored. For this campaign data loggers were attached to the tower segments, which were obtaining acceleration values for time periods of up to 4 weeks. To reduces the occurring vibrations a mitigation concept using passive TMDs. The requirement for these TMDs was that the system should provide a certain degree of supplementary damping for all susceptible installation stages without having to re-adjust the TMD or without using active, semi-active or adaptive systems. Such a robust system can only be achieved when using a rather large mass ratio (effective mass of the TMD system compared to the modal mass of the main system) and big additional masses accordingly, which would have made the handling of the devices during the installation of the wind turbine very complicated. To reduce the weight of the necessary TMD units, an Tuned Mass Inerter Damper was developed which uses the mass amplification effect of these devices.
The following paper shall present the mitigation concept which defines the required TMD parameters , the developed TMID system an the results from tests with a prototype.

Keywords: Onshore Wind Turbine Structures, Vortex Shedding Occurrence, Monitoring Campaign, Multi-Stage Tuned Mass Damper Strategy, Tuned Mass Inerter Dampers (TMID)

1. INTRODUCTION

The fast development of wind turbine technology leads to bigger and bigger facilities which can only effectively operate at Onshore locations with significant hub heights. The bigger the power output, the greater the hub height and wind turbine manufacturers keep stretching the limits for hub height and the required tower design more and more. Accordingly the tower structure and the tower + nacelle structure display low natural frequencies which lead to low critical wind speeds for which resonant vortex shedding vibrations can occur. These vibrations potentially reduce the fatigue life of these structures so mitigation measures in form of TMDs are required. These TMDs shall be applied for different construction stages for which the number of installed tower segments vary and which also consist the state with installed nacelle. A special requirement for a TMD solution was that the passive TMD systems could not be adjusted in situ. To design such a robust system can only be achieved when using a rather large mass ratio (effective mass of the TMD system compared to the modal mass of the main system) and big additional masses accordingly, which would have made the handling of the devices during the installation of the wind turbine very complicated. To reduce the weight of the necessary TMD units, a Tuned Mass Inerter Damper was developed which uses the mass amplification effect of these devices.

2. OBSERVED VORTEX SHEDDING INDUCED EVENTS

To understand the necessity for mitigation measures, acceleration values have been obtained during the installation of wind turbine towers. The purpose of the monitoring campaign was to determine the tower vibrations and the relevant natural frequencies. Figure 1 shows a typical recorded time history of the obtained accelerations and displacements as well as a spectrogram showing the FFT spectrum for time segments of 10 minutes. For the state without nacelle (above in Fig. 1) a resonant VIV event was observed, verifying the calculated max. cross wind oscillations for the determined structural damping ratio. The frequency shift for the state with nacelle (below in Fig. 1) is also clearly identifiable.

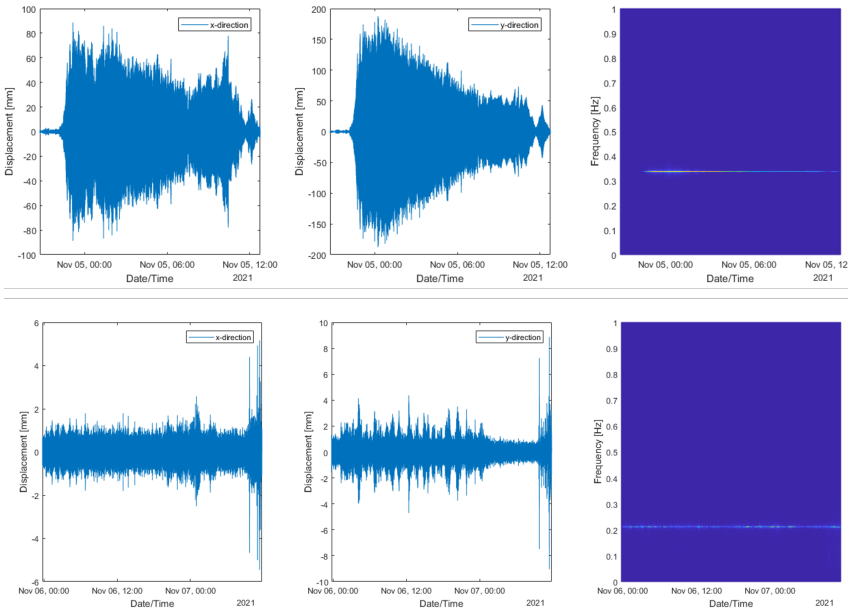

Figure 1. Recorded time histories of the occurring accelerations, displacements and corresponding spectrograms – above: for a tower structure with all segments but without nacelle – below: with nacelle.

3. MITIGATION CONCEPT - REQUIRED TMD PARAMETERS

To determine the optimum TMD parameters for the required range of natural frequencies, modal masses and resulting cross wind amplitudes, an analytical approach in the frequency domain was used which provides the effective overall structural damping and the relative TMD displacements as a function of the generalized mass of the tower, the inherent structural damping of the tower and the natural frequency of the tower. With these values and with the tower geometry (height/diameter) the max. VIV amplitudes were determined acc. to EN 1991-1-4 Wind Actions on structures and are shown in the Figure 2 and considered for the optimization analysis. The optimization curves show the achieved total structural damping ratio and resulting displacements for different tower variations as a function of the natural frequency for the optimized TMD specification. In this particular case an effective TMD mass of 4000kg was required to achieve the required robustness for the relevant installation stages and to keep the relative TMD displacements within a feasible level.

4. IMPLEMENTATION OF THE TMID CONCEPT

To reduce the TMD mass and to improve the handling for the installation of the TMD devices, the mass amplification effect of Tuned Mass Inerter Dampers has been used. To implement

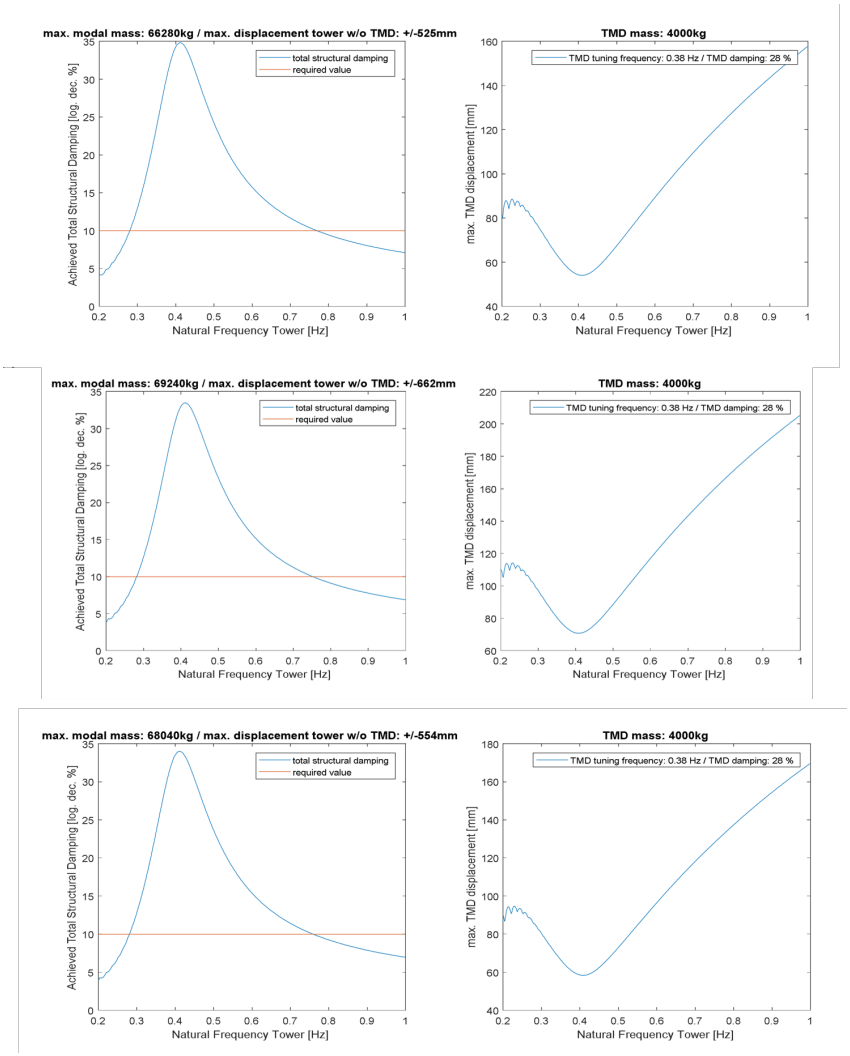

Figure 2. Optimization curves for 3 different installation stages – resulting optimum TMD configuration.

an applicable system, a unidirectional prototype with adjustable eccentric weight arrangements has been developed with the objective to create a maintenance-free, robust TMID system, using an initial rail system with a pinion rack (see Fig. 3). With the prototype deflection tests were performed to obtain the TMD parameters (Tuning frequency, TMD damping ratio). In addition shaking table tests were performed to measure the control force for given dynamic displacements of the shake table.

Figure 4 shows the measured max. mass amplifications that were achieved based on the mass eccentricity of the inerter fly-wheel. The max. amplification was about factor 9.5 so the TMD mass of initially 4000kg could be reduced to 500 kg.

5. SUMMARY

A Tuned Mass Inerter Damper has been developed to reduce the total weight of conventional TMD passive TMD systems that should provide a big robustness to be installed at On-Shore Wind Turbine Tower Structures.

The required TMD parameters were determined using the results of an in-situ monitoring campaign, which helped to verify the max. cross wind amplitudes, the natural frequencies and

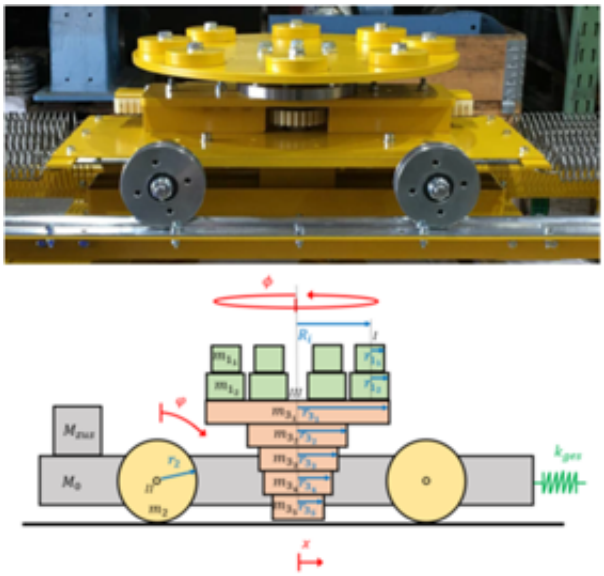

Figure 3. TMID prototype and multi-body model.

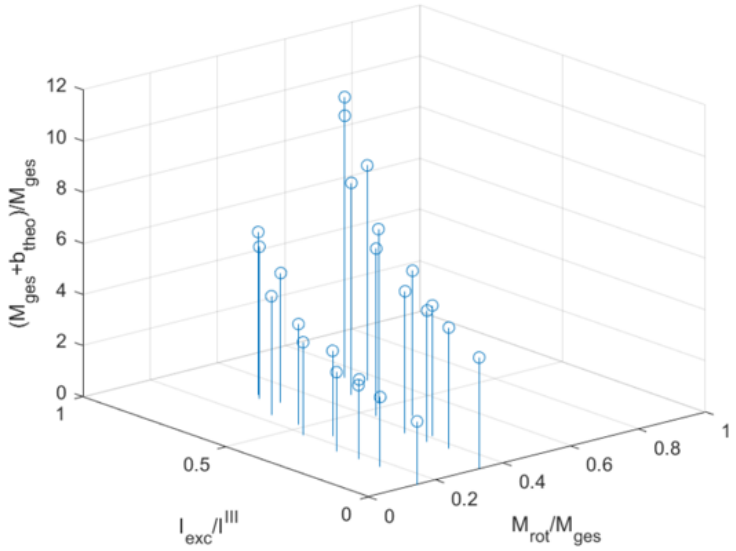

Figure 4. Measured Mass Amplification as a function of the ratio between rotating mass compared to the total mass (M_{rot}/M_{ges}) and the ratio between eccentricity vs. the total moment of inertia (I_{exc}/I^{III}).

inherent damping ratios. This parameters were the adapted by the developed inerter system which could achieve a mass amplification of almost factor 10.

During work shop tests, the theoretical approach could be verified and the suitability for a practical, maintenance free application confirmed.

IN-VENTO 2024
International Conference of the Italian Association for Wind Engineering
Pisa, September 8th – 11th, 2024

Estimation of aerodynamic properties of a polygonal cylinder from full-scale monitoring

Mekdes T. Mengistu[a] and Maria Pia Repetto[b]

[a]*University of Genova, Genova, Liguria, Italy, mekdestadesse.mengistu@edu.unige.it*
[b]*University of Genova, Genova, Liguria, Italy, Maria.Pia.Repetto@unige.it*

SUMMARY:
A novel approach is applied for the calculation of the aerodynamic properties of a 16-sided cylindrical pole from full-scale monitoring data. The simultaneous measurement of wind speed and strain recordings during selected events were used to inverse-calculate the drag and lift coefficients. The calculated coefficients were then compared with the results of previously done wind tunnel testing. The comparison between the results of full-scale monitoring data and the wind tunnel testing showed that the general pattern of the drag coefficient variability with the angle of attack is closely similar. Although the lift coefficients obtained from the wind tunnel testing were shown to be highly variable with small changes in the angle of attack, this variability was not evident from the results of the full-scale monitoring data. The study highlighted the importance of full-scale vibration data for the inverse calculation of aerodynamic coefficients through the proposed approach.

Keywords: Full-scale monitoring, Wind tunnel investigation, Polygonal cylinder

1. INTRODUCTION

The study of aerodynamic loads from full-scale monitoring dates back to more than 40 years ago when researchers monitored pressure on the facades of buildings to validate aerodynamic coefficients obtained through wind tunnel testing. Similar approaches are widely available in the literature (Han et al., 2023). However, the difficulty of monitoring pressure for the long term at various points of a structure makes this approach inconvenient, particularly for slender structures. A different approach for the inverse-calculation of drag coefficient from full-scale vibration data is presented in Acampora et al. (2014), in which the estimated aerodynamic damping from ambient vibration data is used to calculate the drag coefficients using quasi-steady theory. However, this approach did not address the uncertainty propagated due to the high variability of damping ratios obtained through ambient vibration.

This paper proposes a novel approach for the inverse calculation of aerodynamic coefficients from structural response data. Simultaneous measurements of wind speed and strain are used to calculate the aerodynamic coefficients of a 16-sided cylindrical section. The results are compared with the aerodynamic coefficients obtained through wind tunnel testing of a scaled model.

2. DESCRIPTION OF THE STRUCTURE AND THE MONITORING SYSTEM

The full-scale monitored structure is a 16.6m high steel lighting pole made of a 16-sided polygonal shaft with a tapered cross-section that decreases its maximum cross-sectional dimension from 528 mm at the base of the pole to 254 mm at the top. The structure supports an intermediate platform at 10 m and a lighting fixture housed in a rectangular platform at the top. A circular ladder is attached to one of the faces of the polygonal shaft and it runs from the bottom to the top of the pole. In addition to its self-weight, the pole supports, the attached ladder of

mass $\approx$ 180 kg/m, the intermediate platform of mass $\approx$ 60 kg, and the top platform with the lighting accessories of mass $\approx$ 500 kg. The structure is located at the harbor of La Spezia in Italy.

The monitoring system consists of an ultrasonic anemometer installed at 21.7 m for the wind speed and direction measurement, 2 bi-axial accelerometers installed at 11 m and the top of the structure, and 8 uni-axial strain gauges installed at 0.5 m and 1.5 m. The measurement frequencies are 10 Hz for the anemometer, 100 Hz for the strain gauges, and 200 Hz for the accelerometers. The data acquisition system saves consecutive 6 hrs of wind and structural response data. The monitoring system has been registering simultaneous measurements of wind and structural response data continuously except for periods of interruption for maintenance. So far, the monitoring system has registered 4230 hrs of data.

3. INVERSE MODEL FOR ESTIMATION OF AERODYNAMIC LOADS

The dynamic properties of the monitored structure were identified through operational modal analysis techniques using the ambient vibration data registered by the long-term monitoring data. The first mode shapes were identified to be bending modes in two orthogonal directions X and Y at modal frequencies of 0.85 Hz and 0.75 Hz. The orthogonal axes $X-Y$ rotated by 44.5 degrees counterclockwise from the East-North directions.

From the 4230 hrs of data, 10 minutes of wind speed data exceeding a certain threshold of mean wind speed were identified for the back calculation of the aerodynamic coefficients from the full-scale monitoring. For each identified event the strain recordings are calibrated to remove the long-term drift in the strain registrations. The calibrated strains were then used to calculate the deflection of the structure using the Bernoulli-Euler beam equation for small deflections and assuming pure biaxial bending. On the other hand, the mean drag and lift forces were defined using the quasi-steady theory as follows:

$$\bar{F}_d(z,t) = 0.5\rho b(z)\bar{u}^2(z,t)C_d(t) \tag{1}$$

$$\bar{F}_l(z,t) = 0.5\rho b(z)\bar{u}^2(z,t)C_l(t) \tag{2}$$

where $\bar{F}_d(z,t)$ and $\bar{F}_l(z,t)$ are the mean drag and lift forces respectively; ρ is the air density; $b(z)$ is the windward breadth of the structure; $\bar{u}(z,t)$ is the mean wind speed; $C_d(t)$ is mean the drag coefficient; and $C_l(t)$ is the mean lift coefficient.

The mean drag and lift coefficients can be projected on the principal axes of the structure $X-Y$ to obtain the mean aerodynamic forces $\bar{F}_X(z,t)$ and $\bar{F}_Y(z,t)$.

$$\bar{F}_X(z,t) = \bar{F}_d(z,t)\cos\theta(t) + \bar{F}_l(z,t)\sin\theta(t) \tag{3}$$

$$\bar{F}_Y(z,t) = -\bar{F}_d(z,t)\sin\theta(t) + \bar{F}_l(z,t)\cos\theta(t) \tag{4}$$

where $\theta = 44.5 - \beta(t)$ and $\beta(t)$ is the angle the mean wind speed makes with the horizontal East-West axis.

The mean quasi-static displacement at the top of the structure is defined as:

$$\bar{d_X}(t) = \frac{\int_0^H \bar{F_X}(z,t)\psi_X(z)dz}{K_X} \tag{5}$$

$$\bar{d_Y}(t) = \frac{\int_0^H \bar{F_Y}(z,t)\psi_Y(z)dz}{K_Y} \tag{6}$$

where ψ_X and ψ_Y are the mode shapes in the X and Y directions respectively; and K_X and K_Y are the stiffnesses corresponding to the vibration modes in the X and Y direction.

Since the dynamic properties of the structure corresponding to the first modes are known from the operational modal analysis and the mean quasi-static displacement at the top of the structure is obtained from the strain registrations, the only unknowns in Eq. (5) and Eq. (6) are the aerodynamic coefficients $C_d(t)$ and $C_l(t)$ and the vertical profile of the mean wind speed. Considering the vertical profile model of an atmospheric boundary layer wind, the aerodynamic coefficients can be obtained by solving Eq. (5) and Eq. (6) simultaneously.

4. COMPARISON OF AERODYNAMIC COEFFICIENTS OBTAINED FROM WIND TUNNEL TESTING AND FULL-SCALE MONITORING

The wind tunnel investigation was done by Orlando et al. (2023) at the boundary layer wind tunnel of the University of Genova. The test was on two scaled sectional models of the largest and smallest cross-sections at the base and the top of the pole respectively. In addition, a separate test has been done for the platform at the top of the pole. The test considered the presence of the steel ladder on one of the faces of the cross-section and other imperfections. A detailed description of the test and the results can be found in Orlando et al. (2023).

The equivalent height-invariant aerodynamic coefficients obtained from the full-scale monitoring were compared with those obtained from wind tunnel testing. The comparison did not consider all the angles of attack because of the unavailability of full-scale data for wind coming from some sectors. The comparison showed that the general trend of the drag coefficient variation with the angle of attack from the wind tunnel testing is closely similar to the result from the full-scale monitoring data. However, the high variability of lift coefficients with small changes in the angle of attack evident from the wind tunnel result was not observed in the full-scale monitoring data results.

In addition, the results of the full-scale monitoring data highlighted the effect of the attached ladder on the aerodynamic properties of the structure. Fig. 1 compares the mean wind trajectory and mean response trajectory during two examples of events used to back-calculate the drag and lift coefficients. The presence of the ladder attached to the polygonal shaft at approximately 225 degrees plays an important role in the aerodynamic coefficients with the lift force being almost zero when the wind is towards 225 degrees (Fig. 1a) and a significant lift when the wind direction is slightly different (Fig. 1b)

5. CONCLUSIONS

The aerodynamic property of a 16-sided polygonal cylinder is studied using full-scale monitoring and the result is compared with previously done wind tunnel investigation. The drag and

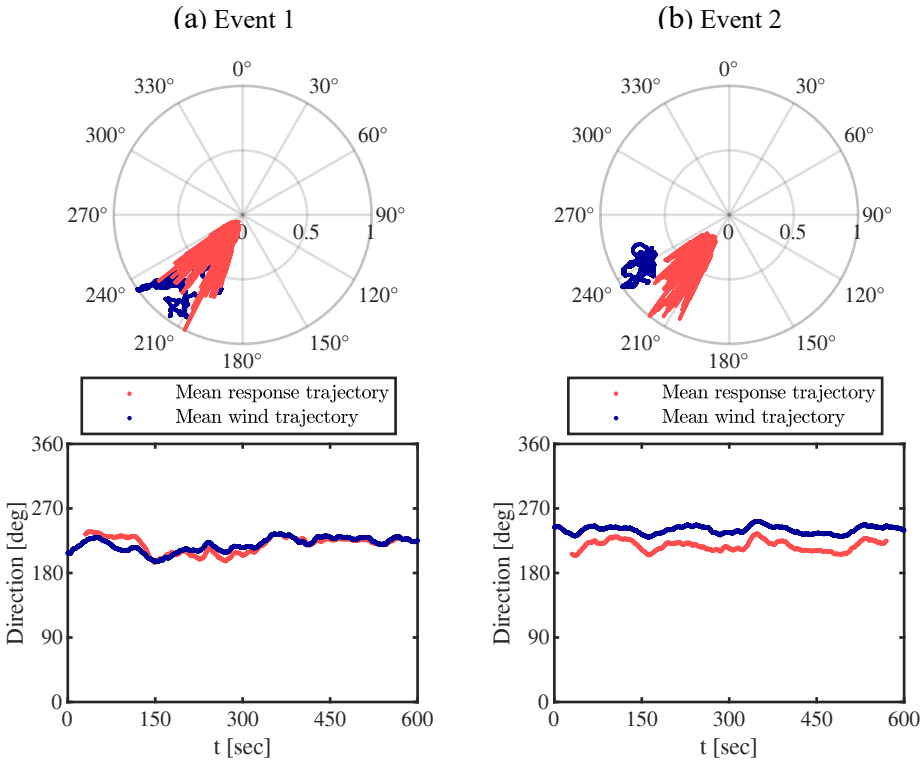

Figure 1. Comparison between the mean wind speed trajectory and mean response trajectory

lift coefficients were inverse-calculated from the structural response through the quasi-steady theory. The general pattern of the equivalent drag coefficient variation with the angle of attack is in close agreement with the results of the wind tunnel investigation. Although the lift coefficients obtained from wind tunnel investigation showed high variability with small changes in the angle of attack, this was not evident in the lift coefficients obtained from the full-scale monitoring data.

ACKNOWLEDGEMENTS

The contribution of the second author is funded by the European Research Council (ERC) under the European Union's Horizon 2020 research and innovation program (grant agreement No. 741273) for the project "THUNDERR - Detection, simulation, modeling and loading of thunderstorm outflows to design wind-safer and cost-efficient structures" – through an Advanced Grant 2016. The monitoring system is co-funded by the Italian Ministry of Instruction and Scientific Research (MIUR), Prot. 2015TTJN95 in the framework of the Research Project of Relevant National Interest (PRIN 2015).

REFERENCES

Acampora, A., J. H. Macdonald, C. T. Georgakis, and N. Nikitas (2014). Identification of aeroelastic forces and static drag coefficients of a twin cable bridge stay from full-scale ambient vibration measurements. Journal of Wind Engineering and Industrial Aerodynamics 124, 90–98.

Han, X.-L., Q.-S. Li, K. Zhou, and M. Li (2023). Investigation of the Aerodynamic Forces on a 600-m-High Supertall Building by Field Measurements and Wind Tunnel Test. Journal of Structural Engineering 149, 1–13.

Orlando, A., L. Pagnini, and M. Pia Repetto (2023). Wind tunnel tests of a hexadecagonal cylinder with imperfections and ancillaries: aerodynamic characterization and technical discussion. Engineering Structures 274, 115114.

IN-VENTO 2024
International Conference of the Italian Association for Wind Engineering
Pisa, September 8th – 11th, 2024

Correlation between predictability of extreme wind speeds and wind directionality

Paraskevi Modé[a], Cristoforo Demartino[b], Nikos D. Lagaros[a], Christos Th. Georgakis[c]

[a]*School of Civil Engr., National Technical University of Athens, Athens, Greece, pmode@mail.ntua.gr – nlagaros@central.ntua.gr*
[b]*Dept. of Architecture, Rome Tre University, Rome, Italy, cristoforo.demartino@uniroma3.it*
[c]*Dept. of Civil and Architectural Engr., Aarhus University, Aarhus, Denmark, cg@cae.au.dk*

ABSTRACT:
Extreme events, such as high wind speeds, pose significant threats to critical infrastructures worldwide, leading to substantial loss and damage. Accurate forecasting of these events is crucial for disaster preparedness and infrastructure protection. This study tackles the problem of understanding the nature of extreme events for developing effective strategies to mitigate their effects and enhance the resilience of vital infrastructures. Specifically, investigates the connection between directionality and the imbalance ratio of extreme wind speeds, which is related to the predictability of extreme winds. In this context, a long short-term memory (LSTM) model is used for predicting the extreme wind speeds in a classification task. The traditional extreme value analysis is used to extract the extreme events in each directional sector and define the threshold for the task of classification.

Keywords: extreme value theory, extreme winds, directionality, LSTM

1. INTRODUCTION

Extreme events, particularly extreme wind speeds (EWSs), pose significant threats to critical infrastructures, leading to substantial loss and damage. The escalating intensity and frequency of these events, often attributed to climate change, necessitate advanced predictive and preventative strategies. Accurate forecasting of EWSs is vital for enhancing disaster preparedness, mitigating impacts, and bolstering infrastructure safety.

However, current research focuses primarily on predicting average wind speeds, neglecting the crucial aspect of EWS forecasting, which is crucial for disaster management and infrastructure protection. Therefore, understanding the relationship between wind directionality, wind distribution, traditional extreme vale analysis (EVA) and the predictability of wind extremes, which is related to the class ratio (Weiss and Provost, 2001), is crucial for various applications, including renewable energy generation, air quality monitoring, and risk assessment for infrastructure and agriculture, and urban planning.

2. METHODOLOGY

The problem is tackled as classification using a deep-learning model, the long short-term memory (LSTM) network. The threshold of the class of the extremes is defined using the traditional extreme value analysis. Specifically, the Block maxima (BM) method is used according to Palutikof et al., 1999:

$$U(T_r) = \begin{cases} \mu + \frac{\sigma}{\xi}[1 - (\ln \frac{T_r}{T_r - 1})^{-\xi}], & \text{for } \xi \neq 0 \\ \mu - \sigma \ln(\ln \frac{T_r}{T_r - 1}), & \text{for } \xi = 0 \end{cases} \quad (1)$$

where T_r is the return period, μ, σ, and ξ are the location, scale and shape parameters of the extreme value distribution, respectively. The parameters of the BM method are calculated using maximum likelihood estimate (MLE) technique.

The wind speeds are divided into 8 equally spaced sectors and the extreme value analysis using Eq. (1) is used for each sector for return periods of 2, 3, 4, 5, and 6 months. For the machine learning part, a return period of 3 months and a prediction horizon of 90 min are chosen. Additionally the wind data, as well as the wind data of each sector are fitted using the 3-parameter Weibull distribution, which is widely used for wind type of data (Hennessey, 1977; Justus et al., 1976).

3. CASE STUDY

Wind speed and wind direction data from the weather station located in Los Angeles international airport (LAX) and O'hare international airport (ORD) are studied herewith. The data constitute 17 years of measurements, from 2006 to 2022 that are obtained from Iowa State University's Environmental Mesonet system, (IEM, 2023). The data consists of the 2 min mean of 5 sec averages and it is stored every 1 min, (NOAA, 1998). The data are cleaned from global and local outliers using statistics and downsampled to 10-min retaining the max 1-min mean wind speed values, in order to improve the computational efficiency.

3.1. Preliminary results and discussion

The results of the directional analysis using Eq. (1) for $T_r = 3$ months, and Weibull distribution are presented in Table 1. A comparison of the results of the Table 1 reveals that the shape (k) and scale (λ) parameters are higher where the wind speeds derived from the EVA analysis are higher. Higher values of k indicate a thinner tail of the Weibull distribution, while higher values of λ parameter indicate a more peaky distribution.

Table 1. Parameters of the fitted Weibull distribution of the wind speed time series and results of the EVA for $T_r = 3$ months at the whole dataset and at 8 equally spaced directional sectors of the Los Angeles international airport (LAX) and O'hare international airport (ORD) weather stations. Results are computed for the full dataset (i.e., 17-year period from 2006 to 2022). The shape parameters of the Weibull distribution are a and k, while λ is the scale parameter.

Dataset	Directional sectors	a [ ]	k [ ]	λ [m/s]	U(3) [m/s]
LAX	(0°, 360°]	3.00	1.16	2.35	13.26
	(0°, 45°]	85.65	0.75	0.45	6.56
	(45°, 90°]	54.91	1.03	0.90	6.06
	(90°, 135°]	103.37	0.98	0.87	6.78
	(135°, 180°]	131.92	0.81	0.51	6.38
	(180°, 225°]	69.10	0.64	0.30	7.73
	(225°, 270°]	9.22	1.92	5.30	12.79
	(270°, 315°]	2.58	1.37	3.33	12.32
	(315°, 360°]	186.60	0.44	0.06	7.00
ORD	(0°, 360°]	5.63	1.35	3.66	16.09
	(0°, 45°]	1.53	1.77	5.01	12.48
	(45°, 90°]	12.13	1.72	4.46	10.49
	(90°, 135°]	112.03	1.95	7.54	10.39
	(135°, 180°]	16.52	1.14	2.43	11.90
	(180°, 225°]	1.04	2.07	6.12	13.97
	(225°, 270°]	1.70	1.59	4.65	13.70
	(270°, 315°]	1.40	1.99	5.68	13.79
	(315°, 360°]	1.33	1.95	5.20	12.98

The extreme wind speeds extracted using the EVA analysis for return periods of $T_r = 2$ to $T_r = 6$ months are depicted in Fig. 1. In the LAX dataset, there is a notable concentration of maximum wind speeds within the third quantile of directions, indicating a stronger directional pattern compared to ORD dataset.

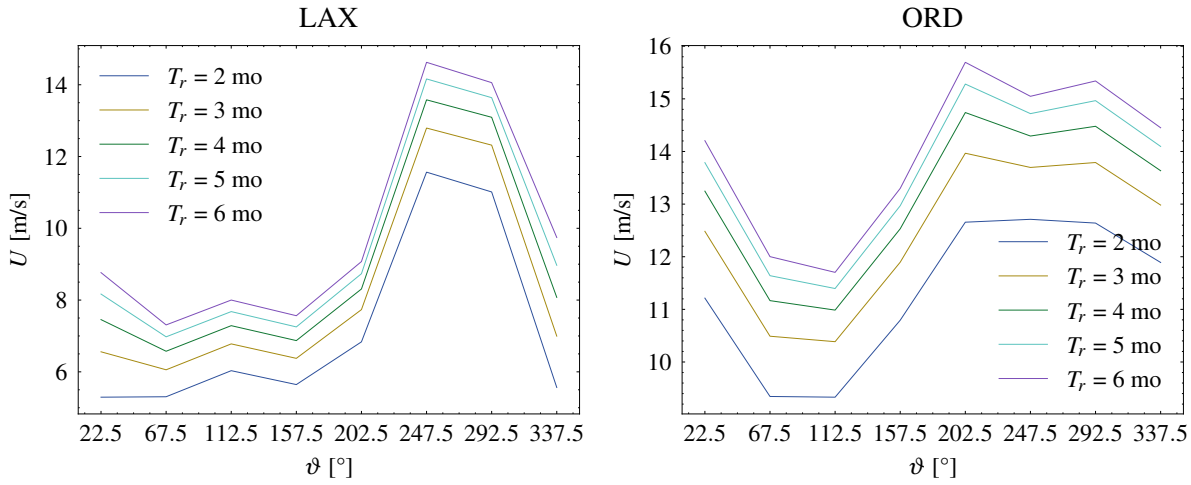

Figure 1. Directional extreme value analysis at 8 equally spaced sectors for return periods of 2, 3, 4, 5 and 6 months that the extreme wind speed values, given in m/s, correspond to the midpoint of each sector. The results are calculated on the 10-min downsampled wind speeds over the 17-year period (01-01-2006 to 31-12-2022) for the two datasets (LAX, ORD).

Extreme wind events extracted from the whole dataset using BM method, for a block of 1-month span, are shown in Fig. 2 (right). The same figure also depicts the probability density histogram of downsampled to 10-min wind speed time series divided into 45 equally spaced bins, and the fitted Weibull distribution, Fig. 2 (left). The two datasets present different wind patterns, with the first data having strong seasonal variations that can also affect wind directionality.

Table 2 presents the evaluation indices of the 3 subsets (train, validation and test). In the LAX dataset, indices are higher than in ORD, as well as the percentage of the extremes defined by the EVA is higher.

Table 2. Percentage of extreme wind speeds for $T_r = 3$ months and evaluation indices for 90 min prediction horizon, for all datasets. F_1, MCC, and BA stand for F_1-score, Mathews' correlation coefficient, and balanced accuracy, respectively.

Dataset	Prediction horizon [min]	Subset [%]	Percentage of extremes [%]	F_1 [%]	MCC [%]	BA [%]
LAX	90	Train	0.934	70.8	70.6	84.1
		Validation	0.844	69.3	69.0	84.8
		Test	0.878	72.0	71.9	84.4
ORD	90	Train	0.630	57.0	56.7	78.1
		Validation	0.514	57.8	57.7	76.8
		Test	0.587	50.4	50.3	77.8

4. CONCLUSION

Analysing historical wind data alongside information about prevailing wind patterns can provide insights into the connection between wind directionality and extreme wind events. The results of the directional EVA in the two datasets leads to a smoother ratio of extreme wind speeds indicating a better capability to fit the extreme wind speed and a robustness in potential outliers.

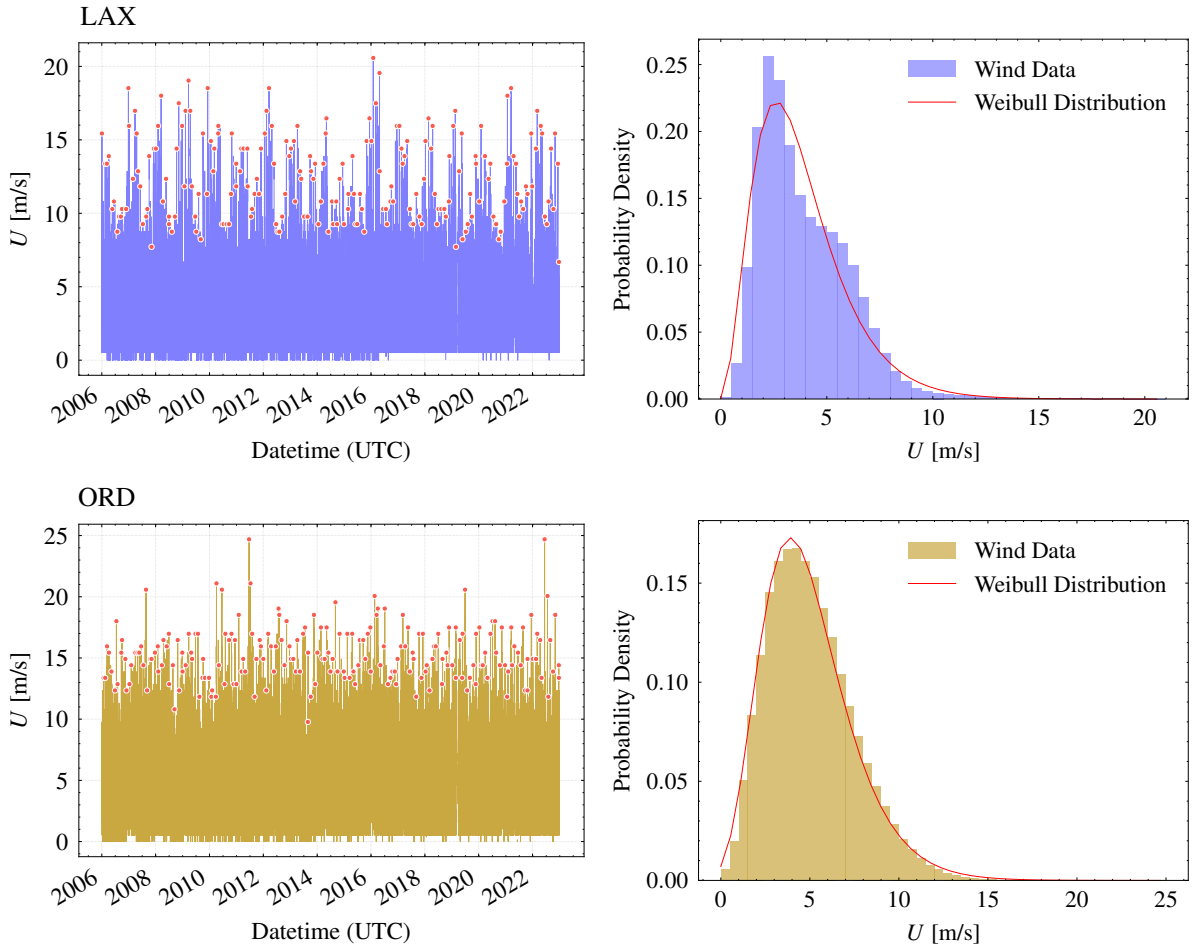

Figure 2. Extreme wind events extracted using BM (right) and probability density histogram (45 bins) and fitted Weibull distribution (left). The results are calculated on the 10-min downsampled wind speeds over the 17-year period (01-01-2006 to 31-12-2022) for the two datasets (LAX, ORD).

ACKNOWLEDGEMENTS

This research has been supported by the ADDOPTML project: "ADDitively Manufactured OPTi-mized Structures by means of Machine Learning" (No: 101007595) belonging to the Marie Skłodowska-Curie Actions (MSCA) Research and Innovation Staff Exchange (RISE) H2020-MSCA-RISE-2020.

REFERENCES

Hennessey, J. P. (1977). Some Aspects of Wind Power Statistics. Journal of Applied Meteorology and Climatology 16, 119–128.

IEM (2023). *ASOS/AWOS Network*. \url{https://mesonet.agron.iastate.edu/ASOS/}.

Justus, C. G., W. R. Hargraves, and A. Yalcin (1976). Nationwide Assessment of Potential Output from Wind-Powered Generators. Journal of Applied Meteorology (1962-1982) 15, 673–678.

NOAA (1998). Automated Surface Observing System (ASOS). Federal Aviation Administration Technical Center Atlantic City, NJ.

Palutikof, J. P., B. B. Brabson, D. H. Lister, and S. T. Adcock (1999). A review of methods to calculate extreme wind speeds. Meteorological Applications 6, 119–132.

Weiss, G. M. and F. Provost (2001). *The effect of class distribution on classifier learning: an empirical study*. Tech. rep.

IN-VENTO 2024
International Conference of the Italian Association for Wind Engineering
Pisa, September 8th – 11th, 2024

Effect of accelerating flows around elongated rectangular cylinders

M. Morello[a], G. Lunghi[a], S. Brusco[b], A. Mariotti[a], M.V. Salvetti[a]

[a]*Dipartimento di Ingegneria Civile e Industriale, Università di Pisa, Pisa, Italy, mario.morello@phd.unipi.it*
[b]*Boundary Layer Wind Tunnel Laboratory, Faculty of Engineering, University of Western Ontario, London, ON, Canada*

SUMMARY:
This investigation explores the dynamics of unsteady high-Reynolds-number flow around 3:1 and 5:1 rectangular cylinders, which can be used to model structures as tall buildings and bridges. Recent attention has moved from steady (constant inflow velocity) to unsteady flows (time-varying inflow velocity), the latter induced, e.g., by thunderstorm phenomena, which cause potential damage to structures. Among them, accelerating flows may lead to significant variations in terms of mean and fluctuating loads, influencing flow dynamics, and surface pressures. This study aims to investigate the characteristic frequencies of the vortex shedding behind elongated rectangular cylinders during accelerating flows, considering the impact on aerodynamic loads. We reproduce the same inflow conditions previously analyzed for the square cylinder in Mariotti et al. (2024): constant-frequency time cells are found for the 3:1 rectangular cylinder in each different accelerating flow, whereas the 5:1 rectangular cylinder shows a more complex dynamics due to the mean-flow reattachment.

Keywords: 3:1 and 5:1 rectangular cylinder, accelerating flow, Large-Eddy Simulations, vortex-shedding frequency, unsteady aerodynamics

1. INTRODUCTION

The present work investigates the unsteady high-Reynolds-number flow around a 3:1 and a 5:1 rectangular cylinder. These flows can be considered as paradigmatic cases of practical interest in the field of wind engineering, such as tall buildings and bridge sections. The flow dynamics around the cylinder strongly depend on the chord-to-depth ratio. In both geometries, the shear layers separate at the upstream edges, rolling up to form vortical structures (Kelvin-Helmholtz instability). These structures are then convected downstream and eventually interact with other vortical structures forming from the separated shear layers. A mean-flow reattachment occurs on the lateral side of the 5:1 rectangular cylinder, resulting in a closed separated-flow region characterizing the mean flow. Further downstream, a second shear-layer separation at the trailing edge leads to Von Karman vortex shedding in the near wake. On the other hand, the 3:1 rectangular cylinder appears to be in an intermediate condition between flows with and without mean-flow reattachment. For these geometries, reattachment is not ensured for the entire duration of the vortex-shedding cycle. Figures 1a,b show a snapshot of the instantaneous field of the spanwise-vorticity from Large-Eddy Simulations (LES) conducted under constant inflow velocity at $Re = 40000$ (based on the freestream velocity, u_∞, and the cylinder depth, D) for the 3:1 and 5:1 rectangular cylinders.

Although the stationary flows around rectangular cylinders with various chord-to-depth ratios have been the subject of several studies (see, for instance, Bruno et al., 2014, for the 5:1 rectangular cylinder), only recently attention has been paid to unsteady inflow conditions. These non-constant flows may be associated with thunderstorm outflows, which are known to in-

duce catastrophic damage to buildings, potentially resulting in significant economic and human losses. The accelerating flows cause a sudden variation in mean and fluctuating loads, affecting the flow dynamics and surface pressures (Li et al., 2022). The nature of flow modifications in unsteady flows was observed in Yang and Mason (2019) to depend on the chord-to-depth ratio and appears to be governed by the separated shear-layer response to changing flow conditions. These modifications induced by accelerated motion can affect the oscillating loads acting on the cylinder's lateral surface: the existence of constant-frequency time cells in the evolution of alternate vortex shedding around a square cylinder during accelerated motion was demonstrated in Brusco et al. (2022), and LES simulations are validated accordingly (Mariotti et al., 2024).

This research activity aims to further investigate the flow dynamics over elongated rectangular cylinders under unsteady inflow conditions representative of thunderstorm winds. The focus is on exploring characteristic frequencies and their dependence on inflow acceleration intensity and the chord-to-depth ratio. The key questions include: (i) does the vortex shedding frequency exhibit a stepwise time behavior as observed for the square cylinder? (ii) Is the impact of these changes in vortex shedding frequency on the fluctuations of aerodynamic loads as significant as observed for the square cylinder? The second question arises due to the different topology of the mean flow on the cylinder surface. Finally, targeted studies will focus on shedding light on the evolution of topological features on the sides of the cylinders, as this significantly affects the near-wake and bulk quantities. Despite the simplicity of the geometries, this study may contribute to expanding our understanding of the dynamic loads on civil buildings caused by thunderstorm outflows.

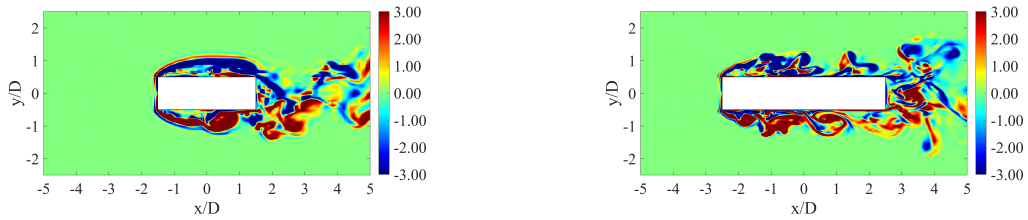

Figure 1. Instantaneous spanwise vorticity at $Re = 40000$ for (a) the 3:1 and (b) the 5:1 rectangular cylinder.

2. NUMERICAL METHOD AND PROBLEM DEFINITION

The incompressible flow around a 3:1 and a 5:1 rectangular cylinder at zero angles of attack is investigated herein. LES simulations are carried out by employing the open-source spectral-element code Nek5000. Each spectral element is rectangular or a suitable coordinate mapping of a rectangle. The basis functions inside the elements are Legendre polynomials of order N for velocity and $N-2$ for pressure in each direction; $N = 6$ has been used herein, as in Mariotti et al. (2024). A third-order backward finite-difference scheme based on the high-order splitting method is used for time advancing. The cylinder center is located at $x/D = y/D = 0$, being D the width of the 3:1 or the 5:1 rectangular cylinder, and the computational domain is sketched in Fig. 2. A uniform unsteady velocity profile with no turbulence is imposed at the inlet, traction-free boundary conditions are used for the outflow and for the upper and lower boundaries of the domain, and no-slip is imposed at the body surface; periodicity boundary conditions are applied in the spanwise direction. The spectral element size and distribution are the same used in Mariotti et al. (2024): the streamwise and crossflow element size is $\Delta x/D = \Delta y/D = 0.125$

near the cylinder, and a uniform spacing of $\Delta z/D = 0.558$ is applied in the spanwise direction. A low-pass filter is applied to the velocity field in the modal space as in Mariotti et al. (2024) because the grid resolution is not fine enough to resolve all turbulent scales at the considered Reynolds number. Since the filter introduces dissipation of the highest resolved modes only, this can be considered as a subgrid-scale dissipation.

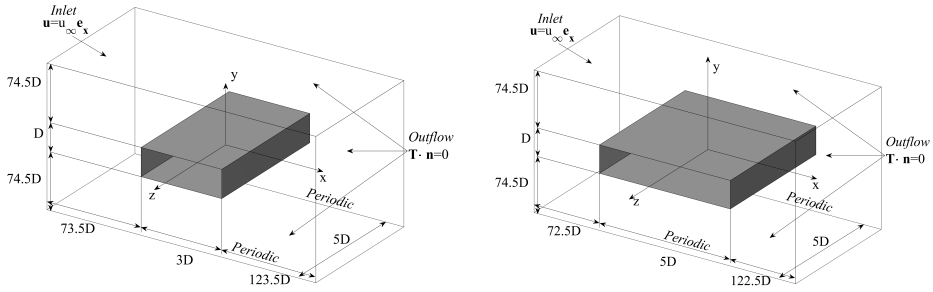

(a) (b)

Figure 2. Sketch of the computational domains for (a) the 3:1 and (b) the 5:1 rectangular cylinder.

The time evolutions of the Reynolds number and the acceleration, normalized by the inflow instantaneous velocity, are depicted in Fig. 3. The reference case (black line) replicates the time histories analyzed experimentally in Brusco et al. (2022) and numerically in Mariotti et al. (2024) around a square cylinder. The Reynolds number varies from $Re = 17200$ to $Re = 65360$, with a maximum non-dimensional acceleration of $aD/u_\infty^2 = 0.0076$. Similar to the study on the square cylinder (Mariotti et al., 2024), the variations in the transients are investigated using time-frequency analysis. Additionally, different acceleration intensities are reproduced as part of a parametric study, aiming to mimic those induced by full-scale thunderstorm outflows.

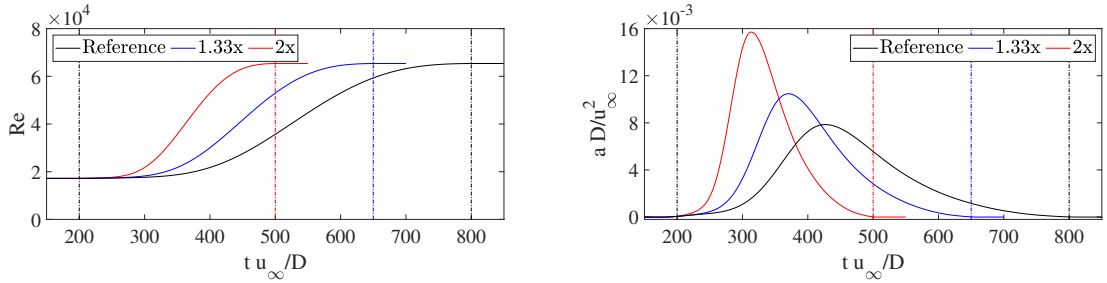

(a) (b)

Figure 3. Time history of (a) the inflow Reynolds number and (b) the non-dimensional acceleration.

3. RESULTS AND DISCUSSION

The final presentation will focus on the impact of inflow-acceleration intensities on the 3:1 and 5:1 rectangular cylinders. We will discuss the mean and fluctuating force coefficients and wake frequencies under unsteady inflow conditions. As an illustrative result, the time behavior of the vortex shedding frequency for the 5:1 rectangular cylinder is shown in Fig. 4: constant-frequency time cells are found for the 3:1 rectangular cylinder in each different accelerating flow, whereas the 5:1 rectangular cylinder shows a more complex dynamics due to the mean-flow reattachment. This information holds significance in predicting potential aeroelas-

tic phenomena arising from vortex shedding induced by the varying flow conditions typical of thunderstorm outflows.

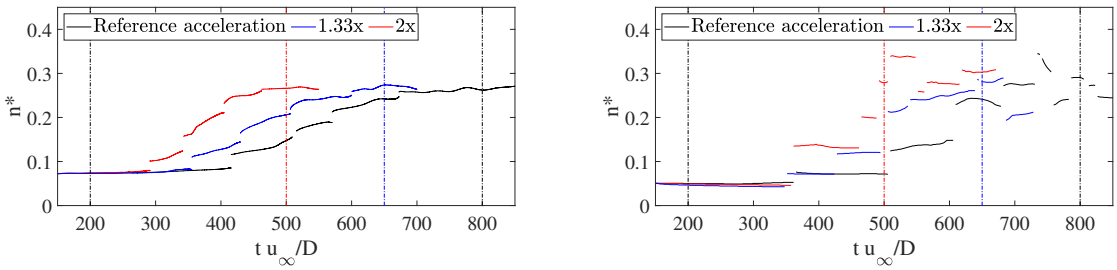

Figure 4. Time behavior of the vortex shedding frequency for (a) the 3:1 and (b) the 5:1 rectangular cylinder.

REFERENCES

Bruno, L., Salvetti, M. V., and Ricciardelli, F. (2014). Benchmark on the aerodynamics of a rectangular 5: 1 cylinder: an overview after the first four years of activity. J. Wind Eng. Ind. Aerod. 126, 87–106.

Brusco, S., Buresti, G., Lo, Y.-L., and Piccardo, G. (2022). Constant-frequency time cells in the vortex-shedding from a square cylinder in accelerating flows. J. Wind Eng. Ind. Aerod. 230, 105182.

Li, X., Li, S., Su, Y., Peng, L., Cao, S., and Liu, M. (2022). Study on the time-varying extreme value characteristic of the transient loads on a 5: 1 rectangular cylinder subjected to a thunderstorm-like wind. J. Wind Eng. Ind. Aerod. 229, 105161.

Mariotti, A., Brusco, S., Lunghi, G., Piccardo, G., and Salvetti, M. V. (2024). Large-Eddy Simulations of the Accelerating Flow Around a Square Cylinder. Marchioli, C. et al. (eds) Direct and Large Eddy Simulation XIII. ERCOFTAC Series 31, 23–28.

Yang, T. and Mason, M. S. (2019). Aerodynamic characteristics of rectangular cylinders in steady and accelerating wind flow. J. Fluids Struct. 90, 246–262.

IN-VENTO 2024
International Conference of the Italian Association for Wind Engineering
Pisa, September 8th – 11th, 2024

Turbulent flow on a 3:2 rectangular cylinder: small-scale rod-induced turbulence and synthetic turbulence methods

Félix Nieto [1], Antonio J. Álvarez [2], Praveen Laws [3], Luca Patruno [4], Kenny Kwok [5]

[1]*CITEEC-University of A Coruña, A Coruña, Spain, felix.nieto@udc.es*
[2] *CITEEC-University of A Coruña, A Coruña, Spain, antonio.jose.alvarez@udc.es*
[3] *CITEEC-University of A Coruña, A Coruña, Spain, pravee.lawrence@udc.es*
[4]*University of Bologna, Bologna, Italy, luca.patruno@unibo.it*
[5]*The University of Sydney, Sydney, Australia, kenny.kwok@sydney.edu*

SUMMARY
A 3D LES modeling is adopted for analyzing the flow features of a 3:2 rectangular prism in smooth flow and under different levels of incoming turbulence. Two different approaches have been applied: i) Synthetic turbulence method as per the SynInflow implementation, and ii) Small-scale rod-induced turbulence, reproducing the experimental approach proposed by Gartshore in the 1970's. The meshing strategy is examined in details, stressing key aspects such as the need for a correct modeling of the turbulent characteristics of the rod-induced wake. Both methods were successful in predicting the fundamental variations in the aerodynamic response depending on the turbulence level.

Keywords: 3:2 rectangular prism, CFD, turbulence.

1. INTRODUCTION

Civil structures are exposed to the atmospheric boundary layer where the wind is intrinsically turbulent. Therefore, it is of great importance to understand how turbulent incoming flow impacts the aerodynamic and aeroelastic responses of bluff bodies. This issue has been addressed by means of wind tunnel tests since the early days of wind engineering as a well-established scientific discipline. In more recent times, a very active line of research has been the computational simulation of free stream turbulent flows and the flow-induced responses of bluff bodies. In this type of CFD problems, scale-resolving models, such as 3D LES are the standard approach, requiring specific methods for the generation of the turbulent fields imposing the divergence-free condition. In this paper, the Synthetic Turbulence Method (STM) based on the PRFG^3 method (Patruno et al., 2017 and 2018), distributed under the name of SynInflow (https://site.unibo.it/cwe-lamc/en), is adopted to study the aerodynamic response of a 3:2 ratio rectangular prism.

Roughly 50 years ago, Gartshore (1973) proposed an alternative to the grid-induced turbulent flow in wind tunnel testing based on placing a small rod upstream of the studied body that generates a small-scale turbulent wake at the stagnation line (Small-Scale Rod-Induced Turbulence Method; SSRITM). According to his work, "*The success of the thin wake in altering the characteristics of the bluff body, apparently as effectively as grid turbulence would do, … suggests that this method could be used in further studies of this sort. The wake technique is more simple and more convenient than the comparable grid method"*. Although this method has been seldom applied in wind tunnel testing (Kwok and Melbourne, 1980; Kwok, 1986) it might have a remarkable impact

in the CFD modeling of turbulent flows as it avoids the complexity associated with the STM. The potential of the method as a simplified approach based on 2D URANS to simulate the response under different intensities of incoming turbulent flow has been demonstrated in Álvarez et al. (2023). In this paper the scale-resolved 3D LES is adopted to study the potential of the method in high-fidelity simulations.

2. COMPUTATIONAL MODELING

The aerodynamic response of the 3:2 rectangular prims is assessed adopting two different methods: STM and SSRITM with the purpose of validating the computational outputs with the wind tunnel tests reported in Mannini et al. (2018) and at the same time compare both computational approaches against each other. The flow domain adopted in the study is relatively large, minimizing the effect of the boundary conditions on the response of the bluff body, being the blockage ratio below *1%*. The simulations are conducted for a Reynolds number $Re = 143000$ based on the prism depth, H. The spanwise dimension of the fluid domain is $4H$. Different meshes have been developed for the STM and RITM approaches as they have different requirements. The 3D LES incompressible and transient fluid motion is solved using the pimpleFoam solver in OpenFOAM. The PIMPLE algorithm ensures pressure-velocity correction and convergence for each time step. The derivatives of time, divergence, gradient and Laplacian terms were solved using second order schemes.

3. RESULTS

3.1. STM simulations

In the STM approach, the turbulent flow characteristics are set as an inlet boundary condition. The main characteristics of the mesh are the following: unstructured conformal mesh with 2.3 million cells, adopting a low Reynolds wall modeling approach, with y^+ values below 2; and 36 layers of cells in the spanwise direction, providing a spanwise discretization $\delta z/H$=0.11. In table 1, the values obtained for the force coefficients in smooth flow and a FST of 5% turbulence intensity are reported along with experimental values for reference. It can be noticed that the drag coefficient decreases as the turbulence intensity increases.

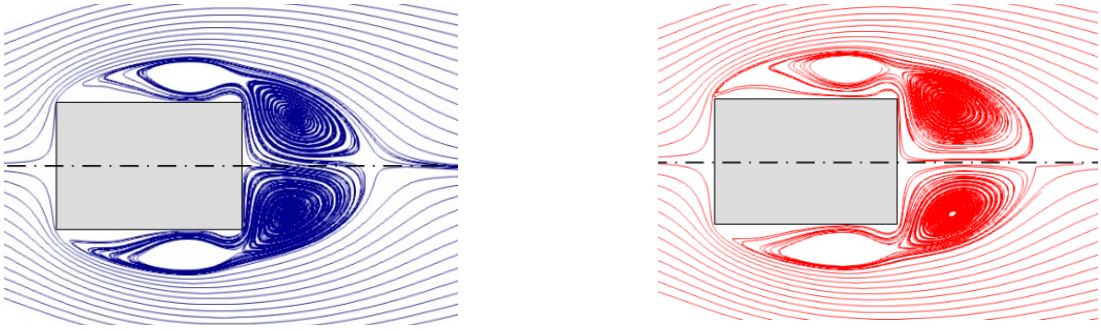

a) b)

Figure 1. Time-averaged stream lines for a) smooth flow and b) 5% turbulence intensity.

In figure 1, the mean streamlines in the vicinity of the 3:2 rectangular prism are depicted, showing the turbulent flow induced modification in the flow topology, with enlarged vortices in the flow direction in the vicinity of the leeward side (figure 1b).

Table 1. Comparison of integral parameters for smooth and turbulent flow.

	Approach	I (%)	$\overline{C_D}$	$\widetilde{C_L}$	St
Present study	CFD (smooth flow)	0	1.76	1.19	0.10
Mannini et al. (2016)	Exp. (Grid turbulence)	1.0	1.76	0.80	0.11
Present study	CFD (SynInflow)	5.0	1.69	1.24	0.11
Mannini et al. (2018)	Exp. (Grid turbulence)	4.3	1.62		

3.2. SSRITM simulations

In figure 2, the scheme of the rectangular prism including the upstream rod is depicted. It is noted that the diameter of the rod D is roughly one order of magnitude smaller than the reference dimension of the 3:2 rectangular prism, H. In this study two different mesh typologies have been adopted: i) a structured non-conformal mesh and ii) a conformal unstructured mesh. A fundamental issue to take into consideration is the ability of the SSRITM to properly model the turbulent characteristics in the wake of the rod, while avoiding very high density meshes posing excessively large computational time burdens.

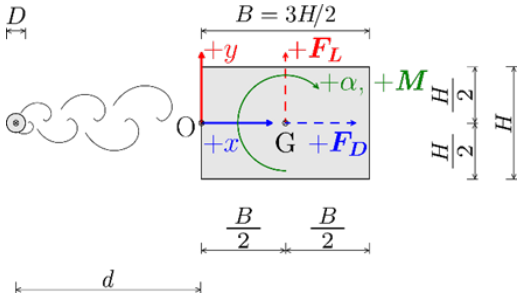

Figure 2. Sketch of the SSRIT approach.

In figure 3, the longitudinal profiles of the turbulence intensity along the wake center line behind the isolated rod (circular cylinder of aspect ratio 48) for two different mesh discretizations adopting a conformal unstructured mesh approach are reported (coarse mesh: 891946 cells and fine mesh: 2805014 cells). In the charts, the resolved and modeled turbulence intensity fractions are reported along with the total turbulence intensity and the time-averaged value for Pope's criterium, (LES simulation should target values close to 0.2, meaning that about 80% of the turbulent energy is resolved by the model). It can be noticed that a high density mesh is required in the wake to simulate the decay in the turbulence intensity in the wake.

In table 2, the results obtained for the 3:2 rectangular prism considering different levels of incoming turbulence intensity are reported (different distances d/D between the rod and the prism) for the 0º angle of attack case, including experimental data for reference. In this case, non-conformal structured mesh has been adopted. The results show the ability of the SSRITM approach to capture the decrease in the drag coefficient as the turbulence intensity level increases.

Table 2. Comparison of simulation and experimental results.

Simulations $Re_H = 143000$						Mannini et al. (2016,2018) $Re_H = 143000 - 146800$					
It_u	AoA	$\overline{C_D}$	$\overline{C_L}$	$\widetilde{C_L}$	St	It_u	AoA	$\overline{C_D}$	$\overline{C_L}$	$\widetilde{C_L}$	St
0.0%	0.0º	1.74	0.00	1.28	0.10	1.0%	≈ 0.0º	1.76	0.01	0.80	0.11
7.5%	0.0º	1.39	0.04	1.02	0.09	6.1%	≈ 0.0º	1.52	0.01		
12.5%	0.0º	1.12	0.01	0.29	0.10	11.5%	≈ 0.0º	1.35	-0.01		

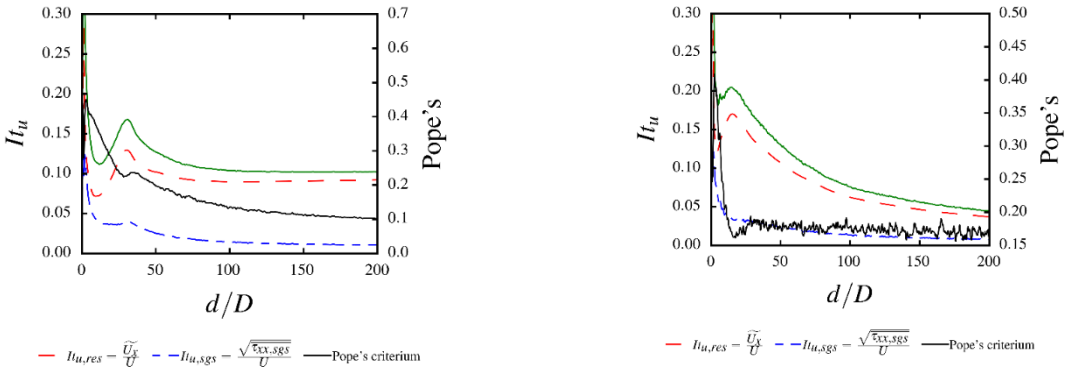

a) b)

Figure 3. Turbulence intensity profiles along the wake centerline of the rod a) coarse and b) fine mesh.

4. CONCLUSIONS

The 3D LES simulations based on the application of the SSRITM and the STM approaches have shown their abilities to reproduce the basic aerodynamic response of a 3:2 rectangular prism under different levels of incoming turbulence. The impact of the mesh discretization in the computational demands and accuracy have been considered. Additional angles of attack have been studied and the results will be reported at the Conference.

ACKNOWLEDGEMENTS

Grant TED2021-132243B-I00 funded by MCIN/AEI/ 10.13039/501100011033 and, by the "European Union NextGenerationEU/PRTR". Funding has also been obtained from the Galician Regional Government through action ED431C 2021/33. The HPC resources at the Galician Supercomputing Centre (CESGA) and the SuperMUC-NG at the Leibniz Supercomputing Centre (Project WES2023 – wind Effects on Structures) have been used for the numerical simulations.

REFERENCES

Álvarez, A.J., Nieto, F., Kwok, K.C.S, Hernández, S., (2023). A simplified CFD approach for bluff-body aerodynamics under small scale free stream turbulent flow. J. Wind. Eng. Ind. Aerodynamics 241, 105500.

Gartshore, I.S., 1973. The effects of the free stream turbulence on the drag of rectangular two-dimensional prisms. Technical report BLWT-4-T3, University of Western Ontario, Canada.

Kwok, K.C.S., Melbourne, W.H., 1980. Freestream turbulence effects on galloping. EM2 J. Eng. Mech. Div. 106 (2), 273-288.

Kwok, K.C.S., 1986. Turbulence effect on flow around circular cylinder. J. Eng. Mech. 112 (11), 1181-1197.

Mannini, C., Massai, T., Marra, A.M., 2018. Unsteady galloping of a rectangular cylinder in turbulent flow. J. Wind. Eng. Ind. Aerodynamics 173, 210-226.

Mannini, C., Marra, A.M., Massai, T., Bartoli, G., 2016. Interference of vortex-induced vibration and transverse galloping for a rectangular cylinder. J. Fluids Struct. 66, 403-423.

Patruno, L. and Ricci, M., 2017. On the generation of synthetic divergence-free homogeneous anisotropic turbulence. Computer Methods in Applied Mechanics and Engineering, 315, pp.396-417.

Patruno, L., Ricci, M., 2018. A systematic approach to the generation of synthetic turbulence using spectral methods. Comput. Methods Appl. Mech. Eng. 340, 881–904

IN-VENTO 2024
International Conference of the Italian Association for Wind Engineering
Pisa, September 8th – 11th, 2024

Drag crisis nonlinear effect on aerodynamic damping of vertical slender structures

Andrea Orlando [1], Luisa Pagnini [2], Mara Pia Repetto [3]

[1]*Polytechnic School, University of Genoa, Italy, Email: andrea.orlando@edu.unige.it*
[2]*Polytechnic School, University of Genoa, Italy, Email: luisa.pagnini@unige.it*
[3]*Polytechnic School, University of Genoa, Italy, Email: maria.pia.repetto@unige.it*

SUMMARY
This paper presents an experimental investigation on the aerodynamic damping and its variability with wind speed in slender vertical structures characterized by strong Reynolds effect. Two lighting towers have been selected as case studies, for which the aerodynamic coefficients evaluated in the wind tunnel showed significant drag crisis. The two structures have been subjected to long-term monitoring providing simultaneous measurements of wind speed and structural response. From the full-scale records, aerodynamic damping has been evaluated in a wide range of wind velocity by applying suitable dynamic identification techniques. Experimental results show a clear non-linear variation of damping in the wind velocity range in which drag crisis occurs. Results are then compared with damping estimates from analytical calculation models gathered from the literature, showing their capability to catch the nonlinear variation of aerodynamic damping when Reynolds effect on aerodynamic coefficients is appropriately taken into account.

Keywords: aerodynamic damping, vertical slender structures, Reynolds effect

1. INTRODUCTION

The wind-induced response of slender structures is strongly influenced by modal damping, where inaccuracies in its assessment could lead to considerable variations in wind effect predictions (Pagnini and Repetto, 2012). In the case of particularly slender and lightweight structures, the dissipation mechanism is mainly of an aerodynamic nature, with damping almost evanishing under low wind excitation. Aerodynamic damping estimation is therefore fundamental for a sound evaluation of wind-induced effects.

Wind codes and standards provide analytical estimates for the aerodynamic damping of slender structures (EN 1991-1-4, 2005). According to these formulations, damping is linearly proportional to wind speed and drag coefficient. Thus, under constant aerodynamic coefficients, damping is expected to increase linearly with wind speed, as it has been observed in several full-scale measurement investigations (Tamura and Suganuma, 1996; Li et al., 2008).

However, a variety of structures are composed of slender elements whose aerodynamic behavior is characterized by a significant reduction of the drag coefficient with increasing Reynolds number *Re*, the so-called “drag crisis”. A common example are vertical slender structures like poles and supporting towers, which are characterized by a cross-section that is typically circular or polygonal with rounded corners. In such cases, aerodynamic damping experiences a nonlinear dependence on wind speed driven by the drag coefficient variation with flow conditions. ESDU (1980) quantifies the variation of the drag coefficient of circular and polygonal cylinders in different

Reynolds regimes, based on a collection of wind tunnel results. However, considerable uncertainties arise from the scatter of the experimental measures in the transition regime, the estimate of surface roughness and turbulence conditions.

Estimating aerodynamic damping therefore remains a challenge; experimental investigations on slender elements mainly are based on wind tunnel tests (Chen et al., 2017; Yang et al., 2023) while full-scale monitoring campaigns are rarely reported (Pagnini et al., 2018). Moreover, to the best of authors' knowledge, no scientific papers have investigated possible nonlinear variation of damping with wind speed due to Reynolds effect on aerodynamic coefficients.

To address these challenges, structural monitoring campaigns have been conducted to characterize aerodynamic damping of two lighting towers. Due to their structural simplicity, these structures are very attractive for a comparison between measured and predicted behavior. This paper describes the experimental campaigns, presents the results of damping identification and discusses the outcomes comparing full-scale measurements and prevision laws from literature.

2. CASE STUDIES

The structures under investigation are two high-mast lighting towers, respectively 16.6 m and 35 m high. The 16.6 m lighting tower stands in the harbour of La Spezia, Italy (Fig. 1a). It is equipped with a steel ladder, a platform at top housing the lighting devices and a security camera, and a resting platform at 10 meters above ground. The 35 m lighting tower stands in the Genova harbour (Fig. 1b); it is free of any appendage and holds a heavy lighting equipment at top. These two structures have been equipped with identical monitoring systems providing simultaneous measurements of wind speed and structural response (Fig. 1c).

A three-axial ultrasonic anemometer installed at the top records the wind speed with a sampling rate of 10 Hz; structural response is recorded at 200 Hz by two biaxial accelerometers (placed at the top of the shaft and at an intermediate level) and by eight uniaxial strain gauges (placed at the base of the shaft). Data are recorded continuously and transmitted by a data acquisition unit installed at the foot of the poles.

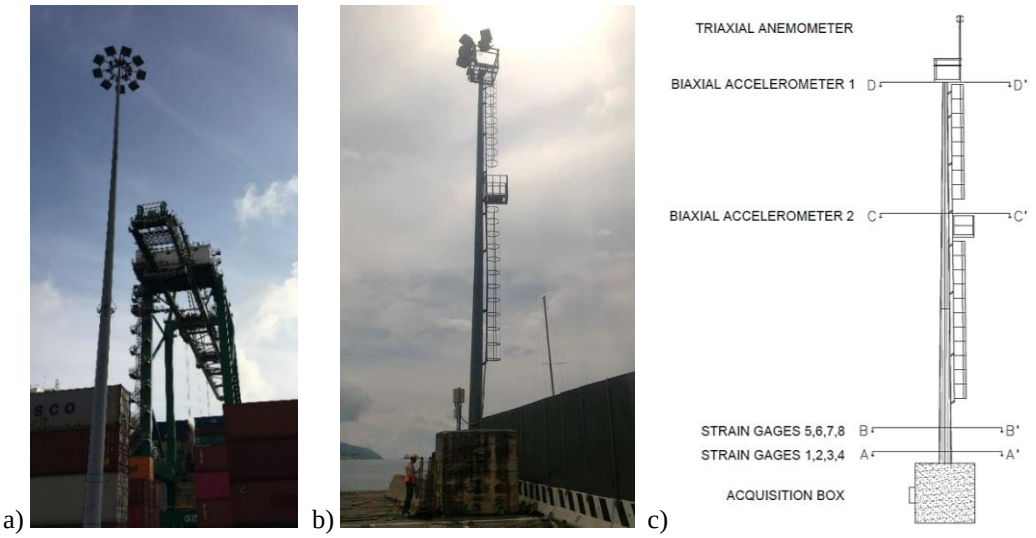

Figure 1. The monitored lighting towers in Genoa (a), La Spezia (b) and their monitoring equipment (c).

Aerodynamic properties of the structures have been evaluated through wind tunnel tests. Both towers are characterized by a 16-sided polygonal shaft with rounded corners. Two sectional models have been realized (Fig. 2a) with different corner radius, representing top and bottom portions of the considered shafts. The external ladder of the pole in La Spezia has been modelled too; it can be attached to both models to evaluate its contribution to the aerodynamic behaviour.

Sectional models have been tested varying angle of attack, mean flow velocity and turbulence intensity (Fig. 2b). Wind tunnel results highlighted a significant decrease of the drag coefficient with increasing *Re* for all wind directions (Orlando et al., 2023).

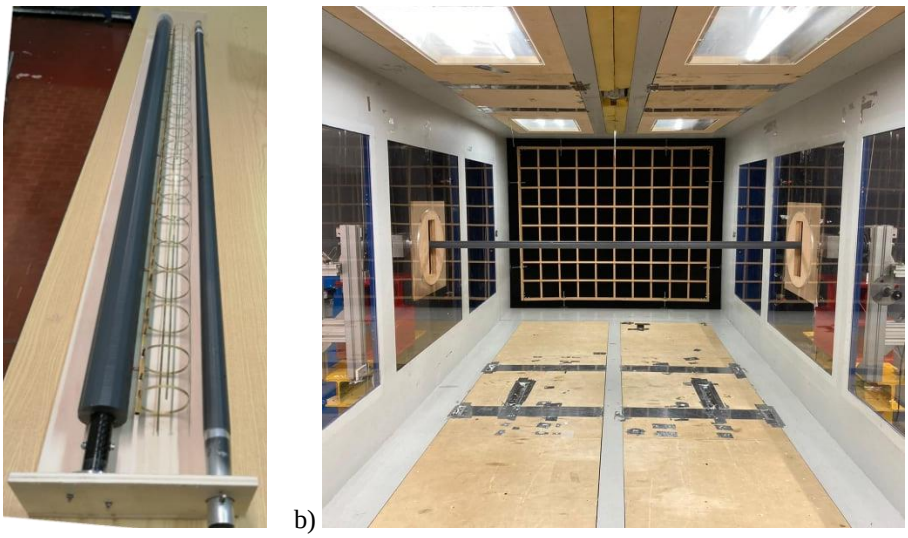

a) b)

Figure 2. The sectional models of the polygonal shafts (a); the model at the wind tunnel test section (b).

3. RESULTS

Starting from the structural acceleration records, damping is evaluated by applying Operational Modal Analysis (OMA) techniques; specifically, the Enhanced Frequency Domain Decomposition (EFDD) technique (Brincker and Ventura, 2015) has been used in the present work.

Experimental results are compared with the analytical predictions from a calculation model specifically tailored for poles and monotubular towers (Pagnini and Solari, 1999). According to the model, the aerodynamic part of the first modal damping ratio in the alongwind direction x is given by:

$$\zeta_{Ax1} = \frac{\rho \bar{u}(z^*) b^* h C_D^* \psi^2_{x1}(h)}{4\pi n_{x1} m_{x1}} (K''_{0x1} + \sum_{k=1}^{N} K''_{kx1}) \quad (1)$$

where $z^* = 0.6h$ with h height of the pole; $b^* = b(z^*)$ where b is the diameter of the cross-section; $\bar{u}$ is the mean wind velocity; ρ is the air density; $C_D^* = C_D(z^*)$ where C_D is the drag mean force coefficient; n_{x1} is the frequency of the first vibration mode in the x direction and m_{x1} is the relevant modal mass of the structure; $\psi_{x1}(z)$ is the first mode shape in the plane xz, being z the vertical axis; K_{0x1} and K_{kx1} are non-dimensional coefficients related to the aerodynamic forces on the lumped masses along the pole.

Experimental values obtained with OMA are compared with the analytical estimates derived by incorporating the aerodynamic coefficients measured in the wind tunnel. As an example, Fig. 3 shows the alongwind aerodynamic damping of the tower in La Spezia versus mean wind speed for wind blowing in the positive *x* direction. Every empty dot derives from 1 hour of recorded data; black dots are the analytical estimates while blue dots are the experimental values; filled dots are the averaged experimental values for every 1 m/s wind speed interval. The diagram shows good agreement between measurements and predictions; moreover, experimental results show a clear non-linear variation of damping in the wind velocity range in which drag crisis occurs. The full paper reports the complete results for the two structures, assessing the capability of analytical models to catch the nonlinear variation of aerodynamic damping when Reynolds effect on aerodynamic coefficients is appropriately considered.

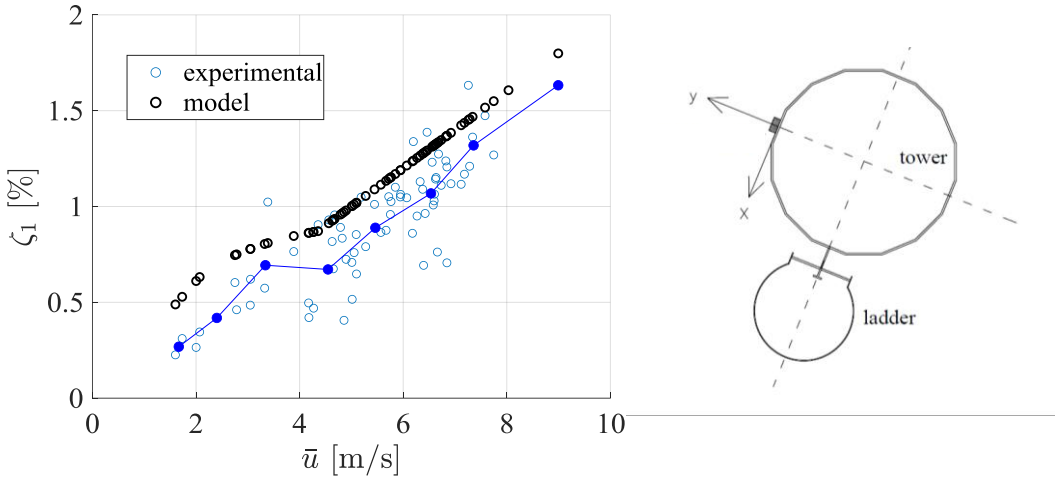

Figure 3. Alongwind aerodynamic damping of the La Spezia tower against wind speed; wind blows in the x direction.

REFERENCES

Brincker R., and C.E. Ventura (2015). Introduction to operational modal analysis. John Wiley & Sons, Ltd.

Chen Z., K.T. Tse, and K.C.S. Kwok (2017). Aerodynamic Damping of Inclined Slender Prisms. 9th Asia-Pacific Conference on Wind Engineering Auckland, New Zealand.

EN 1991-1-4 (2005). Eurocode 1: Actions on Structures – Part 1.4: General Actions – Wind Actions. CEN, European Committee for Standardization, Brussels, Belgium

ESDU 79026 (1980). Mean fluid forces and moments on cylindrical structures: polygonal sections with rounded corners including elliptical shape. London, UK.

Li Q.S., Y.Q. Xiao, J.R. Wu, J.Y. Fu, and Z.N. Li (2008). Typhoon effects on super tall buildings. Journal of Sound and Vibration 313, 581–602.

Orlando A., L. Pagnini and M.P. Repetto (2023). Wind tunnel tests of a hexadecagonal cylinder with imperfections and ancillaries: aerodynamic characterization and technical discussion. Engineering Structures 274, 115114.

Pagnini L., G. Piccardo, and M.P. Repetto (2018). Full scale behavior of a small size vertical axis wind turbine. Renewable Energy 127, 41-55.

Pagnini L., and M.P. Repetto (2012). The role of parameter uncertainties in the damage prediction of the alongwind-induced fatigue. Journal of Wind Engineering and Industrial Aerodynamics 104-106, 227–238.

Solari G., and L. Pagnini (1999). Gust buffeting and aeroelastic behaviour of poles and monotubolar towers. Journal of Fluids and Structures 13(7-8), 877-905.

Tamura Y., and S. Suganuma (1996). Evaluation of amplitude-dependent damping and natural frequency of building during strong winds. Journal of Wind Engineering and Industrial Aerodynamics 59, 115-130.

Yang Q., K. Guo, W. Shan, Y.C. Kim, and Y. Tamura (2023). Identification of nonlinear aerodynamic damping of cross-wind excited slender structures in atmospheric boundary layer flow. Journal of Wind Engineering & Industrial Aerodynamics 241, 105519.

Experimental investigation of monotubular steel poles: case studies and dynamic identification

Andrea Orlando [1], Luisa Pagnini [2], Mara Pia Repetto [3]

[1]*DICCA, University of Genoa, Genoa, Italy, Email: andrea.orlando@edu.unige.it*
[2]*DICCA, University of Genoa, Genoa, Italy, Email: luisa.pagnini@unige.it*
[3]*DICCA, University of Genoa, Genoa, Italy, Email: maria.pia.repetto@unige.it*

SUMMARY
This study presents the main outcomes of an experimental campaign conducted on monotubular steel poles for dynamic identification and estimation of modal damping coefficients. Three distinct case studies were investigated, including a 30 m lightning rod and two lighting towers, respectively 16.6 and 35 m high. The lightning rod was investigated by dynamic identification tests based on pull and release and ambient vibrations measurements. Structural damping has been analysed at low and high vibration levels, supplying the variation with the amplitude of motion. The high-mast lighting towers were investigated by long-term monitoring, providing modal damping coefficients in a wide range of wind velocity. Results are then discussed enriching the obtained data with damping values for lighting poles and high-mast towers gathered from the literature. By leveraging both experimental data and existing literature, main trends are discussed with a view to providing guidance for engineering verifications.

Keywords: monotubular steel poles, dynamic identification, modal damping coefficients

1. INTRODUCTION

Steel monopole cantilevers find applications across a diverse array of structures, including lighting poles, telecom towers, chimneys, traffic signals, wind turbines, and lightning rods. These structures, characterized by slender and lightweight designs, are susceptible to gust actions and aeroelastic phenomena (Solari and Pagnini, 2001). Gust action primarily affects the first vibration mode, inducing alongwind and crosswind vibrations of particular concern at high wind speeds. Certain aerodynamically unstable shapes, such as specific lighting bodies, may lead to aeroelastic instability and galloping conditions. Vortex-induced vibrations (VIVs) resonant with first or second vibration modes may occur at moderate wind velocities (Vickery and Basu, 1983). VIVs on the second mode have been observed primarily in wind tunnel tests. Specific configurations, like high-mast supports enveloped by fiberglass cylinders, can aggravate this phenomenon, potentially inducing synchronous vibrations and lock-in conditions (Repetto and Solari, 2010). Extremely slender columns, such as lightning rods devoid of ancillaries, reduce damping to an extremely low level and eliminate any disruption to the regular pattern of vortex shedding.

In such scenarios, wind actions can induce significant vibrations at both high and moderate wind speeds, exacerbated by low damping levels, leading to repeated stress cycles. Fatigue damage accumulation, primarily observed in the weld area at the base of the column, has been identified as a primary cause of collapse (Zhang et al., 2023). Such collapse of one tower in installations with multiple similar structures can prompt inspections of remaining towers, revealing potential issues necessitating safety interventions (Xhelaj et al., 2024).

Wind codes and standards provide calculation procedures for gust actions and VIVs, with specific documents addressing concerns regarding fatigue cracking and higher mode vortex shedding (EN 1991-1-4, 2005). However, estimating damping in structural design remains a challenge, with errors potentially leading to significant variations in wind effect predictions, highlighting crucial safety engineering considerations (Pagnini and Repetto, 2012).

To address these challenges, experimental campaigns have been conducted to characterize structural behaviour under dynamic loading of an array of high-mast towers. This paper describes the test campaigns, presents the results of dynamic identification and discusses the outcomes, also including other results gathered from the literature, providing insights and guidance for engineering assessments and design optimizations.

2. CASE STUDIES

The experimental activity includes dynamic identification tests on a 30 m lightning rod (Fig. 1a) and long-term monitoring of two high-mast lighting towers, respectively 16.6 m and 35 m high (Fig. 1b, c).

a) b) c)

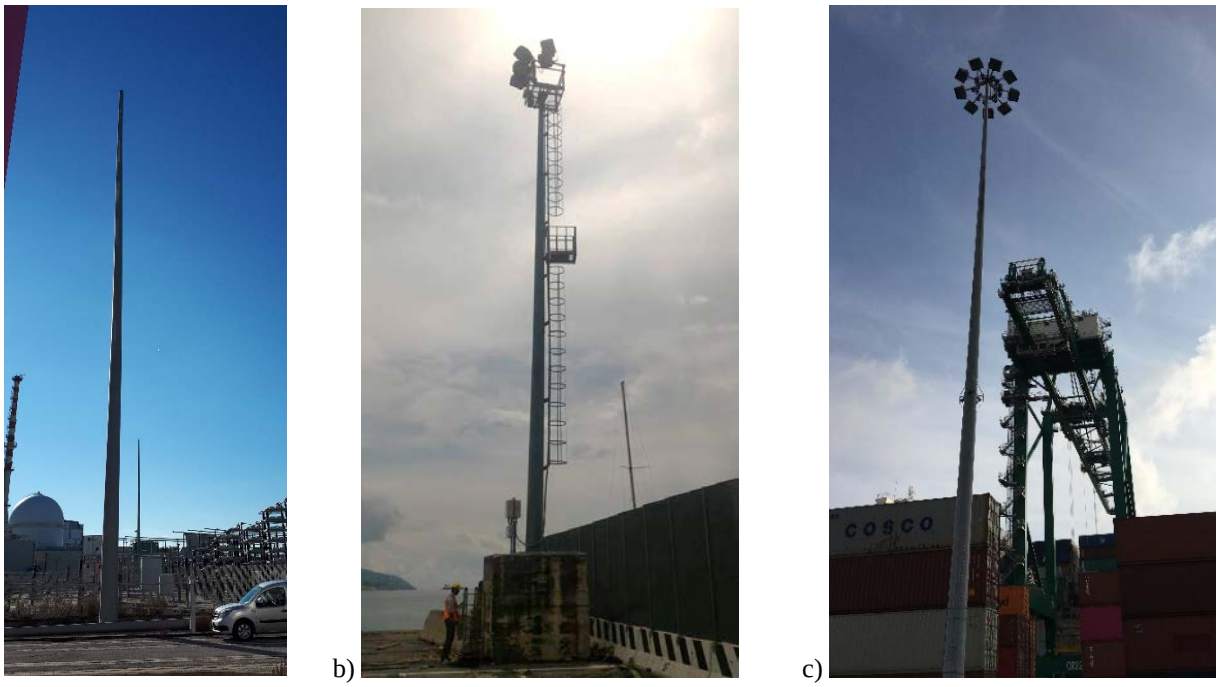

Figure 1. Case studies: 30 m lightning rod (a), 16.6 m lighting tower (b) and 35 m lighting tower (c).

2.1.Lightning rod

The lightning rod is a bare steel column without any ancillary or appendage. It has been investigated by dynamic identification experiments which involved ambient vibration measurements and pull and release tests. Structural motion has been measured by two accelerometers positioned at the top (30 m) and at 16 m, each one recording acceleration in the two horizontal directions. Wind speed measurements, obtained by a portable anemometer, showed lack of wind during the tests (wind speed lower than 2 m/s at top).

Fig. 2a shows the Power Spectra Density (PSD) of the ambient vibration records for each measurement direction *x*, *y*, at the two levels, 30-m and 16-m.

Fig. 2b, c show the acceleration record from pull and release test, respectively for the first and second vibration mode. From these records, modal damping estimates can be obtained straightforward, as a function of the amplitude displacement, by fitting the exponential decay of the free modal response.

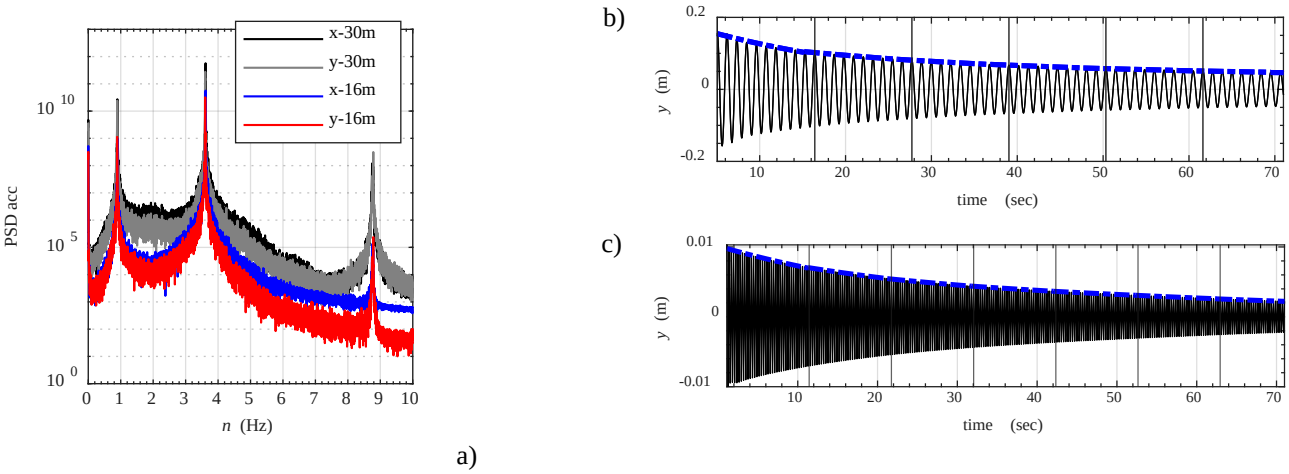

Figure 2. Lightning rod results: PSD of ambient vibrations (a) and free vibration decay for the first (b) and second (c) vibration mode.

2.2.Lighting poles

The 16.6 m lighting tower stands in the harbour of La Spezia, Italy. It is equipped with a steel ladder, a platform at top housing the lighting equipment and a security camera, and a resting platform at 10 meters above ground. The 35 m lighting tower stands in the Genova harbour; it is free of any appendage and holds a heavy lighting equipment at top. These two lighting poles are being monitored by accelerometers, installed at top and at an intermediate level, by strain gauges close to the base and by an ultrasonic anemometer, mounted at top, recording the three components of wind speed. A data acquisition unit at the foot of the structures drives the real-time data transmission.

Fig. 3a shows the PSD of the ambient vibration records at top of the 16.6 m tower in La Spezia along two orthogonal structural axes *u*, alongwind, and *v*, crosswind; *w* is the mean wind speed direction. Therefore, first and second vibration modes in direction *u* are purely alongwind and are characterized by fundamental frequencies denoted by n_{1A} and n_{2A}. Conversely, they are purely crosswind in direction *v*, and are characterized by fundamental frequencies denoted by n_{1B} and n_{2B}.

Fig 3b shows the PSD of the ambient vibration records at top of the 35 m tower in Genova along the two orthogonal structural axes *u*, and *v*. These components both exhibit a dominant modal contribution associated with a first bending mode shape characterized by frequency n_{1A}. Conversely, the second vibration mode in the *u* direction is characterized by the fundamental frequency indicated by n_{2A}, while, in the *v* direction, it is represented by n_{2B}.

From these records, damping estimates can be obtained by OMA techniques (Rainieri and

Fabbrocino, 2014) and are supplied as a function of the wind velocity.

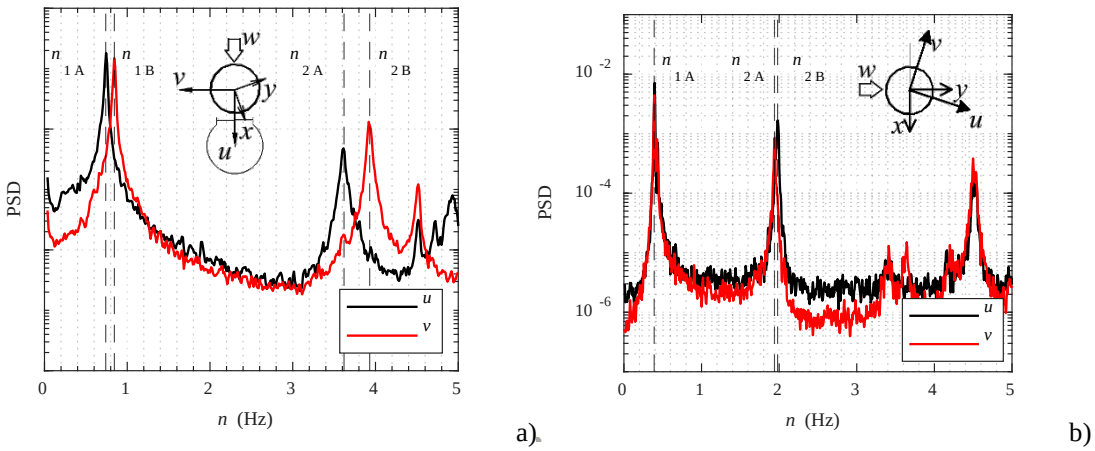

Figure 3. PSD of ambient vibrations along two principal structural directions for the 16.6 m lighting pole (a) and for the 35 m high lighting pole (b).

3. CONCLUSIONS

Considering the diversity of values collected and the case studies reported in the literature (Pagnini, and Solari 1999), certain common trends emerge. At low vibration amplitude, a first modal damping of approximately ξ_1=0.2% can be assumed, aligning with Eurocode guidelines on wind action, albeit this value escalates rapidly with increasing vibration amplitude and wind speed. However, for the second modal coefficient, such an assumption may prove non-conservative, particularly for columns without ancillaries, where even lower values are observed. This presents a significant challenge for safety verifications and for addressing fatigue damage, especially when dealing with critical velocities resonating with the second vibration mode.

REFERENCES

EN 1991-1-4 (2005). Eurocode 1: Actions on Structures – Part 1.4: General Actions – Wind Actions. CEN, European Committee for Standardization, Brussels, Belgium

Pagnini, L.C., and M.P. Repetto (2012). The role of parameter uncertainties in the damage prediction of the alongwind-induced fatigue. Journal of Wind Engineering and Industrial Aerodynamics 104–106, 227–238.

Pagnini L., and G. Solari (2001). Damping measurements of steel poles and tubular towers. Engineering Structures 23, 1085–1095.

Rainieri, C., and G. Fabbrocino (2014). Operational Modal Analysis of Civil Engineering Structures: An Introduction and Guide for Applications. Springer.

Repetto, M.P., and G. Solari (2010). Wind-induced fatigue collapse of real slender structures. Engineering Structures 32, 3888–3898

Solari, G., and L.C. Pagnini (1999). Gust buffeting and aeroelastic behaviour of poles and monotubular towers, Journal Fluid and Structures 13 (7-8), 877-905.

Vickery, B.J., and RI Basu (1983). Across-wind vibrations of structures of circular cross section. Part I: development of a mathematical model for two-dimensional conditions. Journal of Wind Engineering and Industrial Aerodynamics 12 (1), 49–74.

Xhelaj, A., A. Orlando, L. Pagnini, F. Tubino, and M.P. Repetto (2024). Fatigue life assessment of a slender lightning rod due to wind excited vibrations. Structural Integrity Procedia, in press.

Zhang, M., T. Li, Y. Wang, Y. Chen, and G. Zhao (2023). Wind-Induced Vibration and Vibration Suppression of High-Mast Light Poles with Spiral Helical Strakes. Buildings 13, 907.

IN-VENTO 2024
International Conference of the Italian Association for Wind Engineering
Pisa, September 8th – 11th, 2024

Numerical simulation of the aeroelastic response of a long-span bridge subjected to different non-synoptic wind scenarios

Maria Antonietta Pace[a], Filippo Calamelli[b], Tommaso Argentini[c], Daniele Rocchi[d]

[a]*Politecnico di Milano, Milan, Italy, mariaantonietta.pace@polimi.it*
[b]*Politecnico di Milano, Milan, Italy, filippo.calamelli@polimi.it*
[c]*Politecnico di Milano, Milan, Italy, tommaso.argentini@polimi.it*
[d]*Politecnico di Milano, Milan, Italy, daniele.rocchi@polimi.it*

SUMMARY:
Over the past few years, there has been an increase in both the frequency and intensity of extreme climate events, such as thunderstorms and downbursts. These phenomena, which could be characterized by large variations of wind speed and angle of attack, pose a challenge in the numerical simulation of the aerodynamic response of long-span bridges. In this study, employing a non-linear time-varying method, the response of a suspension bridge under various non-synoptic wind scenarios is investigated. The main purpose is to evaluate the influence of non-linear effects due to the slow-varying wind speed and angle of attack on the dynamic response of the structure. The numerical results will be presented and compared to the corresponding outcomes obtained by applying a standard synoptic scenario as a wind input.

Keywords: Non-synoptic winds, Non-linear aerodynamics, Aeroelastic response, Long-span bridges

1. INTRODUCTION

In recent years, technological advancements in monitoring techniques have significantly impacted the research on wind-induced effects on long-span bridges. These progress have allowed to study extreme climate events such as storms and downbursts (see Andersen et al., 2022; Fenerci and Øiseth, 2018), which may exhibit large variations of the wind speed and angle of attack (AoA) with large space coherence. These features could amplify the non-linear effects of aerodynamic forces acting on bridge decks, which depend on both structure motion and wind turbulence. As reported by (Calamelli et al., 2024), low-frequency changes of the wind angle of attack could lead to aeroelastic instabilities which, even persisting for a short period, have the potential to significantly increment the deck amplitude of oscillation. Moreover, sudden increases in the wind speed or angle of attack induce variations of the quasi-steady aerodynamic forces which could substantially alter the motion of the bridge. In this context, predicting the influence of these atmospheric phenomena on the dynamic response of long-span bridges remains a challenging topic of research.

In this study, three non-synoptic wind time histories, acquired during the Hardanger Bridge monitoring campaign (Fenerci and Øiseth, 2018), have been selected and used as numerical input to simulate the dynamic response of a case study based on the Julsundet Bridge in Norway. The first time series selected is characterized by a significant increase in wind AoA and a limited variation in wind speed. On the other hand, the second one features a moderate AoA and a relevant change in wind speed. Finally, the third one combines both effects. The numerical results related to each non-synoptic case are then compared to the corresponding outcomes

obtained through a synoptic scenario, which is generated using the observed turbulence characteristics.

To account for the non-linearities of aerodynamic forces due to the low-frequency variation of wind speed and AoA a time-varying model is employed (Calamelli et al., 2024). Hereafter, the wind scenarios are introduced and a preliminary set of results is presented. In the final version of the work, the full set of results will be reported and discussed considering a three degrees-of-freedom (DoF) sectional model. Moreover, simulations will be extended considering a full-bridge numerical model.

2. CASE STUDY: JULSUNDET BRIDGE

2.1. Structural proprieties

As first, the numerical simulations of the Julsundet Bridge are performed considering a three DoF sectional approach. The bridge structural properties employed in the simulations are reported in Table 1.

Table 1. Structural properties and sign convention of the Julsundet Bridge

Quantity	Description	Value
$m_L[kg/m]$	Mass per unit length	2.23×10^4
$J_L[kgm^2/m]$	Moment of inertia per unit length	2.03×10^6
$B[m]$	Deck chord	27.5
$L[m]$	Sectional length	1
$f_y[Hz]$	Lateral frequency	0.042
$f_z[Hz]$	Vertical frequency	0.118
$f_\theta[Hz]$	Torsional frequency	0.280
$\zeta_y[-]$	Lateral damping ratio	0.0030
$\zeta_z[-]$	Vertical damping ratio	0.0015
$\zeta_\theta[-]$	Torsional damping ratio	0.0015

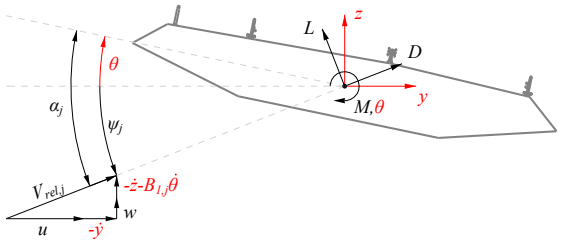

2.2. Aerodynamic proprieties

The aerodynamic properties of the Julsundet Bridge have been experimentally evaluated carrying on wind tunnel tests at Politecnico di Milano (Argentini et al., 2024). As an example, the flutter derivatives, determined through forced-motion tests, are reported in Figure 1, as a function the reduced velocity V^* around different deck static angles of rotation.

2.3. Wind Scenario

Figure 2 shows the wind speed and the AoA of the three non-synoptic time histories, acquired during the Hardanger Bridge monitoring campaign (Fenerci and Øiseth, 2018), selected as input for the numerical simulations. The selection procedure has been performed to investigate separately the non-linear effects due to the slow-varying wind speed and AoA. Specifically, the first wind event (see Figures 2($a1$) and 2($a2$)) is characterized by a variation of the AoA between -5° and 10° and a limited variation of the wind speed. The second time-series, reported in Figures 2($b1$) and 2($b2$), features a smaller AoA variation ($\pm 4^\circ$) and a localized steep variation of wind speed (e.g. around $t = 900s$). In the last time-series (Figures 2($c1$) and 2($c2$)), both features are present (sudden variation of wind speed associated to AoA up to 6°). Moreover, for each case, a synoptic time-history characterized by the average non-synoptic turbulence

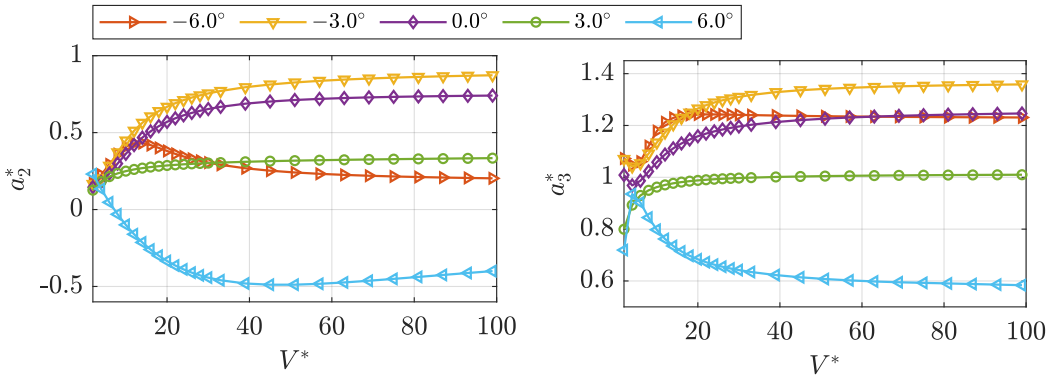

Figure 1. a_2^* and a_3^* flutter derivatives of the Julsundet Bridge, identified for different static angles of attack. According to the definition used (Zasso, 1996), a negative a_2^* represents a negative torsional aerodynamic damping

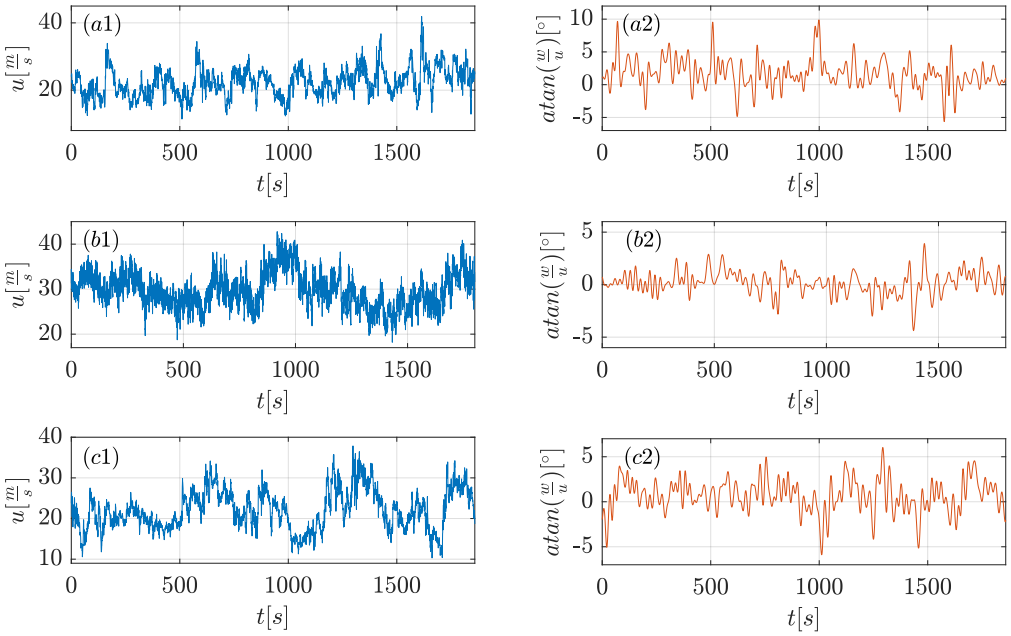

Figure 2. Selected non-synoptic time-histories, acquired during the Hardanger Bridge monitoring campaign (Fenerci and Øiseth, 2018). For each case, the longitudinal wind component (left plots) and the low-pass filtered AoA (using a cut-off frequency defined employing $V^* = 25$) (right plots) are reported

properties has been generated, for comparison purposes.

3. PRELIMINARY RESULTS

Figure 3 shows the response of the Julsundet Bridge deck section subjected to the non-synoptic and synoptic wind scenario of the case (b) (refer to Figure 2). The comparison is expressed in terms of lateral displacement, vertical displacement and torsional rotation. Under the synoptic scenario, the motion of the bridge is characterized by oscillations around constant values. On the other hand, for the non-synoptic case, the low-frequency response slowly varies over time following the trend of the wind speed. Additionally, as the non-synoptic scenario approaches its peak velocity, around $t = 900s$, the torsional response significantly increases (see Figure 3(b)).

In Table 2 the peak value and the standard deviation are reported for the lateral and vertical displacement and rotation, for both wind scenario. A more detailed analysis will be presented in the full version of the work, also considering a full-bridge numerical model.

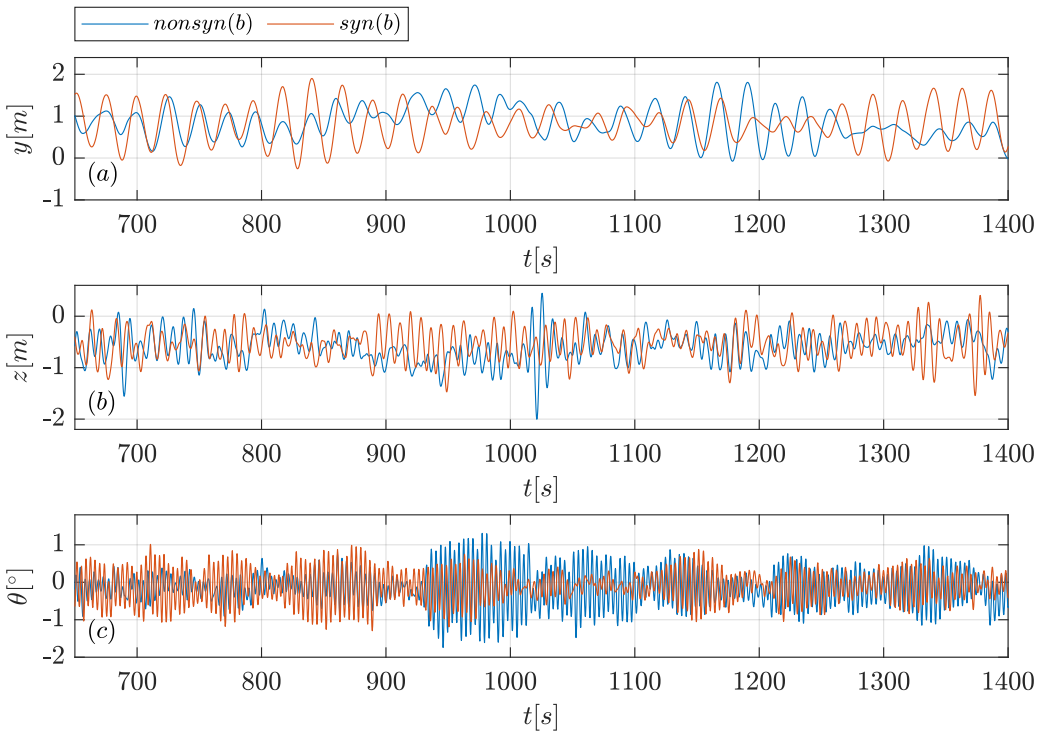

Figure 3. Comparison of the response in terms of lateral displacements, vertical displacements and torsional rotation for the non-synoptic and synoptic case (b)

Table 2. Peak values and standard deviations for the non-synoptic and synoptic scenario related to the time-interval shown in Figure 3

		$y[m]$	$z[m]$	$\theta[^\circ]$
peak value	synoptic	1.90	-1.54	-1.44
	non-synoptic	1.81	-2.00	-1.74
σ	synoptic	0.41	0.30	0.41
	non-synoptic	0.39	0.30	0.42

REFERENCES

Andersen, M. S., B. Isaksen, and S. O. Hansen (2022). Full-Scale Monitoring of the Wind Field, Surface Pressures and Structural Response of Gjemnessund Suspension Bridge. Structural Engineering International 32 (1), 43–54.

Argentini, T., F. Calamelli, A. Zasso, and J. Wang (July 2024). Flutter stability of a single-box deck: effect of geometry details and external factors on the critical wind speed. Proceedings of 9th International Colloquium on Bluff Body Aerodynamics and Applications. University of Birmingham, Birmingham.

Calamelli, F., R. Rossi, T. Argentini, D. Rocchi, and G. Diana (Apr. 2024). A nonlinear approach for the simulation of the buffeting response of long span bridges under non-synoptic storm winds. Journal of Wind Engineering and Industrial Aerodynamics 247, 105681.

Fenerci, A. and O. Øiseth (Jan. 2018). Strong wind characteristics and dynamic response of a long-span suspension bridge during a storm. Journal of Wind Engineering and Industrial Aerodynamics 172, 116–138.

Zasso, A (1996). Flutter derivatives: Advantages of a new representation convention. Journal of Wind Engineering and Industrial Aerodynamics 60, 35–47.

IN-VENTO 2024
International Conference of the Italian Association for Wind Engineering
Pisa, September 8th – 11th, 2024

Towards a general approach for the study of urban heat island

A. Pavan[a], A. Cimarelli[b], P. Costa[c], E. Stalio[d]

[a]*Università degli Studi di Modena e Reggio Emilia, Modena, Italy, anna.pavan@unimore.it*
[a]*Università degli Studi di Modena e Reggio Emilia, Modena, Italy, andrea.cimarelli@unimore.it*
[b]*TU Delft, Process & Energy Departement, Delft, The Netherlands, P.SimoesCosta@tudelft.nl*
[a]*Università degli Studi di Modena e Reggio Emilia, Modena, Italy, enrico.stalio@unimore.it*

SUMMARY:
In the last decades the urban population has increased a lot making cities objects of different studies. In this context, urban climate is an expanding research field and understanding the main features of the urban heat island is one of the challenges. The purpose of this research is to investigate the essential features of the urban heat island phenomenon in a paradigmatic city pattern described by few characteristic parameters and analyzed in a set-up close to the classical Rayleigh-Bénard convection in order to obtain general results applicable also to broader contexts.

Keywords: Urban Heat Island, Roughness, Rayleigh-Bénard convection, Direct Numerical Simulation

1. INTRODUCTION

It is well known that the urban heat island (UHI) is a phenomenon for which urbanized area experiences higher temperature then the surroundings due to multiple factors such as constructions or human activity with several consequences also on human health. As suggested by Masson et al. (2020), and confirmed by different examples in literature, a discrete number of neighborhoods has been object of study for this climate effect with growing interest in recent years, especially focusing on heat mitigation. Despite this and the fact that urban climate is becoming an expanding research field, there is a lack of knowledge due to the complex nature of the problem given by the multi-physics involved, the multiple parameters that govern it and above all, the complexity of the city's geometries that lack generality. In this respect and to keep results applicable in a broader context, the present work aims to establish an idealized framework for the study of these problems. In particular the city will be considered as composed by buildings whose shape is simply an hexahedron. Furthermore, the city pattern will be modelled by the use of a reduced number of parameters that basically describe the main geometrical features of cities. In this paradigmatic context, the urban heat island will be studied by considering only pure convection motion without external wind. Direct numerical simulations of such a flow setup will be performed by using reliable numerical methods for the resolution of the flow around the buildings.

2. TOWARDS A PARADIGM OF CITY PATTERN

Geometrically speaking, urban areas can be very complicated, but if we want to have a general and deep insight in the urban heat island phenomenon we need to simplify the complex geometry to its essential features. For this reason in our model, the city is presented like a rough surface in a circular domain of radius R, made by buildings that are all modelled as cuboids without additional details. No natural element, as vegetation is present and no distinction is

made between the various construction materials. By considering the knowledge of average quantities such as the average ground plan area A_π, the average height of buildings l_z and the average ground plan area aspect ratio l_x/l_y with l_x and l_y the horizontal dimensions of buildings, the city pattern can be characterized by a few global parameters:

$$KC = \frac{R}{\sqrt{A_\pi}} \qquad \text{coverage frequency} \tag{1}$$

$$\rho = \frac{A_{tot}}{A_{occ}} = \frac{\pi R^2}{nA_\pi} \qquad \text{coverage density} \tag{2}$$

$$AR_\pi = \frac{l_x}{l_y} = \frac{l_x^2}{A_\pi} \qquad \text{horizontal aspect ratio of buildings} \tag{3}$$

$$AR_z = \frac{l_z}{\sqrt{A_\pi}} \qquad \text{vertical aspect ratio of buildings} \tag{4}$$

where n is the total number of buildings. At the beginning each cuboids is placed in the domain by following the relations written below which allows us to assign shape, Eq. $(5)-(6)-(7)$ and orientation, Eq. (8) to each one of them:

$$l_x = \sqrt{A_\pi AR_\pi} f_{random} \qquad \text{where} \quad f_{random} \in [0.5;1.5] \tag{5}$$

$$l_y = \frac{l_x}{AR_\pi} f'_{random} \qquad \text{where} \quad f'_{random} \in [0.5;1.5] \tag{6}$$

$$l_z = \sqrt{A_\pi} AR_z f''_{random} \qquad \text{where} \quad f''_{random} \in [0.5;1.5] \tag{7}$$

$$\theta = \frac{\pi}{2} f'''_{random} \qquad \text{where} \quad f'''_{random} \in [-0.5;0.5] \tag{8}$$

On the other hand, Eq. $(9)-(11)$ are used to prevent overlapping among them:

$$x_2 = x_1 + l_{free} + l_x \qquad \text{free length} \tag{9}$$

$$l_{free} = l_{free}^{ref} f''''_{random} \qquad \text{where} \quad f''''_{random} \in [0.5;1.5] \tag{10}$$

$$l_{free}^{ref} = \frac{R}{n} - \sqrt{A_\pi} \qquad \text{free reference length} \tag{11}$$

In Eq. (9), x_1 refers to the first vertex of the previous building while x_2 refers to the firt vertex of the next one. The final pattern is then smoothed with a truncated Gaussian distribution:

$$\begin{cases} g(r) = e^{-\frac{x^2+y^2}{\alpha R^2}} & \text{for} \quad x^2+y^2 \leq R^2 \\ g(r) = 0 & \text{for} \quad x^2+y^2 > R^2 \end{cases} \tag{12}$$

$AR_{zcity} = g(r)Ar_z$ is the final height city aspect ratio in which α in Eq. (12) is an indicator of the rate of decrease of the building heights from the city center to the surrounding. As shown in figures 1 and 2, by varying the city parameters $(KC, \rho, AR_\pi, AR_z, \alpha)$, we can obtain different city patterns that resemble different real case situations.

3. NUMERICAL TECHNIQUE AND SETTING

The Direct Numerical Simulation will be performed by using the massively-parallel open-source code CaNS (Costa, 2018) where spatial discretization is based on a staggered second-order finite-difference scheme, while integration in time is performed using a third-order accurate Runge-Kutta method. In order to import the created geometry in the code it is necessary

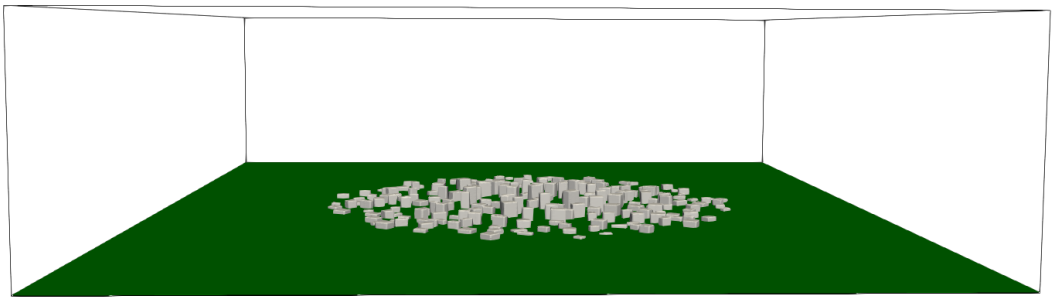

Figure 1. 3D City plan pattern obtained by setting $KC = 20$, $\rho = 0.5$, $AR_\pi = 1.5$, $AR_z = 1.5$, $R = 1$ and $A_\pi = 0.0025$, $\alpha = 1$

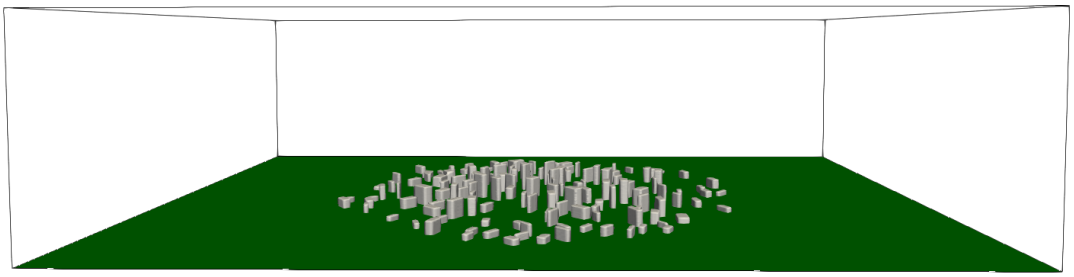

Figure 2. 3D City plan pattern obtained by setting $KC = 20$, $\rho = 0.8$, $AR_\pi = 2.5$, $AR_z = 2.5$, $R = 1$ and $A_\pi = 0.0025$, $\alpha = 2$

to calculate the Signed-Distance field, a scalar quantity defined in the solver grid representing the distance between each grid point to the surface boundary. The flow around this complex composition of structures is solved with the Immersed Boundary Method of Yang and Balaras (2006).

The flow is investigated in a modified Rayleigh-Bénard convection set-up. In fact, differently from the canonical one where a fluid layer is heated from below and cooled from above through two plates at a fixed temperature, here we will use a radial temperature distribution on the bottom plate under the corresponding city pattern. The same temperature distribution will be adopted also for the buildings. Periodic boundary conditions are applied at the lateral sidewalls, whereas no-slip boundary conditions are used on the top and bottom plate. The numerical domain has dimensions $(Lx, Ly, Lz) = (8R, 8R, 1R)$ and will be discretized using $(Nx, Ny, Nz) = (1600, 1600, 199)$ points in order to have the correct number of points to resolve the cuboids. Different simulations will be performed starting to Rayleigh number of $Ra = 10^4$ to increasing, for a given Prandtl number, $Pr = 0.7$. The results will be presented at the conference.

ACKNOWLEDGEMENTS

Project funded under the National Recovery and Resilience Plan (NRRP), Mission 04 Component 2 Investment 1.5 – NextGenerationEU, Call for tender n. 3277 dated 30/12/2021, Award Number: 0001052 dated 23/06/2022

REFERENCES

Costa, P. (2018). A FFT-based finite-difference solver for massively-parallel direct numerical simulations of turbulent flows. Computers & Mathematics with Applications 76, 1853–1862.

Masson, V., A. Lemonsu, J. Hidalgo, and J. Voogt (2020). Urban climates and climate change. Annual Review of Environment and Resources 45, 411–444.

Yang, J. and E. Balaras (2006). An embedded-boundary formulation for large-eddy simulation of turbulent flows interacting with moving boundaries. Journal of computational Physics 215, 12–40.

IN-VENTO 2024
International Conference of the Italian Association for Wind Engineering
Pisa, September 8th – 11th, 2024

Aerodynamic and dynamic behavior of an aeroelastic tree model

Alessia Piazza [1], Maria Pia Repetto[2], Girma T. Bitsuamlak [3]

[1]*University of Genova, Genova, Liguria, Italy, alessia.piazza@edu.unige.it*
[2]*University of Genova, Genova, Liguria, Italy, repetto@unige.it*
[3]*Western University, London, Ontario, Canada, gbistuam@uwo.ca*

SUMMARY
Wind loads are known to have a significant impact on trees that can cause failure by overturning or trunk rupture, leading to damage and fatalities. Therefore, it is important to understand the aerodynamic behavior of trees and consequently their vulnerability to wind induced forces. A 1:6 scale aeroelastic wind tunnel test of a camphor prototype tree was conducted at the BLWTL at Western University with objective of understanding and documenting the relationship between the aerodynamic and dynamic behavior of a tree, and both the wind field characteristics like the wind speed, turbulence intensity and tree characteristics like crown porosity. The lack of tree reconfiguration inhibiting its ability to streamline itself in the flow, suggests supporting the hypothesis that the drag force on a tree varies quadratically with the wind speed, at least in the range of wind speeds considered for this study.

Keywords: tree aerodynamics, sustainability, wind tunnel.

1. INTRODUCTION

Wind flow in urban environment can intensify due to various factors, including separated flow, wake flow, downdraft, or channeling effects, particularly in metropolitan cities with a high density of high-rise buildings. This increased wind intensity poses a greater potential for pedestrian discomfort, fatalities, and property damage in urban areas. The frequency and intensity of such phenomena are on the rise due to increased urbanization and the construction of high-rise buildings (Kang et al. 2020). Recently, there has been significant research on methods to reduce pedestrian discomfort caused by building-induced winds and the associated risks (Adamek et al. 2017; Blocken et al. 2012), and various techniques have been explored, including the use of trees in the urban environment. The use of trees as a porous obstacle to airflow, affecting wind intensity and direction is already well known. Moreover, many major cities worldwide have recently initiated tree-planting programs based on assumed environmental and social benefits of urban trees, such as reducing pollution, mitigating rainwater, and lowering building energy consumption (Novak et al. 2018). However, wind loads are known to have a significant impact on trees that can cause failure by overturning or trunk rupture (Woolsey et al. 2022), becoming a significant risk of falling on sidewalks, roads, or powerlines, and causing disruption, damage, and fatalities It is, therefore, imperative to understand the aerodynamic behavior of trees and consequently their vulnerability to wind induced forces. Therefore, efforts have been made in the wind engineering community over the last few decades to understand the aerodynamics of trees using wind tunnels.

The two methods to estimate aerodynamic force coefficients include experimental modeling in a wind tunnel (Stacey et. al 1994) using a real tree or an aeroelastic model of a tree that can sway and reconfigure in wind and replicate realistic behavior in a wind tunnel. Mayhead (1973)

conducted wind tunnel test for different variety of trees and reported that the frontal crown area varied with windspeed, such that the drag force was observed to vary linearly with windspeed ($\propto U$) instead of quadratically ($\propto U^2$). Contradictorily, (Roodbaraky et al. 1994) does not support that hypothesis, demonstrating a lack of consensus on the dependence of drag force on wind speed for trees. Therefore, to understand the relationship between frontal area, wind speed and aerodynamic forces and how they affect the response of a tree to wind, an aeroelastic model of a tree was used in this study to conduct a wind tunnel test and characterize its aerodynamic behavior and response to wind. The present study is an attempt to augment the existing knowledge about tree aerodynamics by conducting a parametric analysis with varying crown porosities, wind speeds and incoming flow properties.

2. METHODOLOGY AND TEST CASES

The aeroelastic model used for this test has been adopted from (Hao et al. 2020) and is a prototype of a Camphor tree. To achieve geometric similarity, the main dimensions of the tree were replicated and scaled, including trunk height and diameter, crown height and diameter, along with the characteristics of the branches. The leaves used for this test were different from those used in (Hao et al. 2020) in order to achieve a different porosity of the tree. To reproduce the crown, 514 leaves cluster were used to create five different configurations corresponding to different crown densities (100%, 75%, 50%, 25%,0 % of leaves) that are representative of the seasonal changes in a real tree. A 1:6 scale wind tunnel test was carried out at the BLWTL at Western University with three different upstream terrain exposures of increasing turbulence intensities, shown in the Figure 1a. The set up was composed of 4 cobra probes, a JR3 force balance, a Kinect V2 sensor and two accelerometers as shown in Figure 1b.

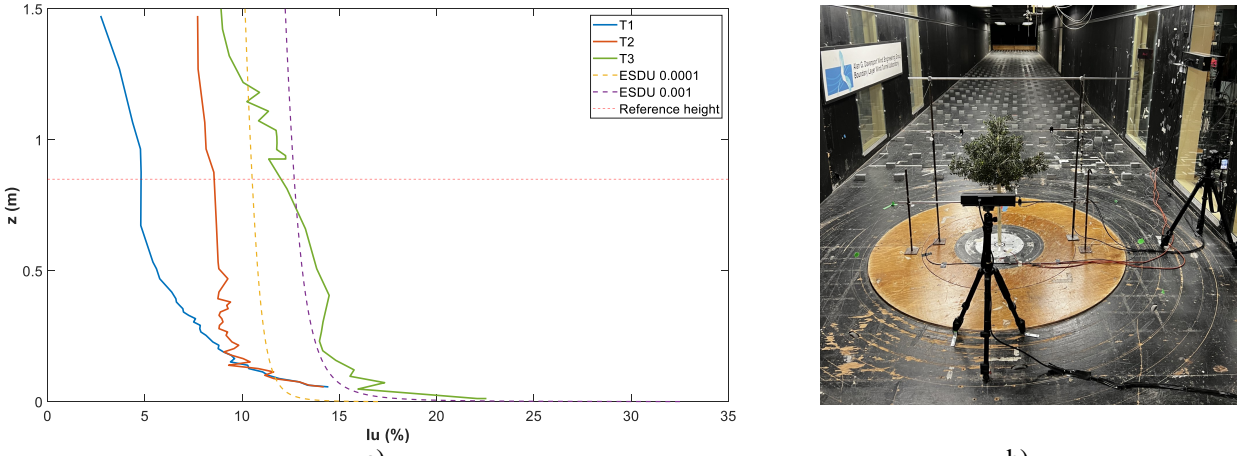

a) b)

Figure 1. a) Variation of turbulence intensity with height for different terrains. b) Wind tunnel set up.

3. RESULTS AND DISCUSSION

The reconfiguration of the crown in response to the wind is one of the most important factors for estimating the drag force and the drag coefficient on a tree. The mean area of the tree during each test was estimated using the images recorded by the Kinect V2 sensor. To estimate the area, a two-step method was adopted, where first the area in pixel dimensions was obtained and then later

converted into meter square. The frontal crown area was estimated for each wind speed up to 7.6 m/s, and it was found that the frontal area increases as the wind speed rises for configurations where the tree has leaves. This is consistent with the findings of (Enus et. al 2020) and (Rudniki et al.2004) who reported a similar increase in frontal area with increasing wind speeds up to 4 m/s. This is indicative of limited reconfiguration of the crown, as evident from the drag force which is seen to increase quadratically with wind speeds according to (Roodbaraky et al. 1994; Gillies et al. 2000)

Trees have characteristic and recognizable swaying patterns that are determined by tree size, shape, and, to a lesser extent, material properties (Dargahi et al. 2020). However, these characteristics change throughout the year due to seasonal variations causing crown shape and mass changes. During the test, two accelerometers were used to measure the motion of the tree model in the wind flow in along-wind direction. It was previously deduced that the use of a stiffer tree limited its ability to reconfigure itself in a wind flow that resulted in an increase in the drag force with increasing wind speed. Therefore, given this increase in drag force with wind speed, it is reasonable to expect an increase in the resulting displacement as well as shown in Figure 2b.

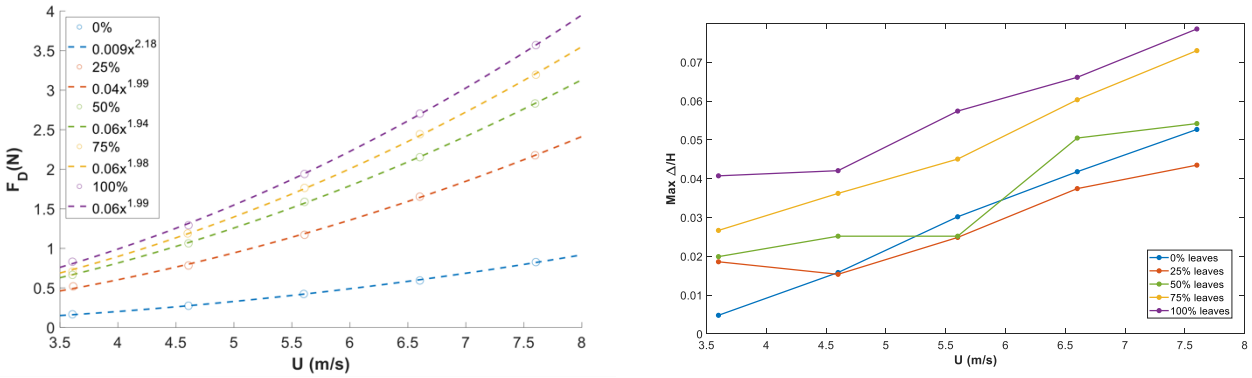

a) b)

Figure 2. a) Variation of mean drag force with wind speed for different crown porosities. b) Peak displacement for each configuration vs mean wind speed.

4. CONCLUSIONS

Based on the experiment and analysis conducted, the following conclusions can be drawn from the present study.

1- It was observed that, in the explored wind speed range, the frontal crown area increased with wind speed, in partial accordance with previous studies, where the frontal crown area was reported to first increase with wind speeds up to 4 m/s, and then decrease at higher wind speeds. This decrement in frontal crown area was not observed in the present study and may occur at higher wind speeds. The effect on frontal crown area is expected to vary among species, such that trees of different kinds and size are affected differently. The reason for an increase, instead of decrease in frontal crown area with wind speed in this study is attributed to several factors such as the stiffness of the adopted tree that limits the branches and leaves to reconfigure at higher wind speeds, the presence of codominant or multiple stems, the limited range of wind speeds considered.

2- The drag force during this experiment was observed to vary quadratically with the wind speed.

This finding is not supported by (Mayhead 1973) and (Rudniki et al. 2004) where the wind force was found to depend linearly on the wind speed, due to the ability of reconfiguring and the flexibility observed in trees. This discrepancy, described by (Gillies et al. 2000) is related to the stiffness of the trees. It is shown that for most of the studies conducted in the wind tunnel, young trees, that are more flexible compared to mature trees, were used. In (Cullen 2005), the relation analyzed extensively, and the conventional quadratic dependance was considered the most appropriate for estimating the drag force in risk management of urban trees.

3- It was observed that at lower wind speeds, the center crown displacement increased but in a disordered way. This is probably due to the use of lower wind speed in the wind tunnel that can create noisy results. However, for higher wind speeds (>5.6 m/s), the center crown displacement was seen to increase monotonically, showing that even if the stiffness of the leaves inhibits the reconfiguration of itself, the tree starts reconfiguring. This phenomenon could also be associated with the increase of the drag force.

REFERENCES

G. Kang, J. J. Kim, and W. Choi (2020). Computational fluid dynamics simulation of tree effects on pedestrian wind comfort in an urban area. Sustain Cities Soc.

K. Adamek, N. Vasan, A. Elshaer, E. English, and G. Bitsuamlak (2017).Pedestrian level wind assessment through city development: A study of the financial district in Toronto. Sustain Cities Soc, vol. 35, pp. 178–190.

B. Blocken, W. D. Janssen, and T. van Hooff. (2012). CFD simulation for pedestrian wind comfort and wind safety in urban areas: General decision framework and case study for the Eindhoven University campus. Environmental Modelling & Software, pp. 15–34.

D. J. Nowak, S. Hirabayashi, M. Doyle, M. McGovern, and J. Pasher (2018).Air pollution removal by urban forests in Canada and its effect on air quality and human health. Urban for Urban Green, pp. 40–48.

S. J. Woolsey (2022). Effects of Climate Change on the Probability of Urban Tree Failures from Wind Gusts.Master thesis , Western University, London.

G. R. Stacey, R. E. Belcher, C. J. Wood, and B. A. Gardiner (1994).Wind flows and forces in a model spruce forest. Boundary Layer Meteorol, pp. 311–334.

G. J. Mayhead (1973). Some drag coefficients for British forest trees derived from wind tunnel studies. Agricultural meteorology, vol. 12, pp. 123–130.

H.J. Roodbaraky, C.J. Baker, A.R. Dawson, C.J. Wright (1994).Experimental observations of the aerodynamic characteristics of urban trees.Journal of Wind Engineering and Industrial Aerodynamics,Volume 52.

Y. Hao, G. A. Kopp, C. H. Wu, and S. Gillmeier (2020).A wind tunnel study of the aerodynamic characteristics of a scaled, aeroelastic, model tree. Journal of Wind Engineering and Industrial Aerodynamics, vol. 197.

M. Enuş, E. Dellwik, J. Mann, H. Hangan, and A. Costache (2020).Three-dimensional measurements of tree crown movement using an infrared time-of-flight camera. Exp Fluids, vol. 61, pp. 1–13.

Rudnicki M, Mitchell SJ, Novak MD (2004).Wind tunnel measurements of crown streamlining and drag relationships for three conifer species. Can J For Res 34(3):666–676

Gillies JA, Lancaster N, Nickling WG, Crawley DM (2000).Field determination of drag forces and shear stress partitioning efects for a desert shrub (Sarcobatus vermiculatus, Greasewood). J Geophys Res Atmos 105(D20):24871–24880.

M. Dargahi, T. Newson, and J. R. Moore (2020). Numerical Approach to Estimate Natural Frequency of Trees with Variable Properties. Forests, vol. 11, no. 9.

Cullen S. (2005). Trees and wind: a practical consideration of the drag equation velocity exponent for urban tree risk management. Journal of Arboriculture 31(3).

IN-VENTO 2024
International Conference of the Italian Association for Wind Engineering
Pisa, September 8th – 11th, 2024

Calibration of Wind Action Partial Factor for the Italian Climate

Vincenzo Picozzi[1], John D. Sørensen[2], Alberto M. Avossa[1], Francesco Ricciardelli[1]

[1] *University of Campania "Luigi Vanvitelli", Aversa, Italy, vincenzo.picozzi@unicampania.it*
[2] *Aalborg University, Aalborg, Denmark*

SUMMARY
In the last years, the debate on partial factors calibration for climatic actions has gained strength, and showed conflicting results concerning the need for their updating. In the case of wind actions, it is stated that such results are based on statistical models not matching the physical model currently adopted by the codes. On the other hand, a calibration at the national level seems appropriate, and this appears particularly important for Italy due to several uncertainty sources often neglected in structural reliability problems. In this framework, this paper investigates the actual reliability level of structures located in Italy and subjected to wind actions, and attempts to recalibrate load factor for knowledge of the Italian extreme wind climate.

Keywords: Wind Action, Structural Reliability, Partial Factor, Extreme Wind Map, Uncertainty.

1. INTRODUCTION

Within the semi-probabilistic approach to structural safety, the use of partial factors has become mandatory in Italy with the entering into force of the 2008 building code (MIT, 2008). The code, and its 2018 update (MIT, 2018) comply with the Eurocode recommendations regarding the load partial factors, therefore adopting a single value of 1.5 for all variable actions (CEN, 2002).

In the last years, the activities carried out for the drafting of second-generation Eurocodes highlighted some critical issues in structural reliability aspects. This led to a discussion about the actual reliability level of available codes and about the calibration of partial factors, which is currently still ongoing. Dealing with the calibration of the Eurocodes, Köhler et al. (2019) stated the need for a revision of the load partial factors currently in use, showing that they "*seem too high for permanent loads*" and "*too low for variable loads*". On the other hand, focusing on climatic actions, Formichi et al. (2023) showed that the bias in current hazard maps meets the Eurocode reliability requirements and, thus, disregarding it would require an "*unjustified increase*" of partial factors. Results are therefore conflicting, and further investigation is required to reach a more widely agreed-upon opinion. Limited to the wind (climatic) action, Picozzi (2023) and Kasperski and Geurts (2005) stated the need for un update of knowledge about uncertainty modelling. Indeed, to reach reliable results, strong statistical models are required in structural reliability assessment. However, current probabilistic model for wind actions could not match the physical (action) model adopted by EN 1991-1-4 (CEN, 2005).

To contribute to the discussion on partial factors calibration for climatic actions, the main purpose of this research is the assessment of the actual reliability level of structures to wind action,

considering the Italian extreme wind climate. Indeed, calibration of codes at the national level should follow the publication of second-generation Eurocodes, including: (1) a wind hazard map providing the characteristic value of wind speed associated with a return period $T = 50$ yrs; (2) an equation accounting for return periods other than *50* yrs; and (3) a set of load factors for the evaluation of the design value of the wind action. Considering the wind hazard map currently adopted in the Italian National Annex to EN 1991-1-4, partial factors are calibrated focusing on the effects of the uncertainty associated with the existing wind map, and on the variability of the reliability level due to the variation of the extreme wind climate across the country.

2. METHODOLOGY

The assessment of structural reliability is performed by estimating the reliability index β or, equivalently, the probability of failure p_f. This requires the definition of a Limit State Function and of the associated Design Equation accounting for both resistance and effects of actions on the structure or its members. According to the EN 1990 (CEN, 2002), for wind action effects the Limit State Function is made explicit by:

$$g(\mathbf{X}, z) = zX_R R - X_E\{(1 - a_Q)G + a_Q\theta_Q Q_0\} \quad (1)$$

where:

- z is the design parameter
- R is the material strength
- G is the dead loads effect
- $\theta_Q Q_0$ is the wind action effect given by the product between a time-invariant component θ_0 and a time-variant component Q_0
- X_R is the model uncertainty for resistance
- X_E is the model uncertainty for load effects
- a_Q is a factor governing the balance between dead loads and wind action effect

The combination $G = a_G G_S + (1 - a_G)G_p$ between self-weight G_s and carried permanent load G_p is commonly used to express the dead load, where a_G is the relative weight between them. The design parameter z is derived by solving the Design Equation:

$$zR_d - \{(1 - a_Q)[a_G G_{sd} + (1 - a_G)G_{pd}] + a_Q Q_d\} = 0 \quad (2)$$

where the subscript d denotes the design value of the corresponding quantity, which is derived by multiplying the characteristic values G_{sk} and G_{pk} of self-weight and permanent loads with the partial factor γ_G, by multiplying the characteristic value Q_k of the wind action effect with the partial factor γ_Q, and by dividing the characteristic value R_k of the resistance by the partial factor γ_M.

Eqs. (1) and (2) can be used for two purposes. First, using the set of partial factors adopted by

current codes allow to estimate the design parameter z from Eq. (2) and the actual reliability index β from Eq. (1). Indeed, since the variables $\mathbf{X}$ are random variables, then $g(\mathbf{X}, z)$ results to be a multivariate random variable. Its integration extended to the boundary $g(\mathbf{X}, z) = 0$ provides the probability of the structure to fail in the assumed Limit State and, therefore, the reliability index β. On the other hand, one can vary the partial factors until finding the optimum values leading to the target reliability index β_t. In attempting to calibrate the partial factor γ_Q for wind actions, the following minimization problem must be solved:

$$\gamma_Q = \arg\min \sum_{i=1}^{L} w_i \left[\beta_i(\gamma_Q) - \beta_t\right]^2 \tag{3}$$

where L is the number of analysed design situations, each of which leading to the design parameter z_i, and where w_i indicates the relative frequency of importance of the i-th design situation, with $\sum w_i = 1$.

The use of Eq. (1) thus requires the definition of a portfolio of typical design situations. This should include different structural materials and a range of weighting factors a_G and a_Q. For the purposes of the current study, concrete and steel structures are analysed in 40 different Italian locations. The portfolio of design situations is therefore defined by considering a_G ranging from 0.6 to 1.0, while a_G is considered ranging between 0.1 to 0.7 in the case of concrete structures and between 0.3 to 0.8 in the case of steel structures. A step of 0.1 is adopted, thus leading to 1400 design situations for concrete structures and 1200 design situations for steel structures.

The uncertainty for the variables in Eq. (1) is modelled according to the Probabilistic Model Code (JCSS, 2001) and the relevant scientific literature (Köhler et al., 2019; Teichgräber et al., 2022; Formichi et al., 2023). In the case of wind action, uncertainty arises from each of the link of the well-known A. Davenport Wind Loading Chain, i.e. velocity pressure, exposure coefficient, pressure coefficient, and dynamic coefficient when applicable. In this study, uncertainty in the last three links are modelled according to the relevant scientific literature, while uncertainty in the velocity pressure is calibrated for the Italian wind climate. This includes for each of the 40 locations:

1. natural variability of yearly maximum velocity pressure, i.e. extreme wind climate;
2. uncertainty in assessing the velocity pressure when adopting current Italian wind map with respect to the actual value of the 50-yrs return wind speed;
3. additional bias due to downsampling (Picozzi et al., 2022; Akbaba et al., 2024).

3. RESULTS

Two main results are observed. First, when adopting the current value of partial actor for variable actions, then the reliability level of steel structures is lower than the target value, while it is larger in the case of reinforced concrete structures. Accordingly, the calibration of partial factors showed the need for increasing the wind load factor for steel structures up to as much as $\gamma_Q = 3.1$, while the current value $\gamma_Q = 1.5$ is acceptable for reinforced concrete structures. On the other hand, the high variability of the reliability index for the analysed design situations highlighted the need of

redrafting the Italian wind map. This must be done with the aim of reducing the scatter of the error in the evaluation of the characteristic wind speed or velocity pressure.

REFERENCES

Akbaba, A., V. Picozzi, A.M. Avossa, and F. Ricciardelli (2024). Effects of Downsampling on the Prediction of the Italian Extreme Winds. In: Proceedings of the XVII Conference of the Italian Association for Wind Engineering IN-VENTO 2022, 41-51.

CEN (2002). EN 1990. Eurocode: Basis of structural design. European Committee for Standardization.

CEN (2005). EN 1991-1-4. Eurocode 1: Actions on Structures – Part 1-4: General actions – Wind Action. European Committee for Standardization.

Formichi, P., F. Landi, and P. Croce (2023). A consistent approach to the calibration of partial factors for permanent and variable loads in the 2nd generation of the Eurocodes. Structure and Infrastructure Engineering.

JCSS (2001). Probabilistic Model Code: Part II – Load Models. Joint Committee on Structural Safety.

Kasperski, M. and C. Geurts (2005). Reliability and code level. Wind and Structures 8, 295-307.

Köhler, J., J.D. Sørensen, and M. Baravalle (2019). Calibration of existing semi-probabilistic design codes. In: Proceedings of the 13th International Conference on Applications of Statistics and Probability in Civil Engineering, ICASP 13.

MIT (2008). D.M. 14/01/2008 Norme Tecniche per le Costruzioni, NTC 2008 (in Italian). Ministero delle Infrastrutture e dei Trasporti.

MIT (2008). D.M. 17/01/2018 Aggiornamento delle "Norme Tecniche per le Costruzioni", NTC 2018 (in Italian). Ministero delle Infrastrutture e dei Trasporti.

Picozzi (2023). Uncertainties in Wind Action: Modelling and Code Calibration. PhD Thesis. University of Campania "L. Vanvitelli"

Picozzi. V., A. Akbaba, A.M. Avossa, and F. Ricciardelli (2022). Correction of historical records to improve the reliability of design wind speeds. Engineering Structures 265(3), 114473.

Picozzi, V., F. Landi, A.M. Avossa, P. Croce, P. Formichi, and F. Ricciardelli (2024). The Climatic Action Uncertainty Chain. Engineering Structures 301, 117357.

Teichgräber, M., J. Köhler, and D. Straub (2022). Hidden safety in structural design codes. Engineering Structures 257, 114017.

IN-VENTO 2024
International Conference of the Italian Association for Wind Engineering
Pisa, September 8th – 11th, 2024

Integrated optimal design of TMDI and structure for slender elements under wind

Matteo Polucci [1], Mattia Francioli [2], Maurizio De Angelis [3], Francesco Petrini [4]

[1] *Sapienza University of Rome, Rome, Italy, polucci.1785223@studenti.uniroma1.it*
[2] *Sapienza University of Rome, Rome, Italy, mattia.francioli@uniroma1.it*
[3] *Sapienza University of Rome, Rome, Italy, maurizio.deangelis@studenti.uniroma1.it*
[4] *Sapienza University of Rome, Rome, Italy, francesco.petrini@uniroma1.it*

SUMMARY
In this paper, the classical tuned mass damper (TMD) is coupled with an inerter, a two-terminal mechanical device designed to provide a reaction force proportional to the relative acceleration between its two terminals. This paper aims to demonstrate how the optimal design of the TMDI can mitigate the wind-induced effects and that, moreover, the TMDI-equipped structure can achieve the same level of performance as a classic TMD despite having less mass attached, thereby reducing structural stress. These devices could be also very useful for improving the performance of existing buildings, already equipped with classical TMDs, without needing to change the attached mass.

Keywords: Tuned mass-damper-inerter, Optimal design

1. INTRODUCTION

The inerter is already utilized in various engineering fields, especially in mechanical engineering. For instance, it is employed in the suspension system of the Formula 1 cars to mitigate their vibration. A simplified model of the inerter is illustrated in Fig. 1a. The reaction force provided by the inerter is proportional to the relative acceleration, denoted by the constant coefficient *b* known as inertance as defined in Eq. (1), where $\ddot{u}_i$ and $\ddot{u}_j$ represent the accelerations of the inerter terminals (the double point represents the second derivative with respect to time); the unit of inertance is mass.

$$F = b\left(\ddot{x}_i - \ddot{x}_j\right) \tag{1}$$

To comprehend the effect of the inerter on the structural behavior when coupled with a TMD, an n-degrees of freedom system with lumped mass can be considered (as shown in Fig. 1b). The mass $\boldsymbol{M}$, the damping $\boldsymbol{C}$ and the stiffness $\boldsymbol{K}$ matrices of this system are given in Eq. (2), where $k_{i,j}$ and $c_{i,j}$ are the (i,j) elements of the structure stiffness and damping matrices, respectively.

$$\begin{aligned}
\boldsymbol{M} &= \boldsymbol{M}_s^{n+1} + (m_{TMDI} + b)\mathbf{1}_{n+1}\mathbf{1}_{n+1}^t + b\mathbf{1}_p\mathbf{1}_p^t - b\left(\mathbf{1}_{n+1}\mathbf{1}_p^t + \mathbf{1}_p\mathbf{1}_{n+1}^t\right) \\
\boldsymbol{C} &= \mathbf{C}_s^{n+1} + c_{TMDI}(\mathbf{1}_{n+1}\mathbf{1}_{n+1}^t + \mathbf{1}_p\mathbf{1}_p^t - \mathbf{1}_{n+1}\mathbf{1}_p^t - \mathbf{1}_\mathrm{p}\mathbf{1}_{\mathrm{n+1}}^\mathrm{t}) \\
\boldsymbol{K} &= \boldsymbol{K}_s^{n+1} + k_{TMDI}(\mathbf{1}_{n+1}\mathbf{1}_{n+1}^t + \mathbf{1}_p\mathbf{1}_p^t - \mathbf{1}_{n+1}\mathbf{1}_p^t - \mathbf{1}_\mathrm{p}\mathbf{1}_{\mathrm{n+1}}^\mathrm{t})
\end{aligned} \tag{2}$$

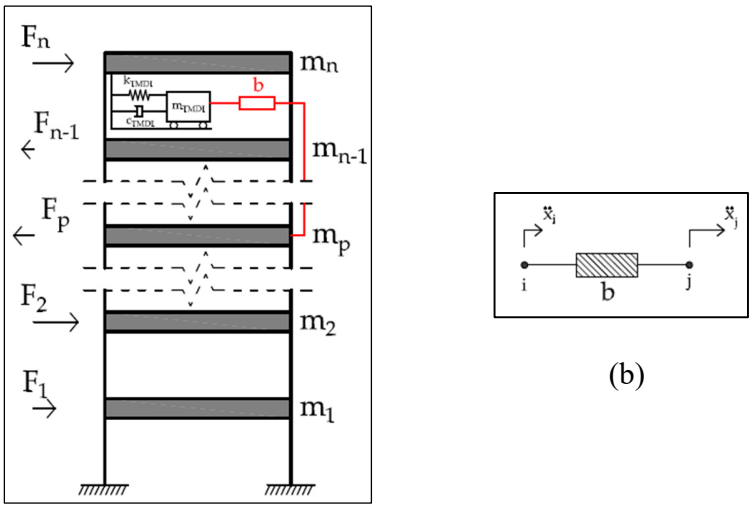

Figure 1: (a) Rheological model of an inerter; (b) Lumped-mass model of a n-DoFs system

$\boldsymbol{M}_s \in \mathbb{R}^{(n+1)x(n+1)}$, $\boldsymbol{C}_s \in \mathbb{R}^{(n+1)x(n+1)}$ and $\boldsymbol{K}_s \in \mathbb{R}^{(n+1)x(n+1)}$, are the mass, damping and stiffness matrices of the primary structure augmented by a zero row (bottom) and zero column (rightmost); m_{TMDI}, c_{TMDI} and k_{TMDI} are the mass, damping and stiffness of the TMD, respectively; additionally, p subscript denotes the floor where the second terminal of the inerter is attached (the first being the floor of the TMD) and the $\mathbf{1}_k$ signifies a zero vector with only a one in the k^{th} row. In this scenario the TMD is assumed to be at the last floor of the model, but the expressions for the matrices remain the same, with only the position of the TMD elements changing. When the inertance is zero the mass matrix of a structure with a classical TMD is retrieved; however, the stiffness and damping matrices remain the same for both cases (classical TMD and TMDI). The mass matrix for a TMDI-equipped structure is non-diagonal due the b terms and the further they are from the diagonal, the greater is the effect on the higher modes; this is an improvement over the classical TMD because it operates only at a single frequency.

2. NUMERICAL MODEL

A lumped-mass system comprising 40 degrees of freedom is selected as the study model, representing a building with a total height (h_{tot}) of 160 meters. This considers a floor-to-floor height (h_{int}) of 4 meters (typical for tall buildings), corresponding to 40 floors with respective floor masses of 1250 tons per floor. The initially chosen cross-section is a square with sides measuring 7 meters, and S355 mass-less steel is used as the material. The model is constructed using the ANSYS MAPDL software. The behavior of this structure will be analyzed under the influence of lateral forces, approximating wind effects in a simplified manner, through a frequency domain analysis with harmonic excitation. For this analysis, an upper triangular distribution (Eq. (3)) is employed to ensure that at each i^{th} floor (and thus degree of freedom), a force of value:

$$F_i = \frac{h_i}{h_{tot}} \cdot 1000kN \tag{3}$$

so as to obtain a force on the node at the top equal to $1000kN$.

3. OPTIMAL DESIGN OF TMDI

In the first step, only two variables are optimized: the stiffness (k_{TMDI}) and the damping (c_{TMDI}) of the TMDI, leaving the other parameters constant. These fixed parameters are detailed in Table 3 where H_{top} *and* H_{bot} represent the height of the TMDI terminals i and j.

Table 1: Parameters fixed for the first optimization

H_{top} $[m]$	H_{bot} $[m]$	m_{TMDI} $[t]$	b_{TMDI} $[t]$
160	148	5000	2500

During the optimization phase, there are numerous possibilities for the selection of the objective function, i.e., the function to be minimized. Therefore, it is decided to proceed with the search for the minimum of two quantities separately:

- The maximum absolute value of the displacement response function.
- The area under the displacement response function.

The optimization it's carried out using the *SURROGATEOPT* function implemented in MatLab; to validate this algorithm the results obtained previously are compared with two response surfaces, Fig. 2, one for each objective function.

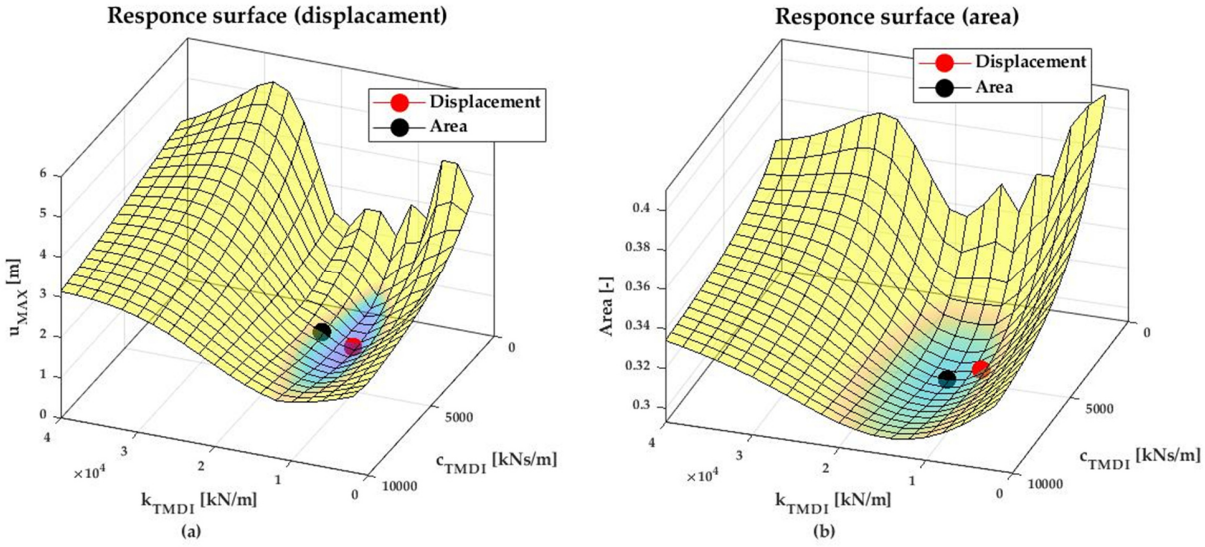

Figure 2: The two response surfaces obtained minimizing the peak displacement (a) and the area under the frequency response function (b)

Table 2: Optimal value for the design variables for the two different optimizations

Displacement opt.		Area opt.	
k_{TMDI} [kN/m]	c_{TMDI} [kNs/m]	k_{TMDI} [kN/m]	c_{TMDI} [kNs/m]
11063	3872	14236	5005

By inserting the optimal values into the response surface plots, it is observed that they indeed correspond to the respective minimum zones of the functions, thus validating the algorithm used. In the final phase of optimization, a global optimization is conducted by setting all parameters involved as design variables, except the mass of the TMDI. The objective is to achieve a final

displacement below a certain threshold ($\bar{u}_0 = 0.85$) by minimizing the cross-sectional area, which can be interpreted as steel savings. In Table 3 h and d are respectively height and base of the rectangular cross-section.

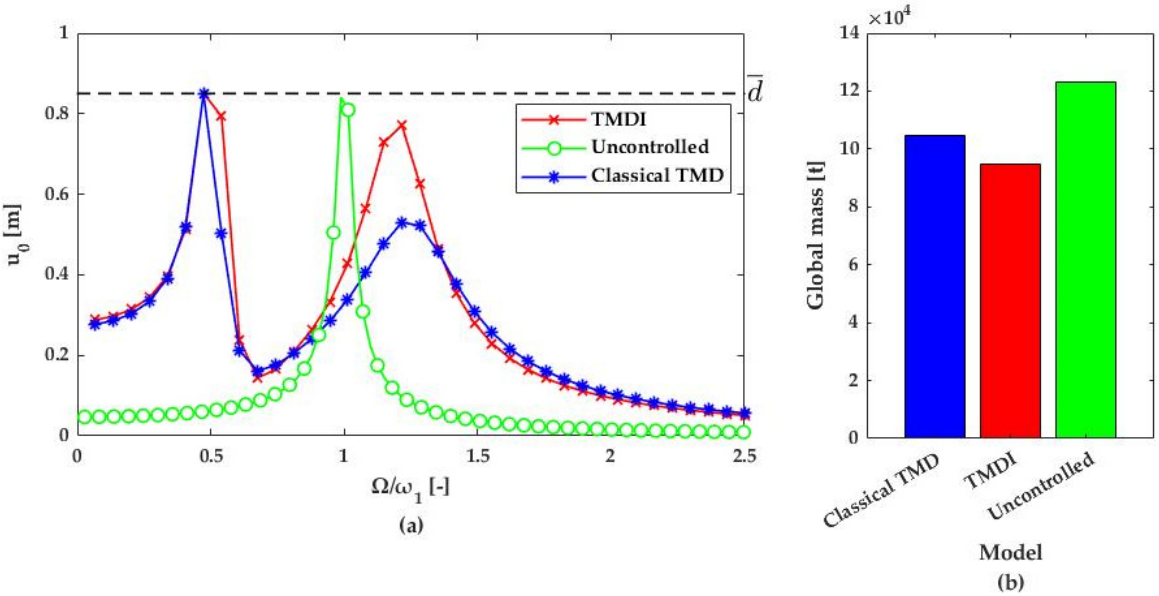

Figure 3: Magnitude of the displacement frequency response function plotted against the frequency ratio for the three different models (a) and the global mass for the same models (b)

Table 3: Optimal design variables for the global optimization

k_{TMDI} [kN/m]	c_{TMDI} [kNs/m]	H_{top} [m]	H_{bot} [m]	b_{TMDI} [t]	h [m]	d [m]
57108	9435	156	96	32061	10	3.15

Figure 3a illustrates the frequency response functions obtained for three distinct models (uncontrolled, classical TMD, and TMDI), all designed to limit displacement. The uncontrolled model involves altering the cross-sectional dimensions, while the classical TMD model employs the TMD parameters as design variables. The results depicted in Figure 3b clearly demonstrate that, for equivalent performance, the TMDI model allows for significant steel savings. This reduction can be attributed, in the former case, to the smaller cross-sectional area, and in the latter, to the reduced mass attached to the TMDI.

REFERENCES

Agathoklis Giaralis, Francesco Petrini, Optimum design of the tuned mass-damper-inerter for serviceability limit state performance in wind-excited tall buildings, Procedia Engineering, volume 199, 2017, Pages 1773-1778, ISSN 1877-7058, https://doi.org/10.1016/j.proeng.2017.09.453.

Giaralis, Agathoklis & Petrini, Francesco. (2017). Wind-Induced Vibration Mitigation in Tall Buildings Using the Tuned Mass-Damper-Inerter. Journal of Structural Engineering (United States). 143. 10.1061/(ASCE)ST.1943-541X.0001863.

IN-VENTO 2024
International Conference of the Italian Association for Wind Engineering
Pisa, September 8th – 11th, 2024

The Italian wind map - part I: a critical analysis of measurements at land anemometric stations

Lorenzo Raffaele[a], Luca Bruno[a], Elisabetta Colucci[a]

[a]*Department of Architecture and Design, Politecnico di Torino, Torino, Italy, lorenzo.raffaele@polito.it, luca.bruno@polito.it, elisabetta.colucci@polito.it*

SUMMARY:
Ongoing climatic changes, modified terrain surface covering and related aerodynamic roughness, different types of structures and infrastructures, evolution of safety format require updated, complete, consistent and detailed maps of the wind hazard, quantified by multiple values of the design wind speed and related probabilities of occurrence. Design wind speeds are traditionally mapped on the basis of time series of records measured at land anemometric stations. This study is intended to critically discuss the reliability of the measured data. 21 stations over the Italian Country land are considered. In order to quantitatively measure the compliance of each station with the standard setup, an overall compliance index is proposed, covering measurement time series duration, completeness and stationarity, site exposure variation in time and over the surroundings of the station.

Keywords: wind map, anemometric station, standard, compliance, Italian Country

1. INTRODUCTION

The determination of the design wind velocities is the first and key constituent ring of the "Alan G. Davenport Wind Loading Chain" (Davenport, 1961) that still grounds contemporary Wind Engineering (Isyumov, 2012; Picozzi et al., 2024). The description of the natural wind is still today mainly grounded on suitable statics of historical time series of speed data measured at land anemometric stations. The well-known WMO-specifications on station setup for synoptic purposes ideally refers to properly maintained, accurate, 10-m high anemometers above a level, open, unobstructed terrain with constant and uniform roughness at microscale, e.g. in the 2km radius fetch upwind the station (WMO-No.8/2021, 2021). However, actual measurements are affected by some weaknesses early pointed out by Davenport itself (Davenport, 1960) and later faced by scholars in a panoply of studies. Among others, let us recall: the duration of the time series usually shorter than the target return period of the design wind speed of interest (Solari and Pagnini, 2009) and uneven among the stations (Ballio et al., 1999); the roughness strongly varying over the station surroundings and/or in time due to growth of trees, seasonal changes of their leaf density (Dolman, 1986), and/or to rapid urbanization growth (Mo et al., 2015); the construction of new buildings locally obstructing the flow (Ballio et al., 1991); the anemometer actual location and eventual relocation (Ballio et al., 1991; Liu et al., 2023); the anemometer onset speed threshold value artificially affecting wind calms (Chiodi and Ricciardelli, 2014), their measurement resolution, their deterioration during the service life, e.g. because of dust-induced friction increase (WMO-No.8/2021, 2021), their data acquisition chain whose malfunctioning is responsible for missing data (Picozzi et al., 2022). Data from actual non-ideal stations can be transformed into WMO-compatible form, provided that minimum requirements for the station anemometer position and its surroundings are fulfilled (Wieringa, 1996), thanks to semi-empirical, approximated corrections, such as the classical Monin–Obukhov similarity theory (Foken, 2006), the well-known roughness-dependent geo-

graphical interpolation (Wieringa, 1986) or the temporally varying exposure adjustment proposed by e.g. Mo et al., 2015Huang et al., 2018.
The assessment of the compliance of the station actual setup with the ideal one, and hence the 'climatological representativeness' at the meso- and macroscale of the measurements recorded therein (Wieringa, 1996) are of paramount importance: in absolute sense, if land anemometric data directly ground the design wind speed mapping; in relative sense, if they are adopted as term of reference to validate the results issued by alternative approaches, e.g. computational simulations and/or reanalysis (e.g. Molina et al., 2021; Raffaele et al., 2024).

2. APPROACH TO COMPLIANCE ASSESSMENT

In order to quantitatively and synthetically measure the compliance of each station against measurements time series duration, completeness, and standard exposure (WMO-No.8/2021, 2021), we define the compliance index $C \in [0,1]$ in its very general form as follows:

$$C = 1 - \frac{\sum_{j=1}^{n} \mu_j I_j}{n}, \tag{1}$$

where $I_j \in [0,1]$ are n partial, maximum-normalised inconsistency indices related to the time series duration (I_T), completeness (I_V) and stationarity (I_s), the site topography (I_t) and roughness (I_r), the anemometer height (I_h), and $\mu_j \in [0,1]$ are the corresponding weights. In particular, each inconsistency index I_j is expressed as:

- $I_1 = I_T = 1 - \frac{T}{\widehat{T}}$, where T is the duration of the time series, and $\widehat{\cdot}$ stands for the maximum value of the generic variable over the ensemble of the considered anemometric stations;
- $I_2 = I_V = \frac{\#V_m + \#V_i}{\widehat{\#V_{m,i}}}$, where # is the cardinality of an ensemble, V_m and V_i are the missing and invalid wind speed data after quality control (Rojas-Labanda et al., 2023). At present, severe threshold values are set, e.g. $(\#V_m + \#V_i)/(T/\Delta t) < 10\%$ in Molina et al., 2021, being Δt the sampling time step;
- $I_3 = I_s = \frac{|a|}{|\hat{a}|}$, where a is the angular coefficient of the linear regression of the time series;
- $I_4 = I_t = \frac{\widetilde{z}}{\widehat{\widetilde{z}}}$, where $\widetilde{\cdot}$ stands for standard deviation over the 2km radius fetch upwind the station, and z is the actual elevation above the sea level. In this study, z is obtained by Digital Terrain Models (Tarquini et al., 2007);
- $I_5 = I_r = \frac{\widetilde{z_0}}{\widehat{\widetilde{z_0}}}$, where z_0 is the aerodynamic roughness. In this study, z_0 is obtained by matching the actual land cover categories in the CORINE Land Cover 2018 (Büttner et al., 2004) to the corresponding z_0 values according to EN 1991-1-4:2005, 2005;
- $I_6 = I_h = \frac{|\Delta h|}{\widehat{|\Delta h|}}$, where $\Delta h = h - h_{ref}$ is the difference between the actual height h of an anemometer and the reference height $h_{ref} = 10$ m. In this study, h values are set equal to those detailed in Ballio et al., 1999.

In this study, all weights are set $\mu_j = 1$, i.e. all inconsistencies are considered equally important. It should be noted that compliance can be assessed by referring to both the evaluation of yearly wind speed extremes $\widehat{V}_y$ and averages $\overline{V}_y$, because their time series may have different degree

of stationarity. A conventional compliance index threshold value can be set (e.g. $C = 0.8$) to identify WMO-'representative' stations that agree with minimum requirements (Wieringa, 1996).

3. PRELIMINARY RESULTS

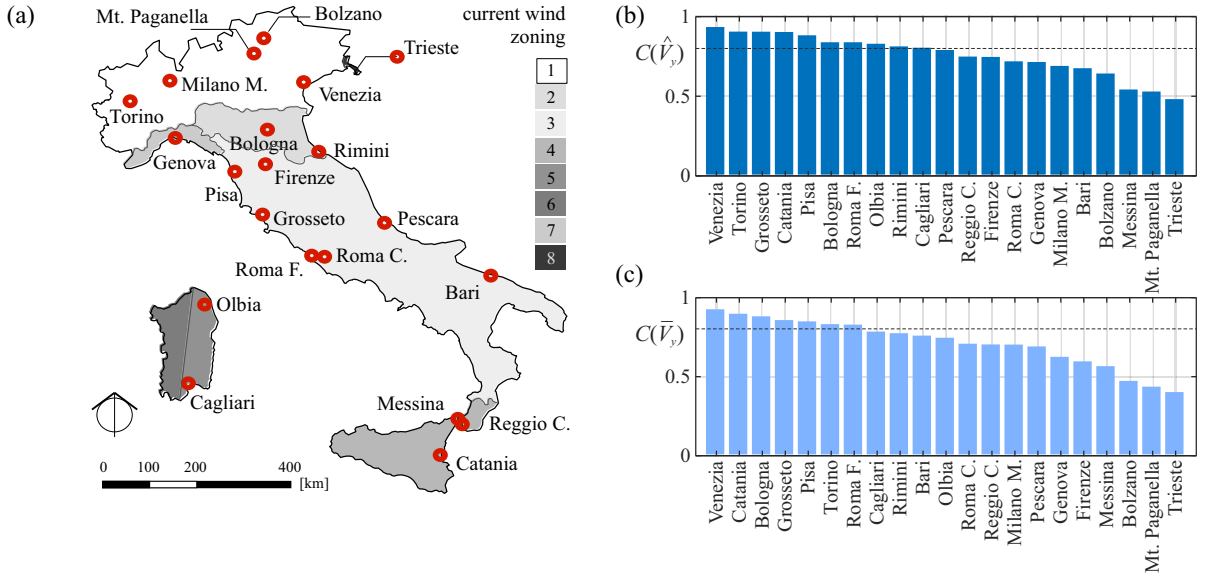

Figure 1. Location of the 21 selected stations with reference to the current wind zoning (CNR-DT 207 R1/2018, 2018; DM 17-01-2018, 2018) (a); compliance indices for yearly maxima (b) and yearly averages (c)

The stations wind speed measurements are provided by the Met Office Hadley Centre's Integrated Surface Database (HadISD, Dunn, 2019), a global subdaily dataset based on the ISD dataset from NOAA's NCDC. A fully automated quality-control procedure of the data is already carried out by applying 15 different tests (Dunn et al., 2016), in order to remove the poorest station records. Stations have been selected on the basis of two main distinct criteria: (i) they are homogeneously spread over the Italian land in order to catch as much wind zones as possible, in accordance to DM 17-01-2018, 2018 (see Fig. 1a); (ii) they share the common available time series duration $T = 42$ years [1981 2022] and same sampling time step $\Delta t = 1$ hour. By setting a compliance index threshold at $C = 0.8$, 10 stations result compliant for the evaluation of extremes, while 7 stations result compliant as regards averages. Among them, Trieste, Mt. Pagnanella, Bolzano and Messina score the lowest C mainly because of the large Δh (e.g. Trieste), the uneven elevation (e.g. Mt. Paganella, Bolzano), the amount of missing data, and the uneven roughness (e.g. Messina), the not-stationary of the time series due to station setup changes (e.g. Milano Malpensa, Firenze) while Venezia results the most WMO-'representative' station.

ACKNOWLEDGEMENTS

This study was carried out within the RETURN Extended Partnership and received funding from the European Union Next-GenerationEU (National Recovery and Resilience Plan – NRRP, Mission 4, Component 2, Investment 1.3 – D.D. 1243 2/8/2022, PE0000005) – SPOKE TS 2. This study was jointly developed in the framework of the research project PROtection Technologies from Eolian Events for Coastal Territories (PROTEECT, http://www.proteect.polito.it/) within the Ministerial Decree no. 1062/2021 and received funding from the FSE REACT-EU - PON Ricerca e Innovazione 2014-2020. This manuscript reflects only the authors' views and

opinions, neither the European Union nor the European Commission can be considered responsible for them.

REFERENCES

Ballio, G., S. Lagomarsino, G. Piccardo, and G. Solari (1991). A first step towards the map of Italian extreme winds. Part 1 : General principles and analysis methodology. Costruzioni Metalliche 3, 147–172.

— (1999). Probabilistic analysis of Italian extreme winds: Reference velocity and return criterion. Wind and Structures 2, 51–68.

Büttner, G., J. Feranec, G. Jaffrain, L. Mari, G. Maucha, and T. Soukup (2004). The CORINE Land Cover 2000 Project. EARSeL eProceedings 3, 331–346.

Chiodi, R. and F. Ricciardelli (2014). Three issues concerning the statistics of mean and extreme wind speeds. Journal of Wind Engineering and Industrial Aerodynamics 125, 156–167.

CNR-DT 207 R1/2018 (2018). *Guide for the assessment of wind actions and effects on structures*. Standard. National Research Council (CNR), Rome, Italy.

Davenport, A. (1960). Rationale for determining design wind velocities. J. Struct. Div. Proc. ASCE 86, 39–68.

— (1961). A Statistical Approach to the Treatment of Wind Loading on Tall Masts and Suspension Bridges. phdthesis, Department of Civil Engineering, University of Bristol, United Kingdom.

DM 17-01-2018 (2018). *Technical Standards for Construction - update DM January 17, 2018*. Standard. Ministry of Infrastructures and Transport, Rome, Italy.

Dolman, A. (1986). Estimates of roughness length and zero plane displacement for a foliated and non-foliated oak canopy. Agricultural and Forest Meteorology 36, 241–248.

Dunn, R. (2019). *Hadisd version 3: monthly updates*. Tech. rep. Met Office Hadley Centre Tech. Note 103.

Dunn, R. J. H., K. M. Willett, D. E. Parker, and L. Mitchell (2016). Expanding HadISD: quality-controlled, sub-daily station data from 1931. Geoscientific Instrumentation, Methods and Data Systems 5, 473–491.

EN 1991-1-4:2005 (2005). *Eurocode 1 – Actions on structures – Part 1- 4: General actions – Wind actions*. Standard. European Committee for Standardization (CEN), Brussels, Belgium.

Foken, T. (2006). 50 Years of the Monin–Obukhov Similarity Theory. Boundary-Layer Met. 119, 431–447.

Huang, M., Q. Li, H. Xu, W. Lou, and N. Lin (2018). Non-stationary statistical modeling of extreme wind speed series with exposure correction. Wind and Structures 26, 129–146.

Isyumov, N. (2012). Alan G. Davenport's mark on wind engineering. Journal of Wind Engineering and Industrial Aerodynamics 104-106. 13th International Conference on Wind Engineering, 12–24.

Liu, Y., L. Zhou, Y. Qin, C. Azorin-Molina, C. Shen, R. Xu, and Z. Zeng (2023). Impacts of anemometer changes, site relocations and processing methods on wind speed trends in China. Atmospheric Measurement Techniques Discussions 2023, 1–21.

Mo, H., H. Hong, and F. Fan (2015). Estimating the extreme wind speed for regions in China using surface wind observations and reanalysis data. Journal of Wind Engineering and Industrial Aerodynamics 143, 19–33.

Molina, M. O., C. Gutiérrez, and E. Sánchez (2021). Comparison of ERA5 surface wind speed climatologies over Europe with observations from the HadISD dataset. International Journal of Climatology 41, 4864–4878.

Picozzi, V., A. Akbaba, A. Avossa, and F. Ricciardelli (2022). Correction of historical records to improve the reliability of design wind speeds. Engineering Structures 265.

Picozzi, V., F. Landi, A. Avossa, P. Croce, P. Formichi, and F. Ricciardelli (2024). The Climatic Action Uncertainty Chain. Engineering Structures 301, 117357.

Raffaele, L., L. Bruno, and E. Colucci (2024). The Italian wind map - part II: an approach based on mesoscale wind modelling. Proceedings of Proceedings of the XVIII International Conference of the Italian Association for Wind Engineering IN-VENTO 2024: Pisa, IT.

Rojas-Labanda, C., F. González-Rouco, E. García-Bustamante, J. Navarro, E. E. Lucio-Eceiza, G. Van der Schrier, and F. Kaspar (2023). Surface wind over Europe: Data and variability. International Journal of Climatology 43, 134–156.

Solari, G. and L. Pagnini (2009). Preliminary Elements for an Innovative Wind Map of Italy. Proceedings of Proceedings of the 5th European & African conference on wind engineering : Florence Italy, July 19th-23rd 2009.

Tarquini, S., I. Isola, M. Favalli, F. Mazzarini, M. Bisson, M. T. Pareschi, and E. Boschi (2007). TINITALY/01: a new triangular irregular network of Italy. Annals of Geophysics 50.

Wieringa, J. (1986). Roughness-dependent geographical interpolation of surface wind speed averages. Quarterly Journal of the Royal Meteorological Society 112, 867–889.

— (1996). Does representative wind information exist? Journal of Wind Engineering and Industrial Aerodynamics 65, 1–12.

WMO-No.8/2021 (2021). Guide to Meteorological Instruments and Methods of Observation, Eighth edition.

IN-VENTO 2024
International Conference of the Italian Association for Wind Engineering
Pisa, September 8th – 11th, 2024

The Italian wind map - part II: an approach based on mesoscale wind modelling

Lorenzo Raffaele[a], Luca Bruno[a], Elisabetta Colucci[a]

[a]*Department of Architecture and Design, Politecnico di Torino, Torino, Italy, lorenzo.raffaele@polito.it, luca.bruno@polito.it, elisabetta.colucci@polito.it*

SUMMARY:
Synoptic extreme winds are traditionally mapped at the macroscale resolution (hundreds of km) on the basis of time series of records measured at land anemometric stations, while the assessment of the design wind speed at the construction site is entrusted to the designer within the so-called return criterion. This study is intended to test an approach able to collect all the fields required to directly assess the wind hazard at the mesoscale resolution (about 2 km) around a construction site. The approach is grounded on data issued from a weather forecast computational model, its reanalysis by means of assimilated remote sensing observations, and an eventual final computational dynamic downscaling. The datasets from three different reanalysis models are tested. The resulting wind speed maps over the Italian Country are critically assessed with respect to anemometric records and standards in force.

Keywords: wind hazard, mesoscale map, current speed, extreme speed, atmospheric reanalysis, Italian Country

1. INTRODUCTION

In the practice, the design wind speed is commonly determined through wind speed maps. The well-known return criterion was formalized by Ballio et al., 1999 and it is traditionally adopted in Italy through the standards in force (DM 17-01-2018, 2018; EN 1991-1-4:2005, 2005). The return criterion relies on the accurate mapping of the basic wind speed v_b, i.e. the characteristic 10-min average wind speed at 10 m above the ground in open field terrain, to evaluate the mean wind speed v_m, defined as a function of the local site conditions (Fig. 1b). The mapping of v_b

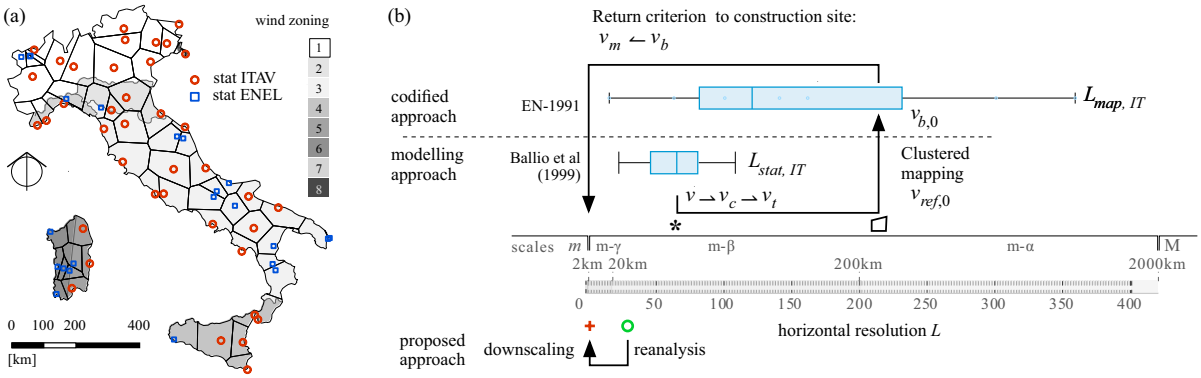

Figure 1. Voronoi discretization of Italian land based on 69 ITAV and ENEL stations together with current codified wind map (a). Comparative workflow between the return criterion and the proposed approach (b).

was pioneered by Ballio et al., 1999 on the basis of wind speed v anemometric measurements resulting from a total of 69 stations distributed over the Italian territory (Fig. 1a). The resulting horizontal resolution of the stations used to define the national design wind speed map $L_{stat,IT}$ is then equal to 69.4 km on average. Wind speeds were corrected (v_c) by filtering and adjusting unreliable data, and transformed (v_t) to homogenize the time averaging period and local site

conditions, in order to get 10-min averaged wind speeds measured at $z = 10$ m, over flat, uniformly open terrain conditions with roughness $z_{0,ref} = 0.05$ m. Wind maps resulted form the definition of the reference wind speed $v_{ref,0}$ as the value of v_t with mean return period $T_R = 50$ years, the clustering of $v_{ref,0}$ into nine geographical zones, and the definition of the basic wind speed at sea level $v_{b,0}$ for each zone. As a result, the transition from v to $v_{b,0}$ inevitably implied the coarsening of the horizontal resolution of the wind speed map $L_{map,IT}$, leading to an average value approximately equal to 170 km and widely uneven over the Italian land.
Recently, other approaches have been implemented to map wind speed in several scientific fields. Climate reanalysis data from numerical weather prediction models (Hersbach, Bell, et al., 2020) are widely adopted in wind energy, agriculture, water resources, insurance, and very recently in Wind Engineering, specifically along transmission lines (Yang et al., 2022). Climate reanalyses combine past observations with models to generate consistent time series of multiple climate variables. Climate reanalyses show massive potentialities since they deliver "a complete and consistent picture of the past weather" (Thépaut et al., 2018), relying "on a numerical weather prediction model to assimilate historical observations (e.g., from satellite, in situ, multiple variables) that are not homogeneously distributed around the globe" (Raffa, Reder, et al., 2021). Furthermore, they enables a high spatial resolution with respect to codified extreme wind maps in Wind Engineering, continuous update, and datasets available worldwide, avoiding conflicts of the national wind maps at boundaries.
This study aims to evaluate if reanalysis models (ERA5, Hersbach, Bell, et al., 2020), eventually coupled with deterministic (ERA5-Land, Sabater, Dutra, et al., 2021) and/or dynamic downscaling (VHR-REA_IT, Raffa, Reder, et al., 2021), can be suited to map extreme winds, and which are the advantages compared to in-force codified wind maps.

2. MODELLING APPROACHES

In the following, reanalysis modelling approaches tested in this study are briefly reviewed by focusing on the main variables of interest. Their space and time resolutions are given in Fig. 2 by referring to the scales of atmospheric processes.

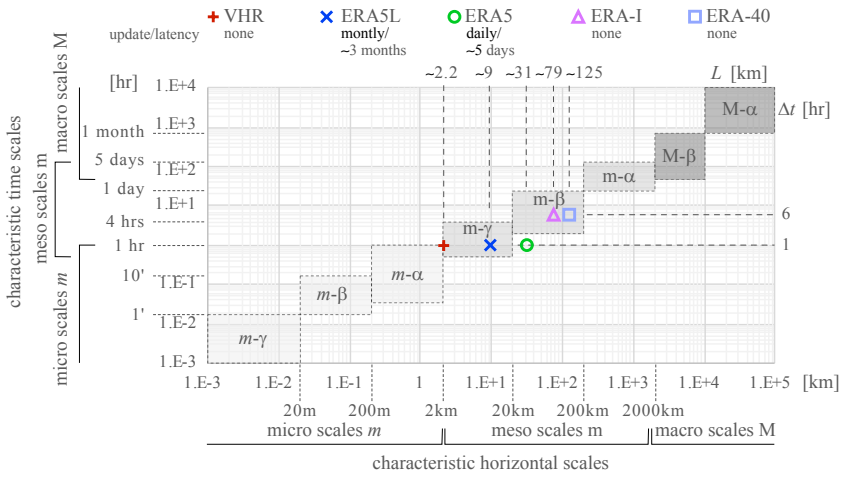

Figure 2. Space and time scales of the atmospheric processes (Fujita, 1986), and synopsis of mean horizontal and time resolutions of ERA-40, ERA-Interim (ERA-I), ERA5, ERA5-Land (ERA5L), VHR-REA_IT (VHR)

ERA5 is the fifth generation reanalysis developed by the European Centre for Medium-Range Weather Forecasts (ECMWF). It provides hourly estimates for a large amount of atmospheric, ocean wave and land surface variables, wind components at 10 m included. Observations used

as input for reanalysis in ERA5 come from satellite instruments and conventional data (Hersbach, Bell, et al., 2020). With regard to wind velocity at $z = 10$ m, measurements made near the sea surface on ships and drifting/moored buoys are retained only, while observations at land airport weather stations are limited to surface pressure. Land characteristics are described using several time-invariant fields, e.g. the soil and vegetation type, and the vegetation cover among others. It follows that the number of worldwide daily actively assimilated observations of wind velocity at 10 m is relatively small, and that the comparison between records at land anemometric stations and reanalysis is not trivial and directly driven by assimilation.
ERA5-Land (ERA5L, in the following) only focuses on land surface variables at an enhanced horizontal resolution. In other terms, ERA5L is a reiteration of the land component of the ERA5 climate reanalysis, using ERA5 atmospheric variables as input (Sabater, Dutra, et al., 2021). As a result, wind speed has purely been deterministically interpolated to the ERA5L grid via a linear interpolation method (Sabater, Dutra, et al., 2021).
VHR-REA_IT (VHR, in the following) is obtained by dynamic downscaling of ERA5 climate reanalysis to the lower bound of the γ meso-scale, also called convection-permitting scale (horizontal resolution lower than 4 km), over the domain covering Italy. The dynamic downscaling is carried out with the regional climate model COSMO-CLM with the module TERRA-URB to model urban environment (Raffa, Adinolfi, et al., 2023; Raffa, Reder, et al., 2021). Land use, surface elevation and soil type are determined through the GLC2000, GLOBE, and FAO Digital Soil Map datasets. Such a dynamic downscaling allows to explicitly resolve atmospheric deep convection, responsible for the formation of synoptic-scale storm systems, and to improve the modelling of wind systems dominated by fine-scale topography (Prein, Langhans, et al., 2015).

3. PRELIMINARY RESULTS

In the following, some preliminary phenomenological results are included to show a glimpse of the potentialities derived from the adoption of climate reanalysis in the Wind Engineering practice. Wind speed daily averages $\overline{V}_d$ resulting from stations measurements, ERA5, ERA5L and VHR modelling approaches throughout a single year are compared in Fig. 3. For purely illustrative purposes, two stations in Northern Italy, i.e. Milano Malpensa (Fig. 3a) and Venezia (Fig. 3b), and the year 2018 are selected. Reanalysis datasets confirm their capability in simu-

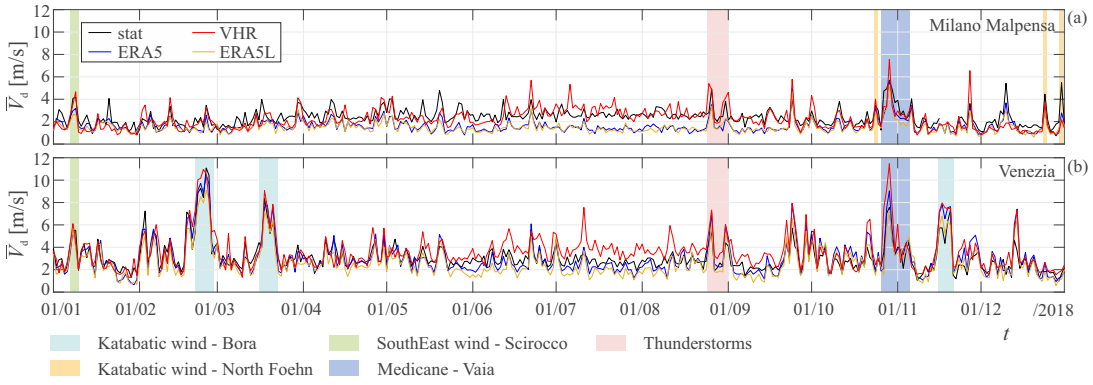

Figure 3. Time series of daily wind speeds for Milano Malpensa (a) and Venezia (b) anemometric stations during the year 2018. Visual comparison among stations, ERA5, ERA5L and VHR datasets.

lating mesoscale phenomena occurring from the larger meso-α to smaller meso-γ scale. Meso-α meteorological phenomena are clearly distinguishable in both time series, among them the medicane Vaia in October (Nimbus Web, 2018a) and a strong Scirocco wind event in January (Nimbus Web, 2018b). Meso-β meteorological events induced by katabatic winds, i.e. Bora in

February and March in Venezia and North Foehn in October and December in Milano, remain localized on the single time series. Meso-γ windstorms induced by convective phenomena in the wake of a cold front extending from Northern Europe towards south are distinguishable at the end of August (Celano and Selvini, 2018). Nevertheless, reanalysis models inevitably lead to different quantitative estimations of the wind speed magnitude. Discrepancies between VHR and ERA models result from their different horizontal resolution and modelling approaches. Conversely, discrepancies between measurements and reanalysis models can be attributed to anemometer specifications not compliant with existing guidelines, and/or subgrid roughness effects occurring at the microscale.
In the light of the above, the resulting wind speed maps over the Italian Country will be critically assessed with respect to anemometric records and standard in force.

ACKNOWLEDGEMENTS

This study was carried out within the RETURN Extended Partnership and received funding from the European Union Next-GenerationEU (National Recovery and Resilience Plan – NRRP, Mission 4, Component 2, Investment 1.3 – D.D. 1243 2/8/2022, PE0000005) – SPOKE TS 2. This study was jointly developed in the framework of the research project PROtection Technologies from Eolian Events for Coastal Territories (PROTEECT, http://www.proteect.polito.it/) within the Ministerial Decree no. 1062/2021 and received funding from the FSE REACT-EU - PON Ricerca e Innovazione 2014-2020. This manuscript reflects only the authors' views and opinions, neither the European Union nor the European Commission can be considered responsible for them. This study would not have been possible without the ECMWF ERA5 (https://doi.org/10.24381/cds.adbb2d47) and ERA5-Land (https://doi.org/10.24381/cds.e2161bac) reanalysis and the CMCC VHR-REA_IT (https://doi.org/10.25424/cmcc/era5-2km_italy) dynamic downscaling.

REFERENCES

Ballio, G., S. Lagomarsino, G. Piccardo, and G. Solari (1999). Probabilistic analysis of Italian extreme winds: Reference velocity and return criterion. Wind and Structures 2, 51–68.

Celano, M. and A. Selvini (2018). *Rapporto dell'evento meteorologico del 24 e 25 agosto 2018*.

DM 17-01-2018 (2018). *Technical Standards for Construction - update DM January 17, 2018*. Standard. Ministry of Infrastructures and Transport, Rome, Italy.

EN 1991-1-4:2005 (2005). *Eurocode 1 – Actions on structures – Part 1- 4: General actions – Wind actions*. Standard. European Committee for Standardization (CEN), Brussels, Belgium.

Fujita, T. T. (1986). Mesoscale Classifications: Their History and Their Application to Forecasting. Ed. by P. S. Ray. American Meteorological Society, Boston, MA, pp. 18–35.

Hersbach, H., B. Bell, et al. (2020). The ERA5 global reanalysis. Quarterly Journal of the Royal Meteorological Society 146, 1999–2049.

Nimbus Web (2018a). *27-30 Ottobre 2018: Scirocco eccezionale, mareggiate e alluvioni in Italia con la tempesta "Vaia"*.

— (2018b). *7-9 Gennaio 2018: Scirocco caldo, piogge record e valanghe sulle alpi occidentali*.

Prein, A., W. Langhans, et al. (2015). A review on regional convection-permitting climate modeling: Demonstrations, prospects, and challenges. Reviews of Geophysics 53, 323–361.

Raffa, M., M. Adinolfi, et al. (2023). Very High Resolution Projections over Italy under different CMIP5 IPCC scenarios. Scientific Data 10, 238.

Raffa, M., A. Reder, et al. (2021). VHR-REA_IT Dataset: Very High Resolution Dynamical Downscaling of ERA5 Reanalysis over Italy by COSMO-CLM. Data 6.

Sabater, J. Muñoz, E. Dutra, et al. (2021). ERA5-Land: A state-of-the-art global reanalysis dataset for land applications. Earth System Science Data 13, 4349–4383.

Thépaut, J.-N., D. Dee, R. Engelen, and B. Pinty (2018). The Copernicus Programme and its Climate Change Service. Proceedings of 2018 IEEE International Geoscience and Remote Sensing Symposium, 1591–1593.

Yang, S., L. E. Chouinard, and S. Langlois (2022). Hourly wind data for aeolian vibration analysis of overhead transmission line conductors. Journal of Wind Engineering and Industrial Aerodynamics 230.

IN-VENTO 2024
International Conference of the Italian Association for Wind Engineering
Pisa, September 8th – 11th, 2024

A combined CFD and ML based approach to perform a feasibility study of wind energy harvesting in the vicinity of the built environment using medium-sized wind turbines

S. K. Raghunathan Srikumar [1], G. Mosca [1], A. Gambale [1]

[1]*BuildWind SRL, Rue Bara 175, 1070 Brussels, Belgium, info@buildwind.net*

SUMMARY
A combined Computational Fluid Dynamics (CFD) and Machine Learning (ML) based tool has been used to perform a feasibility study of the potential Annual wind Energy Production (AEP) from medium-sized wind turbines in the vicinity of the built environment, where the effect of the interaction of wind with buildings is relevant. Specifically, the town of Eggenburg, Austria has been investigated. Wind statistics were extracted for the last 30 years near the selected site and CFD simulations were performed for multiple wind directions and speeds. A surrogate model was then set up based on the simulated results to predict additional wind conditions for the chosen site. Finally, combining the results from simulations and the surrogate model, the total potential AEP was obtained for the entire area for a medium-size wind turbine, and specific locations of interest were selected.

Keywords: CFD, Wind energy, Machine learning

1. MOTIVATION

Wind is a clean and renewable energy source that has the potential to significantly contribute to the electricity supply. In most cases, wind energy is harvested using large wind farms well away from the built environment (Stathopoulos et al., 2018). In closer proximity to buildings, wind is often overlooked as a possible energy source, assuming that wind speed is too low. However, once an accurate siting analysis of the wind turbine is performed, zones having higher wind speed due to local wind acceleration from buildings can be leveraged effectively to harvest wind energy (Stathopoulos et al., 2018).

Computational Fluid Dynamics (CFD) has proven to be the tool of choice to perform wind resource assessment in and around built environments (Toji-Silva et al., 2018;Stathopoulos et al., 2018;Juan et al., 2022). It provides a framework to obtain information with high resolution to accurately identify zones of interest in terms of high enough velocity and low enough turbulence, making it ideal for wind turbine siting analysis, especially in and around the built environment, where such predictions with simpler wind models are not reliable. However, performing a complete analysis often involves running multiple simulations per wind direction, proving to be computationally very expensive (Shiraz et al., 2020). The use of Machine Learning (ML) in tandem with CFD has been shown to significantly reduce the overall computational cost without sacrificing accuracy (Vinuesa and Brunton, 2020;Gambale et al., 2023). Data-driven surrogate models can be trained using data from a lesser number of CFD simulations, and the trained model can be used to obtain instantaneous predictions of other different flow conditions (Brunton et al., 2020). An accurately trained surrogate model can provide speedups of up to 50000 times compared to a conventional CFD simulation (Tanaka et al., 2019). In the present

work, such a surrogate model was developed based on data from the physics-based CFD simulations to reduce the total computational cost. Finally, results obtained from both the surrogate model and the CFD simulations were analyzed in tandem to get the annual wind energy yield map for the chosen site.

2. METHODOLOGY

The combined CFD and surrogate model approach was tested and validated for a neighborhood in Brussels, Belgium to predict the rooftop velocities for the dominant wind direction (Gambale et al., 2023). The current work focussed on assessing the AEP for the town of Eggenburg, Austria. Fig. 1 shows the CAD model of the built area together with the hilly terrain for the considered pilot site, along with a comparison with the satellite image from Google Earth. The considered built area has a circular radius of 1.2 km. CFD simulations were performed using the open source FVM-based solver OpenFOAM v7 with an improved Atmospheric Boundary Layer (ABL) framework implemented on a modified k-ω SST RANS model (Bellegoni et al., 2022; Srikumar et al., 2024). The improved ABL formulation solves the well-known problem of near-ground acceleration of the flow, thus allowing more accurate velocity predictions (Srikumar et al., 2024). Steady-state, incompressible simulations were performed for multiple inlet velocity conditions per wind direction that were defined based on wind statistical data obtained from the nearest meteorological station.

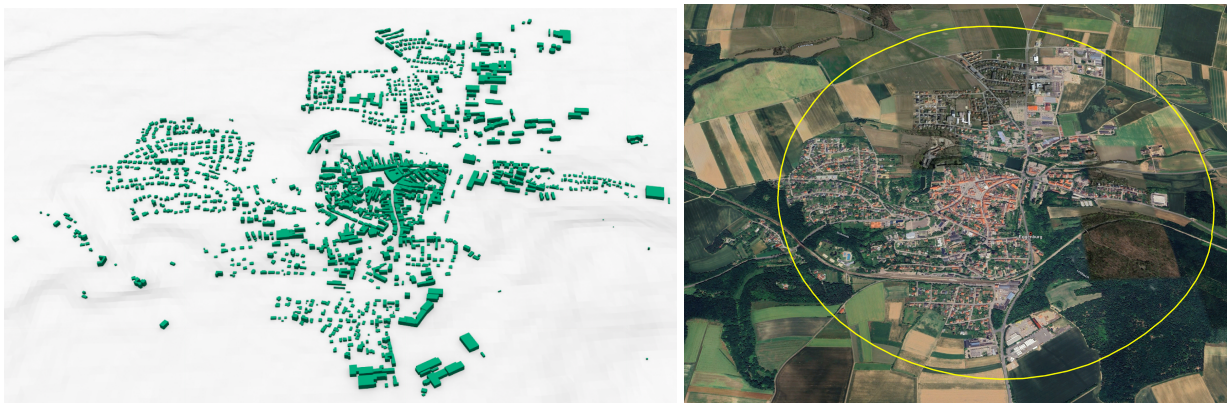

Figure 1. CAD simulated for the town of Eggenburg, Austria (left), and a comparison of the image from Google Earth (right). The built area has a circular radius of 1.2 km

The machine learning framework was implemented in Python using the Keras library, which is a high-level package built on top of the Tensorflow API. A surrogate model was created using Deep Neural Networks (DNN), that consists of a fully connected architecture with multiple hidden layers. Results from CFD simulations in terms of 2D planes of interest were used to train the model as follows: the wind velocities were extracted for zones of interest from different simulations performed for a specific direction, which served as labels for the surrogate model, and their corresponding inlet conditions as features. The trained model was then used to obtain the velocity field for all possible new inlet velocity conditions for the same zones of interest. The predicted velocity fields, combined with CFD data were then utilized to obtain the wind statistics in the zones of interest to finally assess the AEP for a particular wind turbine.

2.1. Estimation of AEP

The procedure involves computing a Weibull distribution for the velocity at each local point in the zones of interest, that is, a probability density function (PDF) of all possible velocity values at that point, as shown in Eq. (1). The distribution is defined by the two parameters: shape factor k and scale factor c. This local velocity Weibull curve can be obtained by performing curve fitting of all possible local velocities predicted by the ML model, for all possible inlet velocity conditions. From the local velocity Weibull curve, a Weibull power distribution (Power PDF) is derived, as shown in Eq. (2), where the power P (Eq. (3)) is a function of the local velocity V, the air density ρ, the wind turbine swept area A, and the wind turbine efficiency Cp. To obtain the total power generated from a particular wind turbine, the derived power Weibull curve can be integrated according to the properties and working limits of the chosen wind turbine. The limits are usually given in terms of cut-in and maximum speeds of the wind turbine. This is shown in Eq. (4). Here θ refers to the specific wind direction simulated. Finally, the AEP corresponding to the simulated wind direction can be computed from the total power by multiplying it with the total working hours of the turbine per year (365*24), and the wind direction frequency f_θ, as shown in Eq. (5). This analysis can be extended for all the wind directions, and the total AEP can be obtained by summing the AEP contributions of each wind direction.

$$PDF_{local}(V) = \frac{k_{local}}{c_{local}}\left(\frac{V}{c_{local}}\right)^{k_{local}-1} e^{-\left(\frac{V}{c_{local}}\right)^{k_{local}}} \quad (1)$$

$$Power\ PDF_{local}(P) = Velocity\ PDF_{local}(V) * \left|\frac{dV}{dP}\right| \quad (2)$$

$$P = 0.5\rho V^3 ACp \quad (3)$$

$$Power_{total}(\theta) = \int_0^{Max\ P} \left\{P * \left[Power\ PDF_{local}(P)\right] dP\right\} \quad (4)$$

$$AEP\ (\theta) = f_\theta * 365 * 24 * Power_{total}(\theta) \quad (5)$$

3. RESULTS

The AEP analyses are performed for vacant regions in the vicinity of the built environment, at specific heights above the ground, depending on the hub heights of the chosen wind turbine. An example of the final AEP distribution that could be achieved with such an analysis is shown in Fig. 2. Here the results are shown considering a 250kW horizontal axis wind turbine with a rotor diameter of 42m and a hub height of 28m above the ground. Zones with high AEP can be clearly identified in the vicinity of the built environment, in the southwest part of the considered CAD. Each point on the ground indicates the total AEP that can be harvested by installing the considered wind turbine at that specific location.

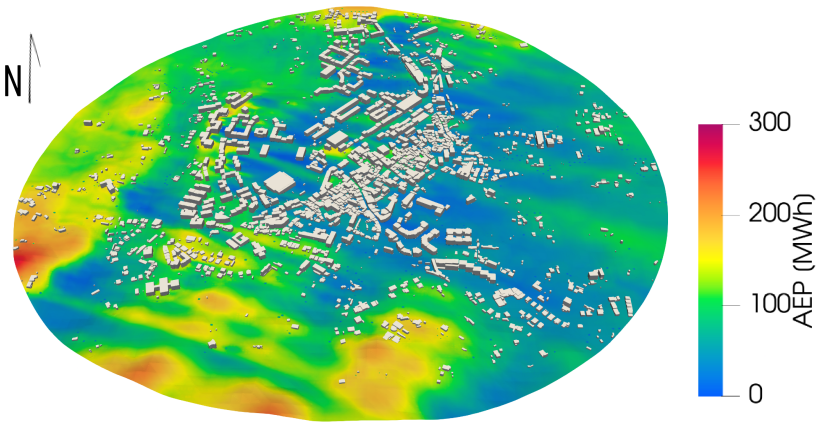

Figure 2. Total achievable AEP considering a 250kW wind turbine

ACKNOWLEDGEMENTS

The authors gratefully acknowledge Innoviris and the Brussels Capital Region for co-funding this research in the context of the project WEB: Wind Energy Brussels, under grant 2022-JRDIC-7a, and the European Climate, Infrastructure and Environment Executive Agency (CINEA) for funding under LIFE Project Grants, project number 101081061, project LIFE21-CET-LOCAL-PLENTY-LIFE: Institutionalised cross-sector PLanning and dedicated capacity building to ENable small and medium-sized municipalities to develop and monitor sustainable strategies for the Transition to clean energY

REFERENCES

Stathopoulos, T., Alrawashdeh, H., Al-Quraan, A., Blocken, B., Dilimulati, A., Paraschivoiu, M. and Pilay, P., 2018. Urban wind energy: Some views on potential and challenges. Journal of Wind Engineering and Industrial Aerodynamics, 179, pp.146-157.

Toja-Silva, F., Kono, T., Peralta, C., Lopez-Garcia, O. and Chen, J., 2018. A review of computational fluid dynamics (CFD) simulations of the wind flow around buildings for urban wind energy exploitation. Journal of Wind Engineering and Industrial Aerodynamics, 180, pp.66-87.

Juan, Y.H., Rezaeiha, A., Montazeri, H., Blocken, B., Wen, C.Y. and Yang, A.S., 2022. CFD assessment of wind energy potential for generic high-rise buildings in close proximity: Impact of building arrangement and height. Applied Energy, 321, p.119328.

Shiraz, M.Z., Dilimulati, A. and Paraschivoiu, M., 2020. Wind power potential assessment of roof mounted wind turbines in cities. Sustainable Cities and Society, 53, p.101905.

Brunton, S.L., Noack, B.R. and Koumoutsakos, P., 2020. Machine learning for fluid mechanics. Annual review of fluid mechanics, 52, pp.477-508.

Vinuesa, R. and Brunton, S.L., 2022. Enhancing computational fluid dynamics with machine learning. Nature Computational Science, 2(6), pp.358-366.

Tanaka, H., Matsuoka, Y., Kawakami, T., Azegami, Y., Yamamoto, M., Ohtake, K. and Sone, T., 2019. Optimization calculations and machine learning aimed at reduction of wind forces acting on tall buildings and mitigation of wind environment. International Journal of High-Rise Buildings, 8(4), pp.291-302.

Bellegoni, M., Cotteleer, L., Srikumar, S.K.R., Mosca, G., Gambale, A., Tognotti, L., Galletti, C. and Parente, A., 2023. An extended SST k− ω framework for the RANS simulation of the neutral Atmospheric Boundary Layer. Environmental Modelling & Software, 160, p.105583.

Srikumar, S.K.R., Cotteleer, L., Mosca, G., Gambale, A. and Parente, A., 2024. Application of a comprehensive atmospheric boundary layer model to a realistic urban-scale wind simulation. Building and Environment, p.111330.

A. Gambale, S.K. Raghunathan Srikumar, G. Mosca, Ioannis Tsionas, Maider Llaguno-Munitxa, André Stephan, 2023. A data-driven surrogate model framework based on CFD simulations to accelerate wind energy yield assessment, International Conference on Wind Engineering, Aug 27-31 2023, Florence, Italy

IN-VENTO 2024
International Conference of the Italian Association for Wind Engineering
Pisa, September 8th – 11th, 2024

A proposal for updating the extreme wind map of Italy

Francesco Ricciardelli, Andaç Akbaba, Vincenzo Picozzi, Alberto M. Avossa

University of Campania "Luigi Vanvitelli", Aversa, Italy
vincenzo.picozzi@unicampania.it

SUMMARY
The available extreme wind map of Italy was drafted in the mid 1990s, based on anemometric measurements mostly carried out between 1951 and 1973, with a minor portion extending to 1992. It contains shortcomings deriving from the pre-processing and statistical analysis of the data, which the authors themselves declared at the time of publication; hence, the need was felt to update it using more recent data and improving the transparency of the procedures. An attempt to propose a new map is made, considering only synoptic winds which have dominated the Italian extreme wind climate until now. Preliminary analysis of data available for the period from 1944 to 2020 suggested that the existing map should be updated both in terms of zoning and of the parameters accounting for the influence of distance from the coast and altitude of the site.

Keywords: Wind Hazard, Design Wind Speeds, Reliability, Extreme Value Analysis, Extreme Wind Map.

1. INTRODUCTION

Establishing the appropriate value of the reference wind speed is the first step towards the assessment of wind actions on structures, indeed corresponding to the first link of the Alan G. Davenport Wind Loading Chain (AGD-WLC) (IAWE, 2011). The reference wind speed or velocity pressure quantifies the wind hazard of a site, and due to its high geographic variability should in principle be evaluated based on the analysis of the local wind climate, as well as of the effects of orography, of roughness, and of the built environment on local circulation. Wind hazard maps, on the other hand, are necessary for code implementation.

The building of an extreme wind map for the purpose of structural design can be separated into two successive steps. First step consists of the evaluation of the extreme wind speed distribution at a number of locations for which data are available. Second step consists of the synthesis of the reference wind speeds in a way to provide a hazard map fulfilling the requirements set by an underlying structural reliability format, e.g. the 50-year return value.

The origins of the current extreme wind map of Italy date back to the early 1990s (Ballio, 1991a; Ballio, 1991b). The current version of the map was presented some years later (Ballio, 1999), drafted using data from a total of 69 meteorological stations. It included 3-hour downsampled measurements of 10-minute averaged wind speeds from 42 stations operated by the Italian Air Force, and contiguous measurements of 10-minute averaged wind speeds from 27 meteorological stations owned by the Italian Electrical Company (ENEL). The former were longer records, in the period from 1951 to 1973 for 38 stations already included in the database analysed in (Ballio, 1991b), and extending to 1991 for the additional 4 stations. The yearly maxima of each of the longer time series were used to fit the parameters of the EV Type I distribution, from which the

50-year return wind speed was calculated. The latter records were used within the framework of the Parent Population Method (PPM) (Gomes and Vickery, 1977), less stringent in terms of record length. Correction of the reference wind speeds retrieved from (Ballio, 1991b) so to adjust the roughness length to 0.05 m, was done by multiplying the speeds by a factor of 1.047. The new map divided Italy into nine geographic areas, for which values of the reference wind speed in the range of 25 to 31 ms^{-1} are given, applicable from sea level to a threshold altitude depending on area, ranging between 500 and 1500 m. Above that, the reference wind speed is to be increased linearly by 12 and 30 ms^{-1} every thousand metres, depending on geographic area, and again without any upper limit.

A slightly modified version of the map was incorporated in first normative version of Eurocode 1 (CEN, 2005), in the 2008 and 2018 versions of the Italian building code (MLP, 2008; MLP, 2018) as well as in the 2008 and 2018 CNR Guidelines (CNR, 2008; CNR, 2018). Differences were in that (*a*) the basic values of the reference wind speed for zones 7 (Liguria) and 8 (Province of Trieste) were reduced from 29 ms^{-1} and 31 ms^{-1} to 28 ms^{-1} and 30 ms^{-1} , respectively; that (*b*) the increase of the reference wind speed with altitude was reduced for all zones, and brought to the range of 10 to 20 ms^{-1} every thousand metres, with unchanged (lower) threshold altitudes; that (*c*) an upper threshold altitude of 1,500 m was added for the validity of the linear variation, above which either the value of the reference wind speed at 1,500 m should be used, or values deriving from specific analyses, yet never lower that the value applicable for an altitude of 1,500 m.

The map contains shortcomings, some of which had already been pointed out by its authors, others have manifested themselves over time, more have appeared during this research. Among the first is the fact that EV analysis was applied to downsampled data (Ballio, 1999), whereas it is now known that on average for Italian data correction factors of 1.08 for 1-hr sampled data, and of 1.16 for 3-hrs sampled data are necessary (Akbaba, 2024). In fact, the authors of the existing map noticed that there was some discrepancy between the return wind speeds evaluated by EV analysis and those evaluated by the PPM, and claimed that such difference was the effect of EV analysis overestimating return wind speeds, and that the overestimate was somehow compensated by the underestimate due to downsampling. Further research by the authors of this paper revealed that indeed EV analysis tends to produce larger values of the return wind speed then the PPM in the order of 12% when using an asymptotic distribution, and 10% when using a penultimate distribution; however there is no final evidence on whether it is EV analysis to overestimate the actual values, or the PPM to underestimate them, with some preference with the latter option; if this is the case, then the compensation referred to by the authors of the existing map would not apply. Another aspect is related to the length of the records used for the analyses and to their period of measurement; the length of the records used for EV analyses was on average 23.2 years, and almost all measurements ended in 1973; the length of the records used for the PPM was on average 6.4 years, and measurements were taken between 1980 and 1992; therefore it is clear that longer and more recent records would improve the accuracy of the estimates. Furthermore, some of the statements and assumptions behind the existing map seem not to be supported by the data; among these, is the separation of Sardinia into two distinct zones and the altitude correction. As to the analyses, roughness and height corrections were performed using the ESDU software (ESDU, 1992); the package has now been withdrawn, as errors were found in it. Finally, the value of 31 ms^{-1} suggested for the islands seem to largely underestimate the actual value, as it is synthesis of 7 statistical values between 35.2 and 40.1 ms^{-1}.

2. METHODOLOGY

The analyses were carried out using 3-hr downsampled SYNOP data from 26 stations and hourly downsampled METAR data from 5 stations, certified by the National Center for Meteorology and Aeronautical Climatology (CNMCA) of the Italian Air Force, which were augmented with METAR data coming from 80 stations, made available within the NOAA Global Hourly-Integrated Surface Database (NOAA).

Wind speed measurements, especially old ones, are imperfect for a number of reasons, among which missing and erroneous data, which require filtering and correction. Techniques for filtering potentially erroneous data have always been applied (Chavez, 2015), together with corrections for roughness, anemometer height, as well as for the effects of surrounding orography (Holmes, 2015). What has received far less attention in the past, is the necessity of correction for downsampling, which has instead been proven essential in the lack of contiguously measured data (Chiodi et al. 2014; Picozzi et al.; 2022, Akbaba, 2024). On the other hand, the issue also arises of what is the most appropriate technique for the statistical treatment of the data. No one single answer exists, as the choice shall be based on the characteristics of the available data (Akbaba, 2024). All these aspects introduce uncertainty in the statistics of extreme wind speeds.

On the other hand, after the extreme value statistics of wind speed or velocity pressure at a number of sites have become available, the second step arrives of translating them into a hazard map. Due to the limited number of sites for which data are available, some judgment has to be necessarily incorporated in the procedure, which introduces subjectiveness. As a matter of fact, there is a number of geographic characteristics that should be considered when preparing a wind hazard map, among which the presence of mountains, the distance from the coast, the existence of large cities. These make almost every station a separate case, and calls for expertise in gluing pieces together (Ballio, 1991a; Miller, 2001; Akbaba, 2024). To make the process as objective as possible, a first simple rule is again that of minimizing the bias between the reference wind speeds given in the map and those coming from statistical analysis. For wind maps divided into zones (as an alternative to contour maps), unbiased values should apply to each zone. On the other hand, the goal of uniform structural reliability over a given region shall also be pursued through minimization of coefficient of variation of uncertainty in reference wind speed (Picozzi, 2023). In doing this, the question arises of whether incorporating also the exposure would be appropriate to improve uniformity; in fact, areas with a larger number of exposed structures, e.g. densely built areas, should weight more when setting an objective function to be minimised then rural or mountainous areas.

In (Finzi, 1967) it was noticed that reference wind speed decreases with the distance from the coast and increases with altitude. This led to a criterion in which the reference velocity pressure is a function of three geographic parameters: geographic coordinates, distance from sea and altitude, such criterion was adopted by the CNR Guidelines in 1967 (CNR,1967). It was also borrowed by (Ballio, 1991b) and (Ballio, 1999), but with the modification that the geographic parameters do not affect only the velocity pressure or wind speed, but also the exposure category. To the authors' opinion, such approach is misleading, as it combines together two rather independent aspects, indeed corresponding to two different links of the AGD-WLC, i.e. wind hazard and site exposure. The current extreme wind map suffers from this choice, which is abandoned in this new study. Therefore, reference wind speeds are given to be used in conjunction with exposure parameters that depend only on site roughness and orography, but are independent from geographic location.

3. EXPECTED RESULTS

Preliminary findings from the statistical analysis of the available data suggest a re-evaluation of the zoning of Italian wind hazard map and of the corresponding parameters. In particular, the following modifications are considered:

1- global revision of zoning;
2- separation of coastal and inland areas for most part of the peninsula, due to the different exposure to sea winds;
3- merge of the two zones in which Sardegna is currently divided;
4- separation of offshore islands from coastal islands, the former having a much stronger extreme wind climate than the latter.

In general, an increase in the reference wind speed for southern Italy and for the islands is found, which combines with almost unaltered values in northern Italy and with either lower or higher values in central Italy.

REFERENCES

Akbaba, A., V. Picozzi, A.M. Avossa, and Ricciardelli F. (2024). Effects of Downsampling on the Prediction of the Italian Extreme Winds. In: Proceedings of the XVII Conference of the Italian Association for Wind Engineering IN-VENTO 2022, 41-51.

Ballio, G., Lagomarsino, S., Piccardo, G., and Solari, G. (1991a). A first step towards a map of Italian extreme wind. Part I: General principles and analysis methodology. Constr. Met., 3, 147–172.

Ballio, G., Lagomarsino, S., Piccardo, G., and Solari, G. (1991b). A first step towards a map of Italian extreme wind. Part II: Results, repercussion on standards, design implications. Constr. Met., 4, 209–242.

Ballio, G., Lagomarsino, S., Piccardo, G., and Solari, G. (1999). Probabilistic analysis of Italian extreme winds: Reference velocity and return criterion. Wind and Structures, 2(1), 51–68. https://doi.org/10.12989/was.1999.2.1.05.1

CEN (2005). EN 1991-1-4. Eurocode 1: Actions on Structures – Part 1-4: General actions – Wind Action. European Committee for Standardization.

Chávez-Arroyo, R. and Probst, O. (2015). Quality assurance of near-surface wind velocity measurements in Mexico, Meteorol. Appl. 22, 165–177 https://doi.org/10.1002/met.1432.

Chiodi, R., and Ricciardelli, F. (2014). Three issues concerning the statistics of mean and extreme wind speeds. Journal of Wind Engineering and Industrial Aerodynamics, 125, 156–167. https://doi.org/10.1016/j.jweia.2013.12.009.

CNR Norme CNR-UNI 10012. (1967). Ipotesi di carico sulle costruzioni.

CNR-DT 207/2008. (2008). Istruzioni per la valutazione delle azioni e degli effetti del vento sulle costruzioni.

CNR-DT 207 R1/2018. (2018). Istruzioni per la valutazione delle azioni e degli effetti del vento sulle costruzioni.

ESDU, Data Item 92032: Computer program for wind speeds and turbulence properties: flat or hilly sites in terrain with roughness changes, Technical Report, Engineering Sciences Data Unit, ESDU, 1992.

Finzi, L., and Paris, L., (1967). The new Italian regulations for wind loads on structures. Proceedings of International Seminar on Wind Effectson Buildings and Structures, pp. 245-264.

Gomes, L., and Vickery, B. (1977). On the prediction of extreme wind speeds from the parent distribution. Journal of Wind Engineering and Industrial Aerodynamics, 2(1), 21–36. https://doi.org/10.1016/0167-6105(77)90003-4.

Holmes, J. D. (2015). Wind Loading of Structures.

IAWE, Announcement of the Alan G. Davenport Wind Loading Chain, (2011). URL: http://iawe.org/about/Wind_Loading_Chain.pdf.

Miller, A., Cook, N., and Barnard, R. (2001). Towards a revised base wind speed map for United Kingdom. Wind and Structures 4, 197-212.

MLP (2008). Nuove norme tecniche per le costruzioni. D.M.14/01/2008.

MLP (2018). Aggiornamento delle «Norme tecniche per le costruzioni». D.M. 17/01/2018

Picozzi. V., Akbaba A., A.M. Avossa, and Ricciardelli F. (2022). Correction of historical records to improve the reliability of design wind speeds. Engineering Structures 265(3), 114473.

Picozzi, V., Ricciardelli, F., and Sørensen, J., (2023). Calibration of partial factors for wind action: an application to the Italian wind climate, Proceedings of 14th International Conference on Application of Statistics and Probability in Civil Engineering.

IN-VENTO 2024
International Conference of the Italian Association for Wind Engineering
Pisa, September 8th – 11th, 2024

Multi-hazard analysis of structural and nonstructural building elements under simultaneous seismic and wind loads

F. Rizzo[a], L. Caracoglia[b], S. Mansour[a], M. F. Sabba'[a], G. Maddaloni[c], D. Foti[a]

[a]*Polytechnic University of Bari, Bari, Italy, fabio.rizzo@poliba.it, sulyman.mansour@poliba.it, mariafrancesca.sabba@poliba.it, dora.foti@poliba.it*
[b]*Visiing Professor, DICAM, University of Trento, Italy, lucac@coe.northeastern.edu*
[c]*University of Sannio, Benevento, Italy, maddaloni@unisannio.it*

SUMMARY:
Due to their slenderness, tall buildings are sensitive to both wind and earthquake loads. Nevertheless, current building standards and most scientific literature neglect the direct interaction of these events, as it is usually considered a rare design case, yielding a limited effect on the structural elements. The simultaneous effect of wind and earthquake action is discussed in this paper on a 300 m tall building by considering six different locations in Italy. The simultaneous occurrence of earthquake and wind loads and their effects are studied, both from the numerical and experimental points of view (i.e., through shake table and wind tunnel tests) to evaluate the consequences on the non-structural elements on the façades of the building case study. Results show that the cumulative effect of moderate, non-catastrophic daily mean wind speed velocity (i.e., in the range 5-10 m/s at a reference 10m height) and a typical and non-catastrophic "daily" seismic shock (i.e., with magnitude in the range 3-5), can trigger large inter-story drift ratio (IDR) values and influence the fatigue life of steel elements.

Keywords: Multi-hazard experiments, wind tunnels, shaking table, aeroelasticity

1. INTRODUCTION

Skyscrapers offered a solution to limited land availability in densely populated urban areas, allowing cities to accommodate growing populations without sprawling into their suburbs. High-rise buildings also became a "status symbol" for cities competing for attention on the global stage. Today, the trend of constructing taller buildings is likely to continue as cities seek to compete for attention in an increasingly globalized world (Szolomicki and Golasz-Szolomicka, 2019). Tall building geometries are increasingly complex and unconventional, making buildings sensitive to multi-hazard events such as the "interaction" between the daily wind or windstorm and the Earthquake swarm or strong Earthquake. As discussed in Li et al. (2012) and Chapain and Aly (2019), no such area in the world is free from natural hazards induced by earthquakes (Asprone et al., 2010), wind (Zhu et al., 2020), rain (Rosowsky et al., 2016), ice (Nguyen Sinh et al., 2016), fire and landslides (Kwag and Hahm, 2018). Earthquakes, tsunamis, landslides, tropical storms, flooding, and coastal inundation are some examples of natural hazards whose occurrence mainly depends on the geographical location. Due to climate change, among other factors, the frequency of natural hazards occurrence is spurred, threatening life and well-being (Kwag and Gupta, 2016, Kwag and Gupta, 2017, Kwag et al., 2021; Kappes et al., 2012, Barbato et al., 2017). The multi-hazard investigation on tall buildings seems necessary because of the occupants' density, the crucial role of non-structural elements on the façades (e.g., effects of internal pressures) and the amplification from the base to the top of the ground acceleration, induced by the seismic loads (Rizzo et al., 2020). The two hazards investigated in this research are the earthquake and the wind that induce significant floor accelerations and displacements, and relevant phenomenon related to the design of flexible tall building structures,

such as façades and elevator shafts in tall buildings due to large displacements of the main building. It is well known that, if we approached the problem in terms of occurrence probability of catastrophic earthquakes combined with catastrophic windstorms, the probability of simultaneous occurrence is basically zero. Nevertheless, several studies have indicated that, in some cases, when a building is designed for a single dominant hazard, this does not necessarily provide satisfactory performance against the other hazard (Kwag and Gupta, 2016, Kwag and Gupta, 2017, Kwag et al., 2021). The basic premise of design standards (ASCE/SEI, 7-05/-10 and CEN, 1990:2002) is that each load combination attempts to account for an extreme load scenario that cannot occur simultaneously with others. Consequently, much research has been focused on the dynamic behavior of the structures subjected to a single dominant hazard, either an earthquake or a high wind (Kwag and Gupta, 2016, Kwag and Gupta, 2017, Kwag et al., 2021). Based on the small number of recorded, simultaneous occurrences of strong earthquake and wind, design standards do not consider the load combination that provide a "sum" of the effects derived from the two hazards. This research assumes that, when a moderate seismic event occurs, a tall building may already be vibrating due to underlying wind loads; this is also relevant for non-catastrophic seismic and wind events. The relevance consists of undesired and unforeseen effects also due to fatigue in steel buildings. The justification for this investigation is because, since building design codes do not usually consider this scenario, designers may underestimate both the reduced capacity of the building and its non-structural elements to withstand the earthquake loads, caused by non-structural damage (i.e., fatigue), induced by the inherent random vibration due to moderate wind loads (Li et al., 2022) and the increase of Inter-story Drift Ratio (IDR).

2. EARTHQUAKE AND WIND EVENT OCCURRENCE

The Europe map given by Taddei and Meskouris (2013) shows that a large part of the south European coastal areas present high seismic hazard and non-negligible wind conditions with reference mean wind speed greater than 5 m/s, e.g., suitable for modern wind turbines. Considering the wind and turbulence velocity profile extrapolated from the ground to h=200 m (rooftop height of the building case study), it is possible to postulate that the mean wind velocity in many areas is sufficient to affect the structure and, especially, its non-structural elements. The map also illustrates that most Italian territory is affected by a high seismic hazard and daily mean wind speed larger than 5 m/s. This research focuses on six different areas of Italy, located on the main islands, west coasts, east coasts, Apennine mountains and Po Valley. These six areas are designated as pilot areas, located around Messina, Cosenza, L'Aquila, Norcia, Pesaro and Modena, respectively. Because the seismic monitoring stations and wind velocity anemometric stations are not co-located and the measurements of seismic and wind activity are not recorded at the same time of the day, the daily averages of the mean velocity (https://www.meteoblue.com/it) were used as a plausibly representative value of the mean wind speed observed during an earthquake occurrence. Finally, the seismic recordings, derived from the National Institute of Geophysics and Volcanology (INGV) dataset (https://itaca.mi.ingv.it), are considered as independent events even though they may be correlated, i.e., part of a "seismic swarm". Table 1 lists the magnitude of strong earthquakes, occurred in the six pilot areas, and the corresponding recorded wind velocity at both, 10 and 300 m. It was also observed that a few days after or before the strong earthquake, large daily mean wind speeds were measured.

Table 1. Seismic events and daily mean wind speed, V_m.

Place	Date	Magnitude	Distance from the epicenter (km)	V_m (m/s)				
				at 10 m	at 300 m	Date	at 10 m	at 300 m
Messina	23/12/2013	4.0	3.2	6.2	12.7	21/12/2013	10.2	21.5
Cosenza	24/02/2020	4.4	8.1	5.3	11.2	27/02/2020	9.1	19.2
L'Aquila	06/04/2009	6.1	2.5	3.8	8.1	24/03/2009	12.1	25.5
Norcia	30/10/2016	6.5	4.6	2.7	5.7	06/11/2016	10.8	22.8
Pesaro	26/10/2016	5.9	120.5	4.6	9.7	23/10/2016	12.7	26.8
Modena	29/05/2012	6.0	17.5	3.8	8.1	21/05/2012	8.4	17.7

3. CASE STUDIES ARCHITECTURE

The aim of this investigation is to propose an approach to estimate effects, induced by both seismic and wind hazards, on tall building structures and their non-structural elements. The discussion focuses on the damage on the façades due to: (i) lateral deformations induced by the IDR of the 300 m tall building (Rizzo et al., 2021a) and (ii) the damage to façade frames due to fatigue (Rizzo et al., 2021b). This procedure involves additional experimental verification, because tall building slenderness can induce undesired aeroelastic effects, and because of the complex aerodynamic shape-dependent loads. Therefore, it is only possible to analyze the structure under wind loads by considering Fluid Structure Interaction (FSI) that may require very high computational or experimental burden. The proposed approach consists of: (I) statistical investigation of hazards (i.e., seismic magnitude and daily mean wind speed); (II) numerical analyses by Finite Element Method (FEM) model using measured seismic ground accelerations and daily mean wind speeds; (III) independent experimental tests in wind tunnel and on the shaking table to estimate seismic- and wind-induced accelerations on the building floors; (IV) planning of simultaneous experiments in wind tunnel through the base excitation by shaking table. The analyses and experiments are: (A-I) numerical analyses: (A-I-a) response spectrum analyses on FEM model by using the seismic load, estimated according to NTC, 2018; (A-I-b) time history analyses, linear and elastic, by FEM model and using recorded seismic ground accelerations given by the INGV data set; (A-I-c) equivalent static analyses by FEM model and wind loads estimated according to CNR (DT 207, 2018); (A-I-d) equivalent static analyses by FEM model and wind loads estimated according to CNR (DT 207, 2018) combined with mean wind speed measured from https://www.meteoblue.com/it. The load combinations on both the main building elements and the curtain walls are: COMB#1 = (A-I-a) enveloped to (A-I-c); COMB#2 = (A-I-b) enveloped to (A-I-d). (A-II) Experimental tests: (A-II-a) measurements of seismic induced floor displacements by shaking table experiments; (A-II-b) measurements of wind-induced floor accelerations through aeroelastic tests in wind tunnel. The load combination on both the main building elements and the curtain walls is: COMB#3 = (A-II-a) enveloped to (A-II-b).

4. CONCLUSIONS

The main study conclusions are: (I) The simultaneous occurrence of seismic events with magnitude larger than 4 and non-negligible daily mean wind speeds is very likely in all the investigated pilot areas. (II) If the envelope of the structural responses induced by the two hazards is considered, safety limit states for both the main structure and its non-structural elements can be established by using code recommendations. If experimentally measured loads are used, some unsatisfactory limit conditions are noticed. (III) If the structural responses induced by the two hazards are summed, unsafe limit conditions are observed for most pilot areas. (IV) If non-structural element resistance is reduced by considering deterioration produced by wind-induced

fatigue and seismic analysis given by design codes is considered, unsafe limit conditions can also be found.

REFERENCES

ASCE/SEI (7-05/-10). (2013). Minimum Design Loads for Buildings and Other Structures.

Asprone, D., Jalayer, F., Prota, A., and Manfredi, G. (2010). Proposal of a probabilistic model for multi-hazard risk assessment of structures in seismic zones subjected to blast for the limit state of collapse. Struct. Saf. 32, 25–34.

Barbato, M., Li, Y., and Padgett, J. (2017). Recent advances in assessment and mitigation of multiple hazards. ASCE J. Struct. Eng. 143, 02017001.

CEN (1990:2002). A1: Basis of structural design.

Chapain, S. and Aly, A. M. (2019). Vibration attenuation in high-rise buildings to achieve system-level performance under multiple hazards. Engineering Structures 197, 109352.

CNR (DT 207, 2018). Guide for the assessment of wind actions and effects on structures. National Research Council of Italy.

Kappes, M. S., Keiler, M., Elverfeldt, K. von, and Glade, T. (2012). Challenges of analyzing multi-hazard risk: a review. Natural hazards 64, 1925–1958.

Kwag, S. and Gupta, A. (2016). Bayesian network technique in probabilistic risk assessment for multiple hazards. 50046, V004T14A016.

Kwag, S., Gupta, A., Baugh, J., and Kim, H.-S. (2021). Significance of multi-hazard risk in design of buildings under earthquake and wind loads. Engineering Structures 243, 112623.

Kwag, S. and Hahm, D. (2018). Development of an earthquake-induced landslide risk assessment approach for nuclear power plants. Nucl. Eng. Technol. 50, 1372–1386.

Kwag, S. and Gupta, A. (2017). Probabilistic risk assessment framework for structural systems under multiple hazards using Bayesian statistics. Nuclear Engineering and Design 315, 20–34.

Li, C., Pan, H., Tian, L., and Bi, W. (2022). Lifetime multi-hazard fragility analysis of transmission towers under earthquake and wind considering wind-induced fatigue effect. Structural Safety 99, 102266.

Li, Y., Ahuja, A., and Padgett, J. E. (2012). Review of methods to assess, design for, and mitigate multiple hazards. J. Perform. Constr. Facil. 26(1), 104–117.

Nguyen Sinh, H., Lombardo, F. T., Letchford, C. W., and Rosowsky, D. V. (2016). Characterization of joint wind and ice hazard in Midwestern United States. Nat. Hazards Rev. 17, 04016004.

NTC (2018). Nuove norme tecniche per le costruzioni, Italian standard.

Rizzo, F., Caracoglia, L., and Piccardo, G. (2021a). Examining wind-induced floor accelerations in an unconventionally shaped, high-rise building for the design of "smart" screen walls. J. Build. Eng. 43, 103115.

Rizzo, F., Franco, A., Bonati, A., Maddaloni, G., Caterino, N., and Occhiuzzi, A. (2021b). Predictive analyses for aerodynamic investigation of curtain walls. Proceedings of Structures. Vol. 29. Elsevier, 1059–1077.

Rizzo, F., Maddaloni, G., Occhiuzzi, A., Prota, A., Pagliaroli, A., et al. (2020). "Earthquake induced floor accelerations on a High-rise building: In Scale Tests on Shaking Table". Proceedings of *IABSE 2020, Resilient Technologies for Sustainable Infrastructures, Christchurch, New Zeeland, 2nd-4th September 2020.*

Rosowsky, D. V., Mudd, L., and Letchford, C. (2016). Assessing climate change impact on the joint wind-rain hurricane hazard for the northeastern US coastline. Risk analysis of natural hazards: Interdisciplinary challenges and integrated solutions, 113–134.

Szolomicki, J. and Golasz-Szolomicka, H. (2019). Technological advances and trends in modern high-rise buildings. Buildings 9, 193.

Taddei, F. and Meskouris, K. (2013). Seismic analysis of onshore wind turbine including soil-structure interaction effects. Proceedings of Seismic Design of Industrial Facilities: Proceedings of the International Conference on Seismic Design of Industrial Facilities (SeDIF-Conference). Springer, 511–522.

Zhu, Z., Lei, W., Wang, Q., Tiwari, N., and Hazra, B. (2020). Study on wind-induced vibration control of linked high-rise buildings by using TMDI. J. Wind Eng. Ind. Aerodyn. 205, 104306.

IN-VENTO 2024
International Conference of the Italian Association for Wind Engineering
Pisa, September 8th – 11th, 2024

Improving post-critical galloping analysis of square-shaped cylinders through Artificial Neural Networks

Fabio Rizzo [1], Luca Caracoglia [2], Giuseppe Piccardo [3]

[1] *Polytechnic University of Bari, Bari, Italy, fabio.rizzo@poliba.it*
[2] *Department of Civil, Environmental & Mechanical Engr. (DICAM), University of Trento, Italy (permanent address: Northeastern Univ., Boston, MA, USA), lucac@coe.neu.edu*
[3] *University of Genoa, Genoa, Italy, giuseppe.piccardo@unige.it*

SUMMARY
Although evaluating post-critical solution branches in nonlinear galloping is feasible using closed-form solutions for single-degree-of-freedom plunge oscillators, it often conceals pitfalls arising from the inherent uncertainty in numerous parameters, particularly the nonlinear vertical force coefficient (aside from the structural damping ratio). Conversely, such evaluations are crucial in energy harvesting endeavors, offering an initial assessment of a new system's potential. To address these challenges, Machine Learning methods (i.e., an Artificial Neural Network – ANN - algorithm trained on simulated experimental data) emerge as a promising tool for more reliable assessment of both critical conditions and nonlinear post-critical responses. In this study, we aim to investigate the benchmark case of a square cross section, incorporating slight roundness at corner edges, for which abundant experimental wind tunnel data exist. Numerical simulation results are presented illustrating nonlinear galloping branches and examining the uncertainties inherent in the corresponding solutions.

Keywords: nonlinear galloping, aerodynamic load variability, Machine Learning methods

1. INTRODUCTION

Galloping, an important aeroelastic phenomenon, holds the potential to either undermine the stability of low-damped, slender structures or be harnessed for energy extraction purposes. While the classical galloping theory relies on the quasi-steady aerodynamic theory (e.g., Païdoussis et al., 2011), which may pose limitations in real scenarios, it remains prevalent in technical analyses; for its simplicity it is also incorporated into design standards (e.g., CNR, 2019; EN 1991-1-4, 2010). Despite ongoing debates about its applicability, the quasi-steady aerodynamic theory has historically been deemed adequate for studying galloping across various structures, spanning from early investigations (e.g., Parkinson and Smith, 1964) to recent applications such as wind-based energy harvesting (e.g., Zhang et al., 2021). Galloping typically arises as a large self-excited transverse oscillation, occurring above a critical threshold of wind speed. It is governed by the adverse effects of the transverse components of lift and drag forces acting on the cross section of the structure. These aerodynamic forces induce negative aerodynamic damping. Consequently, galloping is a velocity-dependent, damping-controlled instability problem (Païdoussis et al., 2011).

The onset of galloping instability hinges upon the static aerodynamic coefficients and their derivatives estimated at an initial angle of attack, aligned with the mean-wind incoming flow direction, as outlined in the classic Den Hartog criterion. A precise estimation of these coefficients, typically attainable only through static wind tunnel testing, is imperative for accurately assessing galloping conditions. Regrettably, numerous uncertainties pervade this estimation process,

stemming from factors like imperfect external flow conditions, experimental errors in coefficient determination, and predictions of structural damping (Pagnini et al., 2017), in addition to modeling approximations of the static coefficients (e.g., Ng et al., 2005). For instance, variations in flow conditions, influenced by factors like turbulence intensity, as well as air density, directly impact galloping assessment. While certain structural properties such as the fundamental frequency of the transverse mode can be precisely determined, others like structural damping are inherently less unpredictable. Aerodynamic parameters may be inferred through extrapolation from similar body shapes or derived from dedicated wind tunnel tests. However, uncertainty persists in both cases, necessitating thorough uncertainty analysis to delineate sensitivity to galloping onset. More specifically, the main issue concerns the variables associated with experimental errors in wind tunnel testing or the extrapolation of coefficient values from design standards, which often offer widely dispersed values in the literature, even for seemingly simple cross-sectional shapes like a square. Uncertainty analysis demands the deployment of stochastic or perturbation methods, or Monte Carlo sampling. However, these methods, though effective in characterizing uncertainty, entail computationally intensive dynamic analyses, either at the onset of instability or to predict post-critical vibration ranges, rendering them less suitable for preliminary design stages. Thus, while crucial for ensuring structural integrity and performance, navigating the complexities of uncertainty in linear and nonlinear galloping analyses remains a formidable challenge.

This study aims to leverage Machine Learning methods, and Artificial Neural Networks (ANNs) in particular, to enhance post-critical galloping analysis, building upon classic closed-form solutions derived through perturbation techniques linked to the polynomial representations of transverse static force coefficients utilized in the quasi-steady formulation (e.g., Parkinson & Smith, 1964; Novak, 1969; Ng et al., 2005). Specifically, we focus on the case of a prismatic square section due to the availability of extensive experimental data from the literature. This research represents a continuation of the authors' prior work, which initially explored the application of ANNs for assessing the incipient galloping critical velocity (Rizzo et al., 2024). By extending this analysis, we aim to refine our understanding of post-critical galloping behavior and its implications for aeroelastic stability. ANNs offer a promising avenue for capturing the complex relationships between input parameters and post-critical galloping characteristics, allowing for more accurate predictions and insights into structural performance. By coupling traditional analytical techniques with the adaptive learning capacity of ANNs, this study plans to enhance the accuracy and efficiency of nonlinear galloping assessment methodologies, thereby advancing the understanding and management of aeroelastic instabilities in slender structures.

2. BACKGROUND ON NONLINEAR GALLOPING

The vertical or transverse force coefficient C_{Fy}, measured on a stationary cylinder at various angles of incidence α, is usually modeled as a polynomial function of α. In the quasi-steady theory analysis, the angle can be expressed as $\dot{y}/U$, approximately equal to $\tan\alpha$, being y the vertical displacement, with dot indicating the time derivative, and U the mean free-stream velocity. Consequently, the polynomial curve fit takes the following form when the mean wind flow aligns along a symmetry axis of the cross-section, with Taylor expansion extended to the 11th order (e.g. Ng et al, 2005):

$$C_{F_y} = A\left(\frac{\dot{y}}{U}\right) + B\left(\frac{\dot{y}}{U}\right)^3 + C\left(\frac{\dot{y}}{U}\right)^5 + D\left(\frac{\dot{y}}{U}\right)^7 + E\left(\frac{\dot{y}}{U}\right)^9 + F\left(\frac{\dot{y}}{U}\right)^{11} \quad (1)$$

A close approximation of the experimental data necessitates at least a seventh-degree polynomial due to significant changes in curvature within the relevant range of the angle of attack during

anticipated transverse vibration amplitudes (e.g., $-16° \leq \alpha \leq 16°$). A is typically the sole coefficient required for assessing the critical condition. However, in certain scenarios, additional coefficients may also be needed to provide a comprehensive analysis that is necessary, for example, to enable energy harvesting applications. The equation governing the motion y of the model in response to the nonlinear vertical (transverse) force, as defined by Eq. (1), is given by:

$$\ddot{y} + 2\xi\omega_0\dot{y} + \omega_0^2 y = \frac{1}{2m}\rho B U^2 C_{F_y} \tag{2}$$

where m is the mass per-unit-length, ξ the structural damping ratio, ω_0 the circular natural frequency, B a characteristic dimension, and ρ the flow density. By employing a perturbation approach, we can derive the following equation (e.g., Parkinson & Smith, 1964; Novak, 1969):

$$\frac{dR}{d\tau} = aR + bR^2 + cR^3 + dR^4 + dR^5 + eR^6 + fR^7 = F(R) \tag{3}$$

in which R is the square of the reduced vibration amplitude, and the coefficients a to f depend on the system parameters. Setting $F(R) = 0$ yields an algebraic equation representing the steady amplitudes, corresponding to limit-cycle oscillations of the post-critical galloping branches.

3. METHODOLOGY PROPOSAL

The ANN (e.g., Rumelhart and McClelland, 1987; Hornik at al., 1989) is a computational algorithm designed to emulate the behavior of brain synapses. It reconstructs the nonlinear relationship between a set of independent input variables x_k and output variables y_i through interconnected "neurons". These neurons are organized into layers: an input layer, hidden layer(s), and an output layer. Each neuron within each layer is connected to every node in the adjacent layers. The hidden layers perform calculations based on the input layer, with results propagated to subsequent layers. The output layer provides the final calculation result. The generic input-output calculation of an ANN involves the use of a transfer or "activation" function g(.) between adjacent layers. In the case of a three-layer ANN, as illustrated in Fig. 1a, the following equation can be used to predict the generic output y_i (with $i = 1,2,\dots,N_o$), accounting for all synapses originating from the inputs x_k (with $k = 1,2,\dots,N_i$ representing the number of inputs):

$$y_i = \mathrm{g}\left[\sum_{j=1}^{N_h}\left(w_{ij}\,\mathrm{g}\left(\sum_{k=1}^{N_i} v_{jk}x_k + \theta_{vj}\right) + \theta_{wi}\right)\right] \tag{4}$$

where w_{ij} are the "connective weights" between any two nodes in the hidden and output layers; v_{jk} are "connective weights" between any two nodes in the input and hidden layers; θ_{vj} and θ_{wi} are bias terms; the symbols, N_i, N_h, and N_o represent the numbers of nodes in the input, hidden and output layers, respectively. An ANN model can be utilized for predictions only after calibration of hyperparameters v_{jk}, w_{ij} etc., which is conducted using an existing set of input-output data. The calibration typically involves three steps: training, validation, and testing. In this study, the training of the ANN is executed through a standard back-propagation algorithm aimed at error minimization. Specifically, the variables x_k with $N_i > 1$ include the dimensionless mass parameter, the structural damping ratio, an estimation of the initial incidence angle α_0 (equal or close to 0), the order of the polynomial used to approximate the vertical force coefficient in Eq. (1), and the coefficients A to F of the polynomial approximation. The output variable y_i with $i = N_o = 1$ represents the limit-cycle amplitude of the nonlinear oscillations associated with the galloping post-critical branches.

4. CONCLUSIONS AND ON-GOING WORK

The study is investigating various ANN architectures, including different numbers of hidden layers and neurons, to predict limit-cycle amplitudes while considering the inherent uncertainties in describing the nonlinear force coefficient as provided by Eq. (1). Additionally, the study will account for imperfections in cross-section geometries, including the possibility of slight roundness at the square section edges. To inform this investigation, insights from a prior study on ANN methods applied to aeroelastic instability (Rizzo and Caracoglia, 2020) will be incorporated. Figure 1b illustrates numerical simulation results depicting galloping critical onset (Rizzo et al., 2024). The dimensionless critical velocity $U_{cr}/(n_0 B)$ is predicted by an ANN model with architecture "1-30-1" (i.e., $N_i = 1, N_h = 30, N_o = 1$). This prediction is compared against the theoretical solution within suitable intervals of Scruton number and parameter A.

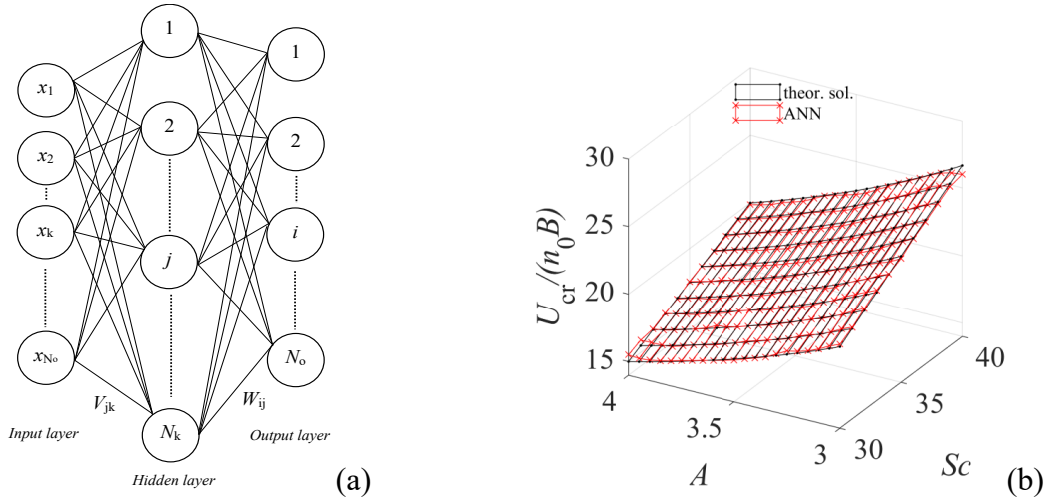

Figure 1. (a) Typical ANN architecture with one hidden layer, (b) square-prism galloping analysis with ANN-based model: Scruton number (Sc) and A coefficients *vs.* galloping critical reduced velocity $U_{cr}/(n_0 B)$.

REFERENCES

CNR, 2019. Guide for the assessment of wind actions and effects on structures – CNR-DT 207 R1/2018, National Research Council of Italy, Rome (in Italian).

EN 1991-1-4, 2010. Eurocode 1: Actions on Structures – Part 1.4: General Actions – Wind Actions. CEN, European Committee for Standardization, Brussels.

Hornik K., Stinchcombe M., White H., 1989. Multilayer feedforward networks are universal approximators. Neural Networks 2, 359-366.

Novak M., 1969. Aeroelastic galloping of prismatic bodies. J. Engineering Mechanics Division ASCE 6394, 115-142.

Ng Y.T., Luo S.C., Chew Y.T., 2005. On using high-order polynomial curve fits in the quasi-steady theory for square-cylinder galloping. Journal of Fluids and Structures 20, 141-146.

Pagnini L.C., Freda A., Piccardo G., 2017. Uncertainties in the evaluation of one degree-of-freedom galloping onset, European Journal of Environmental and Civil Engineering 21(7-8), 1043-1063.

Païdoussis M. P., Price S. J., De Langre E., 2011. Fluid-Structure Interactions, Cambridge University Press, New York, NY.

Parkinson, G.V., Smith, J.D., 1964. The square prism as an aeroelastic non-linear oscillator. Quarterly Journal of Mechanics and Applied Mathematics 17, 225–239

Rizzo F., Caracoglia L., 2020. Artificial Neural Network model to predict the flutter velocity of suspension bridges. Computers and Structures 233, 106236.

Rizzo, F., Caracoglia, L., Piccardo, G., 2024. Enhancing the analysis of galloping instability by Artificial Neural Networks. Proc. Int. Conf. on Wind Engineering ICWE 16, Florence, August 27-31, 2023 (full paper submitted, under review).

Rumelhart D. E., McClelland J. L., 1987. Parallel distribution processing: explorations in the microstructure of cognition: foundations. MIT Press.

Zhang M., Abdelkefi A., Yu H., Ying X., Gaidai O., Wang J., 2021. Predefined angle of attack and corner shape effects on the effectiveness of square-shaped galloping energy harvesters. Applied Energy 302, 117522.

IN-VENTO 2024
International Conference of the Italian Association for Wind Engineering
Pisa, September 8th – 11th, 2024

Thunderstorm gust response factor: application to a full-scale monitored slender vertical structure

Luca Roncallo[a], Mekdes Tadesse Mengistu[b], Federica Tubino[c], Maria Pia Repetto[d]

[a]*University of Genoa, Genoa, Liguria, Italy, luca.roncallo@edu.unige.it*
[b]*University of Genoa, Genoa, Liguria, Italy, mekdestadesse.mengistu@edu.unige.it*
[c]*University of Genoa, Genoa, Liguria, Italy, federica.tubino@unige.it*
[d]*University of Genoa, Genoa, Liguria, Italy, repetto@dicca.unige.it*

SUMMARY:
In this study, the Thunderstorm Gust Response Factor (TGRF) technique is adopted for the estimate of the maximum dynamic response of a full-scale monitored slender vertical structure subjected to the impact of two thunderstorm downbursts. The considered structure is a lighting pole equipped with an ultrasonic anemometer as well as strain gauges and accelerometers. The dynamic response estimated starting from the recorded accelerations and deformations is compared with the maximum response based on the TGRF approach. The parameters of the wind speed are extracted from the time anemometric data and a nose-shaped mean wind profile is assumed. The comparison between the recorded maximum response and the TGRF estimate confirms the reliability of the TGRF, providing slight overestimation of the maximum dynamic response.

Keywords: Thunderstorm outflow, Gust response factor, Monitored structure.

1. INTRODUCTION

Along with extra-tropical cyclones, thunderstorm outflows characterize the wind climate in Europe and provide wind gusts that are often larger than those associated with synoptic winds. Despite the destructive nature of thunderstorm outflows, engineers still lack a shared approach to properly design structures against such extreme wind conditions. In recent years, researchers have proposed different approaches for the prediction of the equivalent wind loading and maximum dynamic response of structures subjected to thunderstorms, pursuing a cost-efficient and safer structural design – i.e. (Kwon and Kareem, 2019; Solari et al., 2015). Among these, the Thunderstorm Gust Response Factor (TGRF) in its closed-form formulation (Roncallo and Tubino, 2023) has proved to be a valuable tool for the generalization of the Davenport gust response factor to thunderstorm winds when compared against time-domain solutions from full-scale thunderstorm records. However, a significant validation can be provided by the comparison with the dynamic response of full-scale monitored structures during thunderstorm outflows. In this framework, the GS-WinDyn research group at the University of Genoa has collected numerous data from a monitored lighting pole located in the La Spezia port of the Tyrrhenian Sea (Mengistu et al., 2023). This study aims to compare the maximum response from the monitoring system with the one estimated with the TGRF, assessing its reliability on a full-scale structure.

2. THUNDERSTORM GUST RESPONSE FACTOR

The maximum dynamic response is estimated employing the TGRF as follows:

$$x_{max} = G_x \bar{x}_{max} \tag{1}$$

where $\bar{x}_{max} = \rho \bar{v}^2_{max}(h) c_D a_1 / 2 m_1 (2\pi n_1)^2$ is the maximum mean part of the response (assumed static), being h the anemometer height assumed as reference, m_1 the first modal mass, n_1 the first modal frequency, c_D the drag coefficient (assumed constant along the height) and a_1 given by:

$$a_1 = \int_0^H \alpha^2(z) b(z) \psi_1(z)\, dz \tag{2}$$

with $b(z)$ the width of the structure, H its height and ψ_1 the first modal shape. In Eq. (1) G_x is the TGRF that generalizes the gust response factor approach from Davenport accounting for the transient dynamic response provided by thunderstorm outflows and reads (Roncallo et al., 2023):

$$G_x = 1 + I_v g_x (\nu_x T_{eq}) \sqrt{B^2 + R^2} \mathscr{C} \tag{3}$$

where I_v is the turbulence intensity, g_x the Davenport peak factor, ν_x the expected frequency of the response, T_{eq} the equivalent period, $\mathscr{C}$ the non-dimensional equivalent standard deviation, B and R the background and resonance factor, respectively. These last are available in closed-form – e.g. (Davenport, 1967; Solari, 1993), while a closed-form solution for T_{eq} and $\mathscr{C}$ was recently proposed and reads (Roncallo and Tubino, 2023):

$$\mathscr{C}^2 = \frac{\gamma^{*20}\left(\frac{T_{max}}{T_{r,0}} - 1\right) + \left(\Lambda^5 - \frac{5}{2}\Lambda^4\Phi + \frac{10}{3}\Lambda^3\Phi^2 - \frac{5}{2}\Lambda^2\Phi^3 + \Lambda\Phi^4 - \frac{1}{6}\Phi^5\right)}{\gamma^{*16}\left(\frac{T_{max}}{T_{r,0}} - 1\right) + \left(\Lambda^4 - 2\Lambda^3\Phi + 2\Lambda^2\Phi^2 - \Lambda\Phi^3 + \frac{1}{5}\Phi^4\right)} \tag{4}$$

$$T_{eq} = \frac{\gamma^{*16}(T_{max} - T_{r,0}) + T_{r,0}\left(\Lambda^4 - 2\Lambda^3\Phi + 2\Lambda^2\Phi^2 - \Lambda\Phi^3 + \frac{1}{5}\Phi^4\right)}{[\mathscr{C}^2]^4} \tag{5}$$

where γ^* is a measure of the intensity of the background wind; $T_{max} = 600$s, $\Lambda = \Phi + \gamma^{*4}$ and $\Phi = \beta(1 - \gamma^{*4})$, being $\beta = 1/[1 + 1/4\xi\tilde{T}]$, $\tilde{T} = T n_1$ with T the duration of the intense phase of the outflow; $T_{r,0} = (T_1 + T_N)$ with $T_1 = T/2$ and:

$$T_N = \begin{cases} T_2, & T_2 <= T_{max}/2 \\ T_{max}/2, & T_2 > T_{max}/2 \end{cases}, \qquad T_2 = T_1[1 + 1/(2\xi\tilde{T})] \tag{6}$$

3. FULL-SCALE WIND AND STRUCTURAL RESPONSE MEASUREMENT

The monitored structure is a tapered steel lighting pole with height $H = 16.6$ m and a polygonal hollow cross-section of width 528 mm at the base and 254 mm at the top. The pole is equipped with an anemometer for the measurement of the wind speed, located at $h = 21.7$ m, accelerometers, located at 10.5 and 16.0 m, and strain gauges, located respectively at 0.5 and 1.5 m, for the structural response detection (Mengistu et al., 2023). The sampling frequencies are 10 Hz for the anemometer, 100 Hz for the strain gauges, and 200 Hz for the accelerometers. Two thunderstorm events are selected for the study and the vertical profile of the mean wind speed is assumed from the literature according to the (Wood and Kwok, 1998) model. The drag coefficient is assumed constant over all the height of the structure and equal to its average value

estimated over the angle of attack (Mengistu et al., 2023), neglecting the presence of a ladder on the pole. The mechanical properties of the structure are calculated using operational modal analysis techniques. The first mode of vibration is found to be bending mode at a frequency of $n_1 = 0.75$ Hz while the structural damping estimation has shown some uncertainties, varying between 0.2% and 1% (Mengistu et al., 2023). The simultaneous measurement of wind speed and structural response during these events are used to validate the TGRF method. Since the validation is intended to be done using the top displacement of the structure, the strain registrations during these events are used to calculate the top displacement. The possibility of obtaining both the quasi-steady and fluctuating components of the top displacement from the strain records is crucial for the direct comparison of the peak displacement estimated from the TGRF.

4. RESULTS

The resulting maximum displacement at the top of the structure estimated through Eq. (1) is compared with the registered maximum displacement. In order to calculate the TGRF in Eq. (3), the parameters γ^* and T, as well as the turbulence intensity and integral length scale, are estimated from the recorded wind speed while the vertical profile is defined by tentatively fixing the height of the nose $z_m = 25$ m. Regarding the dynamic properties of the structure, damping ratios of 0.2%, 0.5% and 1% are considered to account for its uncertainty. Fig. 1 shows the time history of the registered resultant top displacement, compared with the calculated maximum displacement using the TGRS method represented by horizontal lines.

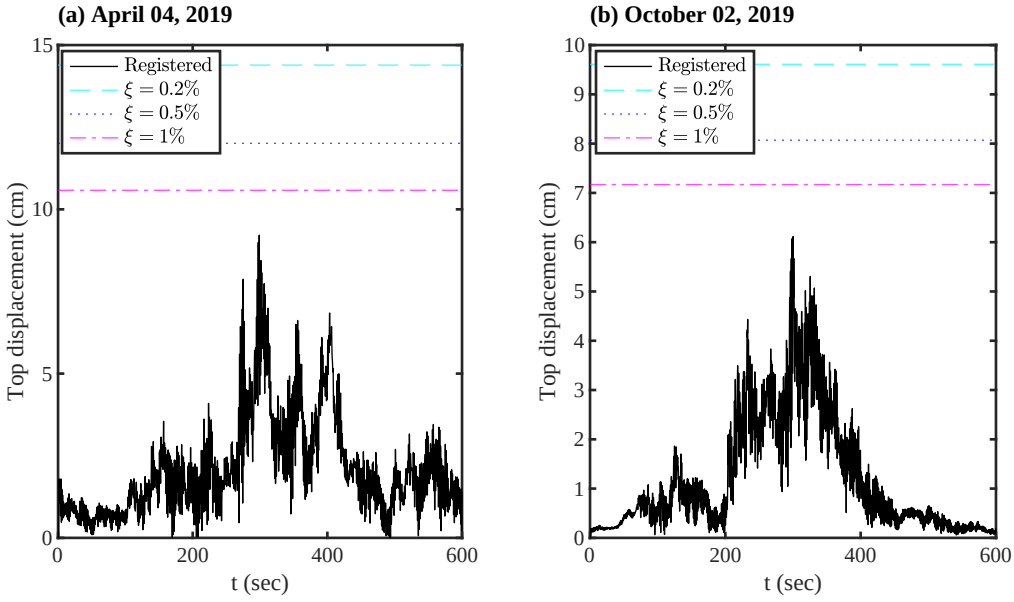

Figure 1. Comparison between the recorded top displacement and the maximum one estimated via TGRF for two thunderstorm cases: (a) 4th April 2019; (b) 2nd October 2019.

It can be observed that the maximum top displacement calculated using the TGRF method is higher than the registered top displacement, especially for low damping ratios. An estimate closer to the recorded value is obtained for higher values of the damping ratio. As previously pointed out by (Roncallo and Tubino, 2023), the overestimation resulting from the Davenport peak factor, especially for low damping ratios, significantly affects the estimate of the TGRF. Moreover, a certain degree of uncertainty is inherent in the estimate of the turbulence intensity (assumed constant with the height) and vertical profile, as well as in the aerodynamic drag

coefficient which does not account for the presence of the ladder. All considered, it can be stated that the TGRF gives a reliable estimate of the maximum response with some levels of conservativism.

5. CONCLUSIONS

In this study the TGRF technique is adopted to estimate the maximum response of a monitored lighting pole subjected to thunderstorm downburst and the results compared with the recorded response collected by the monitoring system. The wind speed parameters required for the application of the TGRF were estimated starting from the time-histories collected by the anemometer located on the structure while for the vertical profile a model from the literature is adopted. The comparison with the registered maximum response indicates that the TGRF method can predict the maximum response with some overestimations, mainly due to the conservatism of the Davenport peak factor. Nevertheless, accounting for the assumptions considered in the estimate of the TGRF, as well as the handiness of the closed-form solution, these results suggest that the TGRF can be a reliable and useful tool for engineers for practical design calculations.

ACKNOWLEDGEMENTS

This research is funded by the European Research Council (ERC) under the European Union's Horizon 2020 research and innovation program (grant agreement No. 741273) for the project THUNDERR - Detection, simulation, modelling and loading of thunderstorm outflows to design wind-safer and cost-efficient structures - supported by an Advanced Grant 2016.

REFERENCES

Davenport, A. G. (1967). Gust loading factors. Journal of the Structural Division 93, 11–34.

Kwon, D. K. and A. Kareem (2019). Towards codification of thunderstorm/downburst using gust front factor: Model-based and data-driven perspectives. Engineering Structures 199, 109608.

Mengistu, M. T., A. Orlando, and M. P. Repetto (2023). Wind and structural response monitoring of a lighting pole for the study of downburst effects on structures. Journal of Wind Engineering and Industrial Aerodynamics 240, 105447.

Roncallo, L., M. Gimondo, and F. Tubino (2023). Dynamic Response of Slender Vertical Structures Subjected to Thunderstorm Outflows. Applied Sciences 13, 11440.

Roncallo, L. and F. Tubino (2023). Thunderstorm gust response factor: A closed-form solution. Journal of Wind Engineering and Industrial Aerodynamics 240, 105487.

Solari, G. (1993). Gust buffeting II. Dynamic alongwind response. Journal of Structural Engineering 119, 383–398.

Solari, G., P. De Gaetano, and M. P. Repetto (2015). Thunderstorm response spectrum: Fundamentals and case study. Journal of Wind Engineering and Industrial Aerodynamics 143, 62–77.

Wood, G. S. and K. C. S. Kwok (1998). An empirically derived estimate for the mean velocity profile of a thunderstorm downburst. Proceedings of 7th Australian Wind Engineering Society Workshop. Auckland, Australia.

IN-VENTO 2024
International Conference of the Italian Association for Wind Engineering
Pisa, September 8th – 11th, 2024

Wind load simulations on bridge decks during a downburst

Luca Salvatori[a], Antonino Maria Marra[b], Mario De Stefano[b], Paolo Spinelli[a]

[a]*Department of Civil and Environmental Engineering, University of Florence, Florence, Italy, luca.salvatori@unifi.it, paolo@gpapartners.com*
[b]*Department of Architecture, University of Florence, Florence, Italy, antoninomaria.marra@unifi.it, mario.destefano@unifi.it*

SUMMARY:
An analytical model for estimating the wind loads caused by the passage of a downburst through bridge decks is proposed. The coefficients of heuristic shaping functions for the wind velocity are calibrated on field recordings and the model is completed by imposing mass conservation. Large angles of attack on the decks during the passage of downbursts with small-medium diameters are predicted, implying also a change in the aerodynamic design procedure of bridge decks, for which wind tunnel tests are commonly conducted only for angles of attack in the range of about $\pm 10°$. The aerodynamic coefficients of an airfoil and a bluff pseudo-rectangular section are used due to the absence in the literature of aerodynamic coefficients of bridge decks for very large angles of attack. Parametric simulations provide useful for the aerodynamic design of bridges, confirming the key role played by the vertical component of the velocity.

Keywords: Downbursts, Long-span bridges, Analytical model, Numerical simulations

1. INTRODUCTION

International codes and standards for wind loading on structures are based on traditional atmospheric boundary layer flows. They are modelled as stationary, ergodic, Gaussian processes with significant simplifications in their mathematical treatment (Davenport, 1961).

Several shreds of evidence in many parts of the world have shown that extreme events are produced by thunderstorms (Holmes, 1999; Letchford et al., 2002). They are small disturbances compared to extra-tropical cyclones but can generate strong winds through downbursts and tornadoes (Holmes, 2018). Limiting the discussion to downbursts, strong downdrafts that reach the ground (like a jet) are produced generating strong winds for a short time (5-10 min).

Downbursts show remarkably three-dimensional velocity fields, in which the wind direction and velocity show significant variations. The maximum velocity profile presents a maximum at 50-100 m over the ground. Hence, larger forces on low and mid-rise buildings are expected than in the case of boundary layer winds. Therefore, Codes and Standards should also account for thunderstorm downburst phenomena in defining the wind loads on structures. Nevertheless, just in recent years, microburst effects on civil structures captured the attention of the wind engineering community.

Vertical structures, such as low-rise buildings (Jesson et al., 2015), lattice transmission towers (Savory et al., 2001), telecommunication antenna masts and towers (Solari et al., 2017), high-rise buildings (Chen and Letchford, 2004), have been extensively studied while very limited research have been devoted to the thunderstorm downburst effects on long-span bridges (Hao and Wu, 2018).

For vertical structures, the simulation of the vertical component of the wind velocity in case of

downbursts is not required. Thus, the literature is mainly focused on the development of models for the maximum wind velocity profiles by considering the horizontal velocity components only (Holmes and Oliver, 2000; Wood et al., 2001). Conversely, for bridge decks, the vertical component combined with the horizontal one results in significant changes in the angle of attack. The issue of the critical role of the angle of attack in bridge response to downburst has been raised by Spinelli et al., 2023 where some specific considerations on the collapse of Polcevera Bridge in Genoa were reported. Thus, three-dimensional models able to simulate also the vertical components of the wind velocity field are necessary for estimating the response of horizontal structures, such as bridge decks.

This typology of models can be found in the aeronautical field to simulate approaches to landing and escape manoeuvres for aircraft (Abd-Elaal et al., 2013; Oseguera and Bowles, 1988; Vicroy, 1991; Wood et al., 2001).

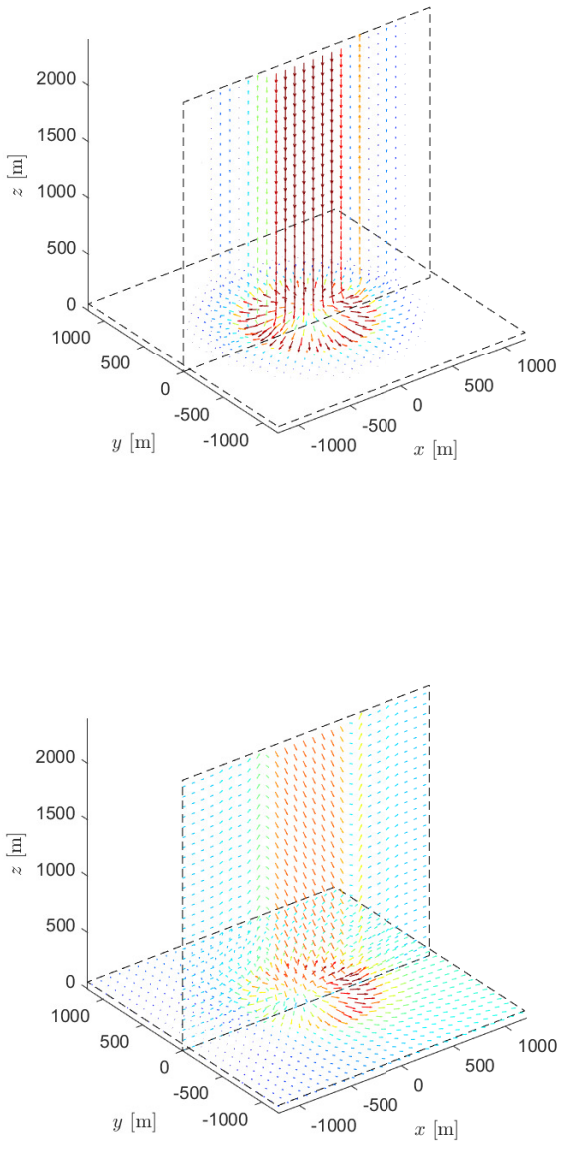

Figure 1. Three-dimensional velocity field of the simulated downbursts: stationary (top) and environmental-driven downbursts (bottom).

2. DOWNBURST MODEL AND SIMULATIONS

A new three-dimensional model is formulated by following the path traced by Oseguera and Bowles (Oseguera and Bowles, 1988), which is based on separated-variable radial and vertical modulations of the wind velocity components. The vertical and radial variations of the horizontal velocity component are defined in the new model as the best fit of the full-scale data including the local increase in velocity in the radial variation. The vertical and radial shape functions of the vertical wind velocities have been derived according to the mass conservation equation. More details on the proposed analytical model are reported by Salvatori et al., 2024. Three-dimensional representations of the velocity field for a stationary and an environmental-wind driven one are shown in Fig. 1.

The passage of the downburst produces a wind velocity field involving very large variations of the angles of attack at the typical bridge deck heights. The model has been applied to both the NACA 0015 wind and a pseudo-rectangular 3:1 cross-sections (Marra et al., 2024). The choice of such sections is due to the lack of aerodynamic coefficient measurements for bridge decks

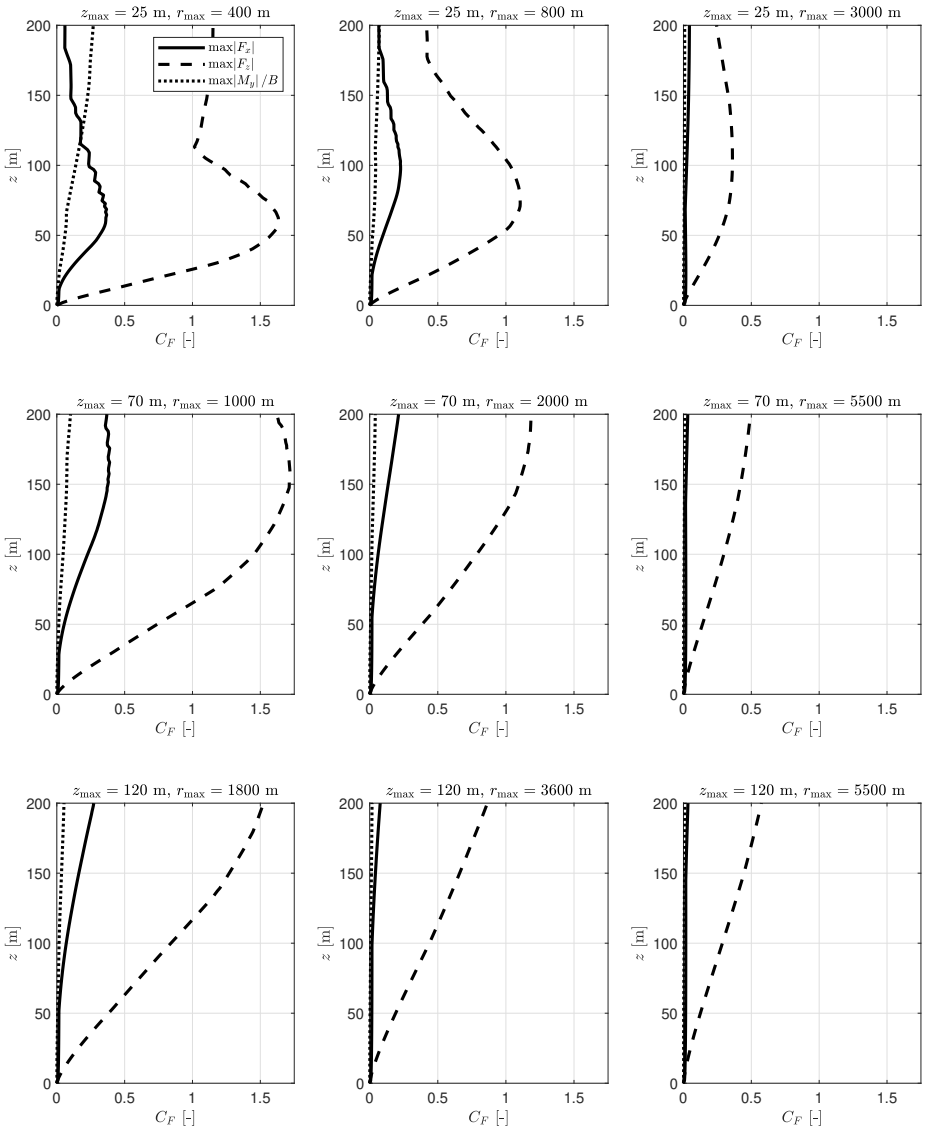

Figure 2. Peak forces varying the deck height for the NACA 0015 profile and different downbursts

at very large angles of attack in the literature. Although unrealistic for a bridge deck these cross-sections represent extreme behaviours, one very streamlined with low drag and large lift variations, the other much bluffer with high drag. Numerical simulations of the passage of a downburst through a bridge deck carried out. Fig. 2 shows the peak force coefficients on the bridge deck as a function of the height of the deck on the ground and for different downburst parameters.

3. CONCLUSIONS

The results of the present work highlight the importance of including the effects of downbursts in the aerodynamic design of bridges. It is also highlighted that the current range of angles of attack investigated in the wind tunnel tests for estimating the aerodynamic coefficients should be extended to supply the input data for downburst simulations. For conventional wind tunnel facilities, this requirement implies using a highly scaled sectional model. This is particularly crucial given the noticeable increase in the blockage ratio at large angles of attack, especially when studying streamlined bridge decks.

REFERENCES

Abd-Elaal, E.-S., J. E. Mills, and X. Ma (2013). An analytical model for simulating steady state flows of downburst. Journal of Wind Engineering and Industrial Aerodynamics 115, 53–64.

Chen, L. and C. Letchford (2004). Parametric study on the along-wind response of the CAARC building to downbursts in the time domain. Journal of wind engineering and industrial aerodynamics 92, 703–724.

Davenport, A. G. (1961). The application of statistical concepts to the wind loading of structures. Proceedings of the Institution of Civil Engineers 19, 449–472.

Hao, J. and T. Wu (2018). Downburst-induced transient response of a long-span bridge: A CFD-CSD-based hybrid approach. Journal of Wind Engineering and Industrial Aerodynamics 179, 273–286.

Holmes, J. (1999). Modeling of extreme thunderstorm winds for wind loading of structures and risk assessment. Proceedings of Wind Engineering into the 21st Century, Proc. of the 10th Intl. Conf. on Wind Eng. eds. A. Larsen et al., Denmark, 1409–1415.

Holmes, J. D. (2018). Wind loading of structures. CRC press.

Holmes, J. D. and S. Oliver (2000). An empirical model of a downburst. Engineering structures 22, 1167–1172.

Jesson, M., M. Sterling, C. Letchford, and M. Haines (2015). Aerodynamic forces on generic buildings subject to transient, downburst-type winds. Journal of wind engineering and industrial aerodynamics 137, 58–68.

Letchford, C., C Mans, and M. Chay (2002). Thunderstorms—their importance in wind engineering (a case for the next generation wind tunnel). Journal of Wind Engineering and Industrial Aerodynamics 90, 1415–1433.

Marra, A. M., B. Nicese, T. Massai, and G. Bartoli (2024). Wind loads on structural members of rack-supported warehouses. Thin-Walled Structures 196, 111458.

Oseguera, R. M. and R. L. Bowles (1988). A simple, analytic 3-dimensional downburst model based on boundary layer stagnation flow.

Salvatori, L., A. Marra, M. De Stefano, and P. Spinelli (2024). Downburst wind loading on bridge decks through an analytical model. submitted to Engineering Structures.

Savory, E., G. A. Parke, M. Zeinoddini, N. Toy, and P. Disney (2001). Modelling of tornado and microburst-induced wind loading and failure of a lattice transmission tower. Engineering Structures 23, 365–375.

Solari, G., D. Rainisio, and P. De Gaetano (2017). Hybrid simulation of thunderstorm outflows and wind-excited response of structures. Meccanica 52, 3197–3220.

Spinelli, P., A. M. Marra, and L. Salvatori (2023). Super-long-span bridges: wind-resistant design developments and open issues. Proceedings of Proceedings of the Institution of Civil Engineers-Bridge Engineering. Emerald Publishing Limited, 1–20.

Vicroy, D. D. (1991). A simple, analytical, axisymmetric microburst model for downdraft estimation. Vol. 104053. National Aeronautics and Space Administration, Langley Research Center.

Wood, G. S., K. C. Kwok, N. A. Motteram, and D. F. Fletcher (2001). Physical and numerical modelling of thunderstorm downbursts. Journal of Wind Engineering and Industrial Aerodynamics 89, 535–552.

IN-VENTO 2024
International Conference of the Italian Association for Wind Engineering
Pisa, September 8th – 11th, 2024

Thunderstorm-induced actions on CAARC building: wind tunnel studies

C. A. Sánchez[a,b], S. Torre[c], E. Ruffini[c], A. Bagnara[c], G. Piccardo[a], F. Tubino[a]

[a]*University of Genoa, Genoa, Italy, camila.aldereguasnchez@edu.unige.it, federica.tubino@unige.it, giuseppe.piccardo@unige.it*
[b]*Technological University of Havana "José A. Echevarría", Havana, Cuba*
[c]*NOVA Fluid Mechanics, London, United Kingdom, anna@novafluidmechanics.com, stefano.torre@novafluidmechanics.com, edoardo.ruffini@novafluidmechanics.com*

SUMMARY:
Thunderstorms pose significant risks, including strong winds which have different properties with respect to classical synoptic events, which can negatively impact buildings. Understanding how these events affect structures through wind tunnel tests may enable engineers to develop better designs and construction techniques to enhance resilience and mitigate damage. In this work, the effects of thunderstorms on tall buildings are analyzed experimentally based on the simulation of nose-shaped and standard boundary layer profiles in the Giovanni Solari Wind Tunnel. The High-Frequency Force Balance technique is used to assess the wind loads on a benchmark structure, namely the CAARC building. The study aims to compare the aerodynamic characteristics and wind-induced response between synoptic and thunderstorm events.

Keywords: CAARC, thunderstorm-induced actions, wind tunnel testing

1. INTRODUCTION

Thunderstorm-downburst typically produces very strong radial wind velocities at around 50-100 meters above the ground (Fujita, 1985). This phenomenon has different features in comparison with synoptic events, including a typical nose-shaped mean wind speed profile, and non-stationary characteristics in time intervals of 10 minutes to 1 hour (Zhang et al., 2018). Thunderstorm velocity can be described by the classical decomposition rule as the sum of a slowly varying mean wind velocity and rapidly varying turbulent fluctuation (Canepa et al., 2020; Zhang et al., 2018). Regarding the variation with the height of downburst outflow, different models have been proposed in the literature (e.g., Abd-Elaal et al., 2013; Wood and Kwok, 1998) that depend mainly on the height of the nose. A consolidated model for the turbulence intensity profile is still not available: in most cases, full-scale measurements in areas close to the sea have provided low values of turbulence intensity (Solari et al., 2015); however, higher values have been measured in some cases as well (Choi, 2000). Despite the efforts in the study of thunderstorms, a codified approach that allows to model their actions on structures has not been developed. Therefore, this type of phenomenon has captured the interest of scientists and engineers due to its complex dynamics and potential impact on urban environments. As urbanization continues to reshape landscapes worldwide, the proliferation of tall buildings is unmistakable, and understanding how thunderstorms interact with tall buildings is imperative for mitigating risks associated with severe weather events.

Wind tunnels represent a fundamental technique to study the unique aerodynamic features of tall buildings (Irwin, 2009). The most common types of wind tunnels are Atmospheric Boundary Layer Wind Tunnels, but they lack the ability to simulate spatial and temporal variation of thunderstorms-downburst. However, the worst-case mean wind speed profile and, in some

cases, the non-stationary flow can be reproduce with some specific techniques, like, redirecting the horizontal flow with an additional device (e.g., Aldereguía Sánchez et al., 2023) or regulating the velocity of each fan in the case of multiple fan wind tunnels (e.g., Li et al., 2023). Aldereguía Sánchez et al., 2023 adopted a simple grid composed by square opening modules that allowed the simulation of the thunderstorm mean wind speed profile with different heights of the nose while neglecting the non-stationary characteristics of the incoming flow.

The Commonwealth Advisory Aeronautical Research Council (CAARC) building is a standard tall building model used as a benchmark for assessing results obtained from various wind tunnel measurements and numerical simulations (Melbourne, 1980). Li et al., 2023 carried out experiments on the CAARC building under synoptic and thunderstorm profiles in a multiple fan wind tunnel. Main results shown that the estimated building response was almost generally lower in the thunderstorm field when compared with synoptic case.

This study, conducted within the ERIES project Thunderstorm Loading on Tall Buildings (TLTB), aims to conduct experimental tests in a classic Boundary Layer Wind Tunnel (BLWT) in order to compare wind actions induced by thunderstorms and synoptic events on the CAARC building. A critical thunderstorm mean wind speed profile is considered with low and high turbulence intensity levels while neglecting non-stationary characteristics. Drawing from prior research (Aldereguía Sánchez et al., 2023), the nose-shaped mean wind speed profile is replicated using a passive device. The analysis includes the assessment of the force coefficients and wind loads.

2. WIND TUNNEL EXPERIMENTS

The experiments were carried out at the Giovanni Solari Wind Tunnel at the University of Genoa. Initially, the mean wind speed and turbulence intensity profiles were simulated for the different wind fields. Once the wind properties were correctly replicated, the High-Frequency Force Balance (HFFB) technique was used in order to evaluate the wind loading on the CAARC building.

2.1. Wind Properties

Aldereguía Sánchez et al., 2023 investigated the feasibility of using a passive device, such as a specially designed grid, to replicate the nose-shaped mean wind speed profile within a BLWT facility. The results indicated a good agreement between the measured and desired mean wind speed profiles based on the Wood and Kwok (1998) model, along with an acceptable turbulence intensity level. Furthermore, the research provided different configurations of the modules to obtain a wide range of values for the height of the nose, which could hold significance for various types of structures, particularly tall buildings. Here, a full-scale nose height of 60 meters above the ground was adopted. In terms of turbulence intensity, two different levels within the range of 10% (TS1) and 14% (TS2) were considered, acknowledging the uncertainty associated with this property. Once the wind properties of thunderstorms were simulated, synoptic profiles were defined to enable comparison between the two phenomena. EN1991-1-4 (2004) was used to obtain the mean wind speed and turbulence intensity considering roughness lengths of 0.003 m (ABL1) and 0.05 m (ABL2) associated with lower and higher turbulence levels, respectively. Fig. 1 shows the target and measured profiles normalized to maximum velocity, i.e. at the height of the nose in the case of thunderstorm profiles and at the top of the building in the case of synoptic profiles.

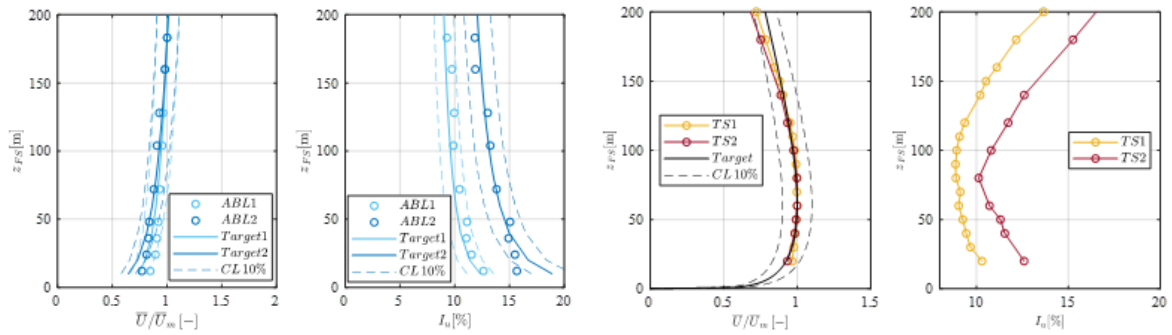

(a) (b)

Figure 1. Mean wind speed and turbulence intensity profiles, a) synoptic, b) thunderstorm.

2.2. Case Study

The measurements were conducted on the CAARC Standard Tall Building model, characterized by a simple prismatic shape with full-scale dimensions of 30.48 x 45.72 x 183.88 m. A model scale of 1:400 was adopted, and the tests were performed in isolation. The shape of the building was made using lightweight foam, internally supported by high-modulus carbon fiber "sting" to provide maximum stiffness, achieving a frequency of 115Hz. Indeed, this configuration ensures that the frequencies of the force balance model are as high as possible to prevent any interference with the frequency spectrum under full-scale conditions. The model was rigidly fixed to an aluminum base plate through the spine to enable connection to the high-frequency response force balance.

3. PRELIMINARY RESULTS AND ONGOING WORK

The fluctuating wind loads were measured in terms of the shear forces, bending moments, and torque (6 components: F_x, F_y, F_z, M_x, M_y & M_z) at ground level for 18 wind directions (10° increments), considering the structural symmetry. Base mean and fluctuating force coefficients were obtained as well as mean, peak static, and dynamic wind loads. Mean force coefficients are normalized by the maximum mean wind speeds for each profile:

$$C_{F,i} = \frac{F_i}{1/2\rho U_m^2 A_{ref}} \tag{1}$$

where i is the component of the force (x, y, z), ρ is the air density, U_m is the maximum mean wind speed at the building height and the nose height for synoptic events and thunderstorms, respectively, A_{ref} is the reference area.

The coordinate system aligns the x-axis with the longer face of the building and the y-axis with the shorter face. Preliminary results show that the mean force coefficients at the base (Fig. 2) between the analyzed flow cases are directly related to the shape of the mean wind speed profiles. In the case of the mean coefficients for the y-component higher differences are observed, specifically for 90°, which is coincident with the along wind of the shorter face of the building. This shows that different along-wind forces may appear from variations in building depth/width ratios and velocity profile shapes. The ongoing work involves evaluating peak static and peak dynamic forces and comparing them with results from the literature.

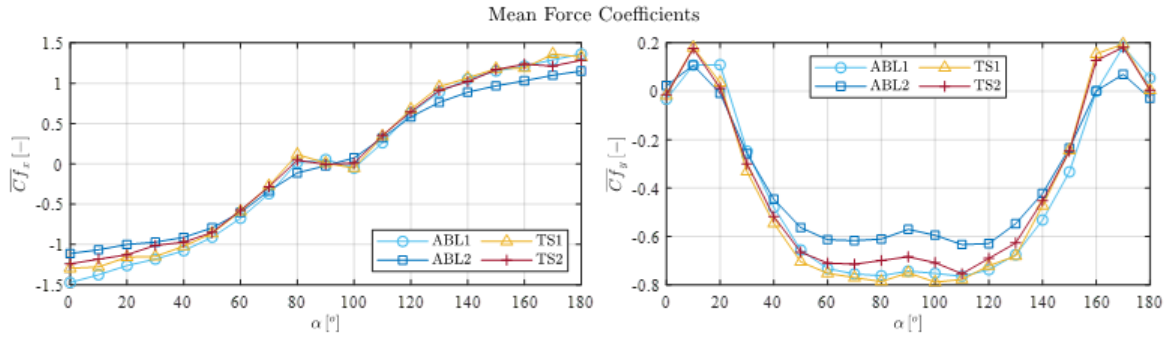

(a) (b)

Figure 2. Base mean force coefficients, a) C_{Fx}, b) C_{Fy}.

ACKNOWLEDGEMENTS

This work is supported by the Engineering Research Infrastructures for European Synergies (ERIES) project (www.eries.eu), which has received funding from the European Union's Horizon Europe Framework Programme under Grant Agreement No. 101058684

REFERENCES

Abd-Elaal, E.-S., Mills, J. E., and Ma, X. (2013). An analytical model for simulating steady state flows of downburst. J. Wind Eng. Ind. Aerod. 115, 53–64.

Aldereguía Sánchez, C., Tubino, F., Bagnara, A., and Piccardo, G. (2023). Experimental Simulation of Thunderstorm Profiles in an Atmospheric Boundary Layer Wind Tunnel. Applied Sciences 13, 8064.

Canepa, F., Burlando, M., and Solari, G. (2020). Vertical profile characteristics of thunderstorm outflows. J. Wind Eng. Ind. Aerod. 206, 104332.

Choi, E. C. C. (2000). Wind characteristics of tropical thunderstorms. J. Wind Eng. Ind. Aerod. 84, 215–226.

Fujita, T. T. (1985). The downburst: Microburst and macroburst. In: SMRP, University of Chicago.

Irwin, P. A (2009). Wind engineering challenges of the new generation of super-tall buildings. J. Wind Eng. Ind. Aerod. 97, 328–334.

Li, Y., Mason, M. S., Bin, H.-Y., and Lo, Y.-L. (2023). Aerodynamic characteristics of a high-rise building in a steady thunderstorm outflow-like flow field. J. Wind Eng. Ind. Aerod. 240, 105501.

Melbourne, W. H. (1980). Comparison of measurements on the CAARC standard tall building model in simulated model wind flows. J. Wind Eng. Ind. Aerod. 6, 73–88.

Solari, G., Burlando, M., De Gaetano, P., and Repetto, M. P. (2015). Characteristics of thunderstorms relevant to the wind loading of structures. Wind Struct. 20, 763–791.

Wood, G. S. and Kwok, K. C. S. (1998). An empirically derived estimate for the mean velocity profile of a thunderstorm downburst. Proceedings of Proceedings of the 7th Australian Wind Engineering Society Workshop, Auckland.

Zhang, S., Solari, G., Yang, Q., and Repetto, M. P. (2018). Extreme wind speed distribution in a mixed wind climate. J. Wind Eng. Ind. Aerod. 176, 239–253.

IN-VENTO 2024
International Conference of the Italian Association for Wind Engineering
Pisa, September 8th – 11th, 2024

Some considerations on the design of a novel, large-scale testing facility (NEWRITE) for non-stationary wind loads

Partha P. Sarkar[a], Alice Alipour[a], Luca Caracoglia[b], Nigel B. Kaye[c], David O. Prevatt[d], Anupam Sharma[a], R. Paneer Selvam[e], Guirong Yan[f], Delong Zuo[g]

[a]*Iowa State University, Ames, Iowa, USA, ppsarkar@iastate.edu, alipour@iastate.edu, sharma@iastate.edu*
[b]*Visiting Professor, University of Trento, Italy (permanent address: Northeastern Univ., Boston, Massachusetts, USA), lucac@coe.neu.edu*
[c]*Clemson University, Clemson, South Carolina, USA, nbkaye@clemson.edu*
[d]*University of Florida, Gainesville, Florida, USA, dprev@ce.ufl.edu*
[e]*University of Arkansas, Fayetteville, Arkansas, USA, rps@uark.edu*
[f]*Missouri University of Science and Technology, Rolla, Missouri, USA, yang@mst.edu*
[g]*Texas Tech University, Lubbock, Texas, USA, Delong.Zuo@ttu.edu*

SUMMARY:
The "National Testing Facility for Enhancing Wind Resiliency for Infrastructure in Tornado-Downburst-Gust Front Events" or NEWRITE is a large-scale facility, university-based that is currently under preliminary design. This facility plans to simulate realistic wind fields with speeds up to 100 m/s mph in non-synoptic wind (NSW) events (tornadoes, downbursts and gust fronts). It will enable physical testing of NSW loading, structural response and damaging effects on civil and defense infrastructures at mid-to-full model scales, between 1 : 10 and 1 : 1. This summary will briefly outline the preliminary conceptual design of the facility and describe the current research status. A multi-university team was assembled to complete the research tasks.

Keywords: Tornadoes, thunderstorms, gust fonts, wind load simulators, large-scale facilities, structural resilience

1. INTRODUCTION

NSW events such as tornadoes (McDonald, 2001), downbursts (Fujita, 1985, 1986), and gust fronts (Cook, 2023) cause billions of dollars of property damage and numerous fatalities (>100 on average) and injuries in the United States of America, annually. It has been found (Lombardo and Zickar, 2019) that over 80% of annual maximum wind speeds over the central and southeast USA are caused by convective storms. Although the destructive nature of tornadoes is well known, the threat from thunderstorm downbursts (Burlando et al., 2017; Mengistu et al., 2023) and gust fronts (Kwon et al., 2012) is likely greater than records indicate. The "tornado alley" — a region in the Central United States that extends from northern Texas to Minnesota and eastern Colorado to western Ohio — is particularly impacted.

Economic losses due to damage to infrastructures and the number of fatalities will only increase in the future with growing urbanization and increased intensification/frequency of such windstorms because of future climate variability. For example, it has been noted (Gensini and Brooks, 2018) that the tornado alley is shifting eastward as tornado frequencies increase in the Gulf States and Mississippi Valley while decreasing in the western Plains. In addition, climate modelers (Ashley et al., 2023) have demonstrated that supercell thunderstorms that produce both the strongest tornadoes and a threat of damaging synoptic, atmospheric boundary layer (straight-line) winds will increase in frequency and intensity, especially in areas east of

traditional tornado alley. Such a shift increases the threat of damage and fatalities due to an increased population density and more built structures farther east.

As evidenced in the past, major tornadoes with an intensity of EF3 or greater (60 m/s or greater, 3-s gust) have struck large USA cities causing multiple fatalities and significant damages to residential and engineered structures, e.g., New Orleans (2017, 39 injured), Moore (2013, 24 fatalities, 212 injured), Joplin, Tuscaloosa (2011, 161 fatalities, 1300+ injured), and Oklahoma City (1999, 41 fatalities, 675 injured). Structural damages and losses from downbursts and gust fronts are also significant because of the larger areas that can be impacted by these straight-line winds (e.g., Burlando et al., 2017). For example, the "derecho" (a large-scale windstorm) that struck the central USA (over 1100 km from Iowa to Ohio states) on August 10, 2020, caused enormous property loss (12 billion US dollars, NCEI (2023)) and was the costliest single thunderstorm event in United States history with greater damage than any single tornado.

2. BRIEF DESCRIPTION OF THE FACILITY

The proposed NEWRITE will be capable of generating wind flow fields with wind speeds (3-s gust) in EF1 to EF5 tornadoes (38-100 m/s), moderately intense downbursts (36-45 m/s) and most intense gust fronts (36-45 m/s). It will enable investigations of the impacts of NSW hazards on civil infrastructures at large enough length scales (1:10 or larger) and velocity scales (1:2 or larger) to study near-ground wind fields, wind loading, wind-borne debris impact, and structural-damage mechanisms (failure modes, component stresses). NEWRITE will be unique and will enable research and testing beyond the capabilities of the world's current state-of-the-art tornado/downburst simulation facilities. This capability will, in turn, allow the study of mitigation and adaptation strategies to minimize the impact of NSW events on the built environment and improve the resiliency of infrastructure, resulting in better sustainability and overall quality of life for communities.

The velocity fields in NSWs are qualitatively different from those of straight-line winds. A tornado is a translating vortex with significant tangential and vertical winds and suction in its core. The most intense tornadoes (EF3-EF5, McDonald (2001)) can produce wind speeds (3-s gust) of 60 to 100 m/s and greater at 33 ft (10 m) ground elevation. Micro-bursts are intense downbursts (400-4000 m in diameter) characterized by a strong, localized down-flow and an outburst of strong winds of up to 76 m/s mph (3-s gust) near the ground surface (Fujita, 1986).

Table 1. Parameter comparison of three existing tornado simulators in North America

	Atmospheric range	ISU[(1)]	VorTECH[(2)]	WindEEE[(3)]
Core diameter [m]	(EF 3-4) 250-440	0.2-1.06	0.08-1.8	0.6 to 1.2 (Mode A) 2.4 (Mode B)
Max. horizontal wind speed, MHWS [m/s]	(EF3) 73.8 (3s) (EF4) 89 (3s)	12.5 at $1/3$ power	15	16 (Mode A) 7.5 (Mode B)
Elevation to MHWS [m]	3 to 10	0.025-0.050	0.025-0.060	N/A
Aspect ratio	0.2-1.0	0.25-1.68	0.50-0.85	0.35-1.0
Swirl ratio	0.05-2	0.08-1.14	0.17-1.8	0.35-1.0
Max. Reynolds number	$10^9 - 10^{11}$	3×10^5	6×10^5	7.5×10^6
Translation speed [m/s]	2-18	0.6	1.5	2.0
Geometric scale		1/75 to 1/150	1/100 to 1/200	1/150 (Mode A) 1/50 (Mode B)
Velocity scale		1/3.5 to 1/6.9	variable	1/3 (Mode A) 1/6 (Mode B)

[Notes: (1) Haan et al. (2008), (2) Tang et al. (2016), (3) Hangan (2014)]

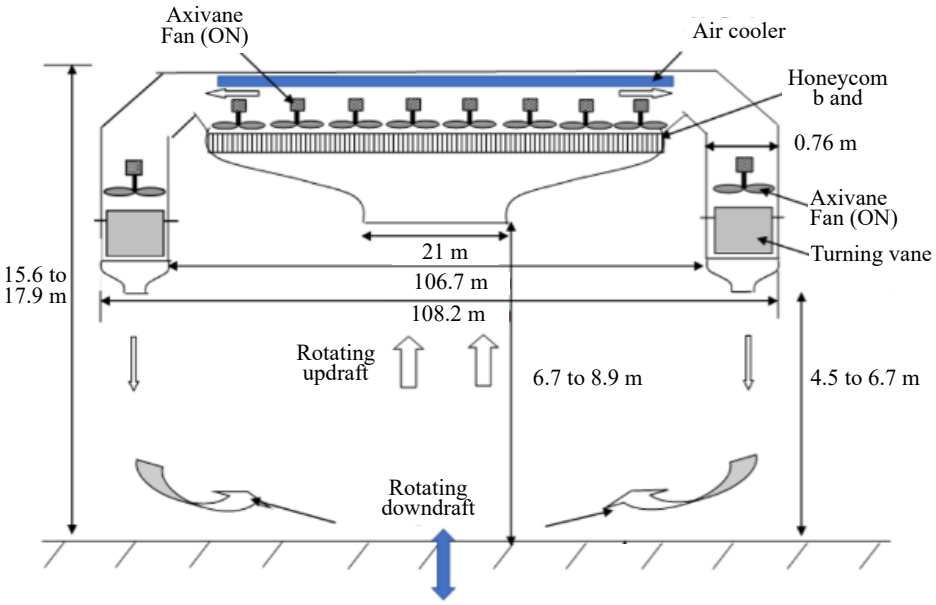

Figure 1. NEWRITE prototype concept (tornado mode) [dimensions indicative only]

Gust fronts cause strong and accelerated wind flow near the ground that is coherent over large structural spans. NSWs have non-stationary characteristics with a strong vertical wind component. They cause structural loading that is transient in nature, and the atmospheric pressure changes associated with them produce additional loading (e.g., Le and Caracoglia, 2021). To address the need for understanding the wind effects on structures in these NSW events, several laboratories have been built in North America (Table 1). The envisioned NEWRITE is potentially transformative, just like its predecessors (Haan et al., 2008; Hangan, 2014; Tang et al., 2016).

The design will allow the study of NWS phenomena at model scales and large-scale testing of civil infrastructure, and to test:
(a) realistic wind fields and wind loads on structures,

(b) larger models and higher wind speeds minimize Reynolds number mismatch,

(c) structures with large footprint (e.g., critical facilities, hospitals) and heights (e.g., towers),

(d) individual structures at larger scales (e.g., single-family residential buildings) to permit damage and failure study,

(e) wind-borne debris impacts, failures, effects on wind loads by changes in internal pressure,

(f) mitigation measures using improved structural and aerodynamic designs, and new standards.

The facility will collect near-ground wind speed and wind load data for validation. Specialized configurations might be considered for developing industry standards for buildings and construction.

Fig. 1 illustrates one of the preliminary concept ideas of the facility operating in a tornado mode. Dimensions are indicative only. Other operational modes will include thunderstorm micro-burst and gust front. The conceptual idea will be further refined during the execution of this four-year project.

3. CONCLUSIONS

The presentation will introduce the research team, the main study objectives and more details about the current state of the research.

ACKNOWLEDGEMENTS

This work was supported in part by the National Science Foundation (NSF) of the USA under grant CMMI-2330150. Any comments, conclusions, opinions or recommendations are those of the authors and do not necessarily reflect the views of the NSF.

REFERENCES

Ashley, W. S., A. M. Haberlie, and V. A. Gensini (2023). The future of supercells in the United States. Bulletin of the American Meteorological Society 104, E1 –E21.

Burlando, M., D. Romanić, G. Solari, H. Hangan, and S. Zhang (2017). Field data analysis and weather scenario of a downburst event in Livorno, Italy, on 1 October 2012. Mon. Weather Rev. 145, 3507–3527.

Cook, N. J. (2023). Automated classification of gust events in the contiguous USA. Journal of Wind Engineering and Industrial Aerodynamics 234, 105330.

Fujita, T. T. (1985). The Downburst: Microburst and Macroburst. ISBN 9996689220. University of Chicago, Illinois, USA.

— (1986). DFW Microburst on August 2, 1985. ISBN 9996689220. University of Chicago, Illinois, USA.

Gensini, V. A. and H. E. Brooks (2018). Spatial trends in United States tornado frequency. NPJ Climate and Atmospheric Science 1, 38.

Haan, F. L., P. P. Sarkar, and W. A. Gallus (2008). Design, construction and performance of a large tornado simulator for wind engineering applications. Engineering Structures 30, 1146–1159.

Hangan, H. (2014). The Wind Engineering Energy and Environment (WindEEE) Dome at Western University, Canada. Wind Engineers, JAWE 39, 350–351.

Kwon, D. K., A. Kareem, and K. Butler (2012). Gust-front loading effects on wind turbine tower systems. Journal of Wind Engineering and Industrial Aerodynamics 104-106. 13th International Conference on Wind Engineering, 109–115.

Le, V. and L. Caracoglia (2021). Life-cycle cost assessment of vertical structures under nonstationary winds: Downburst vs. tornado loads. Engineering Structures 243, 112515.

Lombardo, F. T. and A. S. Zickar (2019). Characteristics of measured extreme thunderstorm near-surface wind gusts in the United States. Journal of Wind Engineering and Industrial Aerodynamics 193, 103961.

McDonald, J. R. (2001). T. Theodore Fujita: his contribution to tornado knowledge through damage documentation and the Fujita Scale. Bulletin of the American Meteorological Society 82, 63 –72.

Mengistu, M. T., A. Orlando, and M. P. Repetto (2023). Wind and structural response monitoring of a lighting pole for the study of downburst effects on structures. Journal of Wind Engineering and Industrial Aerodynamics 240, 105447.

NCEI (2023). *Billion-dollar weather and climate disasters*. { https://www.ncei.noaa.gov/access/billions/state-summary/US }. Accessed: February 24, 2024.

Tang, Z., C. Feng, L. Wu, D. Zuo, and D. James (2016). Simulations of tornado-like vortices in a large-scale Ward-type tornado simulator. Proceedings of 8th International Colloquium on Bluff Body Aerodynamics and Applications. CD-ROM. Boston, Massachusetts, USA.

IN-VENTO 2024
International Conference of the Italian Association for Wind Engineering
Pisa, September 8th – 11th, 2024

Fluid-structure interaction simulations using open-source software couplers

Leonardo Sciarretta[1], Luigi Manes[1], Mao Xu[1], Luca Patruno[1], Stefano de Miranda[1]

[1] *University of Bologna, Bologna, Italy, leonardo.sciarretta2@unibo.it*

SUMMARY:
Problems involving Fluid-Structure Interaction, FSI, are extremely common in Wind Engineering. In the majority of the cases, it is possible to study such phenomena relying on simplified formulations, which can be calibrated based on tests performed in forced/free vibrations on sectional models. However, it is sometimes necessary to fully take into account the structure deformability. In this contribution, we describe the utilization of the open-source coupling platform preCICE in order to study the Vortex-Induced Vibrations, VIVs, of a stack characterized by square cross-section. Results are compared to those obtained in Wind Tunnel Tests adopting an aeroelastic model, showing reasonable agreement.

Keywords: FSI aeroelasticity, Computational Wind Engineering, preCICE.

1. INTRODUCTION

As it is well-known, aeroelasticity, the two-ways interaction between the fluid and the structural motion, is an essential aspect, which need to be accounted for in the wind loading and/or stability assessment of numerous light and flexible structures.

Classically, in order to study Fluid-Structure Interaction problems, FSI, Wind Tunnel Tests, WTT, are adopted. When possible, the assessment is performed relying on Reduced Order Models, ROMs, able to approximate the interaction between the fluid and the structure and which can be calibrated based on the response of sectional models to forced and/or free vibrations. Examples of such models are, for instance, those proposed in (Barni et al., 2021, 2022; Chen and Kareem, 2003) for motion-induced loads and those described in (Tamura, 2020) for Vortex-Induced Vibrations, VIV. Such way of proceeding is extremely convenient, and has the notable advantage to often allow for a deep understanding of the main phenomena which drive the interaction. However, the approach can fall short in numerous conditions such as, between others: difficulties in setting up a reliable ROM, impossibility to apply the strip assumption due to rapidly varying sections, non-uniform flows, often produced by aerodynamic interference and tip-effects. In all such cases, the use of a full-aeroelastic model might be required.

The considerations above, presented for the case of WTT, hold true not only for WTT but also for numerical simulations based on Computational Fluid Dynamics, CFD. In such context, the use of sectional models also has the advantage to allow for substantial savings in terms of computational time, with respect to full-aeroelastic models. Given the well-known inherent difficulties found in performing accurate Computational Fluid Dynamics simulations (Bruno et al., 2023), it is not surprising that the majority of the efforts found in the literature regarding the simulation of aeroelastic phenomena in the field of Wind Engineering focuses on sectional models (see for instance Álvarez et al., 2019; Li et al., 2021; Wang and Chen, 2022).

In this contribution, we present the experience gained by the authors in the setup of numerical

simulations using full-aeroelastic models adopting the open-source software coupling platform preCICE. In particular, OpenFOAM is coupled with the software CalculiX, in order to solve the fluid and the structural motion, respectively. Simulations are performed in order to reproduce VIVs of a stack, characterized by square cross-section, for which aeroelastic tests performed in WTT are available.

2. SOFTWARE COUPLERS: PRECICE

In the context of CFD simulations, FSI can be tackled with two different approaches, denoted as monolitic and partitioned.

As regards the first one (monolitic), the approach requires the resolution of only one set of equations encompassing the fluid and solid equations. Following such an approach a specialized software, able to solve for both the fluid and the solid motion is required. A clear disadvantage of such an approach is that it does not allow to use available software, specialized for the treatment of only the fluid or the solid part.

As regards the second approach (partitioned), it is based on the use of two solvers, one for the fluid and one for the solid parts. The two software exchange data regarding the interface between the fluid and the solid parts, with fluid pressures and shearing stresses acting as forcing terms on the solid part, and velocities of the solid wet surface imposed as boundary conditions for the fluid motion problem. Such an approach allows for the reuse of existing, well-validated software, and it is thus usually preferred in applications.

The coupling platform preCICE (https://precice.org/) is an open-source platform for multi-physics problems based on a partitioned coupling approach. The platform allows for the coupling of numerous open-source programs, including OpenFOAM and CalculiX, used in the following as fluid and solid solvers, respectively.

3. CASE SETUP

As anticipated, the object of this study is a stack of prismatic shape. The stack is characterized by an height, H, equal to 1.4 m, a side length, B, equal to 0.163 m, and a mass of 7 kg fixed to the wind tunnel floor, for which wind tunnel results for an aeroelastic model are reported in (Dongmei et al., 2019).

In the numerical model, for the purpose of a first validation of the coupling strategy, we consider for the fluid part the mesh reported in Fig. 1, which has a total of 1.4 M cells and a characteristic size in the proximity of the stack of $B/10$. A smooth inflow condition is applied at the inflow in agreement with the WTT setup while, wall conditions are applied on all sides, while a pressure outlet is applied at the outflow. As regard numerical schemes, linear schemes are adopted for all terms a part from nonlinear convective terms, for which LUST is employed. Time-integration is obtained relying on the Crank-Nicolson scheme with a non-dimensional time step equal to $dt \cdot U/B = 0.02$, leading to a maximum Courant number equal to 0.55. Simulations are performed adopting the well-known k-equation LES model.

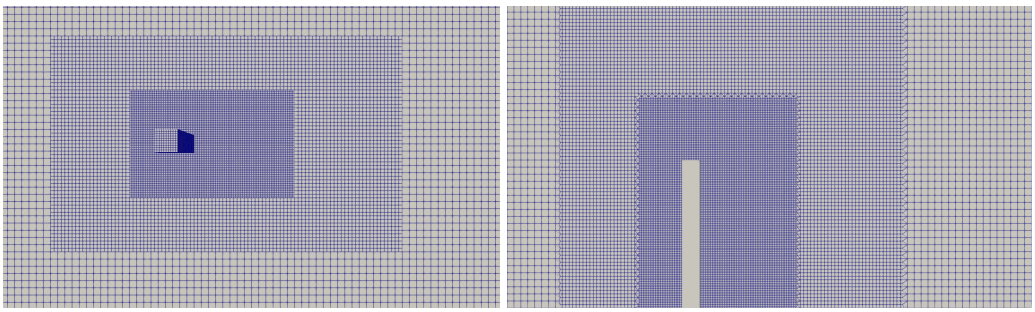

(a) (b)

Figure 1. Overview of the mesh adopted for the fluid part: (a) top view and (b) section.

As regards the solid part, the model consists of shell elements, calibrated in order to reproduce the mass and mode shapes which characterized the WT model (only the first three mode shapes were considered). A summary of the modal properties comparison between the WT and the numerical model is reported in Tab. 1. Damping has been assumed to be equal to 0.4%, in agreement with that measured on the aeroelastic WTT model.

Table 1. Modal parameters of the solid model and experimental model.

Mode	Solid model	Exp
1^{st} (along y axis) [Hz]	5.7	5.54
2^{st} (along x axis) [Hz]	6.5	6.44
3^{st} (around z axis) [Hz]	11.8	11.74

4. RESULTS

Firstly, the model has been tested in static condition without activating the two-way coupling. Figure 2 (a) provides an overview of the main vortical structures in the proximity of the stack. The Strouhal number, based on the dominant frequency of the transverse aerodynamic force has been evaluated to be 0.106, in very good agreement with WT measurements. Subsequently, the body has been allowed to move and subjected to a steady inflow velocity. Different inflow velocity have been tested spanning the range in the proximity of the lock-in condition. Fig. 2 (b) shows the trajectory of the displacement at the top of the model at the critical velocity (U=8.5 m/s). It can be seen that in the proximity of the lock.in velocity the across-wind vibration becomes dominant and the amplitude is significantly increased. Figure 2 (c) shows the standard deviation of the transverse wind displacement, σ_y as a function of the inflow velocity. As it can be seen, a reasonable agreement is obtained in terms of lock-in range, as well as in the overall amplitude of the response at lock-in, despite an overestimation of the response. Simulations resulted to be approximately twice as costly, in terms of cumputational time, with respect to static conditions.

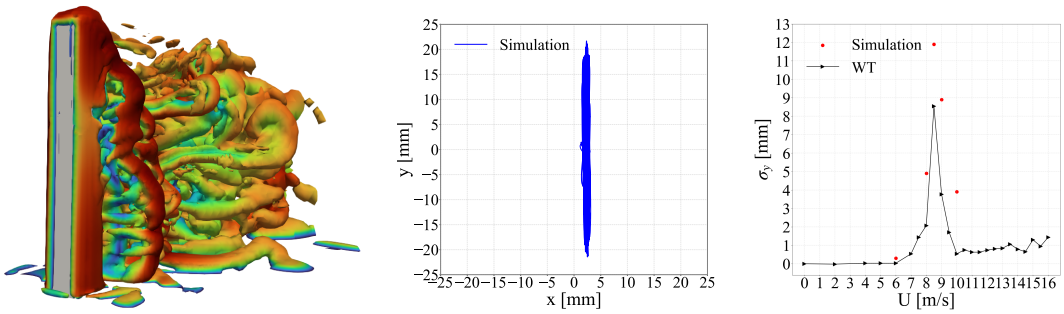

(a) (b) (c)

Figure 2. Simulation results: (a) overview of the vortical structures in the body proximity, Q, (Q=100), (b) orbit of the cross wind displacement at the top of the model with U=8.5 m/s and (c) standard deviation of the cross-wind displacement.

5. CONCLUSIONS

In this contribution, the use of the open-source coupling platform preCICE for Wind Engineering related applications has been investigated. The work-flow is particularly attractive as it allows to use well-established tools such as OpenFOAM to perform potentially complex FSI simulations. The proposed analyses analyzed the cross-wind vibration of a prismatic stack, showing reasonably good agrement with available full-aeroelastic wind tunnel tests. It is expected that further improvements can be obtained by considering finer computational grids. The performed simulations, as expected, highlighted a notable increase of the computational costs with respect to the fixed obstacle, corresponding to approximately a factor 2 for the present model. Despite such shortcomings, preCICE appears to be a potentially interesting tool in the context of Wind Engineering due to its flexibility and modularity.

REFERENCES

Álvarez, A., F Nieto, D. Nguyen, J. Owen, and S. Hernández (2019). 3D LES simulations of a static and vertically free-to-oscillate 4: 1 rectangular cylinder: Effects of the grid resolution. Journal of Wind Engineering and Industrial Aerodynamics 192, 31–44.

Barni, N., O. Øiseth, and C. Mannini (2021). Time-variant self-excited force model based on 2D rational function approximation. Journal of Wind Engineering and Industrial Aerodynamics 211, 104523.

Barni, N., O. A. Øiseth, and C. Mannini (2022). Buffeting response of a suspension bridge based on the 2D rational function approximation model for self-excited forces. Engineering Structures 261, 114267.

Bruno, L, N Coste, C Mannini, A Mariotti, Patruno, P L Schito, and G Vairo (2023). Codes and standards on computational wind engineering for structural design: State of art and recent trends. Wind and Structures, 133–151.

Chen, X. and A. Kareem (2003). Aeroelastic analysis of bridges: effects of turbulence and aerodynamic nonlinearities. Journal of Engineering Mechanics 129, 885–895.

Dongmei, H., H. Teng, and H. Shiqing (2019). Experimental investigation of vortex-induced aeroelastic effects on a square cylinder in uniform flow. Wind and Structures, 30, 37–54.

Li, W., L Patruno, H. Niu, S. de Miranda, and X. Hua (2021). Aerodynamic admittance of a 6: 1 rectangular cylinder: a computational study on the role of turbulence intensity and integral length scale. Journal of Wind Engineering and Industrial Aerodynamics 218, 104738.

Tamura, Y. (2020). Mathematical models for understanding phenomena: Vortex-induced vibrations. Japan Architectural Review 3, 398–422.

Wang, Y. and X. Chen (2022). Extraction of aerodynamic damping and prediction of vortex-induced vibration of bridge deck using CFD simulation of forced vibration. Journal of Wind Engineering and Industrial Aerodynamics 224, 104982.

Structural load mitigation against operational and extreme wind speeds for HAWTs equipped with a friction-based control system.

E. Sorge [1], C. Riascos [2], N. Caterino [1,2]

[1] *Department of Engineering, University of Naples "Parthenope", Naples, Italy,*
[2] *Institute of Technologies for Construction, Italian National Research Council (CNR), San G. Milanese, Milan, Italy*

SUMMARY
This study presents an innovative optimization of a special constraint applied to the base of a 5 MW HAWT wind turbine aimed at mitigating wind-induced stresses. The constraint relies on passive energy dissipation through friction mechanisms. Through a rigorous methodological approach, 98 wind cases were considered, including 12 operational scenarios and 2 parked scenarios. The analysis of the effects of the new configuration was conducted by evaluating the tower base moment and fatigue load. The results show a significant reduction in average peak moment by 15% and average fatigue load by 35%. These findings indicate the effective potential of the optimized system in enhancing structural performance and operational lifespan of the wind turbine under operational and extreme wind conditions.

Keywords: friction device, wind turbine, optimization.

1. INTRODUCTION

Wind turbines are a key pillar in the transition to a low-carbon economy, offering a reliable and sustainable source of renewable energy, (*Global Wind Report*, 2023). However, as the wind industry continues to grow and evolve, significant challenges emerge related to the durability, reliability, and performance of the turbines themselves. Among the most critical issues are the control of vibration, mechanical stress and fatigue, phenomena that can compromise operational efficiency and reduce the useful life of structures. The resulting vibrations and reductions of mechanical stresses can cause structural damage, increase maintenance costs, and reduce the overall efficiency of the plant. To address these challenges effectively, several approaches have been developed over the years (Alkmim et al., 2016 and Enevoldsen & Mørk, 1996). Of these, passive control systems have shown promise (Almajhali, 2023). Unlike active systems that require external energy for their operation, passive devices utilise principles of structural damping and energy dissipation to reduce vibration and mechanical stress, without the need for an external power supply (Zuo et al., 2020).

In this context, this article aims to examine in detail the effectiveness of a passive control system installed at the base of a wind turbine, the hinge-spring-friction-device (HSFD), from Sorge et al. (2024). The HSFD consists of several devices installed at the base of the wind turbine, see Figure 1. The devices installed in parallel are a hinge, friction devices and springs. The design of the HSFD consists of defining the best pair of values $M_{fr,y}$, k_s, where $M_{fr,y}$ is the friction moments and k_s is the rotational stiffness of the springs.

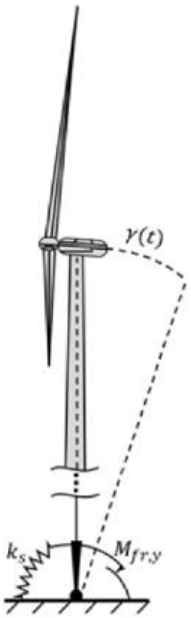

Figure 1. HSFD installed at the base of a wind turbine. $M_{fr,y}$ is the moment of friction, k_s is the spring stiffness and γ is the rigid rotation of the base.

In the present article, the optimization procedure described in the work of Sorge et al. (2024) was performed to optimize the Control System with reference to 16 turbine scenarios. The optimization aims to search for the pair of values ($M_{fr,y}$, k_s) that minimizes both the peak moment reduction of the section at the base of the tower and the fatigue damage compared to the tower condition without HSFD.
It aims to contribute to the growing knowledge base in the field of vibration and mechanical stress control in wind turbines, providing new insights and perspectives for the development of increasingly efficient and sustainable solutions in the renewable energy sector.

2. THE CASE-STUDY 5MW WIND TURBINE

The HSFD analysis was conducted on a 5 MW wind turbine developed by the National Renewable Energy Laboratory (NREL). The specifications of the tower are given in Jonkman's work (Jonkman et al., 2009) and are listed in Tab.1.

Table 1. Properties of NREL 5-MW Baseline Wind Turbine

Number of blades	3	Rotor, Hub Diameter	126,3 m
Cut-in/rated/cut-out wind speed	3/11.4/25 m/s	Hub Height	90 m
Cut-in/rated rotor speed	6.9/12.1 rpm	Tower top diameter	3.87 m
Rotor Mass	110 Mg	Tower base diameter	6.00 m
Nacelle Mass	240 Mg	Thickness bottom	27 mm
Tower Mass	347 Mg	Thickness top	19 mm

The optimization process, based on Exhaustive Research method (described in Sorge et al., 2024), aims to find the optimal pair of mechanical properties (k_s, $M_{fr,y}$), i.e. the one that minimizes a parameter (objective function, f_{obj}) summarizing the structural response of the tower. To this end, the mechanical properties of the HSFD were collected in a vector called $\zeta = [k_s, M_{fr,y}]$. The

performance parameters assumed are two: one related to the peak bending moment demand, $I_1(\zeta)$, the other related to the bending moment fatigue demand, $I_2(\zeta)$, both referring to the base of the tower.
The objective function is defined as in Eq. (1), where w1 and w2 express the weight of the performance I_1 and I_2 (w_1+ w_2=1.0). In this study, the simplified assumption of equal weights for the individual performances was made (w_1= w_2=0.5).

$$f_{obj}(\zeta) = w_1 I_1(\zeta) + w_2 I_2(\zeta) \quad (1)$$

The optimization was conducted considering the 14 wind scenarios generated in accordance with IEC 61400-1 (2019). To capture the variability of wind forces, seven wind cases were generated for each scenario, resulting in a total of ninety-eight 10-minute wind fields.
Table 2 presents the key characteristics of the wind fields generated during specific wind turbine operations. V_{hub} denotes the mean wind speed at the hub, while the wind label indicates the type of wind considered according to IEC 61400-1, including the Extreme Turbulence Model (ETM) or the Extreme Wind Speed Model (EWM) for return periods of 1 year (Tr_1) and 50 years (Tr_{50}). Rpm indicates the rotor revolutions per minute, providing insight into the turbine's operational state or whether it is parked; each Rpm value is associated with a unique pitch angle derived from the Jonkman et al. (2009).

Table 2. Wind loads and grouping.

Scenario	V_{hub}[m/s]	*Label wind*	Rpm	Pitch angle
Cut-in	3	ETM	6.9	0°
C-R_1	5	ETM	8.2	0°
C-R_2	7	ETM	9.5	0°
C-R_3	9	ETM	10.8	0°
Rated	11.4	ETM	12.1	0°
R-C_1	14	ETM	12.1	8.70
R-C_2	16	ETM	12.1	12.06
R-C_3	18	ETM	12.1	14.92
R-C_4	20	ETM	12.1	17.47
R-C_5	22	ETM	12.1	19.94
R-C_6	24	ETM	12.1	22.45
Cut-out	25	ETM	12.1	23.47
$Parked_1$	40	EWM-Tr_1	0	90°
$Parked_2$	50	EWM-Tr_{50}	0	90°

3. RESULTS AND CONCLUSION

This section outlines the results from the HSFD design process aimed at minimizing both the peak moment and the fatigue demand at the base level of the tower. The optimization approach was focused on finding the optimal configuration ζ_{opt} = [$k_{s,opt}$ $M_{fr,y,opt}$].
Tab. 3 gives a clear picture of the performance of the HSFD. It shows the average reduction in structural response in comparison to the 14 different load scenarios considered. Importantly, these results were obtained by configuring the device with specific parameters, i.e. $k_{s,opt}$ = 24’356 MNm/rad and $M_{fr,y,opt}$ = 12.15 MNm.

Table 3. Performance of the HSFD in terms of structural response reduction against each of the 14 Scenario with the device set ζ_{opt}.

Scenario	$I_{1,avg}$	$I_{2,avg}$
Cut-in	0.82	0.60
C-R_1	0.91	0.65
C-R_2	0.92	0.52
C-R_3	0.92	0.53
Rated	0.89	0.60
R-C_1	0.90	0.71
R-C_2	0.88	0.76
R-C_3	0.86	0.75
R-C_4	0.85	0.73
R-C_5	0.82	0.70
R-C_6	0.84	0.69
Cut-out	0.75	0.85
Parked$_1$	0.70	0.98
Parked$_2$	0.65	0.98

In particular, the analysis reveals a significant reduction in the average response of 15% in peak bending moment and a range of 30% to 40% in fatigue. These data not only demonstrate the effectiveness of HSFD in mitigating critical loads on the structure, but also suggest its potential in prolonging the durability and strength of the tower in the operational environment. Specifically, the reduction in maximum bending moment across all scenarios decreases from a value of 131 MNm for the tower condition without the control system to 105 MNm for the tower with the control system.

In conclusion, the paper presents a detailed and convincing picture of the results obtained through the design and optimization process of the HSFD system. These results not only provide a solid basis for further research and development in the field of wind turbine structure engineering, but also indicate significant progress in achieving efficient and sustainable solutions to structural challenges.

REFERENCES

Alkmim, M. H., De Morais, M. V. G., & Fabro, A. T. (2016). Vibration reduction of wind turbines using tuned liquid column damper using stochastic analysis. *Journal of Physics: Conference Series*, *744*(1), 012178.

Almajhali, K. Y. M. (2023). Review on passive energy dissipation devices and techniques of installation for high rise building structures. *Structures*, *51*, 1019–1029.

Enevoldsen, I., & Mørk, K. J. (1996). Effects of a vibration mass damper in a wind turbine tower. *Journal of Structural Mechanics*, *24*(2), 155–187.

Global wind report. (2023). https://gwec.net/wp-content/uploads/2023/04/GWEC-2023_interactive.pdf

IEC 61400-1:2019(E). Wind energy generation systems—part 1: design requirements. Standard, Geneva, CH, International Electrotechnical Commission; 2019. (n.d.).

Jonkman, J., Butterfield, S., Musial, W., & Scott, G. (2009). *Definition of a 5-MW reference wind turbine for offshore system development*. National Renewable Energy Lab.(NREL), Golden, CO (United States).

Sorge, E., Riascos, C., Caterino, N., Demartino, C., & Georgakis, C. T. (2024). Optimal design of a hinge-spring-friction device for enhancing wind induced structural response of onshore wind turbines. *Engineering Structures*. Under Review.

Zuo, H., Bi, K., & Hao, H. (2020). A state-of-the-art review on the vibration mitigation of wind turbines. *Renewable and Sustainable Energy Reviews*, *121*, 109710.

IN-VENTO 2024
International Conference of the Italian Association for Wind Engineering
Pisa, September 8th – 11th, 2024

Advanced insights into stationary downburst phenomena: a POD analysis of LES CFD data

Andi Xhelaj[a], Massimiliano Burlando[a], Djordje Romanic[b], Horia Hangan[c]

[a]*University of Genoa, Genoa, Italy, andi.xhelaj@edu.unige.it - massimiliano.burlando@unige.it*
[b]*McGill University, Montreal, Quebec, Canada, djordje.romanic@mcgill.ca*
[c]*Ontario Tech University, Oshawa, Ontario, Canada,horia.hangan@ontariotechu.ca*

SUMMARY:
This research analyses a stationary downburst by employing Proper Orthogonal Decomposition (POD) on Large Eddy Simulation (LES) data, precisely calibrated with experimental data from the WindEEE Dome. The study delves into the spatial evolution of stationary downburst wind fields during the time of maximum intensity, with particular focus on the primary vortex ring and its influence on the horizontal velocity profiles. It was found that the bimodal structure of these profiles is due to interactions between the primary vortex ring and boundary layer separation. This feature improves our understanding of downburst behavior, helping to refine models that predict these phenomena more accurately.

Keywords: Stationary Downburst, WindEEE Dome, LES data, POD analysis, analytical models, reduced-order models

1. INTRODUCTION

Over the past four decades, the study of intense thunderstorm downbursts and impacts on structures has emerged as an important area of research within the field of wind engineering. Characterized as mesoscale phenomena, thunderstorms develop in convective conditions, exhibiting non-stationary velocity vertical profiles markedly distinct from those commonly observed in the atmospheric boundary layer (ABL). Such phenomena, associated with design wind velocities for mean return periods exceeding 10–20 years, present significant uncertainties and challenges in the development of a universally accepted model for downburst outflows and their structural impacts, analogous to Davenport's (1961) model for synoptic cyclones. Downburst winds display complex fluid dynamics due to the significant influence of a primary vortex (PV) ring that forms during the downdraft's descending stage. This PV ring influences the downburst's characteristic nose-shaped vertical profile, impacting on its spatial structure and temporal variation. Traditional analytical models struggle to accurately simulate the vertical profile of the horizontal wind component, often leading to underestimation of the wind loads on structures (Xhelaj et al., 2023). In order to address these challenges, the present study employs the Proper Orthogonal Decomposition (POD) method to analyze Large Eddy Simulation (LES) CFD data of a spatially stationary downburst. The LES data (Žužul et al., 2024), has been calibrated using experimental tests conducted at the WindEEE Dome facility (Canepa et al., 2022). The POD technique (Holmes et al., 2012), employs modal decomposition to isolate high- energy characteristics of stationary downbursts, categorizing them into spatial modes based on their energy level. This research aims to analyze the spatio-temporal dynamics of the PV ring in a stationary downburst, a key factor influencing the horizontal velocity's vertical profile during the downburst maximum intensity. The findings are intended to enhance the development of analytical or reduced-order models for these weather phenomena.

2. METHODS

The POD technique is an important tool for reducing the complexity of dynamic systems into a manageable, low-dimensional form. However, a key challenge arises from the translational invariance observed in the data, where the PV ring maintains its coherent structure despite spatial displacement. This issue complicates POD's ability to identify the PV as the same entity across different positions, potentially leading to redundant multiple POD modes for a single coherent pattern that merely shifts location. To tackle this challenge, a tracking algorithm was used for the PV ring, involving the calculation of the Q-field (Davidson, 2015) for each LES data snapshots. The Q-field center of mass associated with the PV ring was then used to determine the radial location of the vortex center over time, $r_{PV}(t)$. After identifying the center of the PV ring, snapshots tracking the PV were collected and aligned with its center, enabling the application of the POD technique via the snapshots method (Sirovich, 1987). The transformation technique of the LES data and the subsequent POD analysis is equivalent to consider the downburst simulation dynamics in the form:

$$U_r(r,z,t) \rightarrow U_r(r - r_{PV}(t),z,t) \approx U_r^{(R)}(r - r_{PV}(t),z,t) \tag{1}$$

$$U_z(r,z,t) \rightarrow U_z(r - r_{PV}(t),z,t) \approx U_z^{(R)}(r - r_{PV}(t),z,t) \tag{2}$$

where U_r and U_z represent the radial and vertical velocity components, respectively, while $U_r^{(R)}$ and $U_z^{(R)}$ denote the rank-R POD approximations of these velocity components.

3. RESULTS

Figure 1 represents a direct comparison between LES data (Fig.1a), and its POD-based reduced-order approximation of rank 5, (Fig.1b), at the time of maximum velocity. A rank 5 approximation means that only the first five modes were used for the flow field reconstruction. These five modes capture about 70% of the total energy in the dataset. Each panel in Fig.1 is normalized in the radial and vertical direction by the bell mouth diameter of the WindEEE Dome, $D = 3.2$ m. In both panels the intersection of black dashed lines indicates the PV center identified by the tracking algorithm. The violet color highlights the region of strongest velocity, which is located below and slightly to the left of the vortex center, at about $r/D = 1.2$. Figure 1 shows that the rank 5 approximation is able to capture the important wind intensity features below the vortex rotor marked by two distinct areas of violet colors. This "bimodal-peak" in the velocity field significantly influences the shape of the horizontal velocity vertical profile that develops at this radial location. This comparison demonstrates the POD capability to effectively simplify complex flow field while retaining its critical flow features. Figure 2 illustrates the contribution of the different modes in reproducing the complex structure of the stationary downburst through the decomposition into the first three modes of the POD at the instant of maximum intensity (at about $r/D = 1.2$). Mode 1 (Fig.2a) highlights the primary vortex ring, providing a snapshot of the core energetic structure and its influence on the surrounding flow. Mode 2, shown in Fig.2(b), depicts the rebound phase of the PV upon contact with the ground, identifiable by the vector field's upward direction. Mode 3, depicted in Fig.2(c), describes the dynamic separation in the boundary layer due to the influence of the PV, and consequential formation of a secondary vortex. This phenomenon is responsible for creating the "bimodal-peak" in wind velocity near the ground level that is shown in Fig.1(b). When viewed collectively, these three modes provide a detailed sequence of the downburst's evolution, from initial energy concentration in the PV to its rebound with the ground surface and the resulting interactions with the

boundary layer. Figure 3 compares the vertical profiles of horizontal velocity at $r/D = 1.2$ for both the LES data and the rank 5 POD approximation (Fig.3a). The subsequent panels in Figure 3 display the profiles for modes one, two, and three, respectively. Notably, Fig.3(a) shows that the vertical profile of the horizontal wind has a bimodal structure with two peaks: one close to the ground and another at a higher elevation. This bimodal structure is clarified by the POD analysis, highlighting that it arises from the interplay of mode 1, associated with the primary vortex (PV) ring (Fig.3b), and mode 3, linked to boundary layer detachment and secondary vortex formation (Fig.3d). Mode 2 appears not to influence the bimodal nature of the horizontal velocity profile at this stage (Fig.3c).

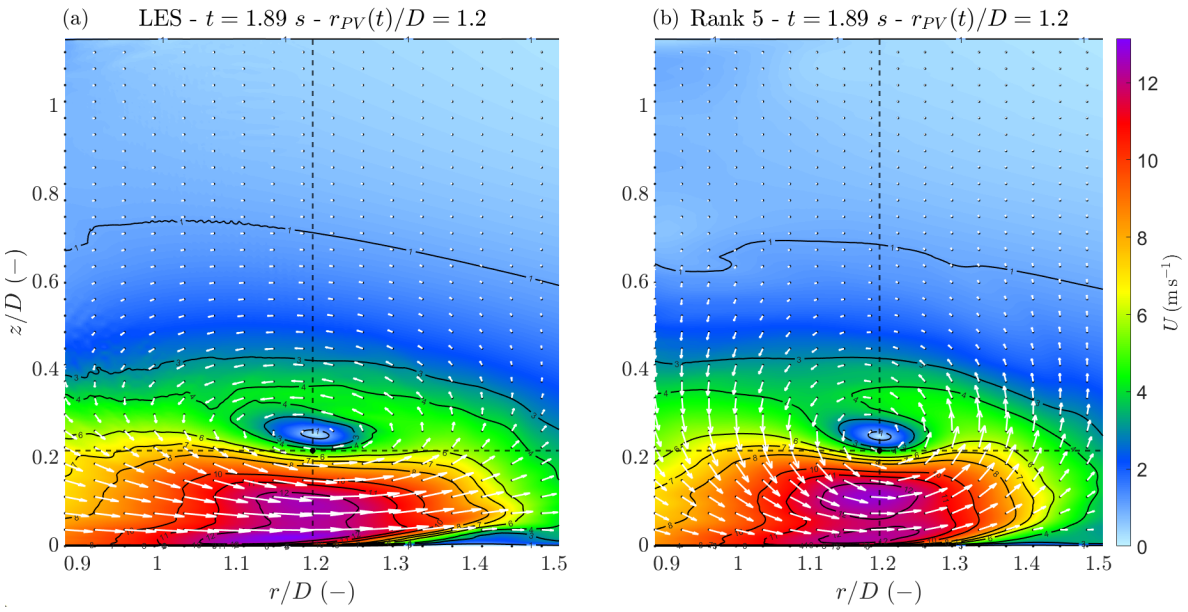

Figure 1. Side-by-side comparison of downburst velocity fields at maximum intensity, with coordinates normalized by the WindEEE dome diameter ($D = 3.2$ m): (a) original LES data; (b) rank 5 POD approximation. The dashed black lines mark the PV center.

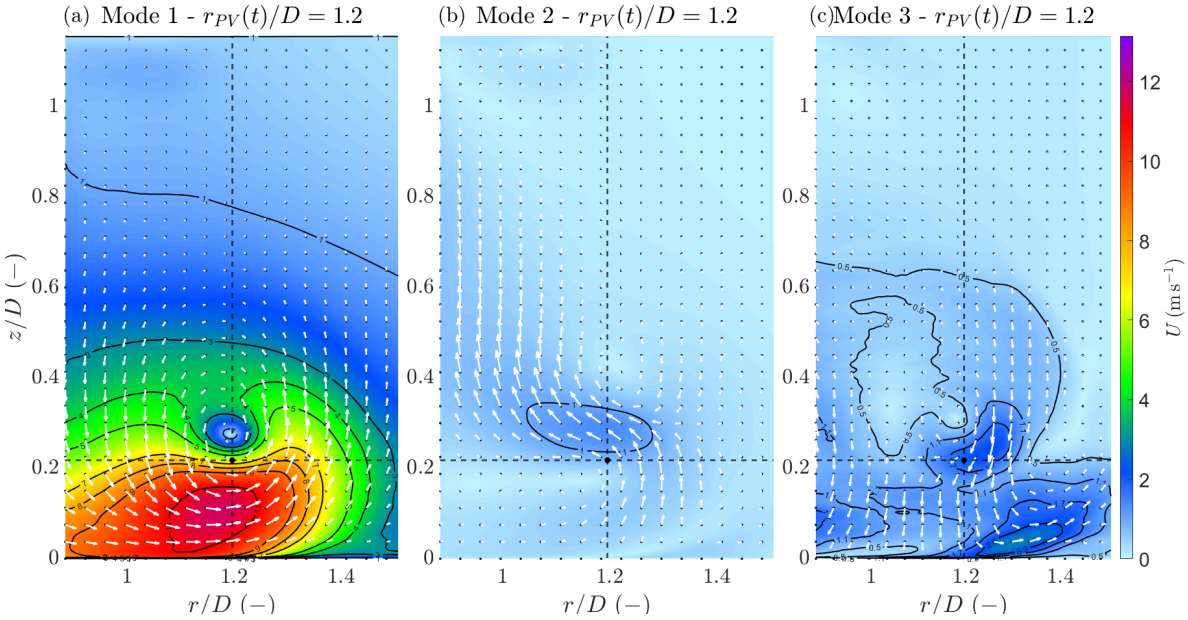

Figure 2. POD decomposition of the LES data. (a) Mode 1: primary vortex ring. (b) Mode 2: rebound phase of the vortex upon ground impact. (c) Mode 3: boundary layer detachment and secondary vortex formation.

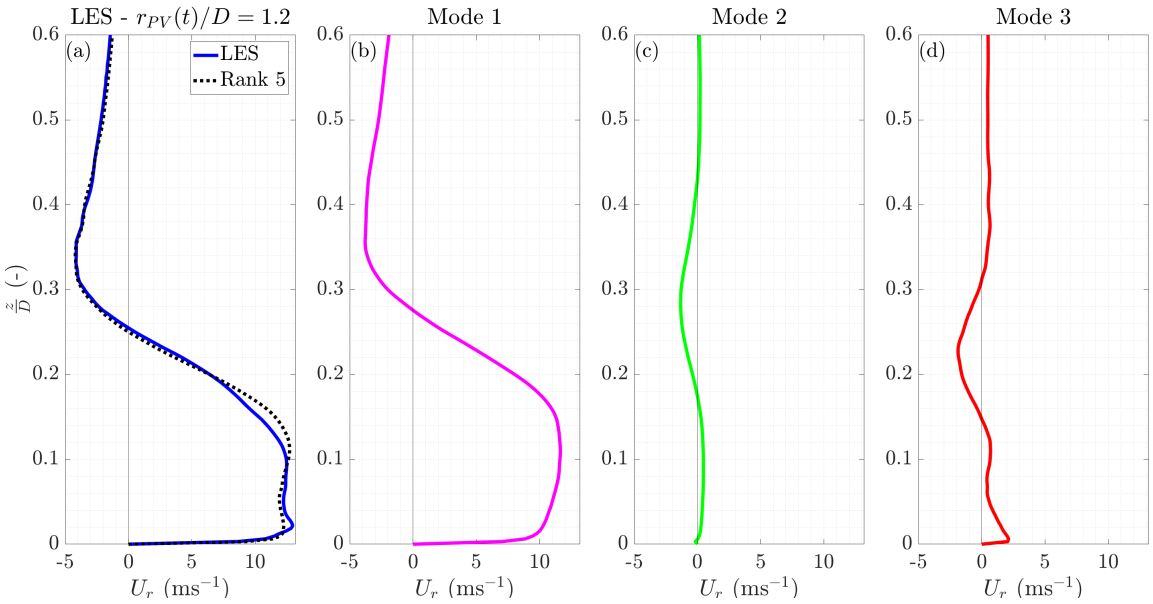

Figure 3. Vertical profiles of the horizontal velocity at $r/D = 1.2$ due to POD decomposition of the LES data; (a) LES Data and Rank 5 approximation. (b) Mode 1; (c) Mode 2; (d) Mode 3.

4. CONCLUSIONS

This research demonstrates the efficacy of the POD technique in analyzing the complex dynamics of stationary downbursts, with particular focus on the primary vortex ring dynamics and its influence on the horizontal velocity profiles during the time of maximum intensity. Key findings indicate that the bimodal structure in the vertical profile of the horizontal wind stems from the interplay of the primary vortex ring effects and boundary layer detachments. These insights significantly improve our understanding of downburst dynamics, contributing to the development of enhanced analytical and reduced-order models for these events.

ACKNOWLEDGEMENTS

The research carried out by A. Xhelaj and M. Burlando was supported by the European Research Council (ERC) under the European Union's Horizon 2020 research and innovation program (grant agreement No. 741273) through the project THUNDERR—Detection, simulation, modelling and loading of thunderstorm outflows to design wind-safer and cost-efficient structures—supported by an Advanced Grant 2016. The authors are deeply grateful to Prof. Giovanni Solari for his essential contributions to the conceptualization and supervision of this research.

REFERENCES

Canepa, F., M. Burlando, D. Romanic, G. Solari, and H. Hangan (2022). Downburst-like experimental impinging jet measurements at the WindEEE Dome. Sci Data 9, 243.

Davidson, P. (2015). Turbulence: An Introduction for Scientists and Engineers. Oxford University Press.

Holmes, P., J. L. Lumley, G. Berkooz, and C. W. Rowley (2012). Turbulence, Coherent Structures, Dynamical Systems and Symmetry. 2nd ed. Cambridge University Press, Cambridge, UK.

Sirovich, L. (1987). Turbulence and the dynamics of coherent structures. I–III. Quarterly of Applied Mathematics 45, 561–590.

Xhelaj, A., J. Žužul, F. Canepa, A. Ricci, D. Romanic, M. Burlando, and H. Hangan (2023). Comparison between stationary downburst-like impinging jets and analytical models. Proceedings of the International Conference on Wind Engineering (ICWE16), 28-31 Aug, Florence, Italy.

Žužul, J., A. Ricci, M. Burlando, B. Blocken, and G. Solari (2024). Vortex dynamics and radial outflow velocity evolution in downburst-like winds. Computers and Fluids (submitted).

IN-VENTO 2024
International Conference of the Italian Association for Wind Engineering
Pisa, September 8th – 11th, 2024

An active-controlled multi-blade system for simulation of downburst outflows in boundary layer wind tunnel

Yangjin Yuan [1], Bowen Yan [2], Qiaowen Ran [3], Xiao Li [4]

[1] *Chongqing University, Chongqing, China, 2658058913@qq.com*
[2] *Chongqing University, Chongqing, China, bowenyancq@cqu.edu.cn*
[3] *Chongqing University, Chongqing, China, 202316021198t@stu.cqu.edu.cn*
[4] *Chongqing University, Chongqing, China, lixiao_seanli@cqu.edu.cn*

SUMMARY
This study presents the design and performance of an active-controlled multi-blade system (AMBS) for simulating downburst outflows in conventional boundary layer wind tunnels. By properly configuring the position and rotation of each blade, the AMBS facilitates the generation of a desired two-dimensional outflow-like wind field with satisfying accuracy. The investigation of this study encompasses analyses of wind speed profiles, power spectra, horizontal homogeneity, and non-stationary characteristics of the generated outflow-like wind fields, aimed to demonstrate the validity of the AMBS technique.

Keywords: Downburst outflow, Wind tunnel testing, Multi-blade system, non-stationary winds

1. INTRODUCTION

The downburst outflow is characterized by violent horizontal winds exhibiting a distinct “nose-shaped” speed profile. However, replicating the outflow wind field in conventional wind tunnels without specific devices (e.g., active fans, impinging and wall jet devices) poses significant challenges. To this end, this study proposes an innovative active-controlled multi-blade system (AMBS) capable of redirecting the flow to generate a two-dimensional (2-D) outflow-like wind field in the wind tunnel. The AMBS offers high levels of customization, allowing the outflow-like wind fields following different target profiles to be generated by simply configuring the height and rotation angle of each blade. It is expected that, with the high versatility and cost-effectiveness, the AMBS offers a practical solution for the wind tunnel simulation of downburst outflows.

2. EXPERIMENTAL SETUPS

A series of tests was carried out in the open-circuit boundary layer wind tunnel, with dimensions of 2.4 m × 1.8 m × 15.0 m (breadth × height × length), at Chongqing University. The AMBS, shown in Figure 1(a), comprises four blades, the associated driving and driven modules, and a supporting frame. Each blade is 2000 mm × 500 mm × 10 mm (span × chord × thickness) in size, and its height can be adjusted within the range of the frame. By manipulating the input signal to a driving module, the associated blade can be rotated around its spanwise axis to a predetermined angle at a specified angular speed. As depicted in Figure 1(b), the rotated blades can redirect the flow direction, and therefore generate an 2D outflow-like wind field in the downstream area.

3. TEST RESULTS

3.1. Wind field visualization

A smoke test was conducted to visualize the 2D outflow-like wind field generated by the AMBS, with a focus on the evolution of the primary vortex. As shown in Figure 1(b), the primary vortex was formed consequent to the airflow impinging to the ground shortly after the blades rotated, and it continued to travel in streamwise direction as evidenced by the smoke front advancing notably.

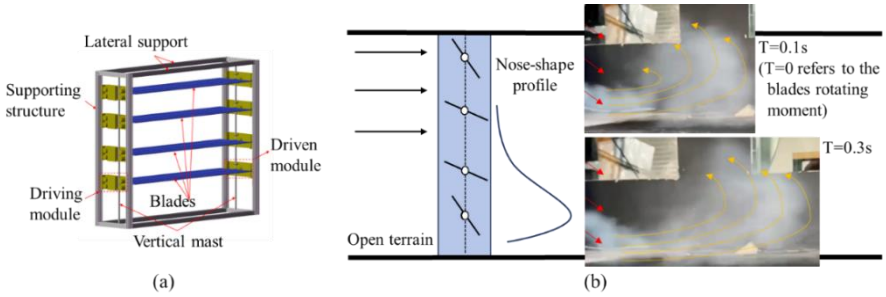

Figure 1. (a) Structure of AMBS, (b) Smoke test

3.2.Wind profiles and horizontal homogeneity

Three longitudinal mean wind speed profiles of outflow-like winds corresponding to different heights of the maximum speed, denoted by Z_{max}, were generated. the selection of target profile was expressed by the model proposed by Wood and Kwok (2001). As illustrated in Figure 2(a), all generated profiles demonstrated a significant "nose-shaped" feature. Notably, the profile corresponding to Z_{max} = 0.15 m closely match the target profile, with the exceptions at the heights very near the ground. On the other hand, regarding the turbulence characteristics, Figure 2(b) plots the normalized spectra of the longitudinal wind speeds of the three generated outflow-like wind field. It is readily observed that all wind spectra well align with the von Karman spectrum, and the attenuation slopes of these spectra all follow the -5/3 law by Kolmogorov.

It is worth noting that endplates were not included in the current design of AMBS, which necessitates examining the horizontal homogeneity of generated wind field. Figure 2(c) illustrates the mean wind speed profiles corresponding to Z_{max} = 0.15 m measured at five different locations in the spanwise direction, i.e., y = [-0.8, -0.4, 0, 0.4, 0.8] m, where y denotes the horizontal distance from the central line of wind tunnel. It is observed that the relative errors for mean wind speed and turbulence intensity are below 5% within the range from y = -0.4 m to y = 0.4 m, indicating that the generated flow field within this range can be reasonably regarded as a 2D outflow-like wind field, even though the endplates were absent in the current design of AMBS.

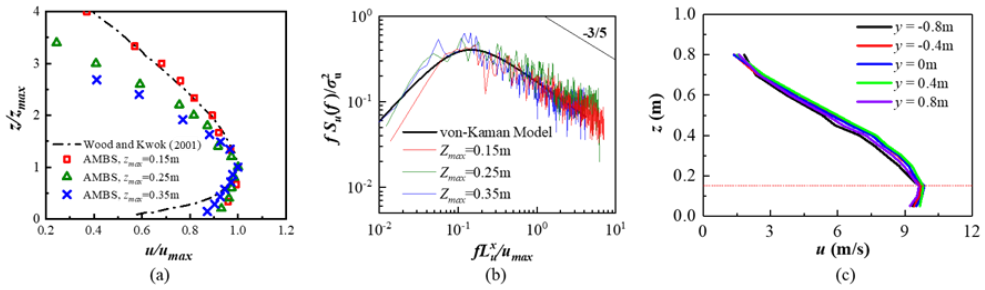

Figure 2. (a) Mean wind speed profiles; (b) wind spectra; (c) Mean wind speed profiles at different locations in spanwise direction

3.3.Non-stationary characteristics

To reflect the non-stationary characteristics of downburst outflows, a transient flow field was generated by first rotating the blades to predetermined angles and then resuming to their initial positions after a very short period of time (e.g., less than 1 s). Figure 3(a) presents the wind speed time histories at z = 0.15 m, where z denotes the height, and a moving average period of T_{avg} = 0.2 s was employed to extract the time-varying mean wind speed, $\bar{u}(t)$. It was found that the total duration of the ramp-up and ramp-down stages directly depends on the duration, while the accelerations of the non-stationary wind speed at these two stages positively correlates to the angular speed of blade rotation. Following Solari et al. (2015), a non-dimensional function $\gamma(t) = \bar{u}(t) / \bar{u}_{max} \geq 0.6$, where $\bar{u}_{max}$ is the maximum value of $\bar{u}(t)$, is defined to estimate the duration of the most intense part of the generated non-stationary outflows, as shown in Figure 3(b). For comparison purposes, a time scale of 1:150 is assumed to match T_{avg} = 30 s suggested by Solari et al. (2015).

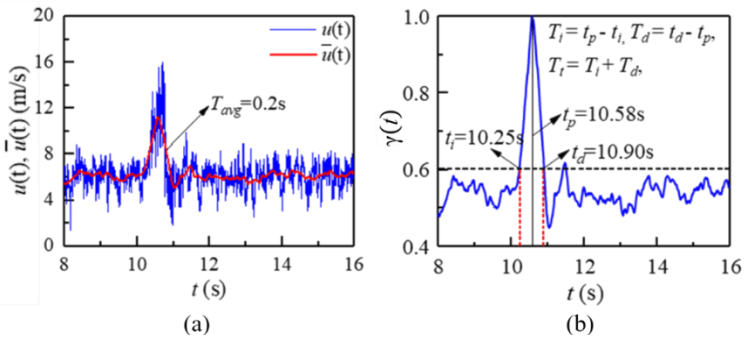

Figure 3. (a) Time histories of instantaneous and time-varying mean wind speeds; (b) Time histories of γ

To validate the AMBS by comparing with the field measurement data of actual downburst outflows, two wind tunnel test cases of non-stationary wind field, referred to as NW1 and NW2 in the following, were generated with reference to the measurement data of outflow events in Genoa and Livorno reported in Solari et al. (2015), respectively. As shown in Table 1, the parameters T_i, T_d, and T_t (see Figure 3(b) for definitions) of the non-stationary wind speed time histories generated in wind tunnel all fall within the ranges of those observed from actual downburst outflow events.

Table 1. Comparisons of T_i, T_d, and T_t (in full scale) obtained from wind tunnel tests and field measurement data

Data source	T_i (s)	T_d (s)	T_t (s)
NW1	142.5	138.0	280.5
Genoa port	102.9-146.2	105.1-171.1	208.3-317.3
NW2	132.0	214.5	346.5
Livorno port	109.8-185.3	149.2-195.3	259.0-380.6

Furthermore, Solari et al. (2015) pointed out that several noteworthy wind speed ratios, defined by Eqs. (1) to (3) according to Solari et al. (2015), are essential to the analysis of downburst-induced loading and responses of structures.

$$R=u_{max}/\hat{u} \tag{1}$$

$$G_{max}=u_{max}/\bar{u}_{max} \tag{2}$$

$$\hat{G}=\hat{u}/\bar{u}_{max} \tag{3}$$

where u_{max}, $\hat{u}$, $\bar{u}_{max}$ are the maximum instantaneous wind speed, the 1-s peak wind speed, and the maximum time-varying mean wind speed with T_{avg}=30s, respectively; $\widehat{G}$ is the generalized definition of the gust factor of downburst-like winds. Table 2 compares the above parameters obtained from the wind tunnel test cases NW1 and NW2 with those reported in Solari et al. (2015), showing that the maximum relative errors for ϵ_R, ϵ_{Gmax}, and $\epsilon_{\widehat{G}}$ are 11.3%, 15.0%, and 10%, respectively. Based on the good agreement in T_i, T_d, and T_t presented in Table 1 and the low relative errors shown in Table 2, it is validated that the AMBS is capable of generating non-stationary downburst outflow-like wind field with a satisfying performance.

Table 2. The values of R, G_{max}, and $\widehat{G}$ using T_{avg}=30s for all non-stationary cases in this study

Cases	R	$Gmax$	$\widehat{G}$	ϵ_R	ϵ_{Gmax}	$\epsilon_{\widehat{G}}$
NW1	1.11	1.46	1.32	4.7%	15.0%	10%
NW2	1.05	1.32	1.26	0.9%	3.9%	5.0%
Solari et al. (2015)	1.06	1.27	1.20	-	-	-

4. CONCLUSIONS

An active-controlled multi-blade system (AMBS) was developed to generate 2-D outflow-like wind fields in conventional wind tunnels. With the proper configuration of AMBS, the generated mean wind speed profile may closely match the profile model proposed by Wood and Kwok (2001), the wind spectrum of longitudinal wind speed may well agree with the von Karman spectrum, and the non-stationary characteristics are similar to those of actual downburst outflows reported in Solari et al. (2015). More details about the design and performance of the AMBS will be reported in an upcoming journal paper by the authors (Yuan et al., under review)

ACKNOWLEDGEMENTS

The authors would like to acknowledge the financial support from the National Natural Science Foundation of China (No. 51878104), 111 Project of China (B18062), and Key Support Program of China for foreign experts (zcsf2021008).

REFERENCES

Solari G, Burlando M, Gaetano P, Repetto M P (2015). Characteristics of thunderstorms relevant to the wind loading of structures. Journal of Wind and Structures. 20, 763–791.

Yuan YJ, Yan BW, Zhou XH, Li X, Yang QS, Zhou X, Shu ZR (under review). An active-controlled multi-blade facility to generate 2-D downburst-like outflows in the boundary layer wind tunnel. Manuscript submitted for publication.

Wood S, Kwok S, Motteram A., Fletcher F, (2001). Physical and numerical modeling of thunderstorm downbursts. *Journal of Wind Engineering and Industrial Aerodynamics*, 89, 535–552.

Advancing towards the creation of a digital twin for Genoa, Italy: Facilitating CFD simulations to produce the wind hazard map

Josip Žužul [1], Alessio Ricci [2], Massimiliano Burlando [1]

[1]*Department of Civil, Chemical and Environmental Engineering, University of Genoa, Genoa, Italy, josip.zuzul@edu.unige.it – massimiliano.burlando@unige.it*
[2]*Department of Science, Technology and Society, University School for Advanced Studies IUSS, Pavia, Italy, alessio.ricci@iusspavia.it*

SUMMARY
The following study aims to present the development of the ongoing research project named ADAPTNOW targeting the numerical reconstruction of the large-scale area surrounding Genoa city, Italy. Preparation of such computational domains for Computational Fluid Dynamics (CFD) applications is a challenging task, requiring several considerations to effectively achieve the desired outcome. This study will therefore showcase and highlight the conducted steps on the route towards the creation of a digital twin of Genoa aiming to finally provide hazard maps of extreme winds. In particular, the preparation and simplification of geometries for both terrain and buildings is discussed here, as well as the effective approach to utilizing large datasets to construct the computational grid in OpenFOAM.

Keywords: Digital Twin, Computational Fluid Dynamics, OpenFOAM

1. INTRODUCTION

Wind Engineering (WE) explores various wind-related phenomena, including pedestrian-level wind comfort, pollutant dispersion, and wind loading, among others. Irrespective of the specific application, studies often encompass various structure types, complex topographies (such as hills and mountains), water surfaces, vegetation, and more. In investigations employing Computational Fluid Dynamics (CFD), practitioners commonly encounter numerous challenges since the preprocessing, from geometry to grid generation. It is essential for users to meticulously evaluate the consequences of possible (and often required) geometry simplifications, as these alterations can have an impact on the resultant flow field (Ricci et al., 2017). While recent efforts have focused on automating geometry preparation in various WE applications (e.g., Alemayehu and Bitsuamlak, 2022; Pađen et al., 2022), a definitive set of recommendations for accurate and effective computational grid generation in complex environments remains missing. This research project aims to address this need within the framework of a high-fidelity digital twin development for the city of Genoa, Italy. Such a digital model would allow studying various topics of broad interest to the local authorities at present. One of the most significant applications will be the development of a hazard map for extreme winds (e.g. non-synoptic thunderstorm winds, downslope winds, etc.). The presented research study will showcase the developments on the project and present the perspectives going forward. Although covering the larger urban area of the city of Genoa, this study will specifically showcase only the geometry and mesh generation solely within a section of its western part close to the port area of Voltri-Pra'. This area was selected as it is equipped with a full-scale wind monitoring network (Solari et al., 2020), and in the longer term will be used also

for validation purposes. More specifically, the case study of a moving thunderstorm that hit Genoa on August 14, 2018 (Burlando et al., 2020) will be used. Recent advancements in CFD have extended its application beyond traditional meteorological simulations, allowing the WE community to analyze temporal and spatial meso-γ scales previously reserved only for weather forecasting models (Ricci et al., 2022). This shift has prompted the selection of a thunderstorm as a validation case, making it an ideal subject for a digital twin model. Moreover, no similar CFD study covering such a large meso-scale area has been documented in existing literature, underscoring the novelty of the present research.

2. GEOMETRY GENERATION

The creation of a numerical model for a large-scale urban area is generally a challenging and time-consuming task commonly involving a substantial amount of manual work. Moreover, the complexity of the model creation is highly dependent on the intricate details of the topography of the analyzed area, which are linked with the dataset used for the reconstruction. To produce the model, one would require two distinct datasets: one for the terrain, and the other for the buildings. Both datasets were hereby provided by the local authorities. More specifically, the terrain dataset was provided in the Digital Terrain Model (DTM) format of 1m resolution, while the data relevant to the buildings was provided in the GeoJSON format typical of geoinformatics and related disciplines.

2.1. Generation of topography geometry

The DTM data, being a point cloud, was then converted into the adequate file format (e.g. stereolithography - STL) in the software of choice (e.g. python) to represent the terrain topography as commonly required by mesh generators. However, raw high-resolution datasets often have to be processed to remove the commonly present outliers and noisy data provided, by smoothing the dataset with some filter over a moving window (e.g. moving average, median average, Gaussian filter, etc.). There is no definitive recommendation on the decision for the filter selection as it depends on the localized interconnections of the terrain with the distribution of buildings in space. In this study, the moving average within a window of 25 m x 25 m was applied to the topography elevation data.

2.2. Generation of buildings geometry

Converting buildings from the commonly used GeoJSON format (where buildings are represented as 2D polygons) into surface triangulations presents a notably more challenging task compared to topography geometry generation. Light Detection and Ranging (LiDAR) measurements introduce errors, requiring the application of the Ramer - Douglas - Peucker (RDP) algorithm for shape simplifications (Douglas and Peucker, 1973). The entire process involves managing buildings that are “too close one to the other”, but also filling small gaps (i.e. narrow passages between buildings) which is addressed through the process of merging nearby buildings. The rationale behind merging nearby buildings stems from the understanding that attempting to individually resolve each building across a large area would significantly increase the number of narrow passages between buildings, thus escalating requirements for computational resources. While this detailed resolution might be beneficial for specific applications focusing on particular smaller areas, the cost-benefit analysis within the scope of the present project suggests it is not advisable. Furthermore, given the large size of the domain in the present study, buildings smaller than 5 meters in height and with an area of less than 25 square meters are removed, while their effect in terms of surface drag will

be accounted for using proper values of the aerodynamic roughness. The simplified and filtered polygons were then used in the open-source software OpenSCAD (OpenSCAD, 2024) to generate an STL representation of buildings. To showcase the entire simplification process and geometry generation (both for buildings and topography), Figure 1 shows the comparison between the same area in the western part of Genoa between the full-scale urban environment depicted in Figure 1a (adopted from Google Earth), and the developed digital twin numerical model showcasing the same area Figure 1b. As can be observed, a large number of "small" buildings were removed from consideration, but in general the area represents properly the reality. The merging operation of nearby buildings creates larger blocks of buildings which are therefore easier to manage at the mesh generation stage.

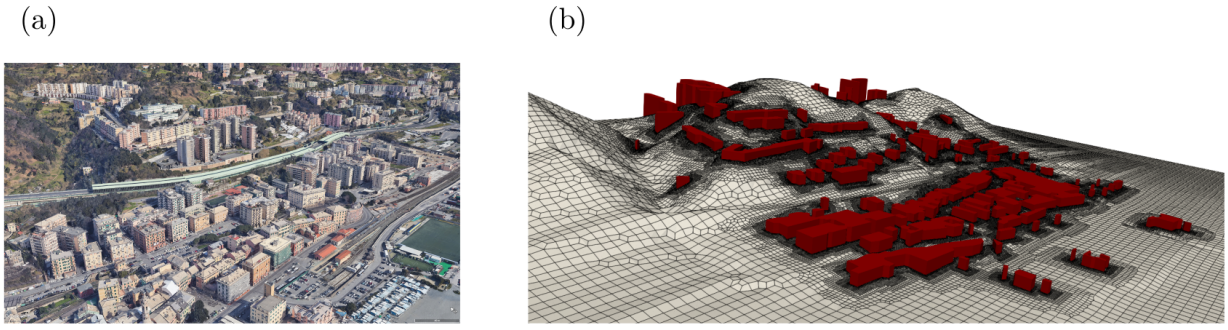

Figure 1. Comparison between the full-scale urban environment representation (a) with the digital twin (b). Full-scale view sub-figure (a) adapted from Google Earth (Version 7.3.6.9796; accessed March 14, 2024).

3. GRID GENERATION

A computational grid of the target area (8.5 km in length and 1.5 km in width) was built based on the input topography and buildings in `cfMesh`, a grid generation software available within the scope of the open-source CFD library `OpenFOAM`. The case study demonstrating the digital twin generation of the western part of Genoa is showcased in Figure 2. Moreover, Figure 2a showcases the intricate terrain details on the target area comprised of mountains, flat areas, sea, and buildings represented in STL files generated based on the approach presented in Section 2. These input files, with the addition of sharp feature edges of buildings, serve as the only input for the grid generator. The entire set of input files is displayed in Figure 2b. Establishing the input geometry definition, the grid generation process proves to be straightforward and practical, requiring only two essential input settings: (i) defining the maximum cell size, and (ii) specifying the input surface file composed of all domain boundaries. In this case study, the maximum cell size for the background grid was set to 100 m, with subsequent refinement levels of 2 for terrain, and 5 for buildings, resulting in cell sizes of 25 m and 3.125 m, respectively. Feature edge refinement was set to level 8. The resulting grid comprises 33 million cells, and is illustrated in Figure 2c.

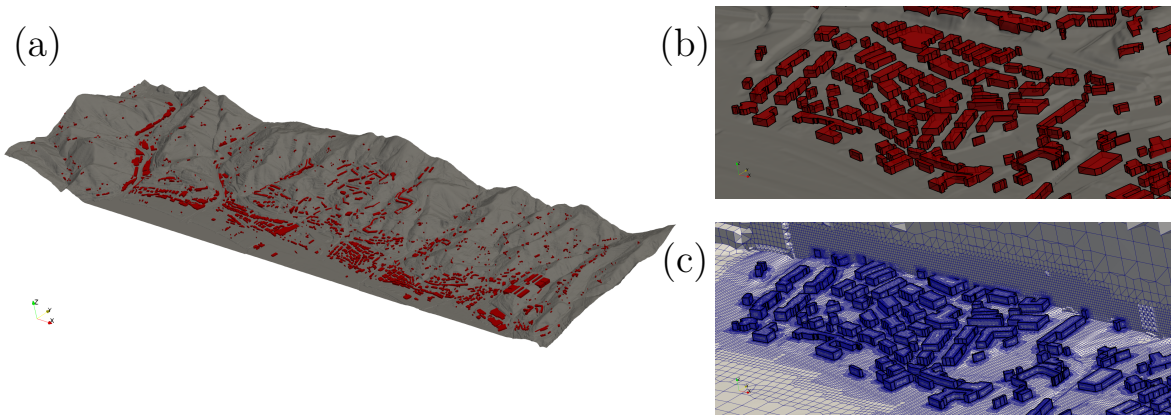

Figure 2. Grid generation procedure to obtain a digital twin of Genoa city: area of interest (a); input data – terrain and buildings STL files and feature edges (b); computational grid (c).

4. CONCLUDING REMARKS

This paper presented the progress and perspectives of the ongoing project aiming to develop the digital twin of the city of Genoa, Italy. In that perspective, the building and terrain topography geometries were built by adopting several simplification hypotheses discussed. The CFD digital twin model of Genoa was built by leveraging the open-source software `cfMesh` available within `OpenFOAM`. Building a digital twin model would allow the conducting of many different WE studies from the perspective of the ADAPTNOW project, with the most significant one targeting the evaluation of the hazard map of extreme winds over the larger area around Genoa. The details and the further development of this ongoing research study will be deeply discussed in the oral presentation.

ACKNOWLEDGEMENTS

This study was funded by ADAPTNOW Project – "ADAPTation Capacity Strengthening for Highly Affected and Exposed Territories in the Alps NOW" (Grant No. ASP0100048). ADAPTNOW is co-financed by the European Regional Development Fund through the Interreg Alpine Space programme. The authors also acknowledge the support of the Italian super- computing center CINECA for providing access to their High-Performance Computing (HPC) facilities needed to carry out the part of the research presented in this paper.

REFERENCES

Alemayehu, T.F. and Bitsuamlak, G.T (2022). Autonomous urban topology generation for urban flow modelling. Sustainable Cities and Society, 87, 104181.

Burlando, M. et al. (2020). Investigation of the Weather Conditions during the collapse of the Morandi bridge in Genoa on 14 August 2018 using Field Observations and WRF Model. Atmosphere 11(7), 724.

Douglas, D.H. and Peucker, T.K (1973). Algorithms for the reduction of the number of points required to represent a digitized line or its caricature. The Canadian Cartographer 10(2), 112–122.

OpenSCAD. (2024). The Programmers Solid 3D CAD Modeller. https://openscad.org.

Pađen I. et al. (2022). Towards Automatic Reconstruction of 3D City Models Tailored for Urban Flow Simulations. Frontiers in Built Environment, 8.

Ricci, A. et al. (2017). Local-scale forcing effects on wind flows in an urban environment: Impact of geometrical simplifications. Journal of Wind Engineering and Industrial Aerodynamics, 170, 238- 255.

Ricci, A. et al. (2022). Static downscaling of mesoscale wind conditions into an urban canopy layer by a CFD microscale model. Building Environment, 225, 109626.

Solari, G. et al. (2020). Detection, simulation, modelling and loading of thunderstorm outflows to design wind-safer and cost-efficient structures. Journal of Wind Engineering and Industrial Aerodynamics 200, 104142.